Technical Physics, Vol. 50, No. 11, 2005, pp. 1391–1401. Translated from Zhurnal Tekhnicheskoĭ Fiziki, Vol. 75, No. 11, 2005, pp. 1–10.

THEORETICAL AND MATHEMATICAL PHYSICS

System of Two Dielectric Cylinders Involving Charge Sources: I. Calculation of the Electric Field

Yu. P. Emets

Institute of Electrodynamics, National Academy of Sciences of Ukraine, Kiev, 03680 Ukraine

e-mail: emets@irpen.kiev.ua

Received September 13, 2004; in final form, March 31, 2005

Abstract—The electric field of two dielectric straight circular cylinders containing line charges on their axes is investigated. The cylindrical bodies in question are parallel and touch each other from the exterior. They have different dielectric permittivities, charges, and radii. Also, they are surrounded by an arbitrary dielectric medium. An analytic solution to the respective boundary-value problem is given, and the most important particular cases are analyzed. Special features of the electric field in the region around the contact of the dielectric cylinders are studied versus the permittivity of the material used and the relationship between electric charges.

INTRODUCTION

This article presents an analytic solution obtained for the electrostatic problem of electric-field formation in the system of two long and straight dielectric cylinders of circular shape in cross section that touch each other from the exterior. Line electric charges are assumed to occur on the axes of these cylindrical bodies. The problem is studied in a general formulation—that is, the permittivities of the cylinders and of the ambient medium are arbitrary and the electric charges are different. Under these conditions, the respective boundary-value problem is two-dimensional and has a closed solution that can be obtained by applying efficient methods of the theory of functions of a complex variable. In the final form, the expressions for the complex-valued electric-field strength are given by infinite series of simple poles of induced charges; in addition, there are simple poles of real-valued charges. A large number of known solutions to problems of electrostatics follow from the above solution as particular cases [1, 2]. Via a limiting transition, one can derive an expression for a line electric dipole in which charges have an insulating coating [3].

The problem under study has an obvious application in electrical engineering. By virtue of the known analogy of electrostatic fields, the results obtained here can also be extended to some similar problems in thermal-conductivity theory, diffusion theory, fluid dynamics, and some other fields of science.

This article is organized as follows. First, we present basic expressions for the electric field in the dielectric cylinders and in the ambient space. After that, we study special features of electric-field formation and consider some particular cases. The concluding part of the article contains an analytic solution to the boundary-value problem and a substantiation of our derivation of basic formulas. This order of exposition (it is inverse to the actual sequence of manipulations) makes it possible to get acquainted with the results of the present investigation without plunging into the technique and details of the calculations (for example, in view of the possibility of applying different methods for solving the problem being studied).

ELECTRIC FIELD OF THE SYSTEM

A schematic cross-sectional view of the system being studied is given in Fig. 1. In an infinite dielectric medium of permittivity ε_1, there occur two long and straight cylinders having dielectric permittivities ε_2 and ε_3 and radii r_1 and r_2, respectively. Charged filaments with line charges q_1 and q_2 are placed at the cylinder centers. The cylinders are parallel and touch each other along the generatrix. In this system, the electric field is two-dimensional.

Suppose, for the sake of definiteness, that the origin of the system of Cartesian coordinates x and y coincides

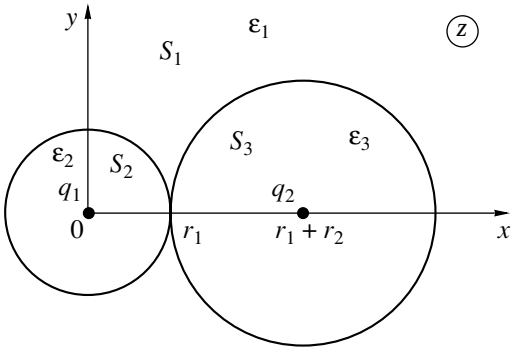

Fig. 1. Dielectric cylinders featuring line charges on their axes.

1063-7842/05/5011-1391$26.00 © 2005 Pleiades Publishing, Inc.

with the center of the cylinder (that is, with the point of intersection of its axis with a plane orthogonal to it) whose permittivity is ε_2 and that the x axis is directed along the line connecting the centers of the cylinders (Fig. 1). In the following, it will be shown that, in this coordinate frame, the electric field is given by

$$E_1(z) = \frac{1}{2\pi\varepsilon_1}\sum_{k=1}^{\infty}\left\{(\Delta_{12}\Delta_{13})^{k-1}\left[Q_1\left(z - r_1\frac{k-1}{k-1+\delta}\right)^{-1}\right.\right.$$
$$+ \Delta_{12}Q_2\left(z - r_1\frac{k-\delta}{k}\right) + Q_2\left(z - r_1\frac{k}{k-\delta}\right)^{-1}$$
$$\left.\left. + \Delta_{13}Q_1\left(z - r_1\frac{k+\delta}{k}\right)^{-1}\right]\right\}, \quad z \in S_1;$$

$$E_2(z) = \frac{1}{2\pi\varepsilon_2}\frac{q_1}{z} + \frac{1-\Delta_{12}}{2\pi\varepsilon_2}\sum_{k=1}^{\infty}\left\{(\Delta_{12}\Delta_{13})^{k-1}\left[\Delta_{13}Q_1\right.\right.$$
$$\left.\left.\times\left(z - r_1\frac{k+\delta}{k}\right)^{-1} + Q_2\left(z - r_1\frac{k}{k-\delta}\right)^{-1}\right]\right\}, \quad z \in S_2; \quad (1)$$

$$E_3(z) = \frac{1}{2\pi\varepsilon_3}\frac{q_2}{z - r_1 - r_2} + \frac{1-\Delta_{13}}{2\pi\varepsilon_3}$$
$$\times\sum_{k=1}^{\infty}\left\{(\Delta_{12}\Delta_{13})^{k-1}\left[Q_1\left(z - r_1\frac{k-1}{k-1+\delta}\right)^{-1}\right.\right.$$
$$\left.\left. + \Delta_{12}Q_2\left(z - r_1\frac{k-\delta}{k}\right)^{-1}\right]\right\}, \quad z \in S_3$$
$$(z = x + iy).$$

Here, $E_1(z) = E_{x1} - iE_{y1}$ is the complex-valued electric-field strength in the region exterior to the cylinders (region S_1 in Fig. 1); $E_2(z)$ is the complex-valued electric-field strength within the cylinder having the permittivity ε_2, the radius r_1, and the axial filament of line charge density q_1 (region S_2); $E_3(z)$ is the complex-valued electric-field strength in the cylinder whose parameters are ε_3, r_2, and q_2 (region S_3); Q_1 and Q_2 are the reduced charges defined as

$$Q_1 = q_1 - \Delta_{12}q_2, \quad Q_2 = q_2 - \Delta_{13}q_1; \quad (2)$$

the geometric parameter δ is given by

$$\delta = \frac{r_2}{r_1 + r_2} \quad (0 \le \delta \le 1); \quad (3)$$

and Δ_{12} and Δ_{13} are the relative dielectric permittivities

$$\Delta_{12} = \frac{\varepsilon_1 - \varepsilon_2}{\varepsilon_1 + \varepsilon_2}, \quad \Delta_{13} = \frac{\varepsilon_1 - \varepsilon_3}{\varepsilon_1 + \varepsilon_3} \quad (-1 \le \Delta_{12}, \Delta_{13} \le 1). \quad (4)$$

From the last formulas, it follows that

$$\frac{\varepsilon_1}{\varepsilon_2} = \frac{1+\Delta_{12}}{1-\Delta_{12}}, \quad \frac{\varepsilon_1}{\varepsilon_3} = \frac{1+\Delta_{13}}{1-\Delta_{13}}. \quad (5)$$

One can see that the electric field of the system being considered is represented by infinite series of first-order poles. These poles are generated by induced (fictitious) charges; there are also two real charges whose poles are situated at the centers of the circles. The charged filaments in space correspond to the real charge sources q_1 and q_2 in the plane.

In the complex plane, the electric field of a simple line pole can be represented as

$$E(z) = E_x - iE_y = \frac{1}{2\pi\varepsilon}\frac{G}{z - a} \quad (z = x + iy), \quad (6)$$

where G is the strength of the pole and a is its coordinate.

In expressions (1), the strength of the poles depends on the line charges q_1 and q_2 and on the dielectric permittivities of all elements of the system—that is, ε_1, ε_2, and ε_3 (Δ_{12} and Δ_{13}); it is noteworthy that this strength is independent of the geometric characteristics of the system (ratio of the radii of the cylinders). For ordinary dielectric materials, the absolute values of the parameters Δ_{12} and Δ_{13} are small ($|\Delta_{12}|, |\Delta_{13}| < 1$), whence it follows that the strength of the induced sources decreases with increasing k; therefore, we can retain a finite number of terms in the sums in expressions (1).

All poles are within the segment $[0, (r_1 + r_2)]$ of the real axis; with increasing k, their density grows as one approaches, from either side, the point $x = r$ at which the circles touch each other.

It should be noted that the coordinates of pairs of poles appearing in expressions (1),

$$a_k = r_1\frac{k-\delta}{k}, \quad b_k = r_1\frac{k}{k-\delta}, \quad (7)$$

are related by inversion with respect to the circle of radius r_1: $a_k b_k = r_1^2$.

In just the same way, the second pair of pole coordinates,

$$c_k = r_1\frac{k-1}{k-1+\delta}, \quad d_k = r_1\frac{k+\delta}{k}, \quad (8)$$

satisfies the relation of inversion with respect to the circle of radius r_2 (this is readily proven by means of some simple algebra upon transferring the coordinate origin to the center of the circle characterized by the parameters ε_3 and r_2).

Expressions (1) give a general solution to the problem being considered. They satisfy all conditions of the problem. Indeed, the electric field tends to zero for $z \longrightarrow \infty$ in the external region; the real charges q_1 and q_2 occur at the centers of the circles; and the normal

components of the displacement vector and the tangential components of the electric-field-strength vector are continuous at the boundaries of the circles, which separate media differing in permittivity (the boundary conditions can easily be tested by means of computer calculations).

The above solution makes it possible to establish some special features of electric-field formation in the inhomogeneous structure being considered. By way of example, we indicate that, for certain relations between the parameters of the system, the electric-field strength has minima in the interior of the cylinders and increases toward their boundary at the point where they touch each other (in the case of a single cylinder featuring a charged filament on the axis, the field strength is known to be in inverse proportion to the radius). We illustrate the aforesaid in Fig. 2, which shows the variation of the electric-field strength along the x axis at the following values of the parameters: $q_2 = -2q_1$, $\varepsilon_1 = 1$, $\varepsilon_2 = 3$, $\varepsilon_3 = 10$ ($\Delta_{12} = -0.5$ and $\Delta_{13} = -0.818182$), and $r_1 = r_2$ ($\delta = 0.5$). At these parameter values, the electric-field strength at the point where the circles touch each other takes the values of $E_{x2} = 2.717949$ and $E_{x3} = 0.815385$. At the points $x = 0.55$ and $x = 1.3$, which are the points of minima on the x axis, we have $E_{x2\,\min} = 1.593578$ and $E_{x3\,\min} = 0.568824$, respectively. The curves in Fig. 2 are given in terms of the relative quantities

$$E_{1,2,3*} = E_{1,2,3}/(q_1/2\pi\varepsilon_1 r_1), \quad x_* = x/r_1. \qquad (9)$$

To avoid encumbering the presentation, the asterisks on the relative quantities are suppressed.

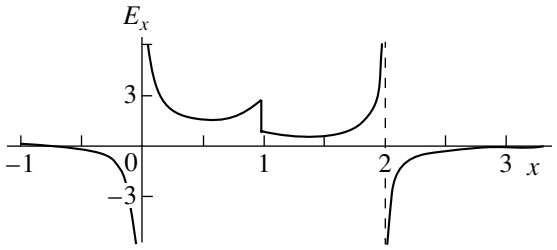

Fig. 2. Variation of the electric-field strength along the x axis.

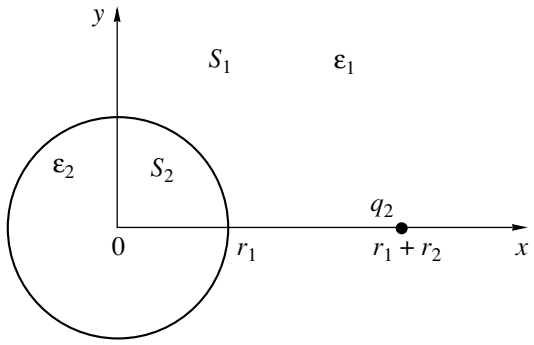

Fig. 3. Dielectric cylinder and charged filament.

SOME PARTICULAR CASES

The general expressions for the electric field in (1) make it possible to obtain a number of particular solutions, which are of interest in themselves. Some of these solutions are discussed in the present section (solutions to some known problems [1, 2] are also given to test our results).

(i) If the line charges do not have a dielectric environment, $\varepsilon_\nu \equiv \varepsilon$ ($\nu = 1, 2, 3$) ($\Delta_{12} = \Delta_{13} = 0$), then we have an elementary system of two parallel charged filaments in a homogeneous medium that are separated by the distance $h = r_1 + r_2$ (the charges lie on the x axis, the origin of the coordinate frame being coincident with the position of the charges whose line density is q_1). In this case, we have

$$E(z) = \frac{q_1}{2\pi\varepsilon z} + \frac{q_2}{2\pi\varepsilon(z-h)}, \qquad E(z) \equiv E_\nu(z) \quad (\nu = 1, 2, 3). \qquad (10)$$

(ii) Let the system being considered consist of one dielectric cylinder characterized by the parameters ε_2, r_1, and q_1. The other cylinder and the other charged filament are absent: $\varepsilon_3 = \varepsilon_1$ ($\Delta_{13} = 0$) and $q_2 = 0$. In this case, expressions (1) reduce to an extremely simple form,

$$E_1(z) = \frac{q_1}{2\pi\varepsilon_1 z} \ (|z| \ge r_1), \qquad E_2(z) = \frac{q_1}{2\pi\varepsilon_2 z} \ (|z| \le r_1), \quad E_3(z) = E_1(z), \qquad (11)$$

where ε_1 is the permittivity of the medium surrounding the cylinder.

(iii) Expressions (1) provide a solution to the well-known problem of the electric field of a dielectric cylinder near which there occurs a charged filament parallel to it [1]. Suppose, for the sake of definiteness, that the parameters of the dielectric cylinder are ε_2 and r_1 and that the charged filament has a line charge density q_2 (see Fig. 3). In accordance with these conditions, we must set

$$q_1 = 0, \quad \varepsilon_3 = \varepsilon_1 \ (\Delta_{13} = 0), \quad h = r_1 + r_2. \qquad (12)$$

As a result, we obtain

$$E_1(z) = \frac{1}{2\pi\varepsilon_1}\left[\frac{q_2}{z-h} - \Delta_{12} q_2\left(\frac{1}{z} - \frac{1}{z - r_1^2/h}\right)\right] \quad (|z| \ge r_1), \qquad (13)$$

$$E_2(z) = \frac{q_2(1-\Delta_{12})}{2\pi\varepsilon_2(z-h)} \ (|z| \le r_1), \quad E_3(z) = E_1(z),$$

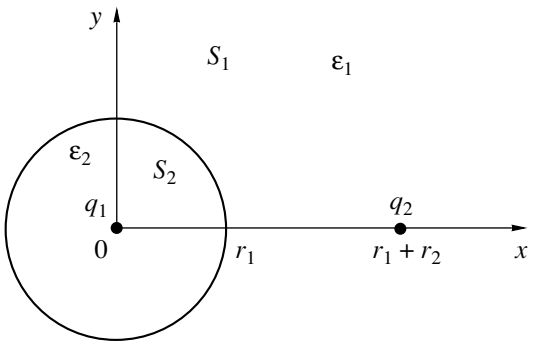

Fig. 4. Dielectric cylinder carrying a line charge on the axis and charged filament outside the cylinder.

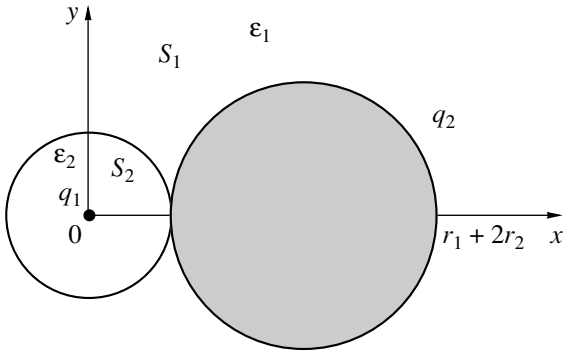

Fig. 5. Dielectric cylinder carrying a charge on the axis and metallic wire.

where, as before, ε_1 is the permittivity of the medium surrounding the cylinder.

(iv) Let only one dielectric cylinder featuring a charged filament (the parameters of the cylinder are ε_2, r_1, and q_1) be in the system considered originally. Furthermore, a charged filament that carries a line charge density q_2 and which is parallel to the cylinder is situated at the distance $h = r_1 + r_2$ from the cylinder axis (see Fig. 4). The solution corresponding to these conditions is obtained from expressions (1) at $\varepsilon_3 = \varepsilon_1$ ($\Delta_{13} = 0$). Specifically, we have

$$E_1(z) = \frac{1}{2\pi\varepsilon_1}\left[\frac{q_2}{z-h} + \frac{q_1 - \Delta_{12}q_2}{z} + \frac{\Delta_{12}q_2}{z - r_1^2/h}\right] \quad (|z| \geq r_1),$$

$$E_2(z) = \frac{1}{2\pi\varepsilon_2}\left[\frac{q_1}{z} + \frac{q_2(1-\Delta_{12})}{z-h}\right] \quad (|z| \leq r_1), \qquad (14)$$

$$E_3(z) = E_1(z).$$

Upon setting $q_1 = 0$, we arrive at the solution quoted in item (iii).

(v) Suppose that all of the conditions listed in item (iv) hold, the only difference being that the filament carrying the charge density q_2 is situated at the cylinder surface, at the point $x = r_1$ on the x axis. The electric field in this system is obtained from expressions (1) by setting $r_2 = 0$ and $\varepsilon_3 = \varepsilon_1$ ($\Delta_{13} = 0$).

We have

$$E_1(z) = \frac{1}{2\pi\varepsilon_1}\left[\frac{q_1 - \Delta_{12}q_2}{z} + \frac{q_2(1+\Delta_{12})}{z-r_1}\right] \quad (|z| \geq r_1),$$

$$E_2(z) = \frac{1}{2\pi\varepsilon_2}\left[\frac{q_1}{z} + \frac{q_2(1-\Delta_{12})}{z-r_1}\right] \quad (|z| \leq r_1), \qquad (15)$$

$$E_3(z) = E_1(z).$$

These expressions also follow from formulas (14) upon setting $h = r_1$.

(vi) If, in expressions (1), the permittivity ε_3 is made to tend to infinity (in electrostatics, this formal transformation corresponds to going over from a dielectric to an ideally conducting material [1]), then we obtain the solution to the problem where a dielectric cylinder characterized by the parameters ε_2, r_1, and q_1 touches a metallic wire of radius r_2, the wire carrying a line charge density q_2 (see Fig. 5). For $\varepsilon_3 \longrightarrow \infty$ ($\Delta_{13} = -1$), expressions (1) assume the form

$$E_1(z) = \frac{1}{2\pi\varepsilon_1}\sum_{k=1}^{\infty}\left\{(-\Delta_{12})^{k-1}\left[Q_1\left(z - r_1\frac{k-1}{k-1+\delta}\right)^{-1}\right.\right.$$

$$+ \Delta_{12}Q_2\left(z - r_1\frac{k-\delta}{k}\right)^{-1} + Q_2\left(z - r_1\frac{k}{k-\delta}\right)^{-1}$$

$$\left.\left. - Q_1\left(z - r_1\frac{k+\delta}{k}\right)^{-1}\right]\right\}, \quad z \in S_1;$$

$$E_2(z) = \frac{1}{2\pi\varepsilon_2}\frac{q_1}{z} + \frac{1-\Delta_{12}}{2\pi\varepsilon_2} \qquad (16)$$

$$\times \sum_{k=1}^{\infty}\left\{(-\Delta_{12})^{k-1}\left[-Q_1\left(z - r_1\frac{k+\delta}{k}\right)^{-1}\right.\right.$$

$$\left.\left. + Q_2\left(z - r_1\frac{k}{k-\delta}\right)^{-1}\right]\right\}, \quad z \in S_2;$$

$$E_3(z) = 0, \quad z \in S_3,$$

where we now have

$$Q_1 = q_1 - \Delta_{12}q_2, \quad Q_2 = q_1 + q_2. \qquad (17)$$

Setting $q_2 = 0$ in expressions (16), we arrive at the solution to the problem where a dielectric cylinder featuring a charged filament on the axis touches an uncharged metallic wire of radius r_2. We note that the electric-field strength in the vicinity of this contact changes nonmonotonically, developing a minimum. The graph representing the variation of the electric-field strength along the x axis is given in Fig. 6; this

graph was constructed at the same parameter values as those used for the curves in Fig. 2, the only difference being that, now, $\varepsilon_3 \longrightarrow \infty$ ($\Delta_{13} = -1$). The dashed curves correspond to the system at $q_2 = 0$.

(vii) Upon supplementing the condition in item (vi) with the limiting transition $\varepsilon_2 \longrightarrow \infty$ ($\Delta_{12} = -1$), we take into account the equality

$$Q_1 = Q_2 = q_1 + q_2 \tag{18}$$

in order to recast expressions (16) into the form

$$E_1(z) = \frac{q_1 + q_2}{2\pi\varepsilon_1}\sum_{k=1}^{\infty}\left[\left(z - r_1\frac{k-1}{k-1+\delta}\right)^{-1} - \left(z - r_1\frac{k-\delta}{k}\right)^{-1} + \left(z - r_1\frac{k}{k-\delta}\right)^{-1} - \left(z - r_1\frac{k+\delta}{k}\right)^{-1}\right], \quad z \in S_1; \tag{19}$$

$$E_2(z) = 0, \quad z \in S_2; \quad E_3(z) = 0, \quad z \in S_3.$$

Expressions (19) give the solution to the problem of the electric field of two straight metallic wires having a circular shape in the cross section, their radii being r_1 and r_2. The wires touch each other and carry the line charge density $q_1 + q_2$.

(viii) From expressions (1), one can obtain the solution to the problem of the electric field generated by the following system. A dielectric cylinder featuring a charged filament on the axis is situated at the interface of two different media. A schematic view of the system and its parameters are given in Fig. 7. The solution to this problem is obtained from expressions (1) upon setting $q_2 = 0$ and going over to the limit $r_2 \longrightarrow \infty$ ($\delta = 1$).

After some simple algebra, we arrive at

$$E_1(z) = \frac{q_1}{2\pi\varepsilon_1}(1 - \Delta_{12}\Delta_{13}) \times \sum_{k=1}^{\infty}\left\{(\Delta_{12}\Delta_{13})^{k-1}\left[\left(z - r_1\frac{k-1}{k}\right)^{-1} + \Delta_{13}\left(z - r_1\frac{k+1}{k}\right)^{-1}\right]\right\}, \quad z \in S_1;$$

$$E_1(z) = \frac{1}{2\pi\varepsilon_2}\frac{q_1}{z} + \frac{q_1}{2\pi\varepsilon_2}\Delta_{13}(1 - \Delta_{12})(1 - \Delta_{12}\Delta_{13}) \times \sum_{k=1}^{\infty}\left[(\Delta_{12}\Delta_{13})^{k-1}\left(z - r_1\frac{k+1}{k}\right)^{-1}\right], \quad z \in S_2; \tag{20}$$

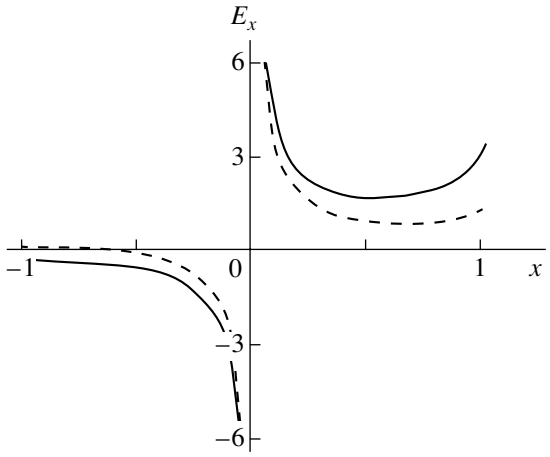

Fig. 6. Variation of the electric-field strength along the x axis in the system depicted in Fig. 5.

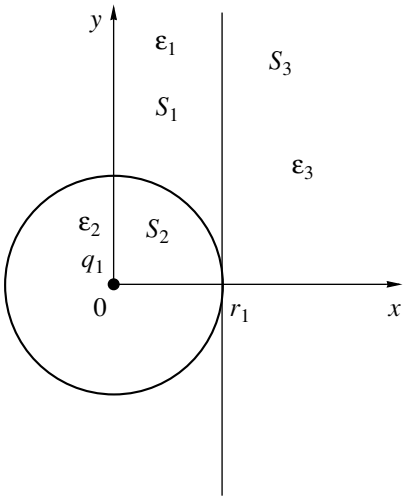

Fig. 7. Dielectric cylinder featuring a line charge on the axis and occurring at the interface of two different media.

$$E_3(z) = \frac{q_1}{2\pi\varepsilon_3}(1 - \Delta_{13})(1 - \Delta_{12}\Delta_{13}) \times \sum_{k=1}^{\infty}\left[(\Delta_{12}\Delta_{13})^{k-1}\left(z - r_1\frac{k-1}{k}\right)^{-1}\right], \quad z \in S_3.$$

This solution was constructed independently in [4] for a specially formulated problem. Also, many particular cases associated with the system being considered were analyzed in that study.

(ix) Expressions (1) make it possible to obtain a formula that determines the electric field of line dipole whose charged filaments have dielectric coatings, which are not identical in general.

Suppose that, in the system considered initially, the cylinders have equal radii, $r_1 = r_2 \equiv r$. Further, charged filaments carrying the charge densities $q_1 \equiv q$ and $q_2 =$

$-q_1$ occur on the cylinder axes. We place the origin of the Cartesian coordinates at the point where the circles touch in the *xy* plane.

Under these conditions, the following asymptotic estimates are valid at large distances from the system (in the plane orthogonal to the cylinder axes):

$$z^2 \gg [r/(2r-1)]^2, \quad z^2 \gg (r/2k)^2. \tag{21}$$

By using these estimates, we can recast the first expression in (1) into the form

$$E_1(z) = \frac{qr}{2\pi\varepsilon_1 z^2}\sum_{k=1}^{\infty}\left[(\Delta_{12}\Delta_{13})^{k-1}\left(\frac{2+\Delta_{12}+\Delta_{13}}{2k-1} - \frac{2\Delta_{12}\Delta_{13}+\Delta_{12}+\Delta_{13}}{2k}\right)\right], \quad z \in S_1. \tag{22}$$

Expression (22) determines the electric field of a line dipole formed by insulated charged filaments. It was derived and studied in detail in [3].

SOLVING THE BOUNDARY-VALUE PROBLEM

The electric field in the system is determined by the linear equations of electrostatics,

$$\mathrm{curl}\mathbf{E} = 0, \quad \mathrm{div}\mathbf{D} = 0, \quad \mathbf{D} = \varepsilon\mathbf{E}, \tag{23}$$

where **E** is the electric-field-strength vector, **D** is the electric-field-displacement vector, and ε is the permittivity of the material being considered.

In the plane orthogonal to the cylinder axes, Eqs. (23) are two-dimensional; therefore, we can introduce the complex-valued functions

$$E(z) = E_x - iE_y, \quad D(z) = D_x - iD_y \ (z = x + iy), \tag{24}$$

which satisfy the Cauchy–Riemann equations.

The electric-field vectors **E** and **D** and the functions $E(z)$ and $D(z)$ are related as

$$\mathbf{E} = \overline{E(z)}, \quad \mathbf{D} = \overline{D(z)}, \tag{25}$$

where an overbar denotes complex conjugation.

A schematic view of the system being considered is given in Fig. 1. Here, the plane of the complex variable z is partitioned by the circles L_1 and L_2 into three regions S_1, S_2, and S_3, where the dielectric permittivities are ε_1, ε_2, and ε_3, respectively. The pointlike charges q_1 and q_2 at the centers of the circles L_1 and L_2 serve as the sources of the electric field. Field sources are described mathematically by simple poles. Thus, the sectionally analytic function $E(z) = \{E_1(z), E_2(z), E_3(z)\}$ consists of the analytic function $E_1(z)$ in the region S_1 and two meromorphic functions, $E_2(z)$ in the region S_2 and $E_3(z)$ in the region S_3.

At infinity, the electric field disappears; that is,

$$E_1(\infty) = 0. \tag{26}$$

The meromorphic functions $E_2(z)$ and $E_3(z)$ are written as

$$E_2(z) = \frac{A}{z} + E_2'(z), \quad z \in S_2;$$
$$E_3(z) = \frac{B}{z-h} + E_3'(z) \ (h = r_1 + r_2), \ z \in S_3, \tag{27}$$

where A and B are constants and $E_2'(z)$ and $E_3'(z)$ are analytic functions in the regions S_2 and S_3, respectively.

The constants A and B are given by

$$A = \frac{1}{2\pi\varepsilon_2}, \quad B = \frac{1}{2\pi\varepsilon_3}. \tag{28}$$

In the absence of free charges at the interface of different media, the electric charge satisfies standard boundary conditions: the normal components of the vector **D** and the tangential components of the vector **E** are continuous. In terms of the function $E(z)$, these conditions are written as

$$\mathrm{Re}\{n(t)\varepsilon_1 E_1(t)\} = \mathrm{Re}\{n(t)\varepsilon_m E_m(t)\},$$
$$\mathrm{Im}\{n(t)E_1(t)\} = \mathrm{Im}\{n(t)E_m(t)\}, \tag{29}$$
$$t \in L_{m-1} \ (m = 2, 3),$$

where $n(t)$ is a unit normal to the boundary contours L_1 and L_2,

$$n(t) = \frac{t}{r_1}, \quad t \in L_1 \ (t = r_1 e^{i\theta}),$$
$$n(t) = \frac{t - r_1 - r_2}{r_2}, \quad t \in L_2 \ (t = r_1 + r_2(1 + e^{i\theta})), \tag{30}$$
$$0 \le \theta \le 2\pi.$$

In an expanded form, the equalities in (29) are written as

$$\varepsilon_1 E_1(t) + \varepsilon_1\left(\frac{r_1}{t}\right)^2\overline{E_1(t)} = \varepsilon_2 E_2(t) + \varepsilon_2\left(\frac{r_1}{t}\right)^2\overline{E_2(t)},$$
$$E_1(t) - \left(\frac{r_1}{t}\right)^2\overline{E_1(t)} = E_2(t) - \left(\frac{r_1}{t}\right)^2\overline{E_2(t)}, \ t \in L_1;$$
$$\varepsilon_1 E_1(t) + \varepsilon_1\left(\frac{r_2}{t - r_1 - r_2}\right)^2\overline{E_1(t)} = \varepsilon_3 E_3(t) + \varepsilon_3\left(\frac{r_2}{t - r_1 - r_2}\right)^2\overline{E_3(t)}, \tag{31}$$
$$E_1(t) - \left(\frac{r_2}{t - r_1 - r_2}\right)^2\overline{E_1(t)} = E_3(t) - \left(\frac{r_2}{t - r_1 - r_2}\right)^2\overline{E_3(t)}, \quad t \in L_2,$$

where we have taken into account the relations

$$\dot{t} = \frac{r_1^2}{t}, \quad \dot{t} - r_1 - r_2 = \frac{r_2^2}{t - r_1 - r_2}. \tag{32}$$

In order to obtain simplified boundary conditions, we eliminate one of the functions, for example, $\overline{E_1(t)}$, from each pair of the relations in (31). As a result, we arrive at

$$\begin{gathered} 2\varepsilon_1 E_1(t) = (\varepsilon_1 + \varepsilon_2)E_2(t) - (\varepsilon_1 - \varepsilon_2)\left(\frac{r_1}{t}\right)^2 \overline{E_2(t)}, \\ t \in L_1; \\ 2\varepsilon_1 E_1(t) = (\varepsilon_1 + \varepsilon_3)E_3(t) \\ -(\varepsilon_1 - \varepsilon_3)\left(\frac{r_2}{t - r_1 - r_2}\right)^2 \overline{E_3(t)}, \quad t \in L_2. \end{gathered} \tag{33}$$

By using relations (4) and (5), we can recast Eqs. (33) into the form

$$\begin{gathered} (1 + \Delta_{12})E_1(t) = E_2(t) - \Delta_{12}\left(\frac{r_1}{t}\right)^2 \overline{E_2(t)}, \quad t \in L_1; \\ (1 + \Delta_{13})E_1(t) \\ = E_3(t) - \Delta_{13}\left(\frac{r_1}{t - r_1 - r_2}\right)^2 \overline{E_3(t)}, \quad t \in L_2. \end{gathered} \tag{34}$$

Thus, a calculation of the electric field in the system being considered reduces to solving boundary-value problem (34) subjected to additional conditions (26) and (27). In the theory of analytic functions, this problem is referred to as the boundary-value problem of Riemann conjugation (in the mathematical literature, it is usually called the boundary-value problem of *R*-linear conjugation). In the present case, a solution to the problem formulated above can be obtained in a closed form by using conformal-mapping methods and the analytic-continuation principle. In the process of calculation, we will obtain a functional equation that has an exact solution. It is this approach to studying the Riemann boundary-value problem that was developed in [4–6].

Let us map the z plane onto the ζ plane by means of the linear-fractional function

$$z = T(\zeta) = r_1\frac{\zeta + 1}{\zeta - 1} \ (\zeta = \xi + i\eta). \tag{35}$$

Under this mapping, the circles L_1 and L_2 go over to the straight lines $\lambda_1 = (\zeta: \mathrm{Re}\,\zeta = 0)$ and $\lambda_2 = (\zeta: \mathrm{Re}\,\zeta = \gamma)$, respectively; the point at infinity goes over to the point $\zeta = 1$; and the regions S_ν ($\nu = 1, 2, 3$) go over to the regions Ω_ν in the ζ plane (see Figs. 1 and 8). Here, we have used the notation

$$\gamma = \frac{1}{\delta} = \frac{r_1 + r_2}{r_2} \ (1 \le \gamma < \infty). \tag{36}$$

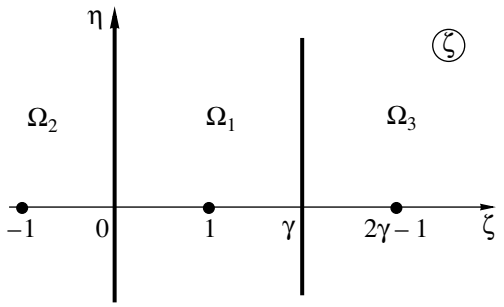

Fig. 8. Conformal map of the system shown in Fig. 1.

The function

$$\zeta = T^{-1}(z) = \frac{z + r_1}{z - r_1} \tag{37}$$

realizes the mapping inverse to (35).

In the mapped plane, the sectionally analytic function

$$f(\zeta) = E(T(\zeta)) \tag{38}$$

satisfies, on the contours λ_1 and λ_2, the boundary conditions

$$\begin{gathered} (1 + \Delta_{12})f_1(\tau) = f_2(\tau) - \Delta_{12}\left(\frac{r_1}{T(\tau)}\right)^2 \overline{f_2(\tau)}, \\ \tau \in \lambda_1; \\ (1 + \Delta_{13})f_1(\tau) \\ = f_3(\tau) - \Delta_{13}\left(\frac{r_2}{T(\tau) - r_1 - r_2}\right)^2 \overline{f_3(\tau)}, \quad \tau \in \lambda_2. \end{gathered} \tag{39}$$

For the function $f(\zeta)$ at the point $\zeta = 1$, the condition in (26) yields

$$f_1(1) = 0. \tag{40}$$

In accordance with expressions (27), the meromorphic functions $f_2(\zeta)$ and $f_3(\zeta)$ in the mapped plane of the variable ζ are written as

$$\begin{aligned} f_2(\zeta) &= A'\frac{\zeta - 1}{\zeta + 1} + f_2'(\zeta), \\ f_3(\zeta) &= \frac{B'(\zeta - 1)}{\zeta - (2r_1 + r_2)/r_2} + f_3'(\zeta), \end{aligned} \tag{41}$$

where $f_2'(\zeta)$ and $f_3'(\zeta)$ are analytic functions in the regions Ω_2 and Ω_3, respectively, and A' and B' are the constants that are related to the constants A and B by the equations

$$A' = \frac{A}{r_1}, \quad B' = -\frac{B}{r_2}. \tag{42}$$

The function $f_1(\zeta)$ can be represented in the form

$$f_1(\zeta) = f_1^+(\zeta) + f_1^-(\zeta), \quad (43)$$

where the function $f_1^+(\zeta)$ is analytic in the half-plane $\mathrm{Re}\,\zeta < \gamma$ and the function $f_1^-(\zeta)$ is analytic in the half-plane $\mathrm{Re}\,\zeta > 0$.

With allowance for relation (43), the equalities in (39) can be recast into the form

$$\begin{aligned}(1+\Delta_{12})f_1^+(\tau) - f_2(\tau) &= -\Delta_{12}\left(\frac{r_1}{T(\tau)}\right)^2\overline{f_2(\tau)}\\ &\quad -(1+\Delta_{12})f_1^-(\tau), \quad \tau\in\lambda_1;\\ (1+\Delta_{13})f_1^-(\tau) - f_3(\tau) &= -\Delta_{13}\left(\frac{r_2}{T(\tau)-r_1-r_2}\right)^2\overline{f_3(\tau)}\\ &\quad -(1+\Delta_{13})f_1^+(\tau), \quad \tau\in\lambda_2.\end{aligned} \quad (44)$$

According to the theorem of analytic continuation as applied to (44), one can introduce two meromorphic functions:

$$\Phi(\zeta) = \begin{cases}(1+\Delta_{12})f_1^+(\zeta) - f_2(\zeta), & \mathrm{Re}\,\zeta \le 0\\ -(1+\Delta_{12})f_1^-(\zeta) - \Delta_{12}\left(\dfrac{r_1}{T(\zeta)}\right)^2\overline{f_2(-\bar\zeta)}, & \mathrm{Re}\,\zeta \ge 0;\end{cases} \quad (45)$$

$$\Psi(\zeta) = \begin{cases}(1+\Delta_{13})f_1^-(\zeta) - f_3(\zeta), & \mathrm{Re}\,\zeta \le \gamma\\ -(1+\Delta_{13})f_1^+(\zeta)\\ -\Delta_{13}\left(\dfrac{r_2}{T(\zeta)-r_1-r_2}\right)^2\overline{f_3(2\gamma-\bar\zeta)}, & \mathrm{Re}\,\zeta \ge \gamma.\end{cases}$$

We note that expressions (45) involve the functions

$$\frac{r_1}{T(\zeta)} = \frac{\zeta-1}{\zeta+1}, \quad \frac{r_2}{T(\zeta)-r_1-r_2} = \frac{\zeta-1}{2\gamma-1-\zeta}. \quad (46)$$

Of these, the first is analytic for $\mathrm{Re}\,\zeta > 0$, while the second is analytic for $\mathrm{Re}\,\zeta < \gamma$.

From the above formulas, it follows that the function $\Phi(\zeta)$ has a simple pole at the point $\zeta = -1$ and a first-order zero at $\zeta = 1$ (under the conformal mapping of the z plane onto the ζ plane, these points appear as the images of, respectively, the coordinate origin and the point at infinity). The function $\Psi(\zeta)$ possesses similar properties.

In the ζ plane, the meromorphic functions $\Phi(\zeta)$ and $\Psi(\zeta)$ admit the existence of simple poles at the points $\zeta = -1$ and $\zeta = 2\gamma - 1$, respectively; therefore, it can be stated on the basis of the generalized Liouville theorem that they are given by

$$\Phi(\zeta) = -A'\frac{\zeta-1}{\zeta+1} + C_1, \quad \Psi(\zeta) = -B'\frac{\zeta-1}{\zeta-2\gamma+1} + C_2, \quad (47)$$

where C_1 and C_2 are constants that are determined from additional conditions—for example, from the behavior of the functions $\Psi(\zeta)$ and $\Phi(\zeta)$ at the points where their values are known. For such a point, we take that at $\zeta = 1$. An analysis reveals that $C_1 = C_2 = 0$.

From expressions (43) and (47), it follows that the sectionally analytic function $f(\zeta)$ admits the representation

$$f(\zeta) = \begin{cases}f_2(\zeta) = (1+\Delta_{12})f_1^+(\zeta) + A'\dfrac{\zeta-1}{\zeta+1}, & \mathrm{Re}\,\zeta < 0\\ f_1(\zeta) = f_1^+(\zeta) + f_1^-(\zeta), & 0 < \mathrm{Re}\,\zeta < \gamma\\ f_3(\zeta) = (1+\Delta_{13})f_3^-(\zeta) + B'\dfrac{\zeta-1}{\zeta-2\gamma+1}, & \mathrm{Re}\,\zeta > \gamma.\end{cases} \quad (48)$$

Thus, the problem being considered has been reduced to that of determining the functions $f_1^+(\zeta)$ and $f_1^-(\zeta)$. They will be found consecutively by solving a functional equation with respect to one of them.

Combining expressions (45) and (47), we obtain two pairs of equalities,

$$\begin{aligned}f_2(\zeta) - (1+\Delta_{12})f_1^+(\zeta) &= A'\frac{\zeta-1}{\zeta+1}, \quad \mathrm{Re}\,\zeta < 0;\\ (1+\Delta_{12})f_1^-(\zeta) + \Delta_{12}\left(\frac{\zeta-1}{\bar\zeta+1}\right)^2\overline{f_2(-\bar\zeta)} &= A'\frac{\zeta-1}{\zeta+1}, \quad \mathrm{Re}\,\zeta > 0;\\ f_3(\zeta) - (1+\Delta_{13})f_1^-(\zeta) &= \frac{B'(\zeta-1)}{\zeta-2\gamma+1}, \quad \mathrm{Re}\,\zeta > \gamma;\\ (1+\Delta_{13})f_1^+(\zeta) + \Delta_{13}\left(\frac{\zeta-1}{\zeta-2\gamma+1}\right)^2\overline{f_3(2\gamma-\bar\zeta)} &= \frac{B'(\zeta-1)}{\zeta-2\gamma+1}, \quad \mathrm{Re}\,\zeta < \gamma.\end{aligned} \quad (49)$$

Subsequent manipulations are aimed at deriving one equality involving one unknown function. In (49), we make the transformation of symmetry with respect to the straight line λ_1 in the second equality and the transformation of symmetry with respect to the straight line λ_2 in the third equality. As a result, we arrive at

$$f_2(\zeta) - (1+\Delta_{12})f_1^+(\zeta) = A'\frac{\zeta-1}{\zeta+1}, \quad \mathrm{Re}\,\zeta < 0;$$

$$(1+\Delta_{12})\overline{f_1^-(-\bar{\zeta})}+\Delta_{12}\left(\frac{\zeta+1}{\zeta-1}\right)^2 f_2(\zeta)$$
$$= A'\frac{\zeta+1}{\zeta-1},\quad \mathrm{Re}\zeta<0;$$
$$\overline{f_3(2\gamma-\bar{\zeta})}-(1+\Delta_{13})\overline{f_1^-(2\gamma-\bar{\zeta})} \tag{50}$$
$$= B'\frac{\zeta-2\gamma+1}{\zeta-1},\quad \mathrm{Re}\zeta<\gamma;$$
$$(1+\Delta_{13})f_1^+(\zeta)+\Delta_{13}\left(\frac{\zeta-1}{\zeta-2\gamma+1}\right)^2\overline{f_3(2\gamma-\bar{\zeta})}$$
$$= \frac{B'/(\zeta-1)}{\xi-2\gamma+1},\quad \mathrm{Re}\zeta<\gamma.$$

After the elimination of the function $f_2(\zeta)$ from the first pair of equalities and the elimination of the function $f_3(\zeta)$ from the second pair, some simple transformations lead to the relations

$$\Delta_{12}\left(\frac{\zeta+1}{\zeta-1}\right)^2 f_1^+(\zeta)+\overline{f_1^-(-\bar{\zeta})} = A''\frac{\zeta-1}{\zeta+1},\quad \mathrm{Re}\zeta<0;$$
$$\Delta_{13}\left(\frac{\zeta-1}{\zeta-2\gamma+1}\right)^2\overline{f_1^-(2\gamma-\bar{\zeta})}+f_1^+(\zeta) \tag{51}$$
$$= \frac{B''(\zeta-1)}{\zeta-2\gamma+1},\quad \mathrm{Re}\zeta<\gamma,$$

where

$$A'' = A'\frac{1-\Delta_{12}}{1+\Delta_{12}},\quad B'' = B'\frac{1-\Delta_{13}}{1+\Delta_{13}}. \tag{52}$$

From relations (51), one can eliminate one of the two unknown functions—for example, $f_1^+(\zeta)$. We then have

$$\overline{f_1^-(-\bar{\zeta})}-\Delta_{12}\Delta_{13}\left(\frac{\zeta+1}{\zeta-2\gamma+1}\right)^2\overline{f_1^-(2\gamma-\bar{\zeta})}$$
$$= A''\frac{\zeta+1}{\zeta-1}-\frac{\Delta_{12}B''(\zeta+1)^2}{(\zeta-1)(\zeta-2\gamma+1)},\quad \mathrm{Re}\zeta<0. \tag{53}$$

In this equality, we perform the transformation of symmetry with respect to the straight line λ_1. This yields

$$f_1^-(\zeta)-\Delta_{12}\Delta_{13}\left(\frac{\zeta-1}{\zeta+2\gamma-1}\right)^2 f_1^-(\zeta+2\gamma)$$
$$= A''\frac{\zeta-1}{\zeta+1}-\frac{\Delta_{12}B''(\zeta-1)^2}{(\zeta+1)(\zeta+2\gamma-1)},\quad \mathrm{Re}\zeta>0. \tag{54}$$

Relation (54) is a functional equation with respect to the unknown function $f_1^-(\zeta)$. Its solution can be found by the method of mathematical induction.

By consecutively substituting into this function an argument that increases by 2γ, we arrive at the relations

$$f_1^-(\zeta+2\gamma) = A''\frac{\zeta+2\gamma-1}{\zeta+2\gamma+1}-\frac{\Delta_{12}B''(\zeta+2\gamma-1)^2}{(\zeta+2\gamma+1)(\zeta+4\gamma-1)}$$
$$+\Delta_{12}\Delta_{13}\left(\frac{\zeta+2\gamma-1}{\zeta+4\gamma-1}\right)^2 f_1^-(\zeta+4\gamma), \tag{55}$$
$$f_1^-(\zeta+4\gamma) = A''\frac{\zeta+4\gamma-1}{\zeta+4\gamma+1}-\frac{\Delta_{12}B''(\zeta+4\gamma-1)^2}{(\zeta+4\gamma+1)(\zeta+6\gamma-1)}$$
$$+\Delta_{12}\Delta_{13}\left(\frac{\zeta+4\gamma-1}{\zeta+6\gamma-1}\right)^2 f_1^-(\zeta+6\gamma),$$

and so on. After the n-fold application of this procedure and the use of relations (55), we reduce Eq. (54) to the form

$$f_1^-(\zeta) = (\zeta-1)^2\sum_{k=1}^{n}\left\{(\Delta_{12}\Delta_{13})^{k-1}\left[\frac{A''}{(\zeta+2(k-1)\gamma)^2-1}\right.\right.$$
$$\left.\left.-\frac{\Delta_{12}B''}{(\zeta+2(k-1)\gamma+1)(\zeta+2k\gamma-1)}\right]\right\} \tag{56}$$
$$+(\Delta_{12}\Delta_{13})^n\left(\frac{\zeta-1}{\zeta+2n\gamma-1}\right)^2 f_1^-(\zeta+2n\gamma),\quad \mathrm{Re}\zeta>0.$$

The last term on the right-hand side of (56) involves the small parameters $|\Delta_{12}|$, $|\Delta_{13}|$, $\gamma<1$, the function $f_1^-(\zeta)$ tending to zero at infinity; therefore, the residual term tends to zero as the number n grows indefinitely. It follows that, for $n\longrightarrow\infty$, the function $f_1^-(\zeta)$ is given by

$$f_1^-(\zeta) = (\zeta-1)^2\sum_{k=1}^{\infty}\left\{(\Delta_{12}\Delta_{13})^{k-1}\left[\frac{A''}{(\zeta+2(k-1)\gamma)^2-1}\right.\right.$$
$$\left.\left.-\frac{\Delta_{12}B''}{(\zeta+2(k-1)\gamma+1)(\zeta+2k\gamma-1)}\right]\right\},\quad \mathrm{Re}\zeta>0. \tag{57}$$

The second unknown function, $f_1^+(\zeta)$, can be found from the second equality in (51) by using expression (57), where it is first necessary to perform the required transformations. The respective calculations yield

$$f_1^+(\zeta) = -(\zeta-1)^2\sum_{k=1}^{\infty}\left\{(\Delta_{12}\Delta_{13})^{k-1}\left[\frac{\Delta_{13}A''}{(\zeta-2k\gamma)^2-1}\right.\right.$$
$$\left.\left.-\frac{B''}{(\zeta-2k\gamma+1)(\zeta-2(k-1)\gamma-1)}\right]\right\},\quad \mathrm{Re}\zeta<\gamma. \tag{58}$$

Thus, both unknown functions, $f_1^-(\zeta)$ and $f_1^+(\zeta)$, have been completely determined. According to relations (48), these functions make it possible to obtain explicit expressions for the sectionally analytic function $f(\zeta)$. Upon returning to the plane of the variable z, we find the required expression for the electric field in the system being considered.

In terms of the variable z, expressions (58) and (57) assume the form

$$f_1^+(z) = -(\delta r_1)^2 \sum_{k=1}^{\infty} \left\{ \frac{(\Delta_{12}\Delta_{13})^{k-1}}{k-\delta} \times \left[\frac{\Delta_{13} A''}{k} \left(z - r_1 \frac{k}{k-\delta} \right)^{-1} \left(z - r_1 \frac{k+\delta}{k} \right)^{-1} - \frac{B''}{k-1} \left(z - r_1 \frac{k}{k-\delta} \right)^{-1} \left(z - r_1 \frac{k-1+\delta}{k-1} \right)^{-1} \right] \right\},$$

$$f_1^-(z) = (\delta r_1)^2 \sum_{k=1}^{\infty} \left\{ \frac{(\Delta_{12}\Delta_{13})^{k-1}}{k-1+\delta} \times \left[\frac{A''}{k-1} \left(z - r_1 \frac{k-1}{k-1+\delta} \right)^{-1} \left(z - r_1 \frac{k-1-\delta}{k-1} \right)^{-1} - \frac{\Delta_{12} B''}{k} \left(z - r_1 \frac{k-1}{k-1+\delta} \right)^{-1} \left(z - r_1 \frac{k-\delta}{k} \right)^{-1} \right] \right\}. \quad (59)$$

In these expressions, the terms of the series have the general form $C/(z-p)(z-q)$, where C, p, and q are constants. Such a term can be decomposed into the sum of simple fractions. The application of this operation makes it possible to recast expressions (59) into the form [with allowance for the notation specified by (52), (42), and (28)]

$$f_1^+(z) = \frac{1}{2\pi\varepsilon_1} \sum_{k=1}^{\infty} \{ (\Delta_{12}\Delta_{13})^{k-1} \times \left[\Delta_{13}(q_1 - \Delta_{12} q_2) \left(z - r_1 \frac{k+\delta}{k} \right)^{-1} - (\Delta_{13} q_1 - q_2) \left(z - r_1 \frac{k}{k-\delta} \right)^{-1} \right] \},$$

$$f_1^-(z) = \frac{1}{2\pi\varepsilon_1} \sum_{k=1}^{\infty} \{ (\Delta_{12}\Delta_{13})^{k-1} \times \left[(q_1 - \Delta_{12} q_2) \left(z - r_1 \frac{k-1}{k-1+\delta} \right)^{-1} - \Delta_{12}(\Delta_{13} q_1 - q_2) \left(z - r_1 \frac{k-\delta}{k} \right)^{-1} \right] \}. \quad (60)$$

With the aid of these formulas, we have obtained the expressions for the electric field in (1), which are given in the second section.

CONSTRUCTIVE METHOD FOR SOLVING THE PROBLEM BEING CONSIDERED

The rigorous method proposed here for solving the boundary-value problem in question is based on well-known statements of the theory of analytic functions. Albeit requiring meticulous calculations, the method is quite straightforward in principle. The expressions that it ultimately yields for the electric field are simple in form, not cumbersome, readily amenable to analysis, and convenient for numerical calculations.

The problem formulated here can also be studied by different methods. Among other methods for solving this problem, the constructive method for analytically calculating the electric field deserves particular attention in view of its extreme simplicity and physical clarity of operations at each step of solving the problem. The essence of the method is as follows. An analysis of solutions to a number of model problems featuring line charge sources gives sufficient grounds to assume that, in the sectionally homogeneous medium being considered, the electric field in each region can be represented as an infinite series of simple poles corresponding to fictitious charges; in addition, there are two simple poles corresponding to real charges.

The general expressions for the electric field in the system can then be represented in the form

$$E_1(z) = \frac{1}{2\pi\varepsilon_1} \sum_{k=1}^{\infty} \sum_{\nu=1}^{4} \frac{p_{\nu k}}{z - z_{\nu k}}, \quad z \in S_1;$$

$$E_2(z) = \frac{1}{2\pi\varepsilon_2} \frac{q_1}{z - z_1} + \frac{1}{2\pi\varepsilon_2} \sum_{k=1}^{\infty} \sum_{\nu=1}^{2} \frac{p_{\nu k}}{z - z_{\nu k}}, \quad z \in S_2; \quad (61)$$

$$E_3(z) = \frac{1}{2\pi\varepsilon_3} \frac{q_2}{z - z_2} + \frac{1}{2\pi\varepsilon_3} \sum_{k=1}^{\infty} \sum_{\nu=1}^{2} \frac{p_{\nu k}}{z - z_{\nu k}}, \quad z \in S_3,$$

where q_1 and q_2 are the line densities of the real charges, $p_{\nu k}$ are the strengths of the poles, z_1 and z_2 are the coordinates of the real charges, and $z_{\nu k}$ are the coordinates of fictitious charges.

The appearance of the double sums in (61) is explained below.

Thus, the problem reduces to that of determining the unknown quantities $p_{\nu k}$ and $z_{\nu k}$.

The coordinates z_{vk} of fictitious charges can be determined from the inversion relations. The validity of this statement was emphasized above in analyzing basic formulas (1). Two real charges generate two chains of fictitious charges [they appear in each circle; therefore, double sums arise in expressions (61)]. The real charge at the center of one of the circles is inversely mapped in the second circle, the fictitious charge obtained at this point is mapped in the original circle, the resulting fictitious charge is then mapped in the second circle, and the process of the inverse mappings of the newly formed charges is repeated infinitely. The other chain of poles is calculated in just the same way, but, for the original charge, one takes, in this case, the charge at the center of the second circle; this charge is inversely mapped in the first circle, the fictitious charge is then mapped in the second circle, etc.

In order to establish the rule according to which one could calculate the strengths p_{vk} of the poles, it is necessary to make use of the auxiliary problem of determining the electric field in a straight circular dielectric cylinder near which there occurs a charged filament parallel to it. The solution to this problem is known [1] [it is given in item (iii) above]. From the solution to this problem, one can find an explicit expression for the strengths of the poles corresponding to fictitious charges associated with inverse mapping. In this way, we can determine all unknown elements p_{vk} in expressions (61).

As a matter of fact, the field-calculation algorithm described immediately above is a version of the image method, which is extensively used in the theory of electromagnetism.

The main drawback of this algorithm is that, in order to determine the parameters of the kth pole, one has to calculate consecutively the coordinates of all $k - 1$ poles preceding it. Although this involves performing operations of the same type, the implementation of the algorithm in question is not always convenient in numerical calculations and in the case where use is made of asymptotic expansions.

If, however, the problem is solved by the rigorous method described in the preceding section, the pole parameters in the resulting analytic expressions are determined for each pole independently, this simplifying, in many cases, the calculations and the analysis of the general expressions (1).

CONCLUSIONS

The present investigation makes it possible to draw some general conclusions.

The problem addressed in this study has an exact analytic solution. This solution has been presented above in a simple form. The physical clarity of the results simplifies the analysis of the electric field in the system considered here, which is rather complicated for a theoretical analysis and which is characterized by many parameters. The latter circumstance explains the presence of a large number of particular cases that follow from the general solution.

The calculations presented here have made it possible to establish some special features of electric-field formation in the region around the contact of the cylinders versus the charges and dielectric permittivities of the cylinder materials and of the ambient medium. Physically, the presence of a minimum of the electric-field strength within the cylinders can be explained by the superposition of the electric fields generated by each of the two real sources.

It is interesting to note that the strength of the poles corresponding to fictitious charges is independent of the geometric properties of the system and is determined by its physical parameters exclusively (that is, by the dielectric permittivities of the materials used and by the charges of the filaments).

REFERENCES

1. L. D. Landau and E. M. Lifshitz, *Course of Theoretical Physics*, Vol. 8: *Electrodynamics of Continuous Media* (Nauka, Moscow, 1982; Pergamon, New York, 1984).
2. W. R. Smythe, *Static and Dynamic Electricity*, 2nd ed. (McGraw-Hill, New York, 1950; Inostrannaya Literatura, Moscow, 1954).
3. Yu. P. Emets, Energetika, No. 2, 127 (2000).
4. Yu. P. Emets, IEEE Trans. Dielectr. Electr. Insul. **4**, 439 (1997).
5. Yu. P. Emets, Yu. V. Obnosov, and Yu. P. Onofriĭchuk, Prikl. Mekh. Tekh. Fiz. **37**, 3 (1996).
6. Yu. P. Emets and Yu. P. Onofrichuk, IEEE Trans. Dielectr. Electr. Insul. **3**, 87 (1996).

Translated by A. Isaakyan

Technical Physics, Vol. 50, No. 11, 2005, pp. 1402–1407. Translated from Zhurnal Tekhnicheskoĭ Fiziki, Vol. 75, No. 11, 2005, pp. 11–16.

THEORETICAL AND MATHEMATICAL PHYSICS

System of Two Dielectric Cylinders Involving Charge Sources: II. Calculation of Forces

Yu. P. Emets

Institute of Electrodynamics, National Academy of Sciences of Ukraine, Kiev, 03680 Ukraine

e-mail: emets@irpen.kiev.ua

Received September 13, 2004; in final form, March 31, 2005

Abstract—The volume and surface forces in the system of two long dielectric cylinders touching each other from the exterior are investigated. Charged filaments on the axes of the cylinders are the sources of the electric field. Analytic expressions for the forces acting on the cylinders are derived, and the most important particular cases following from the general solution under various assumptions about the radii of the cylinders, their permittivities, and the line densities of the charges are studied. A constructive method for calculating the forces that takes into account special features of electric-field formation in the system was proposed on the basis of the exact solution to the field problem. © *2005 Pleiades Publishing, Inc.*

INTRODUCTION

The calculation of forces acting on conducting and dielectric bodies in electric fields is an indispensable part of many calculations that must be performed in developing electrophysical facilities and devices used in electrical engineering. For such calculations, it is necessary at first to determine the electric field in the elements of the structure being considered, and this is the most complicated part of the calculations. Only in individual special cases can one derive, for model problems, exact solutions that make it possible to analyze the dependence of the forces on the shape of the conducting and dielectric bodies involved and on the properties of their materials.

This article presents a calculation of the forces in the system of two long and straight cylinders of circular shape that feature charged filaments with various charges on the cylinder axes. The cylindrical bodies consisting of isotropic dielectric materials touch each other from the exterior. In general, they have different radii and different permittivities. Mechanical (ponderomotive) attractive or repulsive forces whose properties and absolute values depend on the parameters of the system act between the cylinders. Also, surface forces act at the boundaries of the dielectric cylinders.

In the system under consideration, the forces can be calculated analytically on the basis of the solution obtained in [1] for the field problem under the assumption of isothermal conditions and the assumption that electrostriction effects are insignificant in the system. These forces can be calculated by different methods—for example, with the aid of the Maxwell's stress tensor. However, the simplest way to calculate directly the volume forces is to consider the interaction of induced charges with the electric field that is external with respect to these charges. In the last case, general expressions for the forces are represented by double sums that can sometimes be reduced to simple analytic expressions. This method for calculating the forces is motivated by the form of the resulting solution, which is given by the sum of an infinite number of poles corresponding to induced charges that are obtained by repeatedly constructing the images of the real charges with respect to the boundary circles.

FORCES OF INTERACTION BETWEEN THE CYLINDERS

A schematic cross-sectional view and the parameters of the system being studied are presented in [1]. From the solution obtained in [1] for the respective boundary-value problem, one can see that the electric field in the system is determined by an infinite number of induced (fictitious) charges within the cylinders. The charges within one of the cylinders determine the electric field of the other cylinder. In addition, there are the real charges of the filaments on the cylinder axes. The electric field in the surrounding medium is generated by all charges of the two cylinders.

The forces acting on the cylinders can be calculated as the interaction between the charges and the electric field.

In order to calculate the forces, it is sufficient to use the expression for the electric field in the region exterior to the cylinders. This expression has the form [see formulas (1) in [1]]

$$E_1(z) = \frac{1}{2\pi\varepsilon_1}\sum_{k=1}^{\infty}\left\{(\Delta_{12}\Delta_{13})^{k-1}\left[Q_1\left(z - r_1\frac{k-1}{k-1+\delta}\right)^{-1}\right.\right.$$

1063-7842/05/5011-1402$26.00 © 2005 Pleiades Publishing, Inc.

$$+\Delta_{12}Q_2\left(z-r_1\frac{k-\delta}{k}\right)^{-1}+Q_2\left(z-r_1\frac{k}{k-\delta}\right)^{-1} \quad (1)$$

$$+\Delta_{13}Q_1\left(z-r_1\frac{k+\delta}{k}\right)^{-1}\Bigg]\Bigg\}\ (z=x+iy).$$

Recall that, here, $E_1(z)=E_{x1}-iE_{y1}$ is the complex-valued electric-field strength; ε_1 is the permittivity of the external medium; and Δ_{12}, Δ_{13}, Q_1, Q_2, and δ are parameters that are defined by the formulas

$$\Delta_{12}=\frac{\varepsilon_1-\varepsilon_2}{\varepsilon_1+\varepsilon_2},\quad \Delta_{13}=\frac{\varepsilon_1-\varepsilon_3}{\varepsilon_1+\varepsilon_3}\ (-1\le\Delta_{12},\Delta_{13}\le 1),$$

$$Q_1=q_1-\Delta_{12}q_2,\quad Q_2=q_2-\Delta_{13}q_1, \quad (2)$$

$$\delta=\frac{r_2}{r_1+r_2},\quad (0\le\delta\le 1),$$

where ε_2 and ε_3 are the permittivities within the cylinders having the radii r_1 and r_2 and the charge densities q_1 and q_2, respectively. From expression (1), one can see that the electric field $E_1(z)$ is determined by an infinite series of poles corresponding to fictitious charges (there are also two poles corresponding to the real charges situated at the centers of the circles) and having the general form

$$E_p(z)=\frac{1}{2\pi\varepsilon_1}\frac{G_p}{z-a_p}, \quad (3)$$

where G_p is a charge and a_p is its coordinate.

In the plane of the complex-variable, the charges (further labeled with the subscript m)

$$G_m=Q_1\Delta^{m-1},\quad G'_m=\Delta_{12}Q_2\Delta^{m-1} \quad (4)$$

having the coordinates

$$a_m=r_1\frac{m-1}{m-1+\delta},\quad a'_m=r_1\frac{m-\delta}{m}, \quad (5)$$

where $\Delta=\Delta_{12}\Delta_{13}$, and occurring within the circle characterized by the parameters r_1, ε_2, and q_1 are subjected to the effect of the electric field produced by the charges situated within the other circle, which is characterized by the parameters r_2, ε_3, and q_2. The strength of the electric field generated by these charges and the coordinates of the charges will be labeled with the subscript n:

$$E_n(z)=\frac{1}{2\pi\varepsilon_1}\frac{Q_2\Delta^{n-1}}{z-a_n},\quad a_n=r_1\frac{n}{n-\delta},$$
$$E'_n(z)=\frac{1}{2\pi\varepsilon_1}\frac{\Delta_{13}Q_1\Delta^{n-1}}{z-a'_n},\quad a'_n=r_1\frac{n+\delta}{n}. \quad (6)$$

The general term of the force in question (per unit length of the cylinder) can be written as

$$F_{mn}=G_mE_{mn}+G'_mE_{mn}+G_mE'_{mn}+G'_mE'_{mn}, \quad (7)$$

where

$$E_{mn}=\frac{1}{2\pi\varepsilon_1}\frac{Q_2\Delta^{n-1}}{\alpha_m-a_n},$$
$$E'_{mn}=\frac{1}{2\pi\varepsilon_1}\frac{\Delta_{13}Q_1\Delta^{n-1}}{\alpha_m-a'_n}\ (\alpha_m=a_m,a'_m). \quad (8)$$

In the z plane, each charge within the first circle (characterized by the parameters r_1, ε_2, and q_1) is subjected to the effect of the electric field produced by all charges situated within the second circle; therefore, the general expression for the force is

$$F_1=\sum_{m=1}^{\infty}\sum_{n=1}^{\infty}F_{mn}, \quad (9)$$

where the subscript 1 labels the force acting on the first cylinder, which is characterized by the parameters defined above (accordingly, the total force acting on the second cylinder is labeled with the subscript 2).

By performing the same operations for the second cylinder—that is, by considering the interaction of the external field with the charges within this cylinder—we can easily derive the equality

$$F_1=-F_2. \quad (10)$$

Let us substitute formulas (4)–(8) into expression (9). After some simple algebra, we obtain

$$F_1=\frac{1}{2\pi\varepsilon_1r_1\Delta^2}\sum_{m=1}^{\infty}\sum_{n=1}^{\infty}\Bigg\{\Delta^{m+n}\Bigg\{\Delta_{13}Q_1^2\frac{n(m-1+\delta)}{1-m-n-\delta}$$
$$+Q_1Q_2\left[\frac{(n-\delta)(m-1+\delta)}{1-m-n}-\Delta\frac{mn}{m+n}\right] \quad (11)$$
$$+\Delta_{12}Q_2^2\frac{m(n-\delta)}{\delta-m-n}\Bigg\}\Bigg\}.$$

In this expression, the double sums at the factor Q_1Q_2 can be simplified. Indeed, we find after some simple algebra that

$$\sum_{m=1}^{\infty}\sum_{n=1}^{\infty}\left[\Delta^{m+n}\frac{(n-\delta)(m-1+\delta)}{1-m-n}\right]$$
$$=\frac{\Delta^2}{1-\Delta}\left[\frac{\Delta(\Delta-3)}{6(1-\Delta)^2}+\delta(\delta-1)\right], \quad (12)$$

$$\sum_{m=1}^{\infty}\sum_{n=1}^{\infty}\left[\Delta^{m+n}\frac{mn}{m+n}\right]=\frac{\Delta^2(3-\Delta)}{6(1-\Delta)^3}.$$

By using relations (12), we can recast expression (11) into the form

$$F_1 = \frac{Q_1Q_2}{2\pi\varepsilon_1 r_1\delta(1-\Delta)}\left[\frac{\Delta(\Delta-3)}{3(1-\Delta)^2}+\delta(\delta-1)\right]$$
$$+\frac{1}{2\pi\varepsilon_1 r_1\delta\Delta^2}\sum_{m=1}^{\infty}\sum_{n=1}^{\infty}\left\{\Delta^{m+n}\left[\Delta_{13}Q_1^2\frac{n(m-1+\delta)}{1-m-n-\delta}\right.\right. \quad (13)$$
$$\left.\left.+\Delta_{12}Q_2^2\frac{m(n-\delta)}{\delta-m-n}\right]\right\}.$$

By virtue of the method of derivation, expression (13) determines the total force acting on the cylinder characterized by the parameters specified above. According to relation (10), the force applied to the second cylinder is given by the same expression (13) but with an opposite sign.

If the radii of the cylinders are identical, $r_1 = r_2 \equiv r$ ($\delta = 1/2$), expression (13) is radically simplified. In this case, we have

$$F_1 = \frac{Q_1Q_2(\Delta^2-6\Delta-3)}{12\pi\varepsilon_1 r(1-\Delta)^3}$$
$$+\frac{\Delta_{13}Q_1^2+\Delta_{12}Q_2^2}{\pi\varepsilon_1 r\Delta^2}\sum_{m=1}^{\infty}\sum_{n=1}^{\infty}\left[\Delta^{m+n}\frac{m(2n-1)}{1-2(m+n)}\right]. \quad (14)$$

One can show that

$$\sum_{m=1}^{\infty}\sum_{n=1}^{\infty}\left[\Delta^{m+n}\frac{m(2n-1)}{1-2(m+n)}\right] = \frac{\Delta^2}{3(1-\Delta)^3}. \quad (15)$$

Therefore, formula (14) assumes the form

$$F_1 = \frac{1}{3\pi\varepsilon_1 r(1-\Delta)^3}$$
$$\times\left[\frac{1}{4}Q_1Q_2(\Delta^2-6\Delta-3)-\Delta_{13}Q_1^2-\Delta_{12}Q_2^2\right]. \quad (16)$$

It is noteworthy that, although the expression for the electric field is rather cumbersome, the formula for the force acting in the system has a simple form, especially in the last case.

SOME PARTICULAR CASES

A number of particular solutions that are of interest in themselves can be derived from the general expression for the force in (13) by changing the parameters of the system.

(i) If we set $\varepsilon_1 = \varepsilon_2 = \varepsilon_3 \equiv \varepsilon$ ($\Delta_{12} = \Delta_{13} = 0$), expression (13) reduces to a known formula for the forces of interaction in the system of two likely oriented straight charged filaments in a homogeneous medium that are separated by a distance h and which carry the charges q_1 and q_2 (per unit length). Specifically, we have

$$F_1 = \frac{q_1q_2}{2\pi\varepsilon_1 h} \quad (h = r_1 + r_2). \quad (17)$$

(ii) Let the system being considered consist of one long dielectric circular cylinder characterized by the parameters ε_2 and r and a charged filament parallel to it. The charged filament is characterized by a line charge density q and is situated at a distance h from the cylinder. Setting

$$q_1 = 0, \quad q_2 \equiv q, \quad \varepsilon_3 = \varepsilon_1 \ (\Delta_{13} = 0),$$
$$h = r_1 + r_2, \quad r \equiv r_1 \quad (18)$$

and using the general expression (13), we then find that the force acting on the cylinder has the form

$$F_1 = -\frac{\Delta_{12}q^2r^2}{2\pi\varepsilon_1 h(h^2-r^2)}. \quad (19)$$

The force acting on the filament is determined by the same formula but with an opposite sign. Formula (19) is given in [2].

(iii) For

$$r_2 \longrightarrow \infty \ (\delta = 1), \quad q_2 = 0, \quad q_1 \equiv q, \quad r_1 \equiv r, \quad (20)$$

expression (13) takes the form

$$F_1 = -\frac{\Delta_{13}q^2(3-\Delta)}{12\pi\varepsilon_1 r(1-\Delta)}. \quad (21)$$

This formula determines the force acting on a dielectric cylinder touching the plane boundary between two dielectric materials whose permittivities are ε_1 and ε_3. The cylinder is of circular shape in a cross section orthogonal to its axis and is characterized by the parameters ε_2 and r, and a charged filament of line charge density q is situated on the cylinder axis. Formula (21) was derived in [3].

(iv) Let the dielectric cylinders have equal radii and equal charges:

$$r_1 = r_2 \equiv r \ (\delta = 1/2), \quad q_1 = q_2 \equiv q. \quad (22)$$

According to expression (16), the absolute value of the repulsive force acting in this case between the cylinders is given by

$$|F_{1,2}| = \frac{q^2(3+\Delta_{12}+\Delta_{13}-\Delta)}{12\pi\varepsilon_1 r(1-\Delta)}. \quad (23)$$

If the charges are equal in magnitude but different in sign ($q_1 = -q_2 \equiv q$), we have

$$|F_{1,2}| = \frac{q^2(3-\Delta_{12}-\Delta_{13}-\Delta)}{12\pi\varepsilon_1 r(1-\Delta)}. \quad (24)$$

Comparing expressions (23) and (24), one can see that, for identical characteristics of the dielectric mate-

rials used and equal absolute values of the charges, the attractive and the repulsive forces between the dielectric cylinders featuring charged filaments on their axes are in general unequal in absolute value, their values significantly depending on the permittivities of the cylinders and the surrounding medium. They can be equal (in absolute value) only in the case of

$$\Delta_{12} = -\Delta_{13}, \tag{25}$$

which is equivalent to

$$\varepsilon_1 = \sqrt{\varepsilon_2 \varepsilon_3}. \tag{26}$$

The last relation means that, in this case, the permittivity of the surrounding medium takes an intermediate value between the permittivities of the materials of the cylinders.

To illustrate the aforesaid, the dependences $F_a(\Delta_{12})$ and $F_r(\Delta_{12})$, where F_a is the attractive force between the cylinders according to formula (23) and F_r is the repulsive force between the cylinders according to formula (24), are shown in Figs. 1 and 2. The curves are depicted for two values of the parameter Δ_{13} ($\Delta_{13} = 0.5$ in Fig. 1 and $\Delta_{13} = -0.5$ in Fig. 2) in terms of the relative quantities

$$F_{a,r*} = |F_{1,2}|/F_0, \quad F_0 = \frac{q^2}{4\pi\varepsilon_0 r}. \tag{27}$$

The asterisks are omitted for the sake of brevity.

The symmetry of the curves that is observed in these two figures is a consequence of the equivalence of the parameters Δ_{12} and Δ_{13} in formulas (23) and (24).

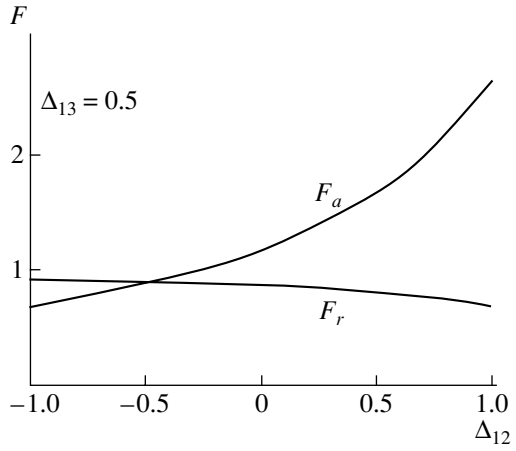

Fig. 1. Dependence of the forces acting between the cylinders on the parameter Δ_{12} at $\Delta_{13} = 0.5$. The attractive force F_a and the repulsive force F_k acting between the cylinders were calculated according to formulas (23) and (24), respectively.

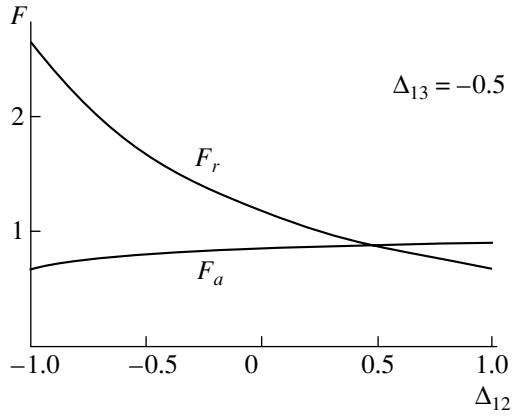

Fig. 2. As in Fig. 1, but for $\Delta_{13} = -0.5$.

SURFACE FORCES

It is well known that, in inhomogeneous dielectric bodies placed in an electric field, there arise mechanical (ponderomotive) forces, whose density is given by

$$\mathbf{f} = -\frac{1}{2}E^2 \mathrm{grad}\varepsilon. \tag{28}$$

In a sectionally homogeneous medium, this expression assumes the form

$$\begin{aligned}\mathbf{f} &= \frac{1}{2}\mathbf{n}(\varepsilon_2 - \varepsilon_1)\left[E_{(+)t}^2 + \frac{\varepsilon_1}{\varepsilon_2}E_{(+)n}^2\right] \\ &= \frac{1}{2}\mathbf{n}(\varepsilon_2 - \varepsilon_1)\left[E_{(-)t}^2 + \frac{\varepsilon_2}{\varepsilon_1}E_{(-)n}^2\right],\end{aligned} \tag{29}$$

where

$$\mathbf{n} = \exp(i\theta) \quad (0 \le \theta < 2\pi) \tag{30}$$

is the vector of a unit normal to the surface separating the materials having the permittivities ε_1 and ε_2 (the vector **n** is directed toward the medium whose permittivity is ε_1); $E_{t(+)}$ and $E_{t(-)}$ are the tangential components of the electric-field-strength vector at the boundary separating the materials characterized by the permittivities ε_1 and ε_2; and $E_{n(+)}$ and $E_{n(-)}$ are the normal components of this vector at the same surface.

In order to calculate the force **f** at the surface of the cylinders, we use the expression for the electric-field strength in the region external to the cylinders, $E_1(z)$ [in formula (29), it is the (+) components of the electric-field-strength vector that corresponds to $E_1(z)$].

At first, we introduce the relative quantities

$$\begin{aligned}E_* &= \frac{E_1}{E_0}\left(E_0 = \frac{q_1}{2\pi\varepsilon_0 r_1}\right), \quad f_* = \frac{f}{f_0}(f_0 = \varepsilon_0 E_0^2), \\ z_* &= \frac{z}{r_1}\varepsilon_{1,2,3*} = \frac{\varepsilon_{1,2,3}}{\varepsilon_0}Q_{1,2*} = \frac{Q_{1,2}}{q_1},\end{aligned} \tag{31}$$

where ε_0 is the dielectric constant and $E_* = \{E_*', E_*''\}$ are the components of the electric field on the surfaces of the cylinders characterized by the parameters r_1, ε_2

and r_2 ε_3, respectively. Below, we omit asterisks for the sake of brevity.

In terms of the relative quantities, expression (29) assumes the form

$$\mathbf{f} = \mathbf{n}\frac{\varepsilon_1\Delta_{12}}{1+\Delta_{12}}\left[E'^2_{t(+)} + \frac{1+\Delta_{12}}{1-\Delta_{12}}E'^2_{n(+)}\right]. \quad (32)$$

From the scalar product $\mathbf{nE}(z)$, where $\mathbf{n}$ is the vector of a unit normal to the cylinder of radius r_1, we find the normal and the tangential component of the electric-field-strength vector at the boundary contour (they are labeled with primes). Specifically, we have

$$E'_{n(+)}(\theta) = \frac{1}{\varepsilon_1}\sum_{k=1}^{\infty}\left\{\Delta^{k-1}\left[\frac{Q_1(1-w\cos\theta)}{1-2w\cos\theta+w^2}\right.\right.$$
$$+\frac{\Delta_{12}Q_2(1-u\cos\theta)}{1-2u\cos\theta+u^2} + \frac{Q_2(1-u^{-1}\cos\theta)}{1-2u^{-1}\cos\theta+u^{-2}}$$
$$\left.\left.+\frac{\Delta_{13}Q_1(1-v\cos\theta)}{1-2v\cos\theta+v^2}\right]\right\},$$
$$E'_{t(+)}(\theta) = \frac{\sin\theta}{\varepsilon_1}\sum_{k=1}^{\infty}\left\{\Delta^{k-1}\left[\frac{Q_1 w}{1-2w\cos\theta+w^2}\right.\right. \quad (33)$$
$$+\frac{\Delta_{12}Q_2 u}{1-2u\cos\theta+u^2} + \frac{Q_2 u^{-1}}{1-u^{-1}\cos\theta+u^{-2}}$$
$$\left.\left.+\frac{\Delta_{13}Q_1 v}{1-2v\cos\theta+v^2}\right]\right\},$$

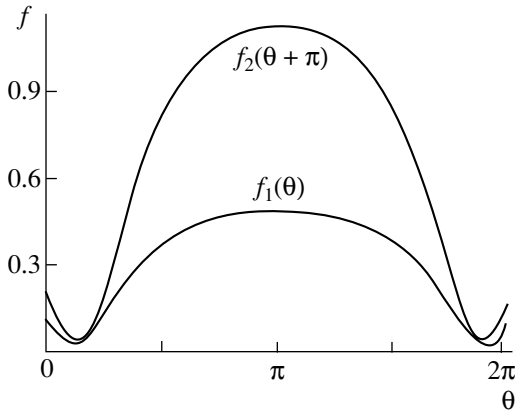

Fig. 3. Distribution of the surface forces in the system characterized by the parameters $\varepsilon_1 = 1$, $\varepsilon_2 = 2$, and $\varepsilon_3 = 10$. Here, it is assumed that $r_1 = r_2$ and $q_1 = q_2$. We have denoted by f_1 the force at the cylinder whose parameters are ε_2 and q_1 and by f_2 the force at the cylinder whose the parameters are ε_3 and q_2.

where

$$w = \frac{k-1}{k-1+\delta}, \quad u = \frac{k-\delta}{k}, \quad v = \frac{k+\delta}{k}. \quad (34)$$

The force density at the cylinder of radius r_2 is determined by an expression similar to (32); that is,

$$\mathbf{f} = \mathbf{n}\frac{\varepsilon_1\Delta_{13}}{1+\Delta_{13}}\left[E''^2_{t(+)} + \frac{1+\Delta_{13}}{1-\Delta_{13}}E''^2_{n(+)}\right]. \quad (35)$$

The components of the electric field at the interface (they are labeled with primes) are given by

$$E''_{n(+)}(\theta) = \frac{1-\delta}{\delta\varepsilon_1}\sum_{k=1}^{\infty}\left\{\Delta^{k-1}\left[\frac{Q_1(1+w\cos\theta)}{1+2w\cos\theta+w^2}\right.\right.$$
$$+\frac{\Delta_{12}Q_2(1+\gamma\cos\theta)}{1+2\gamma\cos\theta+\gamma^2} + \frac{Q_2(1+\alpha\cos\theta)}{1+2\alpha\cos\theta+u^2}$$
$$\left.\left.+\frac{\Delta_{13}Q_1(1+w^{-1}\cos\theta)}{1+2w^{-1}\cos\theta+w^{-2}}\right]\right\},$$
$$E''_{t(+)}(\theta) = -\frac{(1-\delta)\sin\theta}{\delta\varepsilon_1}\sum_{k=1}^{\infty}\left\{\Delta^{k-1}\left[\frac{Q_1 w}{1+2w\cos\theta+w^2}\right.\right. \quad (36)$$
$$+\frac{\Delta_{12}Q_2\gamma}{1+2\gamma\cos\theta+\gamma^2} + \frac{Q_2\alpha}{1+2\alpha\cos\theta+\alpha^2}$$
$$\left.\left.+\frac{\Delta_{13}Q_1 w^{-1}}{1+2w^{-1}\cos\theta+w^{-2}}\right]\right\},$$

where

$$w = \frac{k}{k-1+\delta}, \quad \gamma = \frac{k+1-\delta}{k}, \quad \alpha = \frac{k-1}{k-\delta}. \quad (37)$$

The direction of the force density $\mathbf{f}$ coincides with the direction of the normal $\mathbf{n}$, but its sign depends on the values of the parameters Δ_{12} and Δ_{13}.

In order to illustrate clearly the dependence of the surface forces on the charges, the graphs of $f(\theta)$ are given in Figs. 3–5. These graphs show the distributions of the force density at the surfaces of the cylinders of identical radii, $r_1 = r_2$ ($\delta = 1/2$), at fixed values of the permittivities of the materials of the system, $\varepsilon_1 = 1$, $\varepsilon_2 = 2$, and $\varepsilon_3 = 10$ ($\Delta_{12} = -0.333333$, $\Delta_{13} = -0.818182$). Here, the forces labeled with the subscripts 1 and 2 are associated, respectively, with the cylinder characterized by the parameters ε_2 and q_1 and with the cylinder characterized by the parameters ε_3 and q_2.

The curves in Fig. 3 correspond to the case where the charged filaments have identical line charge densities ($q_1 = q_2$). The data displayed in Fig. 4 were obtained for the case where the charges of the filaments are equal in absolute value and are opposite in sign ($q_1 = -q_2$). For

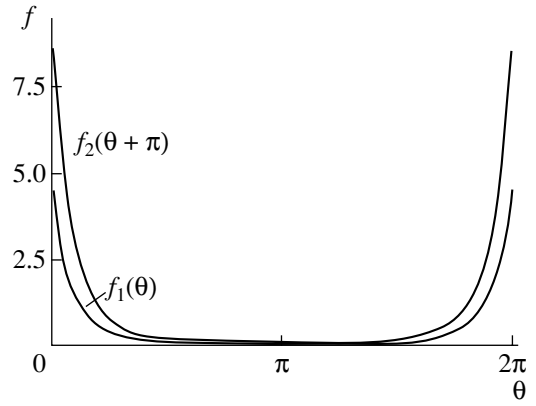

Fig. 4. As in Fig. 3, but for $q_1 = -q_2$.

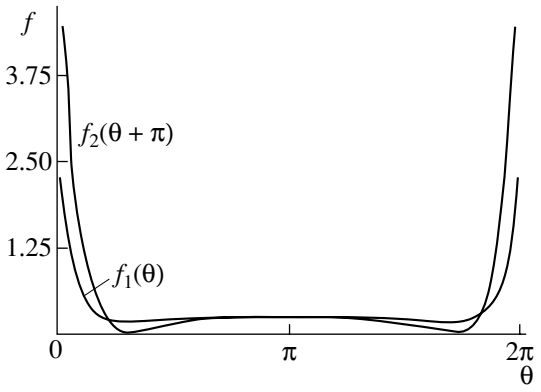

Fig. 5. As in Fig. 3, but for $q_2 = 0$.

Fig. 5, it is assumed that $q_2 = 0$—that is, there is a charge in only one cylinder (in that whose permittivity is ε_2). In order to obtain a clear presentation of the distribution of the forces at the surfaces of the two cylinders, the dependences $f_2(\theta)$ are shifted by an angle of π.

It is noteworthy that the curves in Figs. 3 and 5 have distinct maxima and minima. This distribution of the surface forces can readily be explained by using the qualitative pattern of the electric field in the system and by estimating the polarization phenomena in the dielectric bodies under the conditions adopted here.

Maximum forces arise at $q_1 = -q_2$ in the vicinity of the point where the cylinders touch each other ($\theta \sim 0.2\pi$) (Fig. 4). Approximately the same pattern of the distribution of the forces is also observed in the case of $q_2 = 0$, this being due to a large permittivity of the material of the uncharged cylinder ($\varepsilon_3 = 10$; $\varepsilon_3 > \varepsilon_1, \varepsilon_2$).

CONCLUSIONS

The main objective of the present study was to establish the dependence of the forces acting in a system that includes charged conductors having insulated coating and which is typical of many applications on the permittivities of the materials used. This problem is both of practical importance and of theoretical interest. The investigation of this problem is significantly simplified owing to the availability of the analytic solution to the field problem and the derivation of explicit expressions for the volume and surface forces in the system under consideration on the basis of this solution.

The present investigation has revealed that the permittivities of the cylinders featuring charged conductors within them and the permittivity of the external medium can affect substantially the magnitude of the forces in the system without changing their character. By varying the properties of the dielectric materials, one can purposefully change, within specific limits, the distribution of the surface forces at the interface of different media and reduce the effect of the volume forces between the cylinders.

The conclusion that there exist alternating maxima and minima of the surface forces at the cylinder surfaces in the systems featuring likely charged conducting bodies (or in the systems not involving a charge on one of the conducting bodies) is of special interest. The calculations have shown that, in the systems where the cylinders consist of the same dielectric material, the attractive forces are not equal in magnitude to the repulsive forces at fixed charges, this not being so in only one particular case.

The model problem being considered admits a generalization to the case where charged filaments can be placed not only on the axes of the cylinders and where there can be several charged filaments rather than one. Moreover, charged filaments may also be outside the cylinders. In all of these cases, the electric field in the system and the respective forces can be calculated analytically.

REFERENCES

1. Yu. P. Emets, Zh. Tekh. Fiz. **75**, 11 (2005) [Tech. Phys. **50**, 1391 (2005)].
2. L. D. Landau and E. M. Lifshitz, *Course of Theoretical Physics*, Vol. 8: *Electrodynamics of Continuous Media* (Nauka, Moscow, 1982; Pergamon, New York, 1984).
3. Yu. P. Emets, IEEE Trans. Dielectr. Electr. Insul. **4**, 439 (1997).

Translated by A. Isaakyan

Technical Physics, Vol. 50, No. 11, 2005, pp. 1408–1416. Translated from Zhurnal Tekhnicheskoĭ Fiziki, Vol. 75, No. 11, 2005, pp. 17–25.

THEORETICAL AND MATHEMATICAL PHYSICS

Stochastic Theory of Ultrathin Lubricant Film Melting in the Stick-Slip Regime

A. V. Khomenko and I. A. Lyashenko

Sumy State University, Sumy, 40007 Ukraine

e-mail: khom@phe.sumdu.edu.ua

Received October 4, 2004

Abstract—Melting of an ultrathin lubricant film under friction between atomically smooth surfaces is studied in terms of the Lorentz model. Additive noise associated with shear stresses and strains, as well as with film temperature, is introduced, and a phase diagram is constructed where the noise intensity of the film temperature and the temperature of rubbing surfaces define the domains of sliding, dry, and stick-slip friction. Conditions are found under which stick-slip friction proceeds in the intermittent regime, which is characteristic of self-organized criticality. The stress self-similar distribution, which is provided by temperature fluctuations, is represented with allowance for nonlinear relaxation of stresses and fractional feedbacks in the Lorentz system. Such a fractional scheme is used to construct a phase diagram separating out different types of friction. Based on the study of the fractional Fokker–Planck equation, the conclusion is drawn that stick-slip friction corresponds to the subdiffusion process. © *2005 Pleiades Publishing, Inc.*

INTRODUCTION

Sliding friction of smooth solid surfaces with a thin lubricant film in between has recently become a subject of increased interest [1]. One reason is that weakly rubbing surfaces are widely applied in a variety of advanced high-tech products, such as computer memories, miniature engines, and space-borne devices. A great insight into the physics of friction has been provided by experiments with atomically smooth mica surfaces separated by an ultrathin organic lubricant layer, which behaves as a solid under certain conditions [2]. Specifically, intermittent (stick-slip) motion was observed [3–6], which is inherent in dry friction and causes wear and failure of rubbing parts. Such "mixed" friction conditions arise when a lubricant film less than four molecular layers thick solidifies, being compressed by the walls. The subsequent abrupt transition to melting takes place when the shear stress exceeds a critical value (melting due to shear).

Thus, thin molecular films experience the transition from the solid-like to liquid-like phase [2, 7], the properties of the latter being impossible to describe even qualitatively in the terms (e.g., viscosity) characterizing the properties of a normal liquid occupying a large volume. Such films exhibit a yield stress, which is a characteristic of failure in solids, while the times of molecular diffusion and relaxation in them may by more than 10 orders exceed the corresponding values for a normal liquid or even films that are a little bit thicker.

Investigation of the effect of noise (fluctuations) on sliding friction is also of great fundamental and applied significance, since in real experiments, fluctuations critically affect the frictional behavior, for example, reduce the friction [1, 8, 9]. Thermal noise, observed in any experiments, may carry an ultrathin lubricant film from the stable solid-like state to the liquid-like state and thus, transform dry friction into sliding or stick-slip friction. Therefore, considerable attention has recently been given to the effect of noise and uncontrolled impurities present at the friction boundary on static and dynamic friction [10–12]. It has been shown that surfaces with a regular (periodical) relief have a lower friction coefficient than irregular surfaces.

Earlier [13, 14], we elaborated upon an idea that the solid–liquid transition of an ultrathin lubricant film is the result of thermodynamic and shear melting. The associated processes were considered in terms of self-organization of shear stress and strain fields, as well as of the lubricant film temperature, with allowance for the additive noise of these quantities (Sect. 1). However, the issue as to whether self-organized criticality (SOC) [15] may occur in the system was left aside. In this work, we try to find conditions for SOC using the Lorentz model, which gives a field representation of a elastoviscous medium [16].

The SOC conditions arise in the case of a power-type stress distribution with a fractional exponent. Therefore, in Sect. 2, we generalize (modify) the Lorentz system in order to describe, in accordance with experimental data [2], intermittent melting of a lubricant film and, consequently, the related friction conditions. By analogy with [14], we construct a phase diagram that allows one to trace changes in the domains of sliding, dry, and stick-slip friction depending on the fractional exponent in the modified Lorentz system. With such a generalization, we describe the behavior of the system in terms of nonadditive thermodynamics

1063-7842/05/5011-1408$26.00

[17] (Sect. 3). Such an approach can be implemented in the fractional Lorentz system, where the stress serves as the order parameter, the conjugate field is reduced to nonadditive complexity, and the internal energy is a control parameter. Eventually, it turns out that the stress distribution inherent in SOC is provided by energy fluctuations. This distribution is, on the one hand, a solution to the nonlinear Fokker–Planck equation describing the behavior of a nonadditive system [17] and, on the other hand, stems from the fractional Fokker–Planck equation for Levi flights [18]. Contrasting solutions to these equations, one can establish correlations between the exponent in the stress distribution (the characteristic exponent of multiplicative noise), fractal dimension of the phase space, number of equations needed to describe the self-consistent behavior of the system under the SOC conditions, dynamic exponent, and Tsallis nonadditivity parameter. It is shown that stick-slip friction corresponds to the subdiffusion process.

1. BASIC EQUATIONS AND THE EFFECT OF NOISE

Rheologically describing a viscoelastic heat-conducting medium [13], we derived a set of kinetic equations governing the consistent behavior of shear stresses σ, strains ε, and temperature T in an ultrathin lubricant film between atomically smooth rubbing mica surfaces. Let us write these equations for σ, ε, and T using the following units of measure:

$$\sigma_s = \left(\frac{\rho c_v \eta_0 T_c}{\tau_h}\right)^{1/2},$$
$$\varepsilon_s = \frac{\sigma_s}{G_0} \equiv \left(\frac{\tau_\varepsilon}{\tau_h}\right)^{1/2}\left(\frac{\rho c_v T_c \tau_\varepsilon}{\eta_0}\right)^{1/2}, \quad (1)$$

where ρ is the lubricant density, c_v is the specific heat at constant volume, T_c is the critical temperature, $\eta_0 \equiv \eta(T = 2T_c)$ is the characteristic value of shear viscosity η, $\tau_h \equiv \rho l^2 c_v/\kappa$ is the heat conduction time, l is the heat conduction length, κ is the thermal conductivity, τ_ε is the strain relaxation time, and $G_0 \equiv \eta_0/\tau_\varepsilon$. The corresponding equations are

$$\tau_\sigma \dot{\sigma} = -\sigma + g\varepsilon, \quad (2)$$

$$\tau_\varepsilon \dot{\varepsilon} = -\varepsilon + (T-1)\sigma, \quad (3)$$

$$\tau_h \dot{T} = (T_m - T) - \sigma\varepsilon + \sigma^2. \quad (4)$$

Here, τ_σ is the stress relaxation time, T_m is the temperature of atomically smooth rubbing mica surfaces, $g = G/G_0 < 1$ is a constant, and G is the shear modulus of the lubricant. Equation (2) is reduced to the Maxwell equation for a viscoelastic medium by substituting ε/τ_σ for $\partial\varepsilon/\partial t$. Expression (3) is similar to the Kelvin–Voigt equation [13, 19], which takes into account the dependence of the shear viscosity on dimensionless temperature $\eta = \eta_0/(T-1)$. Expression (4) is the heat conduction expression that involves heat transfer from rubbing surfaces to a lubricant film, dissipative heating of a viscous liquid flowing under stress, and the reversible mechanocaloric effect in the linear approximation. Formally, this set of equations coincide with the synergetic Lorentz system [20, 21], where the shear stress serves as the order parameter, the conjugate field is reduced to the shear strain, and the temperature is a control parameter. As is known, this system is used for describing thermodynamic and kinetic phase transformations.

In [13], melting of an ultrathin lubricant film between atomically smooth rubbing mica surfaces is viewed as a result of shear stresses spontaneously arising upon heating of rubbing surfaces above critical temperature $T_{c0} = 1 + g^{-1}$. The initial reason for self-organization is positive feedback of T and σ with ε (see (3)) due to the temperature dependence of the shear viscosity, which causes its divergence. However, negative feedback of σ and ε with T (see (4)) is also of importance, since it makes the system stable.

In terms of such an approach, a lubricant is seen as a high-viscosity liquid behaving like an amorphous solid: it has a very high effective viscosity and still can be characterized by a yield stress [2, 19]. In the solid-like state, shear stresses $\sigma = 0$, since Eq. (2), describing the elastic properties in the steady state ($\dot{\sigma} = 0$), is omitted from consideration. Equation (3), containing viscous stresses, reduces to the Debye equation, which describes fast relaxation of the shear strain within the microscopic time $\tau_\varepsilon \approx a/c \sim 10^{-12}$ s, where $a \sim 1$ nm is the lattice constant or molecular spacing and $c \sim 10^3$ m/s is the speed of sound. In this case, Eq. (4) turns into the simplest expression for temperature relaxation, which is free of the terms corresponding to dissipative heating and the mechanocaloric effect for a viscous liquid.

If stresses σ are nonzero, Eqs. (2)–(4) describe all the above properties for the liquid-like state of the lubricant. Moreover, if the shear strain is absent, the rms thermal displacement of atoms (molecules) is given by $\langle u^2\rangle = T/Ga$ [6]. The rms displacement due to shear is found from the expression $\langle u^2\rangle = \sigma^2 a^2/G^2$. The total rms displacement is a sum of these two displacements provided that temperature fluctuations and stresses are mutually independent. This means that melting of a lubricant is caused by both heating and stresses generated by rubbing surfaces. This supposition is consistent with the concept of dynamic shear melting, according to which the solid-like state is unstable in the absence of temperature fluctuations. Thus, strain (stress) fluctuations and temperature fluctuations should be considered separately. We will assume that, as the temperature grows, the film becomes progressively closer to the liquid state and the friction force decreases as a result of a decrease in the molecular jump activation energy. In addition, the friction force

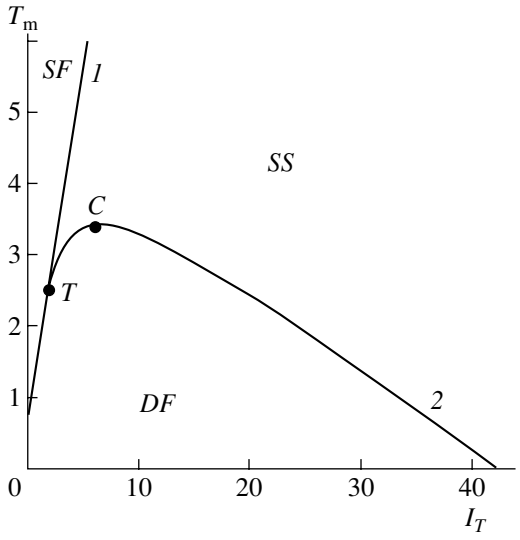

Fig. 1. Phase diagram for $g = 0.5$ and $I_\varepsilon = 1.2$. Curves *1* and *2* are the boundaries between the domains of stable SF, DF, and SS (*T* and *C* are the tricritical and critical points, respectively).

decreases with increasing the velocity of relative motion of contacting surfaces, $V = l\partial\varepsilon/\partial t$, since an increase in the relative velocity causes a rise in shear stresses according to the Maxwell-type relationship $\partial\sigma/\partial t = -\sigma/\tau_\sigma + G\partial\varepsilon/\partial t$ between stress and strain.

In macroscopic Lorentz equations (2)–(4), stress σ, strain ε, and temperature T are averaged over a physically small volume. Fluctuations, which arise over distances on the order of the heat conduction length, will be taken into account by introducing stochastic terms in the form of additive noise intensities $I_\sigma^{1/2}\xi$, $I_\varepsilon^{1/2}\xi$, and $I_T^{1/2}\xi$ into the right-hand sides of Eqs. (2)–(4) (here, intensities I_σ, I_ε, and I_T are given in terms of σ_s^2, $\varepsilon_s^2\tau_\varepsilon^{-2}$, and $(T_c\kappa/l)^2$, respectively, and $\xi(t)$ is a δ-correlated stochastic function [14, 22]). According to experimental data for organic lubricants [2], the stress relaxation time under normal pressure is $\tau_\sigma \sim 10^{-10}$ s and increases by several orders of magnitude under a high pressure. Since the ultrathin lubricant film is less than four molecular layers thick in our case, the temperature relaxes to value T_m for time τ_h that satisfies the inequality $\tau_h \ll \tau_\sigma$. Then, in the adiabatic approximation $\tau_\sigma \gg \tau_\varepsilon$ and τ_h [20, 21], Eqs. (2)–(4) take the form of the Langevin equation [14]

$$\tau_\sigma\dot{\sigma} = f(\sigma) + \sqrt{I(\sigma)}\xi(t), \quad f \equiv -\frac{\partial V}{\partial\sigma}, \tag{5}$$

where force f is specified by the synergetic potential

$$V = \frac{1}{2}(1-g)\sigma^2 + g\left(1 - \frac{T_m}{2}\right)\ln(1+\sigma^2) \tag{6}$$

and the effective noise intensity is given by expression

$$I(\sigma) \equiv I_\sigma + (I_\varepsilon + I_T\sigma^2)g^2d^2(\sigma), \tag{7}$$

which follows from the additivity of dispersions of Gaussian random quantities [22]. The stationary distribution of solutions to Eq. (5),

$$P(\sigma) = Z^{-1}\exp\{-U(\sigma)\}, \tag{8}$$

depends on normalizing factor Z and effective potential

$$U(\sigma) = \ln I(\sigma) - \int_0^\sigma \frac{f(\sigma')}{I(\sigma')}d\sigma', \quad f \equiv -\frac{\partial V}{\partial\sigma}, \tag{9}$$

where V is synergetic potential (6) and $I(\sigma)$ is noise intensity (7) [23].

The equation defining the positions of the maxima of distribution function $P(\sigma)$ has the form

$$(1-g)x^3 + g(2-T_m)x^2 - 2g^2I_Tx + 4g^2(I_T - I_\varepsilon) = 0, \quad x \equiv 1 + \sigma^2. \tag{10}$$

Thus, distribution $P(\sigma)$ does not depend on noise intensity I_σ and stresses σ: it is specified by temperature T_m of rubbing mica surfaces; noise intensities I_ε and I_T for strain ε and lubricant film temperature T, respectively; and parameter g.

With intensity I_ε fixed, the phase diagram has the form shown in Fig. 1, where lines *1* and *2* are those lines where the system loses stability. Above line *1* defined by the equality

$$T^c = 1 + g^{-1} + 2g(I_T - 2I_\varepsilon), \tag{11}$$

the condition $\sigma \neq 0$ is the most plausible and so the lubricant is in the liquid-like state, which provides stable sliding friction (SF) and, accordingly, sliding of the surfaces. Below curve *2*, which touches straight line *1* in tricritical point *T* with the coordinates

$$T_m^c = \frac{2}{3}(1 + 2g^{-1} - 2gI_\varepsilon), \quad I_T^c = \frac{1}{6g}(g^{-1} - 1 + 8gI_\varepsilon), \tag{12}$$

function $P(\sigma)$ has a maximum only at $\sigma = 0$ and we are dealing with dry friction (DF), which is typical of a solid-like lubricant film. Between these lines, where $P(\sigma)$ has maxima at both zero and nonzero stresses, there lies the domain of stick-slip (SS) friction, where the SF–DF and DF–SF transitions periodically occur. Such transitions characterize intermittent melting of the lubricant, when it represents a mixture of liquid- and solid-like states. According to (12), such a scenario is possible even when temperature T_m of rubbing surfaces is zero provided that the amount of strain fluctuations exceeds the critical value $I_\varepsilon = (1 + 2g^{-1})/2g$. Under these conditions, the system behaves as under the SOC conditions [15].

2. SELF-SIMILARITY CONDITIONS

To further investigate the system, it is necessary to find probability distribution (8), which is specified by effective potential (9). Temperature fluctuations ($I_T \gg I_\varepsilon$ and I_σ) lead us to the expression

$$\begin{aligned} P(\sigma) &\approx I_T^{-1}[g\sigma d(\sigma)]^{-2} \\ &\times \exp\{I_T^{-1}g^{-2}\int f(\sigma)[\sigma d(\sigma)]^{-2}d\sigma\}, \\ f(\sigma) &= -\sigma(1-g) + g(T_\mathrm{m}-2)\sigma d(\sigma), \\ d(\sigma) &\equiv (1+\sigma^2)^{-1}. \end{aligned} \tag{13}$$

Since the integral in (13) tends to a constant in the limit $\sigma \longrightarrow 0$ and $d(\sigma) \longrightarrow 1$, distribution (13) has a power-type asymptotics, $P(\sigma) \sim \sigma^{-2}$. Thus, self-similar conditions without a characteristic stress scale are established that are specified by the homogeneous function

$$P(y) = y^{-2a}\mathcal{P}(\sigma), \quad y = \sigma\sigma_s \tag{14}$$

with integer exponent $2a = 2$ [24].

However, this exponent may be fractional in the general case; specifically, the SOC conditions are characterized by $2a = 1.5$. To avoid loss in generality, we replace order parameter σ by σ^a ($0 \le a \le 1$) in all the terms of Eqs. (2)–(4). Then, with regard to stochastic additions, the basic equations in dimensionless variables take the form

$$\tau_\sigma\dot{\sigma} = -\sigma^a + g\varepsilon + \sqrt{I_\sigma}\xi(t), \tag{15}$$

$$\tau_\varepsilon\dot{\varepsilon} = -\varepsilon + (T-1)\sigma^a + \sqrt{I_\varepsilon}\xi(t), \tag{16}$$

$$\tau_\mathrm{h}\dot{T} = (T_\mathrm{m}-T) - \sigma^a\varepsilon + \sigma^{2a} + \sqrt{I_T}\xi(t). \tag{17}$$

Physically, such a replacement of the exponent means that self-similarity is achieved under the assumption that stress relaxation is nonlinear and both positive and negative feedbacks are of fractional character. The adiabaticity conditions ($\tau_\varepsilon, \tau_\mathrm{h} \ll \tau_\sigma$) immediately lead us to the Langevin equation (cf. (5))

$$\tau_\sigma\dot{\sigma} = f_a(\sigma) + \sqrt{I_a(\sigma)}\xi(t), \tag{18}$$

where force $f_a(\sigma)$ and noise intensity $I_a(\sigma)$ are given by

$$\begin{aligned} f_a(\sigma) &\equiv -\sigma^a + g\sigma^a[1-(2-T_\mathrm{m})d_a(\sigma)], \\ I_a(\sigma) &\equiv I_\sigma + g^2(I_\varepsilon + I_T\sigma^{2a})d_a^2(\sigma), \\ d_a(\sigma) &\equiv (1+\sigma^{2a})^{-1}. \end{aligned} \tag{19}$$

The corresponding distribution (cf. (8)),

$$P_a(\sigma) = \frac{Z^{-1}}{I_a(\sigma)}\exp(-V_a(\sigma)), \tag{20}$$

is specified by partition function Z with the effective potential

$$V_a(\sigma) \equiv -\int_0^\sigma \frac{f_a(\sigma')}{I_a(\sigma')}d\sigma'. \tag{21}$$

The extreme points of this distribution are found from the equation

$$\frac{T_\mathrm{m}-2}{1+\sigma^{2a}} + \frac{2ag\sigma^{a-1}}{(1+\sigma^{2a})^3}[2I_\varepsilon - I_T(1-\sigma^{2a})] = \frac{1-g}{g}, \tag{22}$$

according to which the boundary of the SF domain,

$$I_T = 2I_\varepsilon, \tag{23}$$

meets the condition $\sigma = 0$. Expressions (22) and (23) are extensions of equalities (10) and (11). It follows from the above expressions that the results obtained at $a = 1$ differ little from those obtained in the general case $0 \le a \le 1$. In particular, the effect of the random stress distribution is, as before, insignificant, while strain and temperature fluctuations have a crucial effect. The dependence of stationary shear stresses σ_0 on temperature T_m changes most drastically. In the stationary determinate case, set (15)–(17) has the solution

$$\sigma_0 = [g(1-g)^{-1}(T_\mathrm{m}-2)-1]^{1/2a}, \quad g < 1, \tag{24}$$

which generalizes the standard root dependence in the case $a = 1$ (Fig. 2). As strain noise I_ε increases, σ_0 monotonically grows. A rise in I_T produces a barrier near $\sigma_0 = 0$. In addition, the dependence $\sigma_0(T_\mathrm{m})$ becomes nonmonotonic when I_T lies above straight line (23) (Fig. 3). The dashed lines in Fig. 3 cover unstable values of stresses (σ^m); the continuous lines and portions of lines, stable values (σ_0). It follows from Fig. 3 that σ^m may take a zero value only at $a = 1$ or $I_T = 2I_\varepsilon$; otherwise, the curves $\sigma^m(T_\mathrm{m})$ asymptotically tend to

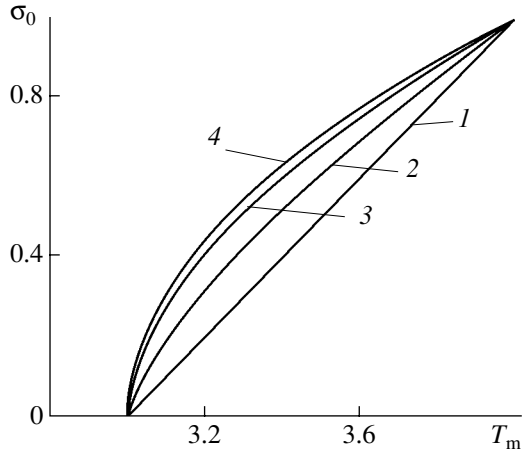

Fig. 2. Shear stresses σ_0 vs. temperature T_m for $g = 0.5$ and $a = (1)$ 0.5, (2) 0.7, (3) 0.9, and (4) 1.0.

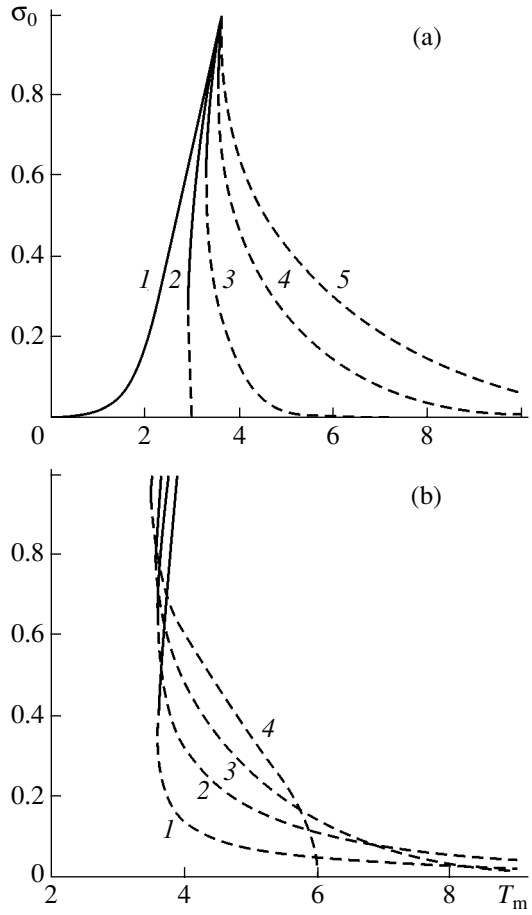

Fig. 3. Shear stresses σ_0 vs. temperature T_m for $g = 0.5$. (a) $a = 0.75$; $I_\varepsilon = 1$; and $I_T = (1)$ 1, (2) 2, (3) 3, (4) 5, and (5) 7. (b) $I_\varepsilon = 1$; $I_T = 5$; and $a = (1)$ 0.25, (2) 0.50, (3) 0.75, and (4) 1.00.

zero. This means that, if $I_T > 2I_\varepsilon$ and $a \neq 1$, there always exists effective potential barrier (21) near the point $\sigma_0 = 0$. In other words, either the lubricant experiences the first-order liquid–solid transition or the DF conditions set in. At $I_T < 2I_\varepsilon$ and $a \neq 1$, SF occurs, which corresponds to a minimum of the potential with $\sigma_0 \neq 0$, since the barrier reaches a maximum in the physically meaningless domain $\sigma^m < 0$.

The phase diagram illustrating the state of the system at different noise intensities I_ε and I_T (Fig. 4) is similar to that corresponding to the case $a = 1$. As a grows, the two-phase SS domain, which is bounded by straight line (23) and a bell-shaped curve, expands. When $a = 1$, the SF regime at small I_ε does not occur, unlike in the case $a \neq 1$. In practice, the noise intensity is, as a rule, low, and so friction is expected to reduce in systems with fractional exponent a.

Figure 5 shows probability distribution (20) corresponding to the points marked in Fig. 4. The positions of maxima in this distribution are specified by a set of parameters I_ε, I_T, I_σ, a, g, and T_m. For point *1* in the two-

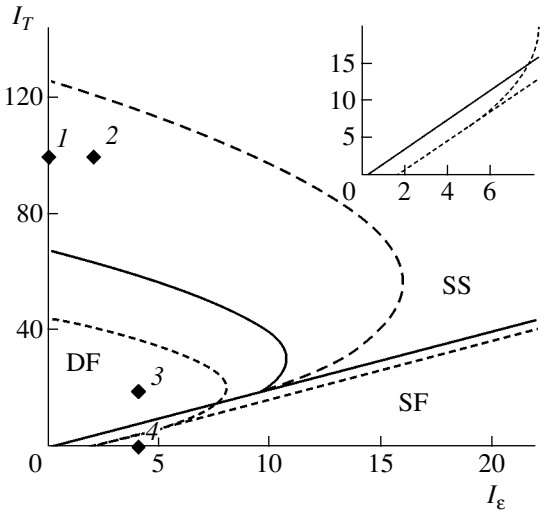

Fig. 4. Phase diagram of the system for $T_m = 0$; $g = 0.5$; I_T and $I_\varepsilon \neq 0$; and $a = 0.50$ (dashed curve), 0.75 (continuous curve), and 1.00 (dotted curve).

phase SS domain, the distribution obeys a power law (typical of the SOC conditions) with external action $T_m = 0$. Such conditions correspond to $\sigma \ll 1$, I_σ, and $I_\varepsilon \ll I_T$. With such values of these parameters, Eq. (20) reduces to canonical form (14), in which function $\mathcal{P}(\sigma)$ is given by

$$\mathcal{P}(\sigma) = Z^{-1} g^{-2} I_T^{-1} d_a^{-2}(\sigma) \times \exp\left\{-I_T^{-1} g^{-2} \int_0^\sigma \frac{1 - g[1 - 2d_a(\sigma')]}{d_a^2(\sigma')(\sigma')^a} d\sigma'\right\}. \quad (25)$$

At point *2*, distribution $P_a(\sigma)$ has maxima at both zero and nonzero stresses. Hence, point *2* lies in the SS domain. Point *3* belongs to the DF domain, where $P_a(\sigma)$ has a single maximum at $\sigma_0 = 0$. Finally, point *4* lies in the domain where the probability distribution has a single maximum at $\sigma_0 \neq 0$ (SF).

3. FRACTAL AND NONADDITIVE NATURE OF FRICTION

A feature of distribution (25) is that it is expressed through integral $\mathcal{I}_{-\sigma}^{1-a}$ of fractional power $1 - a$ (see the Appendix),

$$\mathcal{P}(\sigma) = Z^{-1} g^{-2} I_T^{-1} d_a^{-2}(\sigma) \times \exp\left\{-\frac{\Gamma(1-a)}{I_T g^2} \mathcal{I}_{-\sigma}^{1-a}\{d_a^{-2}(\sigma)[1 - g(1 - 2d_a(\sigma))]\}\right\}, \quad (26)$$

where $\Gamma(x)$ is the gamma function.

At the same time, it is known [18] that an expression of this type is a solution to the fractional Fokker–Planck equation

$$\mathcal{D}_t^{\omega}\mathcal{P}(\sigma, t) = \mathcal{D}_{-\sigma}^{\bar{\omega}}\left\{\sigma\mathcal{P}(\sigma, t) + \frac{I_T g^2}{\Gamma(\bar{\omega})}\mathcal{D}_{-\sigma}^{\bar{\omega}} \times \{d_a^2(\sigma)[1 - g(1 - 2d_a(\sigma))]^{-1}\mathcal{P}(\sigma, t)\}\right\}, \quad (27)$$

where fractional derivative $\mathcal{D}_x^{\bar{\omega}}$ (see A.2) implies the operation inverse to fraction integration (A.1).

Let us multiply equality (27) by $\sigma^{2\bar{\omega}}$ and average the result over σ. Then, for the average

$$|\sigma| \equiv \langle\sigma^{\alpha}\rangle^{\frac{1}{\alpha}}, \quad \langle\sigma^{\alpha}\rangle \equiv \int_{-\infty}^{+\infty}\sigma^{\alpha}\mathcal{P}(\sigma, t)d\sigma, \quad \alpha > 0 \quad (28)$$

with fraction order $\alpha \equiv 2\bar{\omega}$, we obtain

$$|\sigma|^z \sim t, \quad z = \frac{2\bar{\omega}}{\omega}, \quad (29)$$

where z is the dynamic exponent.

Here, we take into account the diffusion contribution alone, which dominates in the long time limit. Combining equalities (26), (29), and (A.1) yields $1 - a = \bar{\omega} = z\omega/2$, or

$$a = 1 - \frac{z\omega}{2}. \quad (30)$$

In the mean field approximation, exponent a in (14) is $a = 3/4$. Then, from expression (30), we have

$$\omega z = \frac{1}{2}. \quad (31)$$

At $\omega = 1$, which corresponds to dynamic exponent $z = 1/2$, the system evolves without traps in the phase space. According to (29), this value of z is smaller than $z = 1$, which is characteristic of ballistic behavior. On the other hand, fractional Fokker–Planck equation (27) leads to the diffusion conditions corresponding to $z = 2$ only when the order of the time derivative is $\omega = 1/4$.

Thus, in the mean field approximation ($a = 3/4$, $\bar{\omega} = 1/4$), stick-slip friction with effective traps in the phase space is established when the order of the time derivative lies in the range $1/4 < \omega < 1/2$ and dynamic exponent z falls into the range $1 < z < 2$. Essentially, such a situation is peculiar to the subdiffusion process, when the displacement of a walking particle is continuous in space but occurs discretely (at particular time instants); hence, the order of the corresponding derivative is fractional, $\omega < 1$. Unlike this situation, the walk of a particle

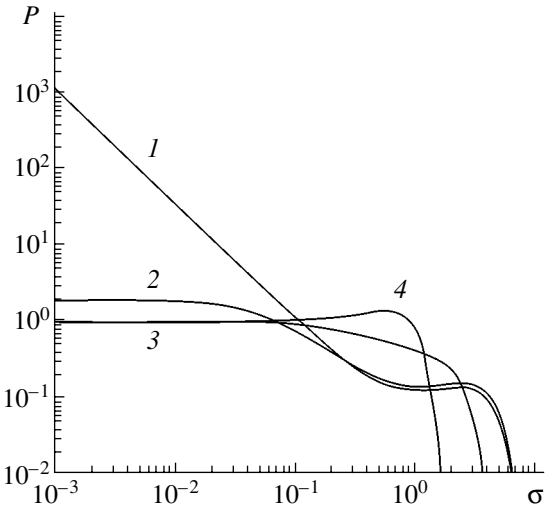

Fig. 5. Distribution function (20) for $a = 0.75$, $g = 0.5$, $T_m = 0$, $I_\sigma = 0$, and conditions shown by points in Fig. 4: (*1*) $I_\varepsilon = 0$ and $I_T = 100$ (SOC), (*2*) $I_\varepsilon = 2$ and $I_T = 100$ (SS), (*3*) $I_\varepsilon = 4$ and $I_T = 20$ (DF), and (*4*) $I_\varepsilon = 4$ and $I_T = 0$ (SF).

at Levi flights (arbitrary, including infinite, displacements) proceeds continuously in time but discretely in space [25]. In accordance with Fokker–Planck equation (27), the Levi process is characterized by order $\omega = 1$ and order $\bar{\omega} \le 1$, the latter being the order of the fractional derivative with respect to the particle coordinate. To avoid confusion, it should be noted that we consider hopping in the phase, rather than in the real geometrical, space.

Following [17], let us analyze the system in terms of nonadditive thermodynamics. It will be assumed that strain is converted to the system's complexity, which is a measure of disorder and, by analogy with the Tsallis entropy, is expressed as

$$S^{(q)} \equiv \frac{1 - \sum_i p_i^q}{q - 1}, \quad (32)$$

where $q \neq 1$ is the nonadditivity parameter.[1] Also, the temperature of the lubricant film is replaced by its internal energy given by

$$\xi^{(q)} \equiv \sum_i \xi_i Q_i, \quad (33)$$

[1] In the limit $q \longrightarrow 1$, expression (32) turns into the formula for conventional entropy, $S(p_i) = S^{(1)}(p_i) = -\Sigma_i p_i \ln p_i$. Considering two independent subsystems A and B yields $p_{ij}^{AB} = p_i^A p_j^B$ for the probability and $S_{AB}^{(q)} = S_A^{(q)} + S_B^{(q)} + (1 - q)S_A^{(q)}S_B^{(q)}$ for the entropy. The latter does not possess the additivity property $S_{AB} = S_A + S_B$, unlike the entropy in the conventional sense.

where distributions $Q_i \equiv p_i^q / \sum_j p_j^q$ and $\{\xi_i\}$ are the eigenvalues of the corresponding Hamiltonian that are obtained in view of boundary conditions [26].

Such a parametrization allows us to relate exponent z, order $\bar{\omega}$, and order ω with parameter q specifying expressions (32) and (33) [17]. The evolution of a nonadditive system is represented by the nonlinear Fokker–Planck equation

$$\mathcal{D}_t^{\omega} P(\sigma, t) = \mathcal{D}_{-\sigma}^{2} P^q(\sigma, t), \tag{34}$$

where order ω and exponent q are fractional, $\mathcal{D}_t^{\omega}$ is the fractional time derivative, and the units of measure are taken so as to exclude the effective diffusion coefficient [27].

For the self-similar normalized function

$$\begin{aligned} P(\sigma, t) &= \sigma_c^{-1} \mathcal{P}(x); \\ \sigma_c \equiv \sigma_c(t), &\quad x \equiv \sigma/\sigma_c, \end{aligned} \tag{35}$$

where σ_c is the critical value [28], we have

$$\sigma_c^{1+q} \sim t^{\omega}, \quad \mathcal{P}^{q-1} \sim x^2. \tag{36}$$

At the same time, the linear fractional Fokker–Planck equation (cf. (27))

$$\mathcal{D}_t^{\omega} P(\sigma, t) = \mathcal{D}_{-\sigma}^{2\bar{\omega}} P(\sigma, t) \tag{37}$$

yields [29]

$$\sigma_c^{2\bar{\omega}} \sim t^{\omega}, \quad \mathcal{P} \sim \begin{cases} x^{2\bar{\omega}-1}, & x \longrightarrow 0 \\ x^{-(1+2\bar{\omega})}, & x \longrightarrow \infty. \end{cases} \tag{38}$$

Comparing the first expressions in (36) and (38) gives the relationship

$$1 + q = 2\bar{\omega}. \tag{39}$$

Since the mean value of $|\sigma|$ in (28) is on the order of σ_c for self-similar systems, we find from (29), (36), and (38) that

$$1 + q = z\omega. \tag{40}$$

From the above consideration, it follows that product $z\omega \le 1$ is typically less than unity (specifically, in the mean field approximation, we have (31)); so, condition (40) holds only if $-1 < q < 0$. Thus, the given thermodynamic system is superadditive ($q < 1$): the total entropy exceeds the sum of partial entropies.

Fractional Lorentz system (15)–(17) can be assigned a fractal phase space. To complete the analysis, let us find a relationship between its fractal dimension D and the exponents and orders of derivative introduced above. To do this, we take advantage of the standard scaling relationships [28]

$$a = \frac{1}{2}\left(1 + \frac{z}{D}\right), \quad a = 1 - D^{-1}. \tag{41}$$

Comparing the last of them with (30), we find that

$$\omega z = \frac{2}{D}. \tag{42}$$

To calculate D, one should take into account that each of the stochastic degrees of freedom (σ, $S^{(q)}$, and $\xi^{(q)}$), the number of which is $n = 3$, is assigned a conjugate momentum; therefore, a smooth phase space must have dimension $D = 2n$. Such a space arises in the absence of feedback (the simplest case), when its related exponent $a = 0$ and noise is additive. As exponent a (which specifies the effective force and noise intensity in relationships (19)) grows ($a > 0$), so does the amount of feedback and the fluctuations (noise) become multiplicative. Accordingly, the phase space becomes fractal [23] and its dimension decreases by $(1 - a)$ times. Eventually, the dimension of the space where a self-organizing system evolves becomes equal to

$$D = 2n(1 - a), \tag{43}$$

where $n = 3$ for the Lorentz system.

In the general case, using equalities (30), (42), and (43), one can find the number of self-consistent stochastic equations to describe SOC at different feedback exponents,

$$n = \frac{1}{2(1-a)^2}. \tag{44}$$

In the range of interest ($a \le 1$), n indefinitely grows, starting from the minimal physical value $n_c = 1$, which corresponds to $a = 1 - 1/\sqrt{2}$. Such a one-parametric case was considered in [30]. With a further increase in a, the number of degrees of freedom needed to describe SOC should be augmented. In particular, the case $a = 1/2$ corresponds to a two-parametric representation of a self-organizing system [28, 31]. For the Lorentz system ($n = 3$ [21, 32]) to be considered, deeper feedback, $a = 1 - 1/\sqrt{6}$, is necessary.

Combining equalities (40), (42), and (43), we come to a final expression for the nonadditivity parameter,

$$1 + q = \frac{1}{n(1-a)}. \tag{45}$$

Substituting expression (44) for number n of equations needed to represent the SOC conditions into (45) yields $q = 1 - 2a$. Hence, as the amount of feedback reduces (a declines), parameter q grows. This parameter tends to a maximal value ($q \longrightarrow 1$) in systems without feedback ($a \longrightarrow 0$). Thus, provided that scaling relationships (41) from the mean field theory are valid, (i) one can reproduce the results obtained with various approaches [33], using expression (44), and (ii) the thermodynamic system under study is superadditive.

The above consideration has demonstrated that stick-slip friction can be described in terms of the con-

cept of SOC. Under the SOC conditions, the film melts at the zero temperature of rubbing surfaces. The basic feature of these conditions is that the system evolves in a self-similar manner and, accordingly, its distribution function has power-type asymptotics. It has also been shown that this fact is embodied in the Lorentz system parametrized by shear stresses, strain, and lubricant film temperature. With the self-similarity conditions taken into account, stress relaxation and feedback in the Lorentz system acquire a fractional character. The associated phase diagram separating out the SF, SS, and DF domains qualitatively coincides with that constructed for the case when this relaxation term and feedbacks are free of a fractional exponent. It should be noted that, when this exponent is other than unity, friction can be reduced if the noise intensity is low. For a system parametrized by stresses, complexity, and internal energy, the fractional Lorentz model allows one to relate the exponent in the stress distribution (multiplicative noise), fractal dimension of the phase space, number of equations needed to represent the system under the SOC conditions, and Tsallis nonadditivity parameter. Finally, it has been demonstrated that stick-slip friction is due to effective traps present in the phase space and can be identified with subdiffusion, which one may speak of when the order of the time derivative in the fractional Fokker–Planck equation is less than unity ($\omega < 1$).

ACKNOWLEDGMENTS

This work was supported by a grant of the cabinet of Ukraine.

APPENDIX

The integral of fractional order ($\bar{\omega} > 0$) is defined as [34]

$$\mathcal{I}_x^{\bar{\omega}} f(x) \equiv \frac{1}{\Gamma(\bar{\omega})} \int_0^x \frac{f(x')}{(x-x')^{1-\bar{\omega}}} dx', \qquad \text{(A.1)}$$

where $f(x)$ is an arbitrary function and $\Gamma(x)$ is the gamma function.

The operation inverse to such integration, $\mathcal{D}_x^{\bar{\omega}} \equiv \mathcal{I}_x^{-\bar{\omega}}$, is called fractional differentiation of order $\bar{\omega} > 0$,

$$\mathcal{D}_x^{\bar{\omega}} f(x) \equiv \frac{1}{\Gamma(-\bar{\omega})} \int_0^x \frac{f(x')}{(x-x')^{1+\bar{\omega}}} dx'. \qquad \text{(A.2)}$$

In the range $0 < \bar{\omega} < 1$, it is convenient to use the expression

$$\mathcal{D}_x^{\bar{\omega}} f(x) \equiv \frac{\bar{\omega}}{\Gamma(1-\bar{\omega})} \int_0^x \frac{f(x) - f(x')}{(x-x')^{1+\bar{\omega}}} dx', \qquad \text{(A.3)}$$

which takes into account that $x\Gamma(x) = \Gamma(x+1)$ for $x \equiv -\bar{\omega}$.

REFERENCES

1. B. N. J. Persson, *Sliding Friction: Physical Principles and Applications* (Springer, Berlin, 1998).
2. H. Yoshizawa, Y.-L. Chen, and J. Israelachvili, J. Phys. Chem. **97**, 4128 (1993); H. Yoshizawa and J. Israelachvili, J. Phys. Chem. **97**, 11300 (1993).
3. E. D. Smith, M. O. Robbins, and M. Cieplak, Phys. Rev. B **54**, 8252 (1996).
4. J. Krim, D. H. Solina, and R. Chiarello, Phys. Rev. Lett. **66**, 181 (1991).
5. J. M. Carlson and A. A. Batista, Phys. Rev. E **53**, 4153 (1996).
6. I. S. Aranson, L. S. Tsimring, and V. M. Vinokur, Phys. Rev. B **65**, 125402 (2002).
7. P. A. Thompson and M. O. Robbins, Phys. Rev. A **41**, 6830 (1990).
8. F. Family, M. O. Braiman, and H. G. E. Hentschel, *Friction, Arching, Contact Dynamics*, Ed. by D. E. Wolf and P. Grassberger (World Sci., Singapore, 1996), pp. 33–41.
9. Y. Braiman, H. G. E. Hentschel, F. Family, *et al.*, Phys. Rev. E **59**, R4737 (1999).
10. O. M. Braun and Yu. S. Kivshar, Phys. Rev. B **43**, 1060 (1991).
11. J. B. Sokoloff, Phys. Rev. B **51**, 15573 (1995).
12. T. Kawaguchi and H. Matsukawa, Phys. Rev. B **56**, 4261 (1997).
13. A. V. Khomenko and O. V. Yushchenko, Phys. Rev. E **68**, 036110 (2003).
14. A. V. Khomenko, Phys. Lett. A **329**, 140 (2004).
15. P. Bak, *How Nature Works: The Science of Self-Organized Criticality* (Springer, New York, 1996).
16. A. I. Olemskoi, Physica A **310**, 223 (2002).
17. C. Tsallis, in *Lecture Notes in Physics*, Ed. by S. Abe and Y. Okamoto (Springer, Heidelberg, 2001).
18. G. M. Zaslavsky, Phys. Rep. **371**, 461 (2002).
19. *Rheology: Theory and Applications*, Ed. by F. R. Eirich (Academic, New York, 1956; Inostrannaya Literatura, Moscow, 1962).
20. H. Haken, *Synergetics: An Introduction* (Springer, Berlin, 1977; Mir, Moscow, 1980).
21. A. I. Olemskoĭ and A. V. Khomenko, Zh. Éksp. Teor. Fiz. **110**, 2144 (1996) [JETP **83**, 1180 (1996)].
22. H. Risken, *The Fokker–Planck Equation: Methods of Solution and Applications*, 2nd ed. (Springer, Berlin, 1989).
23. A. I. Olemskoi, Usp. Fiz. Nauk **168**, 287 (1998) [Phys. Usp. **41**, 269 (1998)].
24. D. J. Amit, *Field Theory, the Renormalization Group and Critical Phenomena* (McGraw Hill, New York, 1978).
25. R. Metzler and J. Klafter, Phys. Rep. **339**, 1 (2000).

26. A. I. Olemskoi, A. V. Khomenko, and D. A. Olemskoi, Physica A **332**, 185 (2004).
27. A. I. Olemskoi and D. O. Kharchenko, Physica A **293**, 178 (2001).
28. A. Vespignani and S. Zapperi, Phys. Rev. Lett. **78**, 4793 (1997); Phys. Rev. E **57**, 6345 (1998).
29. A. I. Olemskoi and D. O. Kharchenko, J. Phys. Stud. **6**, 253 (2002).
30. T. Hwa and M. Kardar, Phys. Rev. A **45**, 7002 (1992).
31. A. Mehta and G. C. Barker, Rep. Prog. Phys. **57**, 383 (1994).
32. A. I. Olemskoi and A. V. Khomenko, Phys. Rev. E **63**, 036116 (2001).
33. A. Chessa, E. Marinari, A. Vespignani, *et al.*, Phys. Rev. E **57**, R6241 (1998).
34. S. G. Samko, A. A. Kilbas, and O. I. Marichev, *Fractional Integrals and Derivatives: Theory and Applications* (Nauka i Tekhnika, Minsk, 1987; Gordon and Breach, Amsterdam, 1993).

Translated by V. Isaakyan

Technical Physics, Vol. 50, No. 11, 2005, pp. 1431–1434. Translated from Zhurnal Tekhnicheskoĭ Fiziki, Vol. 75, No. 11, 2005, pp. 40–43.

GASES AND LIQUIDS

On One Method of Simultaneously Measuring the Mass Flow Rate and Density of a Liquid

E. V. Mayorov and V. A. Onishchuk†

Emanuel Institute of Biochemical Physics, Russian Academy of Sciences, ul. Kosygina 4, Moscow, 119991 Russia

e-mail: sal@deom.chph.ras.ru

Received February 16, 2005

Abstract—The problem of an ideal incompressible liquid flowing in an axisymmetric pipe with a cross section varying in space and time is solved. The case when the area of variation of the cross section is represented by two identical series-connected cylinders is considered. It is shown that, if the cross sections of the cylinders vary with a constant frequency so that one decreases and the other increases, pressure difference oscillations arising at the ends of the cylinders bear information on both the liquid density and the flow rate in the pipe. The feasibility of designing an instrument based on these results and the choice of its performance parameters are discussed. It is noted, in particular, that the length of either cylinder must be no less than the pipe mean diameter.

Among the variety of liquid and gas flowmeters, mass flowmeters are usually of primary interest for the user. These devices measure the oscillations of a flow whirled in a special manner [1], gyroscopic moments acting on the moving parts of pipelines or moments of inertia (Coriolis forces) of turbines (or radial bar rotors) rotating in a flow to be measured [2], or distortion of the temperature field in the pipeline heated from the outside and washed by the medium to be measured from the inside [2].

In this paper, we offer a new method to measure the density and mass flow rate of a liquid. The processes occurring in this flowmeter allow us to categorize it as an inertial mass flowmeter that stands out from other representatives of this class because of its unique properties. Let us perform tentative theoretical calculations based on which we shall proceed further.

Consider an incompressible ideal liquid (Fig. 1) flowing in an axisymmetric pipe the cross section of which is a function of coordinate and time. Cross-sectional area $S(x, t)$ of the pipe is assumed to be given.

Assuming the flow to be quasi-one-dimensional, we can write the set of equations for such a flow in the form [3]

$$\begin{aligned}\frac{\partial S}{\partial t} + \frac{\partial (SV)}{\partial x} &= 0,\\ \frac{\partial V}{\partial t} + V\frac{\partial V}{\partial x} &= -\frac{1}{\rho}\frac{\partial \rho}{\partial x}.\end{aligned} \tag{1}$$

Here, ρ is the liquid density, $S(x, t)$ is the pipe's cross-sectional area, and $V(x, t)$ is the velocity averaged over the cross section. The average velocity is related to the mass flow rate as[1]

$$Q(x, t) = \rho V(x, t)S(x, t), \tag{2}$$

where $p(x, t)$ is the pressure averaged over the cross section.

If constant of integration $C(t)$ is time-independent and equal to Q_0/ρ, where Q_0 is the mass flow rate in the unperturbed part of the pipe, the first equation of system (1) yields

$$V = \frac{1}{S}\left(C(t) - \int\frac{\partial S}{\partial t}dx\right) = \frac{1}{S}\left(\frac{Q_0}{\rho} - \int\frac{\partial S}{\partial t}dx\right). \tag{3}$$

Substituting Eq. (3) into the second equation of (1) and carrying out appropriate calculations, we obtain

$$\begin{aligned}\frac{1}{\rho}\frac{\partial p}{\partial t} &= \frac{1}{S^3}\frac{\partial S}{\partial x}\left(\frac{Q_0}{\rho} - \int\frac{\partial S}{\partial t}dx\right)^2\\ &+ \frac{2}{S^2}\frac{\partial S}{\partial t}\left(\frac{Q_0}{\rho} - \int\frac{\partial S}{\partial t}dx\right) + \frac{1}{S}\int\frac{\partial^2 S}{\partial t^2}dx.\end{aligned} \tag{4}$$

Of interest is a solution to this equation for the case when the cross section varies over a part of the pipe by the law

$$S = \begin{cases} S_0 + G(t, x) = S_0 + a_0\sin\left(\dfrac{x\pi}{L}\right)\sin(\omega t)\\ = S_0\left(1 + \delta\sin\left(\dfrac{x\pi}{L}\right)\sin(\omega t)\right) \text{ at } -L \le x \le L,\\ S_0, \text{ at } -L > x, L > x.\end{cases} \tag{5}$$

† Deceased.

[1] In this formula, the mass flow rate may have both signs according to the sign of velocity $V(x, t)$ relative to the x axis.

1063-7842/05/5011-1431$26.00 © 2005 Pleiades Publishing, Inc.

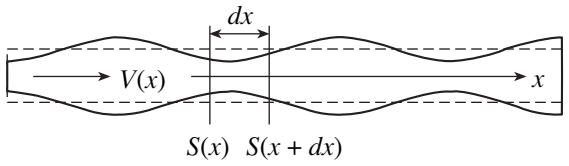

Fig. 1.

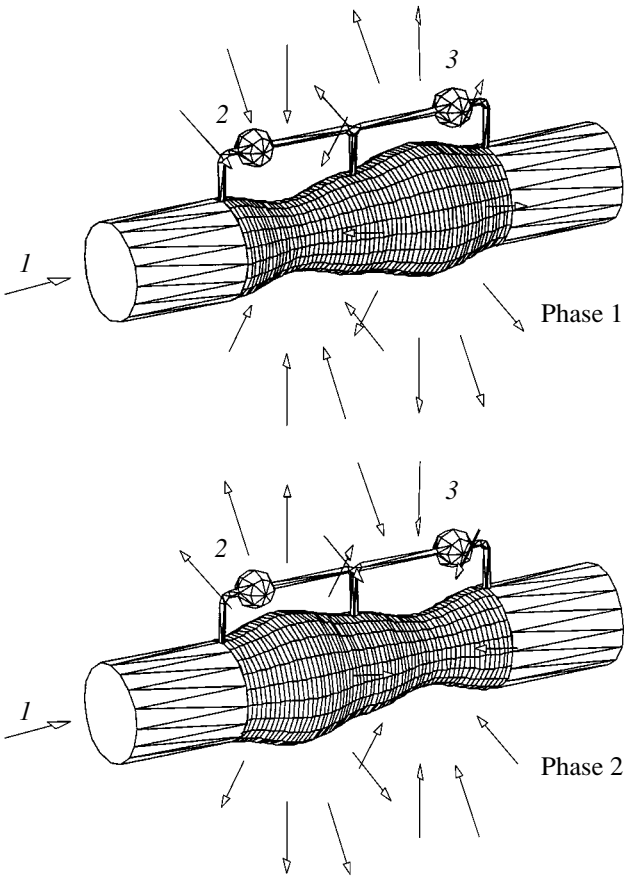

Fig. 2. (*1*) Flow to be measured, (*2*) left pressure meter, and (*3*) right pressure.

Here, $\delta = a_0/S_0$. We shall seek an expression for the pressure difference between points $x = -L$, $x = 0$, and $x = +L$; i.e., $\Delta p_{\text{left}}(t) = p(0, t) - p(-L, t)$ and $\Delta p_{\text{right}}(t) = p(L, t) - p(0, t)$. By way of illustration, Fig. 2 shows two phases in variation of the cross section: phase *1* corresponds to time intervals when $\sin(\omega t) > 0$; phase *2*, to those when $\sin(\omega t) < 0$ (the positive direction of the x axis coincides with the flow direction). We linearize Eq. (4), assuming that δ is small and the inequality

$$\frac{Q_0\pi}{\rho S_0 \omega L} > 1$$

is satisfied.[2] Eventually, we arrive at the following equation:

$$\frac{\partial \rho}{\partial x} = \frac{\delta\omega^2 L\rho}{\pi}\sin(\omega t)\left(\cos\left(\frac{x\pi}{L}\right) + 1\right)$$
$$+ Q_0\frac{2\delta\omega}{S_0}\cos(\omega t)\sin\left(\frac{x\pi}{L}\right) + \frac{Q_0^2}{\rho}\frac{\delta\pi}{S_0^2 L}\sin(\omega t)\cos\left(\frac{x\pi}{L}\right).$$

Integrating over x yields an expression for the pressure of a nonviscous liquid flowing within the portion $x \subset [-L, L]$ of a moving-wall pipe and obeying law (5) in the quasi-one-dimensional approximation (the motion of the walls is small, $\delta \ll 1$),

$$p(x, t) = \frac{\delta\omega^2 L^2\rho}{\pi^2}\sin(\omega t)\sin\left(\frac{x\pi}{L}\right)$$
$$+ \frac{\delta\omega^2 L\rho}{\pi}\sin(\omega t)(x + L)$$
$$- Q_0\frac{2\delta\omega L}{S_0\pi}\cos(\omega t)\left(\cos\left(\frac{x\pi}{L}\right) + 1\right) \quad (6)$$
$$+ \frac{Q_0^2}{\rho}\frac{\delta}{S_0^2}\sin(\omega t)\sin\left(\frac{x\pi}{L}\right) + P_0,$$

where P_0 is a constant of integration, which may be equal, for example, to the hydrostatic pressure.

The pressures at the points of interest are

$$p(-L, t) = P_0,$$
$$p(0, t) = \frac{\delta\omega^2 L^2\rho}{\pi}\sin(\omega t) - Q_0\frac{4\delta\omega L}{S_0\pi}\cos(\omega t) + P_0,$$
$$p(L, t) = \frac{2\delta\omega^2 L^2\rho}{\pi}\sin(\omega t) + P_0.$$

Now we construct the desired pressure differences,

$$\Delta p_{\text{left}}(t) = p(0, t) - p(-L, t)$$
$$= \rho\frac{\delta\omega^2 L^2}{\pi}\sin(\omega t) - 4Q_0\frac{\delta\omega L}{\pi S_0}\cos(\omega t),$$
$$\Delta p_{\text{right}}(t) = p(+L, t) - p(0, t)$$
$$= \rho\frac{\delta\omega^2 L^2}{\pi}\sin(\omega t) + 4Q_0\frac{\delta\omega L}{\pi S_0}\cos(\omega t), \quad (7)$$
$$\Delta p(t) = p(+L, t) - p(-L, t)$$
$$= 2\rho\frac{\delta\omega^2 L^2}{\pi}\sin(\omega t).$$

According to formulas (7), if the cross sections of two series-connected identical portions of a pipe with a

[2] It will be shown that this stringent condition reduces the practical value of the results obtained.

flowing liquid vary harmonically in antiphase so that the oscillation amplitude is much smaller than the diameter of the unpertubed part of the pipe, variable pressure differences arise within those portions. Separately measuring the amplitudes of the mutually orthogonal components of the pressure differences, one can independently find the density and mass flow rate of the liquid. From Eq. (7), the amplitude of the in-phase and orthogonal components are given, respectively, by

$$A_\rho = \rho\frac{\delta\omega^2 L^2}{\pi} = \left[\frac{\text{dyn}}{\text{cm}^2}\right], \quad (8)$$

$$A_Q = 4Q_0\frac{\delta\omega L}{\pi S_0} = \left[\frac{\text{dyn}}{\text{cm}^2}\right]. \quad (9)$$

In essence, to measure the density and/or mass flow rate, one should apply identical periodical axisymmetric antiphase impulses to two series-connected portions of the pipe perpendicularly to the axis of the pipe (Fig. 2; such an action on a flow changes its axial momentum within the portions of interest) and then analyze a variable pressure difference in any of these portions. The pressure difference is due to axial inertial forces arising in the moving liquid.

Below, we would like to answer the questions that inevitably arise in an attempt to implement a measuring device.

FORCE PULSER

As an impulse-generating unit (force pulser), we offer a thin elastic cylindrical membrane clamped at its center and at both ends in such a way that the inner surface faces the flow to be measured and the outer surface is in a closed cylindrical vessel divided into two strictly identical isolated semicylinders at the place of the central clamp.

It is assumed that each of the isolated semicylinders is hermetically connected to a bellows through holes in the outer wall. The free end of one of the bellows is rigidly connected to the free end of the other semicylinder, and the inner spaces of the semicylinders are disconnected and filled with a special bubble-free liquid (Fig. 3). The joint of the bellows with a baffle in between will be called the head of the bellows couple. The case considered in [4] shows that the pressure dependence of the deflection of the cylindrical membrane is linear. Hence, a sinusoidal pressure variation above the membrane will cause sinusoidal perturbation ΔR of its radius R_0. It can be shown that, if $\delta_r = \Delta R/R_0$ is small, the relative increment of the pipe's cross-sectional area, $\delta = a_0/S_0$, may be set equal to $\delta = 2\delta_r$; hence, the variation of the cross-sectional area is also sinusoidal. Thus, a sinusoidal displacement of the head of the bellows couple will lead to a sinusoidal variation in the cross section of the cylindrical membrane. In other words, to make the cross section vary by law (5) is quite realistic.

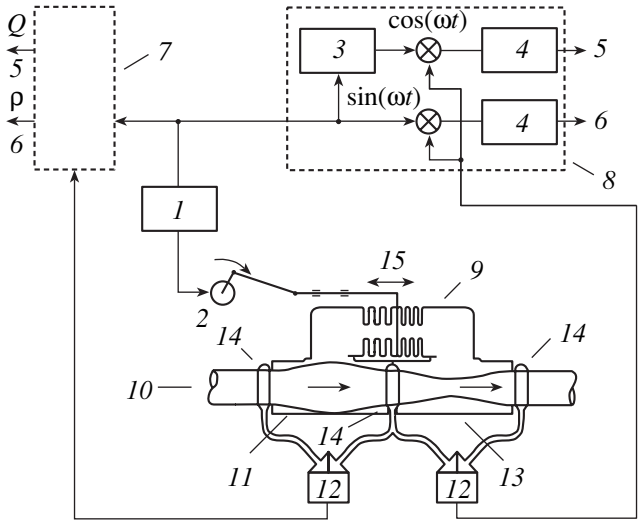

Fig. 3. (*1*) Driving oscillator with frequency ω, (*2*) synchronous motor, (*3*) π/2 phase shifter, (*4*) integrator over the interval $0 < t < 2\pi/\omega$, (*5*) value proportional to the mass flow per second, (*6*) value proportional to the liquid density, (*7*) left analyzer, (*8*) right analyzer, (*9*) bellows couple, (*10*) flow being measured, (*11*) elastic cylindrical membrane fixed at the center and at the ends, (*12*) pressure difference sensor, (*13*) body of meter, (*14*) ring chamber hermetically closed from the inside by the elastic cylindrical membrane of diameter equal to the pipeline diameter, and (*15*) displacement direction of bellows couple head.

Such a balance scheme of flow perturbation by law (5) is very convenient: the equilibrium position of the head of the bellows couple does not depend on a strong variation of the hydrostatic pressure provided that an external force displacing the head is absent; otherwise, the mass flow rate and the density of the liquid would have to be measured separately.

How long should length L of the cylindrical membrane be? For a flow about a body vibrating with an amplitude much less than its characteristic dimension [5], it is argued that the velocity of the liquid experiences perturbations on the order of the vibrating body velocity over a distance roughly equal to the dimension of the body. Then, taking the length of the "breathing" wall for the length of a vibrating body and setting it equal to the diameter of the pipe, one can assume that the flow velocity will vary roughly by the wall velocity over any cross section of the "modulated" part of the pipe. That is, all the liquid will have an alternating-sign momentum over the length of the modulated part. Accordingly, the length of the measuring device with a balance force pulser must be no less than two diameters of the pipe. A more accurate selection of the dimensions of the force pulser can be made after a careful consideration of the flow velocity distribution over the time- and coordinate-dependent cross section.

SENSOR

We recommend pressure-difference sensors based on a single-crystalline silicon membrane. Silicon pressure sensors offer a high precision, sensitivity, and overload endurance; wide dynamic range; extremely small hysteresis; and operating reliability. In addition, they are almost inertialess.

ANALYZER

Analysis of the signal from the pressure sensor implies harmonic separation. In general, measuring the amplitudes of two harmonics with frequency ω and mutually orthogonal initial phases is a task of spectral analysis. Such a problem can be solved, e.g., with a device described in [6].

The amplitude of the variable pressure-difference component that is in phase with the moving membrane is proportional to the flow density, and that of the orthogonal component to the mass flow rate in the pipe. From the expressions for $\Delta p_{\text{left}}(t)$ and $\Delta p_{\text{right}}(t)$ in (7), it readily follows that measuring the difference between the output signals from the left and right analyzers improves the sensitivity of mass-flow measurement twofold. Similarly, measuring the sum of the output signals improves the sensitivity of density measurement by the same factor. A wide variety of different circuit-design approaches and devices that may be applied to solve this problem saves us any comment on this issue.

Let us perform a tentative calculation. For pipe radius $R_0 = 5$ cm, driving frequency $f = \omega/2\pi = 60$ Hz, half-length of the variable section of the pipe $L = 30$ cm, liquid density $\rho = 1$ g/cm^3, and relative change in the pipe diameter $\delta_r = 0.005$, the partial pressure amplitude proportional to the density of the liquid is $A_\rho \approx 0.41 \times 10^6$ dyn/cm^2 $\approx 0.41 \times 10^4$ mm H_2O/cm^2 ≈ 0.41 atm (see formula (8)). To calculate the partial pressure amplitude proportional to the mass flow rate, we substitute the value of the mass flow taken with regard to the limitation mentioned above (see footnote 2) into Eq. (9). This is a critical value starting from which the theory presented here adequately describes the processes taking place in the measuring device suggested. In our case, this value is $Q_0 = 2.84 \times 10^5$ g/s and the partial pressure responsible for the mass flow rate is $A_Q \approx 1.27 A_\rho$.

As was mentioned above, our theory is invalid when $\delta \sim 1$. We suppose that, without this limitation, the response of the device (pressure difference) will also depend on both the density and the mass flow rate of the liquid, possibly in another form. It seems that a relationship between the components involving the measurands will be more suitable for the combined measurement. This issue will be clarified after solving this more complicated problem.

ACKNOWLEDGMENTS

We are grateful to A.A. Ovchinnikov†, E.B. Burlakova, and V.M. Misin for encouragement and support.

REFERENCES

1. A. Sh. Kiyasbeĭli and M. E. Perel'shteĭn, *Vortical Measuring Instruments, Ser. Instrument-Making Engineer's Bookshelf* (Mashinostroenie, Moscow, 1978), pp. 113–125 [in Russian].
2. *Proceedings of the Scientific–Technical Conference on Methods and Instruments for Measuring the Consumption and Amount of Liquids, Gases, and Vapors, Moscow, 1965*, pp. 132–172.
3. I. P. Ginzburg, *Applied Hydro- and Gas Dynamics* (Leningr. Gos. Univ., Leningrad, 1958), p. 40 [in Russian].
4. V. I. Feodos'ev, in *Strength of Materials, Ser. "Mechanics in Technical University,"* (Bauman Gos. Tekh. Univ., Moscow, 1999), Vol. 2, pp. 429–432 [in Russian].
5. L. D. Landau and E. M. Lifshitz, *Course of Theoretical Physics*, Vol. 6: *Fluid Mechanics* (Nauka, Moscow, 1986; Pergamon, New York, 1987).
6. A. A. Kharkevich, *Spectra and Analysis* (Fizmatlit, Moscow, 1962; Consultants Bureau, New York, 1960), p. 111.

Translated by M. Astrov

† Deceased.

Technical Physics, Vol. 50, No. 11, 2005, pp. 1417–1422. Translated from Zhurnal Tekhnicheskoĭ Fiziki, Vol. 75, No. 11, 2005, pp. 26–31.

GASES AND LIQUIDS

Calculation of the Velocity of a Molecular Gas Slipping over a Sphere with Regard to Accommodation Coefficients

A. V. Latyshev, V. N. Popov, and A. A. Yushkanov

Lomonosov State University, Arkhangelsk, 163002 Russia

e-mail: avlatyshev@comail.ru

Received July 12, 2004

Abstract—The velocity of molecular gas slipping over a spherical surface is calculated by exact analytical methods including the accommodation coefficients for the first two moments of the distribution function. An extension of the BGK approach to the Boltzmann kinetic model for the case of rotational degrees of freedom is used as the basic equation. © *2005 Pleiades Publishing, Inc.*

INTRODUCTION

Description of molecular gases is basically more difficult than that of simple (monoatomic) gases. [1]. The state of the latter is fully described by the distribution function specified as a function of coordinates $\mathbf{r}'$ of the center of inertia of molecules and their velocities $\mathbf{v}$. For a molecular gas, the distribution function also depends on rotational and vibrational degrees of freedom. Except for ultralow temperatures, the rotational degrees of freedom of molecular gases can be described in classical terms. The vibrational degrees of freedom are described only in terms of quantum theory. However, for a wide temperature range (10–1000 K), it may be assumed that the vibrational degrees of freedom are not excited and molecules of the gas are in the ground state [2].

The kinetic theory of rarefied gas is based on the Boltzmann equation [2]. Since the fivefold collision integral appearing on the right of this equation is nonlinear, its exact solutions are impossible to obtain in the general case. In light of this, the Boltzmann equation is usually replaced by related model equations. The simplest model of the collision integral seems to be the BGK collision integral

$$I(f) = \nu_0(f_{eq} - f). \tag{1}$$

Here, f is the gas molecule distribution function, f_{eq} is the locally equilibrium Maxwellian, and ν_0 is the collision parameter of the model. For polyatomic gases, f and f_{eq} depend on coordinates $\mathbf{r}'$ of the centers of inertia of gas molecules and on their translational, $\mathbf{v}$, and rotational, ω, velocities.

The BGK model of the Boltzmann kinetic equation can be generalized for the case of molecular gases, where rotation is classical and vibration is "frozen," as follows. Consider a diatomic gas. A molecule of such a gas rotates in the plane normal to the vector of rotational moment $\mathbf{M}$ of the molecule. In actual physical problems, the distribution function can be considered as independent of the orientation of the molecule axis of symmetry in this plane [2]. Therefore, the rotation of a molecule of a diatomic gas is fully described by specifying the magnitude of the rotational moment vector, $M = J\omega$ (J is the magnitude of the moment of inertia of a molecule). Then, function f_{eq} for a diatomic gas can be written in the form

$$f_{eq} = n_{eq}\left(\frac{m}{2\pi k_B T_{eq}}\right)^{3/2}\frac{J}{k_B T_{eq}}\left[-\frac{m(\mathbf{v}-\mathbf{u})^2}{2k_B T_{eq}} - \frac{J\omega^2}{2k_B T_{eq}}\right],$$

where

$$n_{eq} = \int f\omega d\omega d^3v, \quad \mathbf{u} = \frac{1}{n_{eq}}\int \mathbf{v} f\omega d\omega d^3v, \tag{2}$$

$$T_{eq} = \frac{2}{5k_B n_{eq}}\int\left[\frac{m(\mathbf{v}-\mathbf{u})^2}{2} + \frac{J\omega^2}{2}\right] f\omega d\omega d^3v. \tag{3}$$

Here, m is the molecular mass weight and k_B is the Boltzmann constant. Let us turn to the stationary BGK equation written in the spherical coordinates [2] with collision operator (1),

$$v_r\frac{\partial f}{\partial r'} + \frac{v_\theta}{r'}\frac{\partial f}{\partial \theta} + \frac{v_\varphi}{r'\sin\theta}\frac{\partial f}{\partial \varphi} + \frac{v_\theta^2 + v_\varphi^2}{r'}\frac{\partial f}{\partial v_r} + \frac{v_\varphi^2\cot\theta - v_r v_\theta}{r'}\frac{\partial f}{\partial v_\theta} - \frac{v_\varphi v_\theta\cot\theta + v_r v_\varphi}{r'}\frac{\partial f}{\partial v_\varphi} = \nu_0(f_{eq} - f). \tag{4}$$

We assume that

$$|T/T_0 - 1| \ll 1, \quad \lambda|\nabla \ln T| \ll 1,$$

$$\sqrt{m/2k_B T_0}\,u_{eq} \ll 1,$$

1063-7842/05/5011-1417$26.00 © 2005 Pleiades Publishing, Inc.

where T_0 is the temperature at the origin, λ is the molecule free path, and $\mathbf{u}_{eq}$ is the mass-averaged gas velocity.

Then, the distribution function takes the form

$$f(\mathbf{r}, \mathbf{v}, \omega) = f_0(v, \omega)[1 + Y(\mathbf{r}, \mathbf{v}, \omega)]. \quad (5)$$

Here,

$$f_0(v, \omega) = n_s\left(\frac{m}{2\pi k_B T_s}\right)^{3/2} \frac{J}{k_B T_s} \exp\left[-\frac{mv^2}{2k_B T_s} - \frac{J\omega^2}{2k_B T_s}\right]$$

is the distribution function with parameters specified on the surface over which the gas slides, and n_s and T_s are the gas concentration and temperature on this surface.

In view of (2), (3), and (5), we obtain

$$f_{eq} = f_0(v, \omega)\left(1 + \frac{\delta n}{n_s}\right)\left(1 + \frac{\delta T}{T_s}\right)^{-5/2} \times \exp\left[\frac{m\mathbf{v}\cdot\mathbf{u}}{k_B T_s} + \frac{mv^2 + J\omega^2}{2k_B T_s}\frac{\delta T}{T_s}\right] \quad (6)$$

$$= f_0(v, \omega)\left[1 + \frac{\delta n}{n_s} + \frac{m\mathbf{v}\cdot\mathbf{u}}{k_B T_s} + \left(\frac{mv^2 + J\omega^2}{2k_B T_s} - \frac{5}{2}\right)\frac{\delta T}{T_s}\right],$$

where

$$\delta n = \int f_0(v, \omega) Y(\mathbf{r}, \mathbf{v}, \omega)\omega d\omega d^3 v,$$

$$\delta T = \frac{2}{5k_B n_s}\int\left[\frac{mv^2}{2} + \frac{J\omega^2}{2}\right] f_0(v, \omega) Y(\mathbf{r}, \mathbf{v}, \omega)\omega d\omega d^3 v.$$

Substituting (5) and (6) into (4) and passing to dimensionless quantities, we arrive at

$$C_r\frac{\partial Y}{\partial r} + Y(\mathbf{r}, \mathbf{C}, \nu) + k\left[C_\theta\frac{\partial Y}{\partial\theta} + \frac{C_\varphi}{\sin\theta}\frac{\partial Y}{\partial\varphi} + (C_\theta^2 + C_\varphi^2)\frac{\partial Y}{\partial C_r} + (C_\varphi^2\cot\theta - C_r C_\theta)\frac{\partial Y}{\partial C_\theta} - (C_\varphi C_\theta\cot\theta + C_r C_\varphi)\frac{\partial Y}{\partial C_\varphi}\right] = \int k(\mathbf{C}, \nu, C'; \nu') Y(\mathbf{r}, \mathbf{C}', \nu') d\Omega. \quad (7)$$

Here, $l = 2$; $d\Omega = 2\pi^{-3/2}\exp(-C^2 - \nu^2)\nu d\nu d^3 C$; $k = 3\mathrm{Kn}/(3\sqrt{\pi}\,\mathrm{Pr})$ for thermodynamic slip or $k = 2\mathrm{Kn}/(\sqrt{\pi}\,\mathrm{Pr})$ for thermal slip,

$$k(\mathbf{C}, \nu; \mathbf{C}', \nu') = 1 + 2\mathbf{C}\cdot\mathbf{C}' + \frac{1}{l + 1/2}(C^2 + \nu^2 - l - 1/2)(C'^2 + \nu'^2 - l - 1/2),$$

$\mathbf{C} = \mathbf{v}\sqrt{m/2k_B T_s}$; $\nu = \omega\sqrt{J/2k_B T_s}$; $\mathbf{r} = 3\sqrt{\pi}\,\mathrm{Pr}/(4\lambda)\mathbf{r}'$ for thermodynamic slip or $\mathbf{r} = \sqrt{\pi}\,\mathrm{Pr}/(2\lambda)\mathbf{r}'$ for thermal slip; $\lambda = \nu_g(\pi m/2k_B T_s)^{1/2}$; ν_g is the kinematic viscosity of the gas; Kn is the Knudsen number; and Pr is the Prandtl number.

For a polyatomic gas (number N of atoms in a molecule is greater than three), the distribution function depends not only on rotational moment $\mathbf{M}$ of the molecule but also on the angles specifying the orientation of the axes of the molecule about vector $\mathbf{M}$ [2]. Therefore,

$$f_{eq} = n_{eq}\left(\frac{m}{2\pi k_B T_{eq}}\right)^{3/2}\frac{(J_1 J_2 J_3)^{1/2}}{(2\pi k_B T_{eq})^{3/2}} \times \exp\left[-\frac{mv^2}{2k_B T_{eq}} - \frac{\Sigma_{i=1}^3 J_i\omega_i^2}{2k_B T_{eq}}\right],$$

$$n_{eq} = \int f d^3\omega d^3 v, \quad \mathbf{u} = \frac{1}{n_{eq}}\int\mathbf{v} f d^3\omega d^3 v,$$

$$T_{eq} = \frac{2}{5k_B n_{eq}}\int\left[\frac{m(\mathbf{v} - \mathbf{u})^2}{2} + \frac{J\omega^2}{2}\right] f d^3\omega d^3 v, \quad (8)$$

$$f_0(v, \omega) = n_s\left(\frac{m}{2\pi k_B T_s}\right)^{3/2}\frac{(J_1 J_2 J_3)^{1/2}}{(2\pi k_B T_s)^{3/2}} \times \exp\left[-\frac{mv^2}{2k_B T_s} - \frac{\Sigma_{i=1}^3 J_i\omega_i^2}{2k_B T_{eq}}\right].$$

Here, J_i (i = 1–3) are the components of the moment of inertia of gas molecules. Linearizing (8) in view of (5) and passing to dimensionless quantities, we arrive, as in the case of a diatomic gas, at Eq. (7) with the only difference being that, for a polyatomic gas, $l = 5/2$ and $d\Omega = \pi^{-3}\exp(-C^2 - \nu^2)d^3\nu d^3 C$. Thus, the extension of the BGK model of the Boltzmann equation for molecular gases has been constructed and has form (7).

Next, using this extension and the two-moment accommodation boundary condition [4], we will calculate the velocity of a molecular gas slipping over a solid spherical surface with a small radius of curvature ($0.01 < \mathrm{Kn} = \lambda/R' < 0.4$, where R' is the dimensional radius of an aerosol particle).

For a molecular gas, the two-moment accommodation boundary condition is written as

$$Y(\mathbf{r}, \mathbf{C}, \nu)|_s = 2d_1 C_\theta + 2d_2 C_r C_\theta, \quad C_r > 0,$$

where d_1 and d_2 are found from the conditions

$$(1 - q_1)\int\limits_{C_r < 0} f(\mathbf{r}, \mathbf{C}, \nu)|_s C_r C_\theta dg = -\int\limits_{C_r > 0} f(\mathbf{r}, \mathbf{C}, \nu)|_s C_r C_\theta dg,$$

$$(1-q_2)\int\limits_{C_r,0} f(\mathbf{r},\mathbf{C},\nu)|_s C_r^2 C_\theta dg$$

$$= \int\limits_{C_r>0} f(\mathbf{r},\mathbf{C},\nu)|_s C_r^2 C_\theta dg.$$

Here, $dg = 2\pi^{-3/2}\nu d\nu d^3C$ or $dg = \pi^{-3}d^3\nu d^3C$ for a polyatomic and diatomic gas, respectively, and

$$f(\mathbf{r},\mathbf{C},\nu)|_s = f_0(C,\nu)[1 + Y(\mathbf{r},\mathbf{C},\nu)|_s].$$

For a monoatomic gas, the problem in such a statement was solved in [5]. The case of the gas flow about a direct circular cylinder was considered in [6]. At $q_1 = q_2 = \alpha_\tau$, the above boundary condition closely approximates the Maxwell specular–diffuse boundary condition. In [5], we showed that, for a rarefied gas slipping over a flat solid surface, the discrepancies between the α_τ dependences (α_τ is the accommodation coefficient of the tangential momentum) of the thermal and isothermal slip coefficients that are obtained with the above boundary condition and those given in [7] differ by 0.72 and 0.005%, respectively, throughout the α_τ range.

It is noteworthy that the BGK model of the Boltzmann equation, though simple, adequately describes a first-order slip (i.e., slip of a rarefied gas about a flat solid surface). For a monoatomic gas slipping over a flat solid surface, the thermal and isothermal slip coefficients derived by means of rigorous analytical techniques exactly coincide with those obtained with the ellipsoidal statistical model, $K_{TS}^{(0)} = 1.149996$ and $C_m^{(0)} = 1.14665627$. It is important here that the ellipsoidal statistical model in the hydrodynamic limit yields the true value of the Prandtl number, Pr = 2/3. For comparison, in [8], where gas molecules are considered as hard spheres, these coefficients calculated from the linearized Boltzmann model were found to be $K_{TS}^{(0)} = 1.00217$ and $C_m^{(0)} = 1.11132$. Temperature steps C_T equal 2.2037 in the BGK model and 2.12703 in the model used in [8]. The discrepancy between the values of $K_{TS}^{(0)}$ stems from different approaches to establishing a relationship between the molecule mean free path in a gas and its kinematic viscosity—the parameters used in reducing the physical quantities appearing in this work and [8] to dimensionless form. In calculating $C_m^{(0)}$ and C_T such a relationship is unneeded, and so the associated discrepancies are smaller: within 3.17 and 1.69%.

1. PROBLEM DEFINITION AND BASIC EQUATIONS

Consider an aerosol particle suspended in a rarefied molecular gas flow. Let the center of curvature of the particle be coincident with the origin of the spherical coordinate system with the polar axis aligned with temperature gradient ∇T away from the surface. Since the temperature in the gas volume is distributed nonuniformly, derivatives $\partial T/\partial r$ and $\partial T/\partial\theta$ at the surface of the particle will be other than zero. The first derivative causes a temperature jump at the surface of the particle; the other, a thermal slip of the gas over its surface. Let us assume that the gradient component normal to the surface slowly varies over the surface. In this case, quantity $\partial^2 T/\partial r\partial\theta$ is also nonzero and contributes to gas slip (the so-called second-order thermal slip).

Let us also assume that the shear component of the mass velocity of the flow slowly varies along the normal to the surface. The nonuniformity of the mass velocity distribution in the Knudsen layer causes the gas to flow about the surface (isothermal slip). One more reason for gas slip about the surface (Barnett slip) is the presence of volume thermal stresses. Thus, in the problem thus stated, derivatives $k_1 = \partial U_\theta/\partial r|_\infty$, $k_2 = \partial \ln T/\partial\theta|_\infty$, $k_3 = \partial^2 T/\partial r\partial\theta|_\infty$, and $k_4 = T_{r\theta}/2T|_\infty$ are other than zero.

Following [9], we seek $Y(\mathbf{r}, \mathbf{C}, \nu)$ in the form of expansion in parameter k,

$$Y(\mathbf{r},\mathbf{C},\nu) = Y_1(\mathbf{r},\mathbf{C},\nu) + kY_2(\mathbf{r},\mathbf{C},\nu) + \ldots. \quad (9)$$

In view of (9), the hydrodynamic parameters of the gas, specifically, mass velocity component U_θ that is normal to the surface, are also expanded in parameter k,

$$U_\theta = U_\theta^{(1)} + kU_\theta^{(2)} + \ldots. \quad (10)$$

Substituting (9) into (7) and equating coefficients multiplying powers of k, we arrive at equations for $Y_1(\mathbf{r}, \mathbf{C}, \nu)$ and $Y_2(\mathbf{r}, \mathbf{C}, \nu)$,

$$C_r\frac{\partial Y_1}{\partial r} + Y_1(\mathbf{r},\mathbf{C},\nu) = \int k(\mathbf{C},\nu;\mathbf{C}',\nu')Y_1(\mathbf{r},\mathbf{C}',\nu')d\Omega, \quad (11)$$

$$C_r\frac{\partial Y_2}{\partial r} + Y_2(\mathbf{r},\mathbf{C},\nu) = \int k(\mathbf{C},\nu;\mathbf{C}',\nu')Y_2(\mathbf{r},\mathbf{C}',\nu)d\Omega$$

$$-\left[(C_\theta^2 + C_\varphi^2)\frac{\partial Y_1}{\partial C_r} + (C_\varphi^2\cot\theta - C_rC_\theta)\frac{\partial Y_1}{\partial C_\theta}\right. \quad (12)$$

$$\left. -(C_\varphi C_\theta\cot\theta + C_rC_\varphi)\frac{\partial Y_1}{\partial C_\varphi}\right] - C_\theta\frac{\partial Y_1}{\partial\theta}.$$

Solutions to Eqs. (11) and (12) are sought in the form

$$Y_1(\mathbf{r},\mathbf{C},\nu) = C_\theta\varphi_1(x,C_r) + C_\theta(C_\theta^2 + C_\varphi^2 + \nu^2 - l - 1)\varphi_2(x,C_r) + [\varphi_3(x,C_r) + \gamma(C^2 + \nu^2 - l - 1/2)\varphi_4(x,C_r)]k_2, \quad (13)$$

$$Y_2(\mathbf{r}, \mathbf{C}, \nu) = C_\theta \psi_1(x, C_r) + C_\theta(\nu^2 - l + 1)\psi_2(x, C_r) + \sum_{k=3}^{\infty} b_k(C_\theta, C_\varphi)\varphi_k(x, C_r, \nu). \quad (14)$$

Here, $x = r - R$ and $\varphi_3(x, C_r)$ and $\varphi_4(x, C_r)$ are the functions that were constructed for the temperature jump problem in [10]. Quantities $\gamma^2 = 1/(l + 1/2)$, $b_k = (C_\theta, C_\varphi)$, and C_θ constitute a complete set of orthogonal polynomials with weight $\exp(-C^2)$ in the velocity space. As such polynomials, one can take Hermitean polynomials widely used in the kinetic theory of gases [3].

Substituting (13) and (14) into (11) and (12) and integrating the right-hand sides of the resulting equations over C_θ', C_φ', and ν' yields a set of equations for $\varphi_i(x, \mu)$ and $\psi_i(x, \mu)$ ($i = 1, 2$; $\mu = C_r$),

$$\mu\frac{\partial\varphi_1}{\partial x} + \varphi_1(x, \mu) = \frac{1}{\sqrt{\mu}}\int_{-\infty}^{\infty}\exp(-\tau^2)\varphi_1(x, \tau)d\tau, \quad (15)$$

$$\mu\frac{\partial\varphi_2}{\partial x} + \varphi_2(x, \mu) = 0;$$

$$\mu\frac{\partial\psi_1}{\partial x} + \psi_1(x, \mu) = \frac{1}{\sqrt{\mu}}\int_{-\infty}^{\infty}\exp(-\tau^2)\psi_1(x, \tau)d\tau + \mu\varphi_1(x, \mu) - 2\frac{\partial\varphi_1}{\partial\mu} + 2\mu\varphi_2(x, \mu) - 4\frac{\partial\varphi_2}{\partial\mu} - [\varphi_3(x, \mu) + \gamma(\mu^2 + 1/2)\varphi_4(x, \mu)]k_3, \quad (16)$$

$$\mu\frac{\partial\psi_2}{\partial x} + \psi_2(x, \mu) = 4\mu\varphi_2(x, \mu) - 2\frac{\partial\varphi_2}{\partial\mu}.$$

With regard to the way of linearization of distribution function (5) and the form of expansions (13) and (14), the boundary conditions for functions $\varphi_i(x, \mu)$ and $\psi_i(x, \mu)$ ($i = 1, 2$) can be written as

$$\varphi_1(\infty, \mu) = 2U_\theta^{(1)}\big|_s - 2\mu k_1 - \left(\mu^2 - \frac{1}{2}\right)k_2 - 2\mu\left(\mu^2 - \frac{1}{2}\right)k_4; \quad (17)$$

$$\varphi_1(0, \mu) = 2d_1^{(1)} + 2\mu d_2^{(1)}, \quad \mu > 0, \quad (18)$$

$$\varphi_2(\infty, \mu) = -k_2, \quad \varphi_2(0, \mu) = 0, \quad \mu > 0;$$

$$\psi_1(\infty, \mu) = 2U_\theta^{(2)}\big|_s, \quad \psi_1(0, \mu) = 2d_1^{(2)} + 2\mu d_2^{(2)}, \quad \mu > 0, \quad (19)$$

$$\psi_2(\infty, \mu) = 0; \quad \psi_2(0, \mu) = 0, \quad \mu > 0.$$

Since desired components $U_\theta^{(i)}\big|_s$ ($i = 1, 2$) in expansion (10) of the mass velocity of the gas on the particle surface in parameter k enter into only boundary conditions (17) and (19), we will solve only Eqs. (15) and (16) with boundary conditions (17)–(19).

Thus, calculation of the molecular gas slip velocity by using the two-moment accommodation condition has been reduced to the solution of Eqs. (15) and (16) with boundary conditions (17)–(19).

2. BASIC RESULTS

The set of Eqs. (15) and (16) with boundary conditions (17)–(19) is solved with the Case method of elementary solutions [11]. With regard to expansion (10) and results obtained in [12–14], the desired velocity of a rarefied gas slipping over a spherical surface is written (in view of the accommodation coefficients for the first two moments of the distribution function) in the form

$$U_\theta\big|_s = kU_\theta^{(1)}\big|_s + k^2U_\theta^{(2)}\big|_s + \ldots,$$

$$U_\theta^{(1)}\big|_s = \zeta_{is}k_1 + \zeta_T k_2 + \zeta_B k_4,$$

$$U_\theta^{(2)}\big|_s = \zeta_1 k_1 + \zeta_2 k_2 + \zeta_3 k_3,$$

$$\zeta_{is} = (2 - q_2)\frac{(q_1^{-1} - 1)(\sqrt{\pi} + \pi Q_1/2) - (1 - \pi/4)Q_1}{1 - \pi/4 + (1 - q_2)(1 + \pi/4 + \sqrt{4}Q_1)},$$

$$\zeta_T = -\frac{(2 - q_2)(1 - \pi/4)(Q_2 + 1/2)/2 - (1 - q_2)(\sqrt{\pi}Q_1/2 + \pi/4)}{1 - \pi/4 + (1 - q_2)(1 + \pi/4 + \sqrt{4}Q_1)},$$

$$\zeta_B = (2 - q_2) \times \frac{(2Q_3 - Q_1)(1 - \pi/4) - \sqrt{\pi}(q_1^{-1} - 1)(2 + \sqrt{\pi}Q_1)}{2(1 - \pi/4)(2 - q_2) + \sqrt{\pi}(1 - q_2)(\sqrt{\pi} + 2Q_1)}, \quad (20)$$

$$\zeta_1 = -\gamma,$$

$$\gamma = \frac{(2 - q_2)(1 - \pi/4)}{(2 - q_2)(1 - \pi/4) + \sqrt{4}(1 - q_2)(Q_1 + \sqrt{\pi}/2)},$$

$$\zeta_2 = \gamma[Q_3 + Q_1Q_2],$$

$$\zeta_3 = 0.5\gamma[(Q_2 - 1/2)\varepsilon_T + Q_1 - 2Q_3 - \varepsilon_n].$$

Here, $Q_1 = -1.01619$, $Q_2 = -1.2663$, $Q_3 = -1.8207$ are Loyalka integrals [15]. For diatomic gases, $\varepsilon_T = 1.2168$ and $\varepsilon_n = -0.6716$. For polyatomic gases, $\varepsilon_T = 1.1914$ and $\varepsilon_n = -0.6525$. Thus, for diatomic gases, $\zeta_3 = 0.5740\gamma$ and for polyatomic gases, $\zeta_3 = 0.5873\gamma$.

Passing in (20) to dimensional quantities and writing these expressions in the form adopted in the kinetic theory of rarefied gas, we obtain

$$U_\theta'\big|_s = [C_m^{(0)} - (C_m^{(0)})^* C_m^{(1)}\mathrm{Kn}]\lambda\frac{\partial U_\theta'}{\partial r'}\bigg|_\infty$$

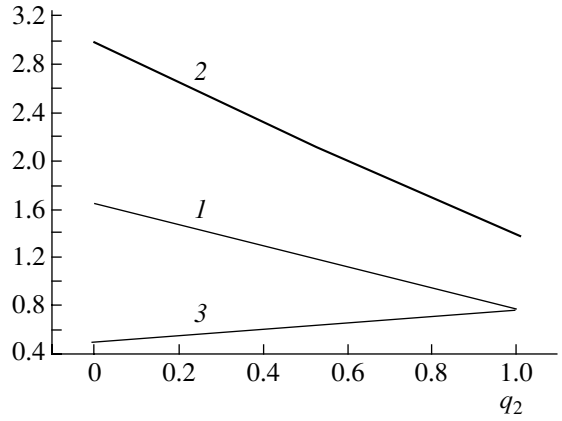

Fig. 1. Coefficients (*1*) $C_m^{(0)}$ at $q_1 = 1$, (*2*) $C_m^{(1)}$ at $q_1 = 2$, and (*3*) $K_{TS}^{(0)}$ vs. q_2 for Pr = 1.

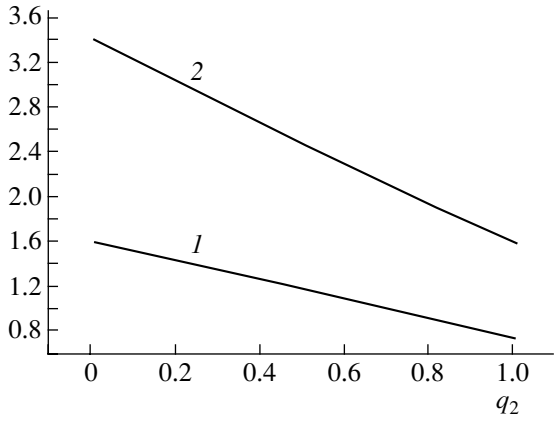

Fig. 2. Coefficients (*1*) $C_m^{(1)}$ and (*2*) β' vs. q_2 for Pr = 1.

$$+ [K_{TS}^{(0)} - (K_{TS}^{(0)})^*\beta' \mathrm{Kn}]\nu_g \frac{\partial \ln T}{\partial \theta}\bigg|_\infty \qquad (21)$$

$$+ (K_{TS}^{(0)})^*\beta_R \nu_g \mathrm{Kn}\frac{\partial^2 \ln T}{\partial r' \partial \theta} - (K_{TS}^{(0)})^*\beta_B \nu_g \mathrm{Kn}\frac{T_{r\theta}}{2T}\bigg|_\infty,$$

where

$$C_m^{(0)} = 0.7524\mathrm{Pr}^{-1}\zeta_{is}, \quad K_{TS}^{(0)} = 2\mathrm{Pr}^{-1}\zeta_T,$$

$$C_m^{(1)} = 0.7403\mathrm{Pr}^{-1}\gamma,$$

$$\beta' = 1.5723\mathrm{Pr}^{-1}\gamma, \quad \beta_B = 2.9454\mathrm{Pr}^{-1}\zeta_B.$$

Here, $(C_m^{(0)})^* = 0.7645\mathrm{Pr}^{-1}$ and $(K_{TS}^{(0)})^* = 0.7662\mathrm{Pr}^{-1}$ are the associated coefficients for the case of complete accommodation of the first two moments of the distribution function ($q_1 = q_2 = 1$), $\beta_R = 0.6934\mathrm{Pr}^{-1}\gamma$ for diatomic gases and $\beta_R = 1.7299\mathrm{Pr}^{-1}\gamma$ for polyatomic gases.

Relationship (21) defines the velocity of a molecular gas slipping over a sphere with a small radius of curvature.

It is seen from (21) that taking into account the rotational degrees of freedom of gas molecules renders the slip coefficients functions of the Prandtl number. For a monoatomic gas, such a dependence is absent. For most gases under normal conditions, Pr is close to 2/3, i.e., to the value for a monoatomic gas. For example, for N_2 and O_2, Pr = 0.76; for air, 0.7; and for Cl_2, 0.64. Therefore, the velocity of slip over a surface and the rate of thermophoresis for molecular gases differ from those calculated for monoatomic gases insignificantly. However, the above dependence should be borne in mind in calculation of the rate of thermophoresis for particles suspended in gases, since Pr for such particles much differs from 2/3 (for example, for particles suspended in the steam, Pr = 1.01 at 100°C).

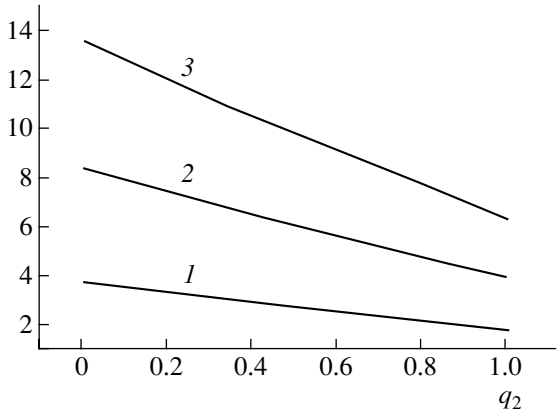

Fig. 3. Coefficients (*1*) β_R, (*2*) β_B at $q_1 = 1$, and (*3*) β_B at $q_1 = 0.5$ vs. q_2. Pr = 1.

As for a monoatomic gas [4–6], the slip coefficients strongly depend on the accommodation coefficient for the second moment of the distribution function. In particular, when q_2 varies between 0 and 1 at $q_1 = 1$, coefficients $C_m^{(0)}$, $C_m^{(1)}$, β', β_B, and β_R change by 53.67%; and $K_{TS}^{(0)}$, by 35.25%. Also, coefficients $C_m^{(0)}$ and β_B significantly depend on accommodation coefficient q_1: when q_1 varies between 0 and 0.5 at $q_2 = 1$, $C_m^{(0)}$ and β_B change by 44.69% and 38.48%, respectively. The variation of the slip coefficients with the accommodation coefficients for Pr = 1 is shown in Figs. 1–3.

CONCLUSIONS

In this work, we calculated the velocity of a molecular gas slipping over a spherical aerosol particle with a small radius of curvature, using the two-moment boundary condition in the approximation linear in Knudsen number. The slip coefficients are shown to

considerably depend on the Pr number and accommodation coefficient of the second moment of the distribution function.

REFERENCES

1. V. M. Zhdanov and M. Ya. Alievskiĭ, *Transfer and Relaxation in Molecular Gases* (Nauka, Moscow, 1989) [in Russian].
2. E. M. Lifshitz and L. P. Pitaevsky, *Physical Kinetics* (Nauka, Moscow, 1979; Pergamon, Oxford, 1981).
3. M. N. Kogan, *Rarefied Gas Dynamics* (Nauka, Moscow, 1967; Plenum, New York, 1969).
4. A. V. Latyshev and A. A. Yushkanov, Inzh.-Fiz. Zh. **74** (3), 63 (2001).
5. A. V. Latyshev, V. N. Popov, and A. A. Yushkanov, Prikl. Mekh. Tekh. Fiz., No. 1, 23 (2004).
6. V. N. Popov, Zh. Tekh. Fiz. **73** (5), 19 (2003) [Tech. Phys. **48**, 541 (2003)].
7. C. E. Siewert and F. Sharipov, Phys. Fluids **14**, 4123 (2002).
8. T. Ohwada and Y. Sone, Eur. J. Mech. B/Fluids **11**, 389 (1992).
9. Y. Sone, in *Proceedings of the 6th International Symposium on Rarefied Gas Dynamics* (Academic, New York, 1969), Vol. 1, pp. 243–253.
10. A. V. Latyshev and A. A. Yushkanov, Prikl. Mat. Mekh. **66**, 845 (2002).
11. C. Cercignani, *Mathematical Methods in Kinetic Theory* (Plenum, New York, 1969; Mir, Moscow, 1973).
12. A. V. Latyshev, V. N. Popov, and A. A. Yushkanov, Sib. Zh. Ind. Mat. **5** (3), 103 (2002).
13. A. V. Latyshev, V. N. Popov, and A. A. Yushkanov, Poverkhnost, No. 6, 111 (2003).
14. A. V. Latyshev, V. N. Popov, and A. A. Yushkanov, Sib. Zh. Ind. Mat. **6** (1), 60 (2003).
15. S. K. Loyalka, Transp. Theory Stat. Phys. **4**, 55 (1975).

Translated by V. Isaakyan

Technical Physics, Vol. 50, No. 11, 2005, pp. 1423–1430. Translated from Zhurnal Tekhnicheskoĭ Fiziki, Vol. 75, No. 11, 2005, pp. 32–39.

GASES AND LIQUIDS

Analysis of an Arc-Formed Gas-Plasma Jet in the Arc Method of Fullerene Production

N. I. Alekseev and G. A. Dyuzhev

Ioffe Physicotechnical Institute, Russian Academy of Sciences, Politekhnicheskaya ul. 26, St. Petersburg, 194021 Russia

e-mail: NIalekseyev@ilip.itc.etu.ru; aleks@mail.ioffe.ru

Received August 3, 2004

Abstract—A two-component fan-shaped gas jet forming in the discharge gap of a chamber for fullerene production is analyzed. Under standard fullerene production conditions, the averaged parameters of the jet can be found with a reasonable accuracy using the well-known solution for an incompressible liquid jet. Based on the analysis performed in this work, a simple model of gap–jet transition, and the fullerene formation kinetics considered earlier, the dependences of the fullerene yield on observable experimental parameters (current, helium pressure, gap width, and electrode radii) are constructed. The calculated and experimental results are in good agreement. The analytical data obtained in this work may be helpful in considering the fullerene production kinetics in a real, finite-dimension chamber of a given geometry. © *2005 Pleiades Publishing, Inc.*

INTRODUCTION

It is known that wide application of fullerenes, which are viewed as promising materials for a number of advanced technologies, is retarded by their high cost. While it has been reported that fullerenes can be produced in industrial amounts by burning-out of hydrocarbons [1], a major part of this material is produced around the world from fullerene soot, which is formed by an arc discharge between graphite electrodes in a buffer gas [2, 3]. The disadvantage of this technique from the commercial standpoint is a high energy consumption [1]; however, its potential is far from being exhausted. Further refinement of this technique may lie in improving gas dynamics in the discharge chamber.

Such an approach calls for a careful theoretical analysis of gas dynamics in the chamber and the fullerene formation kinetics. The gasdynamic problem can be solved, e.g., using a quasi-one-dimensional simulation of plasma parameters in the gap (see, for instance, [4]). An insight into the fullerene formation kinetics can be gained by physicochemical simulation of assembling fullerene molecules from multiring hydrocarbon clusters [5] with subsequent extension of simulation results for the general process of carbon evolution from atoms to fullerenes upon cooling the vapor [6]. However, a combined consideration of fullerene assembling kinetics and gas dynamics in a specific discharge chamber requires that several subproblems be first solved, at which this paper is aimed. These subproblems are the following.

(1) Simulation of the dynamics of a free two-component (carbon and helium as a buffer gas) gas jet with regard to its nonisothermality and fan-type (or radial–slot [7, 8]) symmetry. The need for tackling this problem is due to two reasons. First, the velocity field in the jet specifies the gas flow in the outer (relative to the jet) space. Second, in our early work [6], the evolution of the atomic carbon vapor to fullerenes was considered as the evolution of an impurity present in the free jet of an incompressible liquid in small amounts. Such a significant simplification was not substantiated: it was used just because the theory of free turbulent jets of an incompressible liquid is rather simple and well developed [7–9].

(2) Derivation (based on the dynamics simulation results) of the dependences of the absolute and relative fullerene yield on initial velocity V_0 of the jet at the exit from the electrode gap, jet initial temperature T_0, and initial concentration $n_C^{(0)}$ of the carbon vapor (as was done in [6]).

(3) Finding the fullerene yield as a function of arc parameters (current, pressure, and gap configuration). To solve this problem, it is necessary to devise an adequate technique for converting the results of arc quasi-one-dimensional simulation to parameters V_0, T_0, and $n_C^{(0)}$ [4], which are not determined from the above simplified model.

Let us outline the basic features of fullerene production from an arc. The discharge is initiated in helium (hereafter gas) at a pressure of 100–300 Torr, a pressure of 100 Torr being regarded as optimal [3]. Carbon evaporating from the anode surface generates a plasma. In our laboratory conditions, the diameter of graphite electrodes was equal to $2r_0 \approx 6$ mm; the optimal width of the electrode gap was the same, $2b_0 \approx 6$ mm. In the developmental setup [10], we used electrodes of larger diameter, $2r_0$ = 10–12 mm, and an electrode gap of

1063-7842/05/5011-1423$26.00

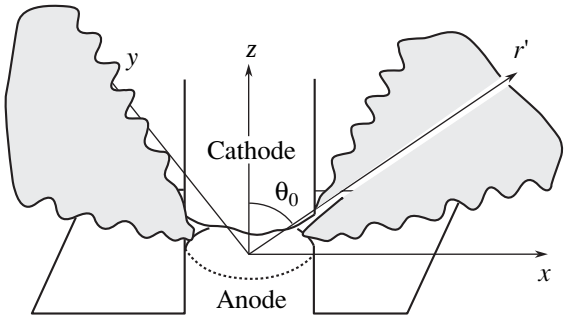

Fig. 1. Discharge gap, jet (dark area) propagating along the *r* axis, and coordinate axes.

$2b_0$ = 2–3 mm. The working pressure was raised to 300 Torr.

As follows from calculations [4], the discharge plasma is near local thermodynamic equilibrium and its temperature at the center of the gap is T_0 = 0.8–1.0 eV. Under such conditions, carbon exists in the form of atoms and ions. The carbon vapor cools down away from the arc, and so one can speak (to a certain degree of convention) of condensation, which results in the formation of fullerenes [6] and other components of the fullerene soot. Fullerenes appear at distance x = 2.0–3.5 cm from the arc axis [11]. Hereafter, x refers to the radial coordinate in the cylindrical coordinate system related to the discharge axis; r, to the same coordinate in the spherical system (Fig. 1); and the discharge axis runs from the anode to the cathode in the transverse (z) direction.

The simulation made in [4] helps in visualizing the variation of carbon temperature and concentration across the gap at any given current, pressure, and gap width. Then, one may evaluate the radial gas-plasma flow, where the carbon vapor condenses. Observation, theoretical estimates of the flow initial velocity [6], and experiments with carbon deposition on probes [11] show that the flow is a turbulent gas jet. However, under optimal conditions for fullerene production, the Reynolds number is no higher than 20–50. It is therefore of interest to analyze both viscous and turbulent jets under various conditions.

We assume that the jet forms near the source as a result of carbon diffusion toward the periphery and convective flow of the buffer gas. Visually, the jet makes angle $\theta_0 < \pi/2$ with the z axis (Fig. 1). The jet is at least two-component (the carbon and gas), the initial concentrations of both components coinciding in order of magnitude. The components play different roles in jet formation. For the carbon, the arc area acts as a source and any other surfaces as absorbers. As for the gas, its flow in the absence of pumping is confined within the discharge chamber. Therefore, taking into account that the discharge gap is narrow, one can assume without loss in generality that the radial gas velocity at the exit from the gap is much lower than that of the carbon vapor within the domain $x \sim r_0$. If it is also assumed that total pressure P is constant, the difference between the component velocities in the two-component system (thermal diffusion is ignored) is given by [9]

$$\mathbf{V}_C - \mathbf{V}_g = \frac{DP}{P - n_C T}\left(\frac{\nabla n_C}{n_C} + \frac{\nabla T}{T}\right) \quad (1)$$

(subscripts C and g refer to carbon and gas, respectively). This difference specifies carbon initial velocity $V_C^{(0)}$, which is virtually coincident with initial mass velocity V_0 of the jet (subscript or superscript 0 refers to the parameter values at $x = r_0$). In (1), n_C is the carbon concentration, which is defined as the number of carbon particles in a unit volume and D is the coefficient of interdiffusion. Calculation by (1) supports the fact that $V_C^{(0)} \approx V_0$ = 20–50 m/s under optimal fullerene production conditions. This range is consistent with estimates [12] made from radically differing standpoints.

VARIATION OF GAS PARAMETERS IN TURBULENT AND VISCOUS GAS JETS

(i) The procedure of calculating the parameters of a turbulent two-component gas jet with its initial velocity given that was described elsewhere [7, 8] can also be applied to a fan-shaped jet. Over the main part of the jet (Fig. 2), the radial mass velocity at the jet axis, u_{max}; relative weight concentration $\xi = n_C m_C/\rho$ of the carbon at the axis, ξ_{max}; axial temperature T_{max}; and half-width $\delta(x)$ of the jet can be calculated by the method of integral relations, i.e., using the laws of conservation of fluxes of momentum, excessive enthalpy $i - i_\infty$, and carbon:

$$2\pi \int_0^{\delta(x)} dz \rho x u^2 = 2\pi r_0 b_0 \rho_0 u_0^2, \quad (2)$$

$$2\pi \int_0^{\delta(x)} dz \rho x u (i - i_\infty) = 2\pi r_0 b_0 \rho_0 u_0 (i_0 - i_\infty), \quad (3)$$

$$2\pi \int_0^{\delta(x)} dz \rho x u \xi = 2\pi r_0 b_0 \rho_0 u_0 \xi_0 \quad (4)$$

(ρ is the gas mixture density), as well as from the integral relation for energy [7]

$$2\pi \frac{d}{dx} \int_0^{\delta(x)} dz \rho x u^3 = 2\pi x \int_0^{\delta(x)} dz \rho \langle u'V' \rangle \frac{\partial u}{\partial y}. \quad (4')$$

These relations should be complemented by the assumption that the curves of velocity $f_u = u/u_{max}$, concentration $f_\xi = \xi/\xi_{max}$, and excessive enthalpy, as well as correlation function $\langle u'V' \rangle$ of turbulent pulsations of radial velocity u and transverse velocity V, have a trans-

verse form. (Hereafter, the subscripts max and ∞ denote the parameter values at the jet axis and outside the jet, respectively.) Temperature T_∞ outside the jet was taken to be the same throughout the chamber. Such an assumption is valid, since the jet originates not only in the electrode gap but also from a nearby narrow region on the lateral surface of the anode that is heated to 2000–3000 K. Beyond this region, the anode temperature sharply drops to 1200–1500 K, as follows from the calculation [4], and so the relative variation of this parameter outside the jet is much smaller than along its axis.

If we replace integral relation (4') by the simpler relationship

$$q d\delta/dx = 2/(1 + \rho_\infty/\rho_{max}) \quad (5)$$

with empiric constant $q = 0.26$ [9] and assume that the profiles of the excessive enthalpy and concentration f_ξ are identical, the problem is reduced to solving three equations for three unknown functions of x, which are jet half-width δ, dimensionless velocity $U_{max} = u_{max}/u_0$, and dimensionless carbon concentration $\gamma_{max} = \xi_{max}/\xi_0$,

$$x\delta(x)U_{max}^2\int_0^1 d\Lambda f_u^2(\Lambda)\frac{1-f_\xi(1-\mu)}{1-f_\xi(1-\mu\tau)}\frac{1}{1-\xi_0 f_\xi\gamma_{max}(1-\mu)} = \frac{r_0 b_0}{\tau}\frac{1}{1-\xi_0(1-\mu)},$$

$$x\delta(x)U_{max}\gamma_{max}\int_0^1 d\Lambda f_u f_\xi \times\frac{1-f_\xi(1-\mu)}{1-f_\xi(1-\mu\tau)}\frac{1}{1-\xi_0 f_\xi\gamma_{max}(1-\mu)} = \frac{r_0 b_0}{\tau}\frac{1}{1-\xi_0(1-\mu)}, \quad (6)$$

$$q\frac{d\delta}{dx} = \frac{2}{1+\tau(1-\xi_0\gamma_{max}(1-\mu))}.$$

In (6), gas-to-carbon atomic mass ratio $\mu = m_g/m_C = 1/3$ and parameter $\tau = T_0/T_\infty$ characterizes an initial heating of the jet. The velocity distribution over the jet's cross-sectional area is assumed to obey the Ginevskiĭ profile $f_u(\Lambda) = 1 - 8\Lambda^2 + 6\Lambda^3 - 3\Lambda^4$ [8]. As concentration and excessive enthalpy profiles, we used the experimentally found relationship $f_\xi(\Lambda) = f_u(\Lambda\mathrm{Pr})$ (Pr = 0.6) [8], which assumes that the temperature boundary of the jet is an outer boundary relative to the velocity boundary. In going from the enthalpy profile to the temperature profile in (3) and in the third equation in (6), it is assumed that both carbon and helium remain monoatomic.

System (6) was solved by iterations at each x. In the particular case of a heated jet of the heavy carbon vapor striking a light buffer gas, the solution simplifies greatly, because the density of the binary gas mixture varies insignificantly along the jet axis. Figure 3 shows the variation of the relative density of the mixture, ρ/ρ_∞, calculated for $\tau = 6$ and $P/n_C^{(0)}T_0 = 3/2$ (these values are typical of fullerene production conditions). In this case, ρ_0/ρ_∞ is ~1.2 (i.e., fairly close to unity); therefore, as an initial iteration, one can use the well-known solution for the main portion of a fan-shaped jet of an incompressible liquid [8],

$$\frac{u_{max}}{u_0} = \frac{1}{\sqrt{A_2}}\sqrt{\frac{b_0}{12\kappa r_0}}\frac{1}{\sqrt{(x^2/r_0^2)-1}}, \quad (7)$$

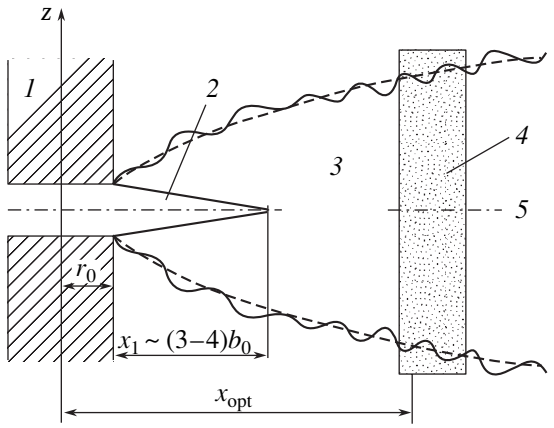

Fig. 2. Structure of a radial–slot jet propagating normally to the discharge axis: (*1*) discharge axis, (*2*) potential core of the jet, (*3*) main portion of the jet, (*4*) fullerene production region, and (*5*) axial plane of the jet.

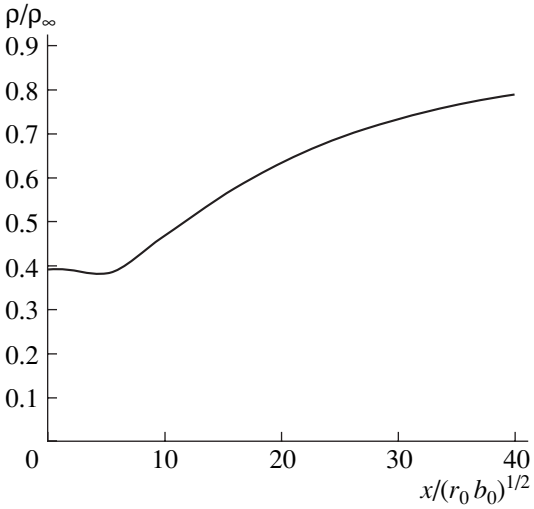

Fig. 3. Variation of the density of the carbon–buffer gas (helium) mixture along the jet axis. The jet overheating parameter $\tau = 6$, the carbon relative partial pressure at the exit from the gap is $n_C^{(0)}T_0/P = 2/3$, $T_0 = 0.6$ eV, and $T_\infty = 0.1$ eV.

$$\frac{n_{\max}}{n_0} = \frac{\xi_{\max}}{\xi_0} = \frac{T_{\max} - T_\infty}{T_0 - T_\infty} = \frac{\sqrt{A_2}}{A_{u\xi}}\sqrt{\frac{b_0}{12\kappa r_0}}\frac{1}{\sqrt{(x^2/r_0^2) - 1}}, \quad (8)$$

$$\delta = 12\kappa r_0\left(\frac{x}{r_0} - \frac{r_0}{x}\right), \quad (9)$$

where

$$A_p = \int_0^1 d\Lambda f_u^p(\Lambda), \quad A_{u\xi} = \int_0^1 d\Lambda f_u(\Lambda) f_\xi(\Lambda),$$

and $\kappa \approx 0.01$ is a phenomenological parameter of the theory of turbulence [8] (it is related with parameter a used in [7] as $\kappa \approx a/10$).

As follows from calculations, the relative discrepancy between the velocity curve and initial iteration is within 15% even early in the main portion of the jet and decreases further with distance from the source. Such a result was expected, since the calculations made in [9] for a jet heated to $\tau = 6$ (though in the planar configuration) showed that the velocity decreases relative to $\tau = 1$ by no more than twofold even if the jet gas and buffer gas are the same (the compensating effect of a heavier component is absent in this case). Below, it will be shown that, under conditions appropriate for fullerene production, the carbon initial concentration and the initial temperature of the gas mixture are so high that the density of the mixture can be put constant along the jet.

Formulas (6) are valid for a fan-type source, i.e., imply the presence of a symmetry plane. The conditions under which the jet makes an angle with the cross section of the chamber are typical of the fullerene-producing arc geometry. This case can be reduced to equations for a symmetric jet by making the substitutions $x \longrightarrow r$, $z \longrightarrow y$, $u \longrightarrow V_r$, and $V \longrightarrow V_\theta + uy/r$ [13] (the coordinate system is shown in Fig. 1, angle θ is measured from the positive direction of the z axis).

The solution given by (7)–(9) refers to the main portion of the jet. The technique of measuring the variation of the thickness of the layer where the carbon vapor and gas mix up at the initial portion (Fig. 2) and also of the length of this layer (over which the longitudinal velocity remains nearly constant) is described elsewhere [8]. Radius x_1 of the initial portion, which is found from the relationship

$$\kappa\frac{(x_1/b_0)^2 - (r_0/b_0)^2}{2x_0/b_0} = \frac{A_2 - A_3}{2A_2A_4}, \quad (10)$$

equals $(3–4)b_0$. Calculations show that taking into account the initial portion of the jet influences the final result insignificantly.

(ii) At low carbon concentrations and initial velocities of the get, the Reynolds number is no greater than 10. Therefore, it is of interest to analyze a viscous gas jet. Carbon in this case can be considered as a small impurity. Relevant calculations were performed in [14] for the plane-parallel geometry using the Dorodnitsyn transformation [9]. Similar consideration can be applied to a fan-shaped jet. In the boundary layer approximation [13, 15], the complete set of equations for a viscous fan-shaped jet includes the continuity equation, Navier–Stokes equation, energy balance equation, and equation of state of gas,

$$\frac{\partial}{\partial x}(\rho x u) + \frac{\partial}{\partial z}(\rho x V) = 0, \quad (11)$$

$$\rho u\frac{\partial u}{\partial x} + \rho V\frac{\partial u}{\partial z} = \frac{\partial}{\partial z}\left(\eta\frac{\partial u}{\partial z}\right), \quad (12)$$

$$\rho u\frac{\partial}{\partial x}\left(\frac{5}{2}T\right) + \rho V\frac{\partial}{\partial z}\left(\frac{5}{2}T\right) - \frac{\partial}{\partial z}\left(\chi\frac{\partial T}{\partial z}\right) = \sigma'_{ik}\frac{\partial V_i}{\partial x_k}, \quad (13)$$

$$P = \frac{\rho T}{m_g} = \text{const}, \quad (14)$$

where the term $\sigma'_{ik}(\partial V_i/\partial x_k)$ allows for viscous energy losses and ρ, η, and χ are, respectively, the density, viscosity, and thermal conductivity of the gas.

If the temperature gradient is high and the gas velocity is low, viscous losses in energy balance equation (14) can be ignored. Then, it follows from (12) and (13) that

$$T\left(\frac{5\eta}{2\chi}\mathbf{r}\right) \sim V(\mathbf{r}).$$

In the elementary theory of gases, $\chi/\eta = 3/2$; in the rigorous kinetic theory of gases, $\chi/\eta \geq 15/4$ [16]. For inert gases, $\chi/\eta = 15/4$ is accurate to within 5%, so that $T(\mathbf{r}) \sim V(0.7\mathbf{r})$. If $\chi/\eta = 5/2$, the radial velocity (u) and temperature (T) profiles are in full accordance,

$$T = T_0\frac{u}{u_0} + T_\infty \quad (15)$$

this result being valid for both the initial and main portions of the jet.

If (15) holds, set (11)–(14) has a solution in two cases: $\eta = \eta_0 = \text{const}$ and $\eta \sim T$. Since the viscosity actually behaves as $\eta \sim T^{0.6}$ [17], it would be of interest to obtain both solutions and compare the final results.

For $\eta = \text{const}$, a solution to the continuity equation at $T \gg T_\delta$ is trivial, $V/u = -z/x$, and the Navier–Stokes equation

$$x(\partial u/\partial x) - z(\partial u/\partial z) = \zeta x(\partial^2 u/\partial z^2)$$

(where $\zeta = T_0\eta/m\text{Pu}_0$) transforms into the equation of diffusion along an infinite axis after passing to variables $\Omega = xz$ and $\xi = x^3/3$. For $2b_0 \ll r_0$ and $x \gg b_0$, its solution

has the form

$$u = \frac{6b_0 r_0 u_0}{\zeta\sqrt{\pi(x^3 - r_0^3)}}\exp\left(-\frac{3x^2z^2}{4\zeta(x^3 - r_0^3)}\right). \quad (16)$$

Hence, it follows that, when the conditions $x \gg r_0$ and $T \gg T_{max}$ are met simultaneously, the jet width $\delta \sim \sqrt{x}$ and $u_{max} \sim 1/x^{3/2}$.

At $\eta \sim T$, system (11)–(14) is reduced to the equations for an incompressible viscous liquid by means of the Dorodnitsyn transformation $V \longrightarrow \bar{V} = (\rho/\rho_0)V + u(\partial Y/\partial x)$ and $z \longrightarrow Y = \int_0^z dy'\,(\rho/\rho_0)$; so, the well-known solution will suffice provided that a relation between u and T is specified.

For a fan-type source in an incompressible liquid [13], the asymptotics for u has the form

$$u = (\omega^2/2\nu x)/\cosh^2\frac{\omega(z/x)}{2\nu}, \quad (17)$$

where $\nu = \eta_0/\rho_0$ and constant ω is found from the condition of conservation of momentum in the jet.

For the gas, Eq. (17) with regard to (15) transforms into an integral equation for u that is easy to solve,

$$\frac{2u_0}{\sqrt{2\nu}}\left(\frac{T_0}{T_0 - T_\infty}\right)|z| = \sqrt{\frac{\omega^2}{2\nu} - ux} + \frac{\varepsilon u_0 x}{\sqrt{\omega^2/2\nu}}\ln\frac{\sqrt{\omega^2/2\nu} + \sqrt{\omega^2/2\nu - ux}}{\sqrt{\omega^2/2\nu} - \sqrt{\omega^2/2\nu - ux}}, \quad (18)$$

where $\varepsilon = T_\infty/(T_0 - T_\infty)$.

Since $\varepsilon \sim 0.1 \ll 1$, the last term in (18) can be disregarded; then, the solution has the form (at $|z| < \omega/u_0$)

$$ux = \frac{\omega^2}{2\nu}\left(1 - \frac{u_0^2 z^2}{\omega^2}\right) \quad (19)$$

(i.e., $u_{max} \sim 1/x$), which somewhat differs from the law $u_{max} \sim 1/x^{3/2}$ described in (16). From (19), it follows that parameter ω/u_0 has the meaning of effective jet width δ at $T \gg T_\infty$: it equals several centimeters and depends on x insignificantly. Constant ω calculated by (18) is $\omega = (3u_0^2\eta_0 r_0 d/\rho_0)^{1/3}$.

From the definition of mass velocity $\langle V\rangle$, formula (1), and the continuity equation, it is easy to find for carbon concentration n_C that

$$\mathrm{div}\left(n_C\langle\mathbf{V}\rangle - D\frac{m_g P}{\rho T}n_C\left(\frac{\nabla n_C}{n_C} + \frac{\nabla T}{T}\right)\right) = 0, \quad (20)$$

where $\langle\mathbf{V}\rangle_x = u$ and $\langle\mathbf{V}\rangle_z = V$.

If n_C is small and varies in the longitudinal direction much more slowly than in the transverse one (as well as velocity u in the boundary layer approximation), (20) reduces to

$$\frac{\partial}{\partial x}(un_C) - \frac{z}{x}\frac{\partial}{\partial z}(un_C) - \frac{\partial}{\partial z}\left(Dn_C\left(\frac{\partial \ln n_C}{\partial z} + \frac{\partial \ln u}{\partial z}\right)\right) = 0. \quad (21)$$

At a constant pressure, the dependence $D(T)$ is described well by the Fuller–Schletter relation $D(T) \sim T^{1.7}$ [16]. Therefore, we considered two simple cases: $D(T) \sim T$ and $D(T) \sim T^2$. If $D(T) \sim T$, (21) transforms to the form

$$\frac{\partial}{\partial x}(un_C) - \frac{z}{x}\frac{\partial}{\partial z}(un_C) - \frac{D_0}{u_0}\frac{\partial^2}{\partial z^2}(un_C) = 0,$$

which coincides with the equation for velocity u if $\lambda = D_0/u_0$ is substituted for ζ. Hence,

$$un_C \sim \frac{1}{x^{3/2}}\exp\left(-\frac{3z^2}{4\lambda x}\right). \quad (22)$$

If the density of the carbon vapor is low, its velocity is given by $\mathbf{V}_C = \mathbf{V} - D\nabla\ln(un_C)$, so that, at $D \sim T$, $(\mathbf{V}_C)_z = uz/2x$ and $(\mathbf{V}_C)_x \approx u$.

Based on these relationships, one can easily show that the region of the most efficient fullerene production is to the side of the jet axis. In [6], it was demonstrated that assembling of a fullerene molecule, which can be represented as the transformation of its precursor, a two- or three-ring carbon cluster in a buffer gas, into fullerene, takes place in a narrow interval near optimal temperature $T_{opt} \approx 0.25$ eV. If $\nu = \text{const}$ and $\eta = \rho\nu \sim T$, this region, as follows from (15) and (19), is the surface of revolution of a parabola,

$$T_{opt} = \frac{T_0}{u_0}\frac{\omega^2}{2\nu x}\left(1 - \frac{u_0^2 z^2}{\omega^2}\right). \quad (23)$$

However, transformation of the precursor into fullerene is possible only if the carbon has already evolved from the atomic state to multiring clusters [5, 6]. The stages of evolution are assembling of carbon atoms into chains, twisting of the chains to form ring clusters, and coalescence of the clusters. These transformations, viewed as chemical reactions, have a low energy of activation (within 1 eV [5, 6]) and proceed at an elevated temperature. Therefore, we may assume for simplicity that total time t' taken to complete all the stages depends on temperature insignificantly, unlike the stage of fullerene assembling from multiring clusters, which has a high energy of activation and critically depends on temperature [6]. Therefore, the "readiness" to assemble, i.e., the presence of multiring clusters in an amount sufficient for fullerene formation, can be roughly estimated from the condition $t' = t$, where t is the time for which the impurity moves along the

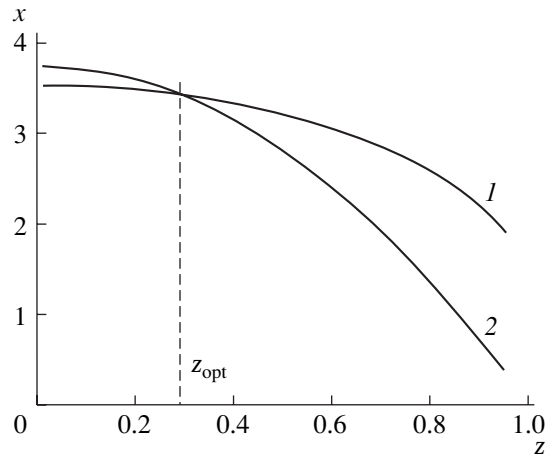

Fig. 4. (*1*) Curve of readiness and (*2*) curve of efficient fullerene production.

streamline that passes through a given point with coordinates (x, z). If $\eta \sim T$, these coordinates are related to initial coordinates (x_S, z_S) as $z = z_S(x/x_S)^{1/2}$ and the time of motion along the streamline is given by

$$t = \frac{2\nu x^2}{\omega^2}\frac{\omega^2}{u_0^2 z^2}\left(\frac{\omega^2}{u_0^2 z^2}\ln\frac{1}{1-u_0^2 z^2/\omega^2} - 1\right). \qquad (24)$$

The surface of revolution given by (24) at $t = t'$ can be named the "surface of readiness." While quantity t' is somewhat conventional, it is clear that the surface of readiness must cross the axis $z = 0$ before an optimal temperature is reached; that is, an optimal coordinate of transformation into fullerene, x_{opt}, is larger than quantity $(T_0/u_0)(\omega^2/2\nu T_{opt})$ in (23). Numerical analysis performed with typical values of the parameters shows that the surface of readiness (curve *1* in Fig. 4) crosses curve (23) (curve *2* in Fig. 4) at $z = z_{opt} < \omega/u_0$ and runs above curve (23) at $|z| > z_{opt}$. Thus, at $|z| > z_{opt}$, the clusters cannot yet produce fullerenes. At the same time, the carbon flow velocity near z_{opt} is much lower than near the jet axis and so fullerenes at point z_{opt} are bound to form with a maximal rate.

The same result, though after more awkward mathematics, was obtained in the turbulent case under the assumption that the jet density is constant.

FULLERENE YIELD VERSUS DISCHARGE PARAMETERS

Because of a small variation in the jet density, the fullerene yields as a function of the jet initial parameters (carbon concentration $n_C^{(0)}$, temperature T_0, and velocity $V_C^{(0)}$ is virtually the same as in [6]: the amount of fullerenes drastically drops with increasing $V_C^{(0)}$ and

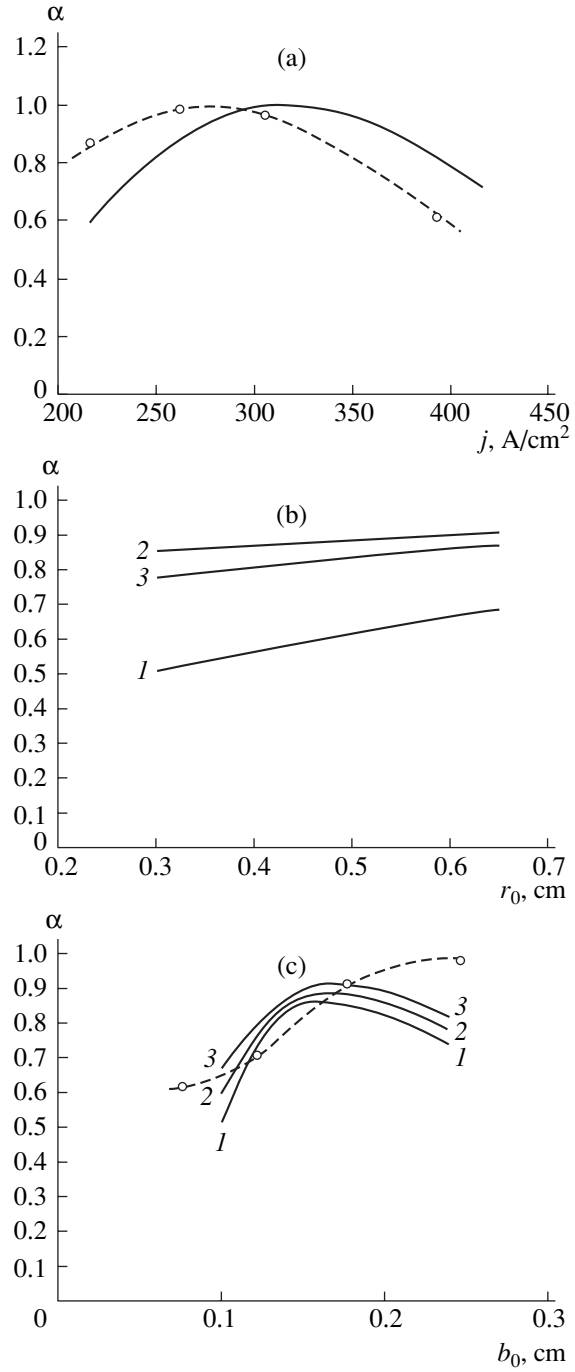

Fig. 5. (a) Relative content of the fullerene in the soot (fullerene yield), α, vs. the current density in the arc. The electrode radius is $r_0 = 0.5$ cm, $2b_0 = 0.32$ cm, and $P = 100$ Torr (the dashed line fits experimental data). (b) Fullerene yield vs. electrode radius r_0. The electrode gap width $2b_0$ is (*1*) 0.20, (*2*) 0.32, and (*3*) 0.45 cm. (c) Fullerene yield vs. electrode gap half-width b_0 at the optimal current. r_0 = (*1*) 0.30, (*2*) 0.45, and (*3*) 0.60 cm (the dashed line fits experimental data).

decreasing $n_C^{(0)}$, the effect of the latter parameter being stronger).

The procedure for finding these initial parameters at a given current and gas pressure is the following. Using the earlier developed algorithm [4], we determined the variation of the carbon concentration and temperature across the electrode gap (i.e., along coordinate z, Fig. 1). The gap-averaged values were taken to be the initial concentration of carbon and initial temperature at $x = 0$. To calculate the average concentration of the carbon, the curves for carbon atoms and ions were added up at each point.

The radial run of the temperature and concentration up to the beginning of the main portion of the jet, $x = x_1$, was assumed to obey a power-type law, and the exponent was found by joining with (8) at point x_1. In this way, the initial velocity of the jet at $x = r_0$ was determined. It was assumed that the width of the jet varies linearly in the interval $r_0 < x < x_1$, and the velocity variation was found from the conditions that the carbon flux $2\pi x\delta(x)V_C n_C$ remains constant.

The calculated dependences of the fullerene yield on the current, pressure, gap width, and electrode radii are shown in Fig. 5.

For the reasons noted in [6], the absolute fullerene yield cannot be calculated exactly. This is because the barrier due to the Gibbs energy, which must be overcome when a fullerene molecule is generated, cannot be calculated with a reasonable accuracy by the methods of quantum chemistry. Therefore, α in Fig. 5 is the ratio of the actual yield to the absolute maximum obtained by calculation.

The dependence of α on the current density (Fig. 5a) peaks at a current density of about 300 A/cm^2, the position of this peak being dependent on the other parameters only slightly. As the electrode radius increases, α grows insignificantly, all other parameters being the same (Fig. 5b). Such a dependences reflects the competition of the following tendencies, which are embodied in the model suggested: (i) as r_0 increases, the initial velocity of the carbon jet remains almost unchanged but the spatial scale of conservation of this velocity in the potential core expands, thereby diminishing α; (ii) as r_0 increases, the carbon vapor concentration in the potential core decreases more rapidly, which also causes a decrease in α; and (iii) the discharge heats up, since the radiation goes outside only from the circumferential regions of the arc, which occupy a progressively smaller area. This leads to an increase in both the carbon concentration and the initial velocity of the jet, the former factor having a stronger effect on an increase in α [11].

The α versus gap width dependence (Fig. 5c) is nonmonotonic. At a narrow gap, α decreases. This is because the carbon temperature and concentration drop as a result of shrinkage of the local thermodynamic equilibrium area. Other factors (a decrease in radiation losses, an increase in factor $DP/(P - n_C T)$ in (1) and, hence, velocity $V_C^{(0)}$) play a minor role.

The curves shown in Fig. 5 are consistent with our experimental data obtained in [3] (dashed lines). The fullerene yield versus r_0 (Fig. 5b) was not verified experimentally. However, the associated curves are in qualitative agreement with the results obtained in [18].

CONCLUSIONS

The basic results of this work are as follows.

(1) The presence of the hot discharge area with a high carbon density and a low gas density generates a two-component gas jet.

(2) Evaluation of the gas jet parameters is straightforward, since the initial portion of the jet is formed by the heavier component (carbon) under the conditions of interest for fullerene production. Accordingly, the density of the binary gas mixture varies along the jet axis insignificantly. This allows one to use the well-known solution for a jet of an incompressible liquid (at least, as a first approximation).

(3) The rate of fullerene production is the highest at the periphery of the jet rather than on its axial plane. This finding holds true for both the turbulent and viscous jet.

(4) Combined use of the 1D model of the discharge gap, fan-shaped gas jet analysis, simple model of gap–jet transition, and simple fullerene production kinetics has made it possible to construct the dependences of the fullerene yield on the width and radius of the electrode gap, which are in good agreement with experimental data.

The analysis performed in this work may serve as a basis for considering the fullerene production kinetics in a real finite-dimension reactor of a given geometry.

REFERENCES

1. H. Murayama, S. Tomonoh, J. M. Alford, and M. E. Karpuk, Fullerenes Nanotubes Carbon Nanostructures **14**, 1 (2004).
2. W. Kratschmer, L. D. Lamb, K. Fostiroupoulos, and D. R. Huffman, Nature **347**, 354 (1990).
3. D. V. Afanas'ev, A. A. Bogdanov, G. A. Dyuzhev, and A. A. Kruglikov, Zh. Tekh. Fiz. **64** (10), 76 (1994) [Tech. Phys. **39**, 1017 (1994)]; Zh. Tekh. Fiz. **67** (2), 125 (1997) [Tech. Phys. **42**, 234 (1997)].
4. N. I. Alekseev and G. A. Dyuzhev, Zh. Tekh. Fiz. **71** (5), 41 (2001) [Tech. Phys. **46**, 577 (2001)].
5. N. I. Alekseev and G. A. Dyuzhev, Zh. Tekh. Fiz. **71** (5), 71 (2001) [Tech. Phys. **46**, 573 (2001)].
6. N. I. Alekseev and G. A. Dyuzhev, Zh. Tekh. Fiz. **72** (5), 121 (2002) [Tech. Phys. **47**, 634 (2002)].
7. G. N. Abramovich, *The Theory of Turbulent Jets* (Nauka, Moscow, 1984; MIT, Cambridge, 1963).
8. A. S. Ginevskiĭ, *The Theory of Turbulent Jets and Wakes* (Mashinostroenie, Moscow, 1969) [in Russian].

9. G. N. Abramovich, *Applied Gas Dynamics* (Nauka, Moscow, 1969) [in Russian].
10. G. A. Dyuzhev, I. V. Basargin, B. M. Filippov, *et al.*, PCT Int. Appl. WO 02/096800, RU02/00083.
11. G. A. Dyuzhev and V. I. Karataev, Fiz. Tverd. Tela (St. Petersburg) **36**, 2795 (1994) [Phys. Solid State **36**, 1528 (1994)].
12. N. I. Alekseev, F. Chibante, and G. A. Dyuzhev, Zh. Tekh. Fiz. **71** (6), 122 (2001) [Tech. Phys. **46**, 761 (2001)].
13. L. G. Loitsyansky, Tr. Leningr. Politekh. Inst. im. M.I. Kalinina, No. 5, 5 (1953).
14. Yu. T. Reznichenko, Tr. Leningr. Politekh. Inst. im. M.I. Kalinina, No. 5, 33 (1953).
15. N. A. Slezkin, *Dynamics of Viscous Incompressible Fluid* (GITTL, Moscow, 1955) [in Russian].
16. S. Chapman and T. G. Cowling, *Mathematical Theory of Non-Uniform Gases*, 2nd ed. (Cambridge Univ. Press, Cambridge, 1952; Inostrannaya Literatura, Moscow, 1960).
17. R. Reid, J. Praustniz, and T. Sherwood, *The Properties of Gases and Liquids*, 3rd ed. (McGraw-Hill, New York, 1977; Khimiya, Leningrad, 1982).
18. R. Dubrovsky and V. Bezmelnitsyn, Fullerenes Nanotubes Carbon Nanostructures **14**, 17 (2004).

Translated by V. Isaakyan

Technical Physics, Vol. 50, No. 11, 2005, pp. 1431–1434. Translated from Zhurnal Tekhnicheskoĭ Fiziki, Vol. 75, No. 11, 2005, pp. 40–43.

GASES AND LIQUIDS

On One Method of Simultaneously Measuring the Mass Flow Rate and Density of a Liquid

E. V. Mayorov and V. A. Onishchuk†

Emanuel Institute of Biochemical Physics, Russian Academy of Sciences, ul. Kosygina 4, Moscow, 119991 Russia

e-mail: sal@deom.chph.ras.ru

Received February 16, 2005

Abstract—The problem of an ideal incompressible liquid flowing in an axisymmetric pipe with a cross section varying in space and time is solved. The case when the area of variation of the cross section is represented by two identical series-connected cylinders is considered. It is shown that, if the cross sections of the cylinders vary with a constant frequency so that one decreases and the other increases, pressure difference oscillations arising at the ends of the cylinders bear information on both the liquid density and the flow rate in the pipe. The feasibility of designing an instrument based on these results and the choice of its performance parameters are discussed. It is noted, in particular, that the length of either cylinder must be no less than the pipe mean diameter.

Among the variety of liquid and gas flowmeters, mass flowmeters are usually of primary interest for the user. These devices measure the oscillations of a flow whirled in a special manner [1], gyroscopic moments acting on the moving parts of pipelines or moments of inertia (Coriolis forces) of turbines (or radial bar rotors) rotating in a flow to be measured [2], or distortion of the temperature field in the pipeline heated from the outside and washed by the medium to be measured from the inside [2].

In this paper, we offer a new method to measure the density and mass flow rate of a liquid. The processes occurring in this flowmeter allow us to categorize it as an inertial mass flowmeter that stands out from other representatives of this class because of its unique properties. Let us perform tentative theoretical calculations based on which we shall proceed further.

Consider an incompressible ideal liquid (Fig. 1) flowing in an axisymmetric pipe the cross section of which is a function of coordinate and time. Cross-sectional area $S(x, t)$ of the pipe is assumed to be given.

Assuming the flow to be quasi-one-dimensional, we can write the set of equations for such a flow in the form [3]

$$\begin{aligned}\frac{\partial S}{\partial t} + \frac{\partial (SV)}{\partial x} &= 0,\\ \frac{\partial V}{\partial t} + V\frac{\partial V}{\partial x} &= -\frac{1}{\rho}\frac{\partial \rho}{\partial x}.\end{aligned} \tag{1}$$

Here, ρ is the liquid density, $S(x, t)$ is the pipe's cross-sectional area, and $V(x, t)$ is the velocity averaged over the cross section. The average velocity is related to the mass flow rate as[1]

$$Q(x, t) = \rho V(x, t)S(x, t), \tag{2}$$

where $p(x, t)$ is the pressure averaged over the cross section.

If constant of integration $C(t)$ is time-independent and equal to Q_0/ρ, where Q_0 is the mass flow rate in the unperturbed part of the pipe, the first equation of system (1) yields

$$V = \frac{1}{S}\left(C(t) - \int\frac{\partial S}{\partial t}dx\right) = \frac{1}{S}\left(\frac{Q_0}{\rho} - \int\frac{\partial S}{\partial t}dx\right). \tag{3}$$

Substituting Eq. (3) into the second equation of (1) and carrying out appropriate calculations, we obtain

$$\begin{aligned}\frac{1}{\rho}\frac{\partial p}{\partial t} &= \frac{1}{S^3}\frac{\partial S}{\partial x}\left(\frac{Q_0}{\rho} - \int\frac{\partial S}{\partial t}dx\right)^2\\ &+ \frac{2}{S^2}\frac{\partial S}{\partial t}\left(\frac{Q_0}{\rho} - \int\frac{\partial S}{\partial t}dx\right) + \frac{1}{S}\int\frac{\partial^2 S}{\partial t^2}dx.\end{aligned} \tag{4}$$

Of interest is a solution to this equation for the case when the cross section varies over a part of the pipe by the law

$$S = \begin{cases} S_0 + G(t, x) = S_0 + a_0\sin\left(\dfrac{x\pi}{L}\right)\sin(\omega t)\\ = S_0\left(1 + \delta\sin\left(\dfrac{x\pi}{L}\right)\sin(\omega t)\right) \text{ at } -L \le x \le L,\\ S_0, \text{ at } -L > x, L > x.\end{cases} \tag{5}$$

† Deceased.

[1] In this formula, the mass flow rate may have both signs according to the sign of velocity $V(x, t)$ relative to the x axis.

1063-7842/05/5011-1431$26.00 © 2005 Pleiades Publishing, Inc.

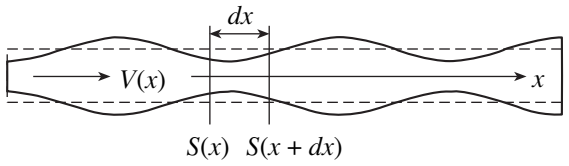

Fig. 1.

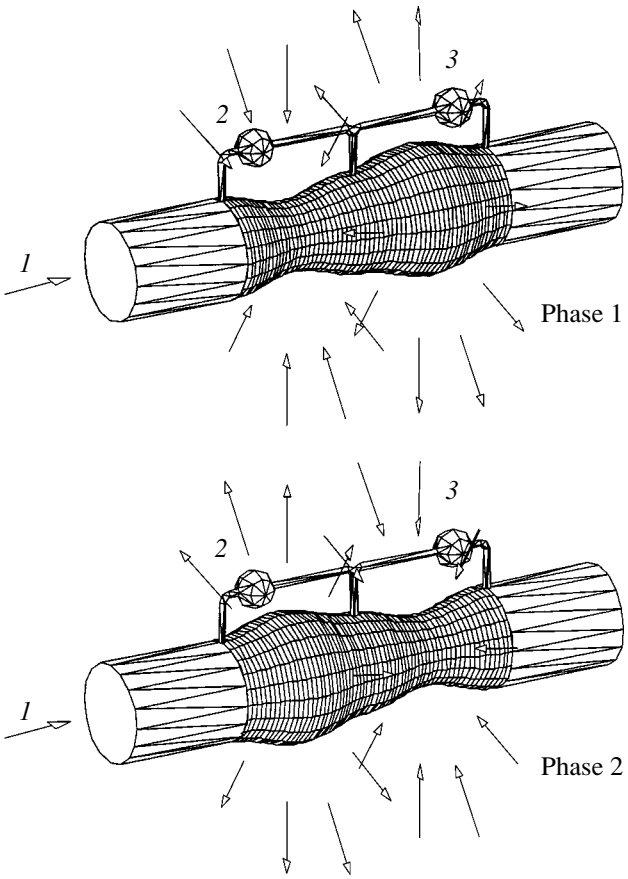

Fig. 2. (*1*) Flow to be measured, (*2*) left pressure meter, and (*3*) right pressure.

Here, $\delta = a_0/S_0$. We shall seek an expression for the pressure difference between points $x = -L$, $x = 0$, and $x = +L$; i.e., $\Delta p_{\text{left}}(t) = p(0, t) - p(-L, t)$ and $\Delta p_{\text{right}}(t) = p(L, t) - p(0, t)$. By way of illustration, Fig. 2 shows two phases in variation of the cross section: phase *1* corresponds to time intervals when $\sin(\omega t) > 0$; phase *2*, to those when $\sin(\omega t) < 0$ (the positive direction of the x axis coincides with the flow direction). We linearize Eq. (4), assuming that δ is small and the inequality

$$\frac{Q_0\pi}{\rho S_0 \omega L} > 1$$

is satisfied.[2] Eventually, we arrive at the following equation:

$$\frac{\partial \rho}{\partial x} = \frac{\delta\omega^2 L\rho}{\pi}\sin(\omega t)\left(\cos\left(\frac{x\pi}{L}\right) + 1\right)$$
$$+ Q_0\frac{2\delta\omega}{S_0}\cos(\omega t)\sin\left(\frac{x\pi}{L}\right) + \frac{Q_0^2}{\rho}\frac{\delta\pi}{S_0^2 L}\sin(\omega t)\cos\left(\frac{x\pi}{L}\right).$$

Integrating over x yields an expression for the pressure of a nonviscous liquid flowing within the portion $x \subset [-L, L]$ of a moving-wall pipe and obeying law (5) in the quasi-one-dimensional approximation (the motion of the walls is small, $\delta \ll 1$),

$$p(x, t) = \frac{\delta\omega^2 L^2\rho}{\pi^2}\sin(\omega t)\sin\left(\frac{x\pi}{L}\right)$$
$$+ \frac{\delta\omega^2 L\rho}{\pi}\sin(\omega t)(x + L)$$
$$- Q_0\frac{2\delta\omega L}{S_0\pi}\cos(\omega t)\left(\cos\left(\frac{x\pi}{L}\right) + 1\right) \quad (6)$$
$$+ \frac{Q_0^2}{\rho}\frac{\delta}{S_0^2}\sin(\omega t)\sin\left(\frac{x\pi}{L}\right) + P_0,$$

where P_0 is a constant of integration, which may be equal, for example, to the hydrostatic pressure.

The pressures at the points of interest are

$$p(-L, t) = P_0,$$
$$p(0, t) = \frac{\delta\omega^2 L^2\rho}{\pi}\sin(\omega t) - Q_0\frac{4\delta\omega L}{S_0\pi}\cos(\omega t) + P_0,$$
$$p(L, t) = \frac{2\delta\omega^2 L^2\rho}{\pi}\sin(\omega t) + P_0.$$

Now we construct the desired pressure differences,

$$\Delta p_{\text{left}}(t) = p(0, t) - p(-L, t)$$
$$= \rho\frac{\delta\omega^2 L^2}{\pi}\sin(\omega t) - 4Q_0\frac{\delta\omega L}{\pi S_0}\cos(\omega t),$$
$$\Delta p_{\text{right}}(t) = p(+L, t) - p(0, t)$$
$$= \rho\frac{\delta\omega^2 L^2}{\pi}\sin(\omega t) + 4Q_0\frac{\delta\omega L}{\pi S_0}\cos(\omega t), \quad (7)$$
$$\Delta p(t) = p(+L, t) - p(-L, t)$$
$$= 2\rho\frac{\delta\omega^2 L^2}{\pi}\sin(\omega t).$$

According to formulas (7), if the cross sections of two series-connected identical portions of a pipe with a

[2] It will be shown that this stringent condition reduces the practical value of the results obtained.

flowing liquid vary harmonically in antiphase so that the oscillation amplitude is much smaller than the diameter of the unpertubed part of the pipe, variable pressure differences arise within those portions. Separately measuring the amplitudes of the mutually orthogonal components of the pressure differences, one can independently find the density and mass flow rate of the liquid. From Eq. (7), the amplitude of the in-phase and orthogonal components are given, respectively, by

$$A_\rho = \rho\frac{\delta\omega^2 L^2}{\pi} = \left[\frac{\text{dyn}}{\text{cm}^2}\right], \quad (8)$$

$$A_Q = 4Q_0\frac{\delta\omega L}{\pi S_0} = \left[\frac{\text{dyn}}{\text{cm}^2}\right]. \quad (9)$$

In essence, to measure the density and/or mass flow rate, one should apply identical periodical axisymmetric antiphase impulses to two series-connected portions of the pipe perpendicularly to the axis of the pipe (Fig. 2; such an action on a flow changes its axial momentum within the portions of interest) and then analyze a variable pressure difference in any of these portions. The pressure difference is due to axial inertial forces arising in the moving liquid.

Below, we would like to answer the questions that inevitably arise in an attempt to implement a measuring device.

FORCE PULSER

As an impulse-generating unit (force pulser), we offer a thin elastic cylindrical membrane clamped at its center and at both ends in such a way that the inner surface faces the flow to be measured and the outer surface is in a closed cylindrical vessel divided into two strictly identical isolated semicylinders at the place of the central clamp.

It is assumed that each of the isolated semicylinders is hermetically connected to a bellows through holes in the outer wall. The free end of one of the bellows is rigidly connected to the free end of the other semicylinder, and the inner spaces of the semicylinders are disconnected and filled with a special bubble-free liquid (Fig. 3). The joint of the bellows with a baffle in between will be called the head of the bellows couple. The case considered in [4] shows that the pressure dependence of the deflection of the cylindrical membrane is linear. Hence, a sinusoidal pressure variation above the membrane will cause sinusoidal perturbation ΔR of its radius R_0. It can be shown that, if $\delta_r = \Delta R/R_0$ is small, the relative increment of the pipe's cross-sectional area, $\delta = a_0/S_0$, may be set equal to $\delta = 2\delta_r$; hence, the variation of the cross-sectional area is also sinusoidal. Thus, a sinusoidal displacement of the head of the bellows couple will lead to a sinusoidal variation in the cross section of the cylindrical membrane. In other words, to make the cross section vary by law (5) is quite realistic.

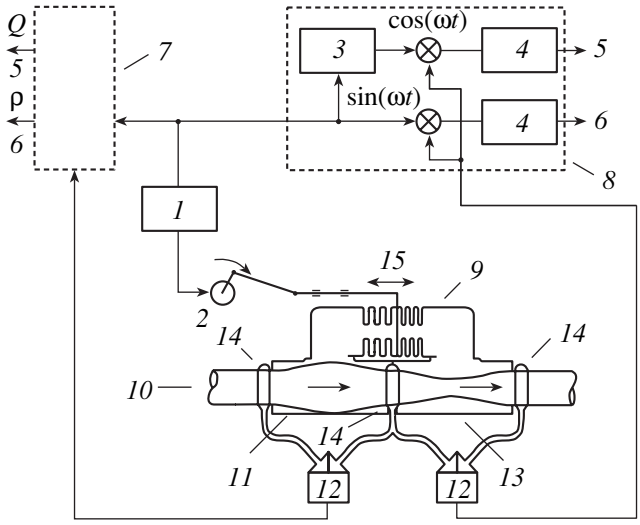

Fig. 3. (*1*) Driving oscillator with frequency ω, (*2*) synchronous motor, (*3*) π/2 phase shifter, (*4*) integrator over the interval $0 < t < 2\pi/\omega$, (*5*) value proportional to the mass flow per second, (*6*) value proportional to the liquid density, (*7*) left analyzer, (*8*) right analyzer, (*9*) bellows couple, (*10*) flow being measured, (*11*) elastic cylindrical membrane fixed at the center and at the ends, (*12*) pressure difference sensor, (*13*) body of meter, (*14*) ring chamber hermetically closed from the inside by the elastic cylindrical membrane of diameter equal to the pipeline diameter, and (*15*) displacement direction of bellows couple head.

Such a balance scheme of flow perturbation by law (5) is very convenient: the equilibrium position of the head of the bellows couple does not depend on a strong variation of the hydrostatic pressure provided that an external force displacing the head is absent; otherwise, the mass flow rate and the density of the liquid would have to be measured separately.

How long should length L of the cylindrical membrane be? For a flow about a body vibrating with an amplitude much less than its characteristic dimension [5], it is argued that the velocity of the liquid experiences perturbations on the order of the vibrating body velocity over a distance roughly equal to the dimension of the body. Then, taking the length of the "breathing" wall for the length of a vibrating body and setting it equal to the diameter of the pipe, one can assume that the flow velocity will vary roughly by the wall velocity over any cross section of the "modulated" part of the pipe. That is, all the liquid will have an alternating-sign momentum over the length of the modulated part. Accordingly, the length of the measuring device with a balance force pulser must be no less than two diameters of the pipe. A more accurate selection of the dimensions of the force pulser can be made after a careful consideration of the flow velocity distribution over the time- and coordinate-dependent cross section.

SENSOR

We recommend pressure-difference sensors based on a single-crystalline silicon membrane. Silicon pressure sensors offer a high precision, sensitivity, and overload endurance; wide dynamic range; extremely small hysteresis; and operating reliability. In addition, they are almost inertialess.

ANALYZER

Analysis of the signal from the pressure sensor implies harmonic separation. In general, measuring the amplitudes of two harmonics with frequency ω and mutually orthogonal initial phases is a task of spectral analysis. Such a problem can be solved, e.g., with a device described in [6].

The amplitude of the variable pressure-difference component that is in phase with the moving membrane is proportional to the flow density, and that of the orthogonal component to the mass flow rate in the pipe. From the expressions for $\Delta p_{\text{left}}(t)$ and $\Delta p_{\text{right}}(t)$ in (7), it readily follows that measuring the difference between the output signals from the left and right analyzers improves the sensitivity of mass-flow measurement twofold. Similarly, measuring the sum of the output signals improves the sensitivity of density measurement by the same factor. A wide variety of different circuit-design approaches and devices that may be applied to solve this problem saves us any comment on this issue.

Let us perform a tentative calculation. For pipe radius $R_0 = 5$ cm, driving frequency $f = \omega/2\pi = 60$ Hz, half-length of the variable section of the pipe $L = 30$ cm, liquid density $\rho = 1$ g/cm^3, and relative change in the pipe diameter $\delta_r = 0.005$, the partial pressure amplitude proportional to the density of the liquid is $A_\rho \approx 0.41 \times 10^6$ dyn/cm^2 $\approx 0.41 \times 10^4$ mm H_2O/cm^2 ≈ 0.41 atm (see formula (8)). To calculate the partial pressure amplitude proportional to the mass flow rate, we substitute the value of the mass flow taken with regard to the limitation mentioned above (see footnote 2) into Eq. (9). This is a critical value starting from which the theory presented here adequately describes the processes taking place in the measuring device suggested. In our case, this value is $Q_0 = 2.84 \times 10^5$ g/s and the partial pressure responsible for the mass flow rate is $A_Q \approx 1.27 A_\rho$.

As was mentioned above, our theory is invalid when $\delta \sim 1$. We suppose that, without this limitation, the response of the device (pressure difference) will also depend on both the density and the mass flow rate of the liquid, possibly in another form. It seems that a relationship between the components involving the measurands will be more suitable for the combined measurement. This issue will be clarified after solving this more complicated problem.

ACKNOWLEDGMENTS

We are grateful to A.A. Ovchinnikov†, E.B. Burlakova, and V.M. Misin for encouragement and support.

REFERENCES

1. A. Sh. Kiyasbeĭli and M. E. Perel'shteĭn, *Vortical Measuring Instruments, Ser. Instrument-Making Engineer's Bookshelf* (Mashinostroenie, Moscow, 1978), pp. 113–125 [in Russian].
2. *Proceedings of the Scientific–Technical Conference on Methods and Instruments for Measuring the Consumption and Amount of Liquids, Gases, and Vapors, Moscow, 1965*, pp. 132–172.
3. I. P. Ginzburg, *Applied Hydro- and Gas Dynamics* (Leningr. Gos. Univ., Leningrad, 1958), p. 40 [in Russian].
4. V. I. Feodos'ev, in *Strength of Materials, Ser. "Mechanics in Technical University,"* (Bauman Gos. Tekh. Univ., Moscow, 1999), Vol. 2, pp. 429–432 [in Russian].
5. L. D. Landau and E. M. Lifshitz, *Course of Theoretical Physics*, Vol. 6: *Fluid Mechanics* (Nauka, Moscow, 1986; Pergamon, New York, 1987).
6. A. A. Kharkevich, *Spectra and Analysis* (Fizmatlit, Moscow, 1962; Consultants Bureau, New York, 1960), p. 111.

Translated by M. Astrov

† Deceased.

Technical Physics, Vol. 50, No. 11, 2005, pp. 1435–1443. Translated from Zhurnal Tekhnicheskoĭ Fiziki, Vol. 75, No. 11, 2005, pp. 44–51.

GASES AND LIQUIDS

Nonlinear Periodic Waves on the Charged Surface of a Finite-Thickness Ideal Liquid Layer

S. A. Kurochkina and A. I. Grigor'ev

Demidov State University, Sovetskaya ul. 14, Yaroslavl, 150000 Russia

e-mail: grig@uniyar.ac.ru

Received February 17, 2005

Abstract—In the fourth order of smallness in the amplitude of a periodic capillary–gravitational wave travelling over the uniformly charged free surface of an ideal incompressible conducting liquid of a finite depth, analytical expressions for the evolution of the nonlinear wave, velocity field potential of the liquid, electrostatic field potential above the liquid, and nonlinear frequency correction that is quadratic in a small parameter are derived. It is found that the dependence of the amplitude of the nonlinear correction to the frequency on the charge density on the free liquid surface and on the thickness of the liquid layer changes qualitatively when the layer gets thinner. In thin liquid layers, the resonant wavenumber depends on the surface charge density, while in thick layers, this dependence is absent. © *2005 Pleiades Publishing, Inc.*

(1) Nonlinear waves on the charged surface of an incompressible liquid are the subject of considerable scientific and applied interest (see, for example, reviews [1–4]). This phenomenon is most frequently encountered when the depth of the liquid layer is finite [1–4]. Therefore, it would be reasonable to see how the depth of the layer influences the liquid flow and stability of the charged liquid surface. This issue has been repeatedly considered in the linear statement [5], in the nonlinear statement for the uncharged liquid surface [6, 7], and in the soliton statement [8–10]. A variety of works [11–19] have been devoted to studying nonlinear periodic capillary–gravitational waves on the charged surface of an infinitely deep ideal liquid. The general approach to analyzing nonlinear periodic waves on the free liquid surface has long been formulated, and several regular asymptotic methods of investigation have been developed [20–23], among which the method of many scales is the most efficient. This method will be used in this work. Here, we aim at finding an expression for the profile of a nonlinear capillary–gravitational wave travelling on the charged free surface of an ideal conducting liquid of a finite depth. The expression will be sought in the fourth order of smallness in the wave amplitude, which is assumed to be small compared with the wavelength (the velocity field potential of the wave liquid flow and the electrostatic field potential above the liquid will be sought in the same order of smallness). Our second goal is to find a nonlinear correction to the frequency.

The issues mentioned above are also topical because of the fact that the solutions to the related problems obtained recently for nonlinear periodic waves on the charged surface of a viscous liquid of both infinite [24, 25] and finite thickness [4, 26] are very awkward even in the second order of smallness. Accordingly, investigation of relations between the physical parameters of a nonlinear wave that is based on numerical analysis of these awkward analytical expressions is very difficult. Therefore, many physical parameters of the nonlinear wave process on the charged liquid surface we are interested in, specifically, nonlinear frequency corrections, are more convenient to analyze using the ideal liquid model, which gives compact analytical expressions up to the fifth order of smallness [19].

(2) Let an ideal incompressible conducting liquid layer of density ρ and surface tension coefficient σ that is infinite in the horizontal direction occupy the domain $0 \le z \le h$. The layer is subjected to the gravitational field and an electric field of strength $\mathbf{E}_0$, which is collinear with free fall acceleration $\mathbf{g}$. Unit vector $\mathbf{e}_z$ of the Cartesian coordinate system is directed oppositely to $\mathbf{g}$. Let a plane wave of small amplitude a, wavenumber k, and frequency ω,

$$t = 0: \xi(x, t) = a\cos(kx - \omega t); \quad ka \ll 1, \qquad (1)$$

travel over the surface of the layer in the positive Ox direction. This wave disturbs the equilibrium free surface of the liquid, $z = h$, so that the equation for the surface takes the form $z = h + \xi(x, t)$.

Mathematically, the problem of nonlinear wave flow on the surface of an ideal incompressible conducting liquid of a finite depth bordering a vacuum and placed in an electrostatic field with strength $\mathbf{E}_0$ normal to the free liquid surface is stated as

$$0 < z < h + \xi: \Delta\phi = 0,$$

$$\xi < z < \infty: \Delta\Phi = 0,$$

$$z = h + \xi: \frac{\partial\xi}{\partial t} + \frac{\partial\xi}{\partial x}\frac{\partial\phi}{\partial x} = \frac{\partial\phi}{\partial z},$$

1063-7842/05/5011-1435$26.00 © 2005 Pleiades Publishing, Inc.

$$\rho\frac{\partial\phi}{\partial t}+\frac{1}{2}\rho\left(\frac{\partial\phi}{\partial x}\right)^2$$
$$+\frac{1}{2}\rho\left(\frac{\partial\phi}{\partial z}\right)^2+\rho g\xi+P_\sigma+P_g-P_E=0,$$
$$\Phi=0,$$
$$z=0:\ \frac{\partial\phi}{\partial z}=0,$$
$$z\to\infty:\quad \Phi\to E_0 z.$$
$$P_\sigma\equiv\sigma\frac{\partial^2\xi}{\partial x^2}\left(\left(\frac{\partial\xi}{\partial x}\right)^2+1\right)^{-3/2},$$
$$P_E\equiv\frac{E^2(\xi)}{8\pi},\quad P_g\equiv\rho g(h+\xi), \tag{2}$$

where P_σ, P_E, and P_g are the pressure of surface tension forces under the free liquid surface disturbed by the flow, pressure of electric field forces, and gravitational pressure, respectively.

It is assumed that hydrodynamic velocities are much lower than the velocity of electromagnetic waves. In this approximation, the Maxwell equations for a time-varying electric field above the time-varying free liquid surface are reduced to the Laplace equation (with appropriate boundary conditions) for the electric field potential above the liquid, since the rate of equalization of the electrostatic potential over the wave-disturbed surface of an ideally conducting liquid may be taken as infinitely high.

To uniquely solve the problem stated by (1) and (2), it is necessary to set one more initial condition. In problems of this kind, preset initial conditions may exceedingly complicate a final solution. Therefore, as is customary in this case [11–14, 17–26], the second initial condition will be chosen during the solution of the problem in such a way as to simplify final expressions for free surface perturbation $\xi(x, t)$, velocity field potential $\phi(\mathbf{r}, t)$ of the wave flow, and electric field $\Phi(\mathbf{r}, t)$ as much as possible.

(3) Let us split the problem into several subproblems of different orders of smallness under the assumption that the unknown functions are perturbation $\xi = \xi(x, t)$ of the free surface, velocity field potential $\phi = \phi(x, z, t)$, and electric potential $\Phi = \Phi(x, z, t)$. We shall seek them in the form of expansions in small dimensionless parameter $\varepsilon \equiv ak$,

$$\xi=\varepsilon\xi_1+\varepsilon^2\xi_2+\varepsilon^3\xi_3+\varepsilon^4\xi_4+O(\varepsilon^5),$$
$$\phi=\varepsilon\phi_1+\varepsilon^2\phi_2+\varepsilon^3\phi_3+\varepsilon^4\phi_4+O(\varepsilon^5), \tag{3}$$
$$\Phi=-E_0z+\varepsilon\Phi_1+\varepsilon^2\Phi_2+\varepsilon^3\Phi_3+\varepsilon^4\Phi_4+O(\varepsilon^5).$$

In accordance with the basic idea of the method of many scales [6, 22, 23], we assume that desired functions $\xi_n(x, t)$, $\phi_n(x, z, t)$, and $\Phi_n(x, z, t)$ depend not only on coordinates x and z, but also on time scales, specifically on the main scale $T_0 = t$, and slower ones $T_1 = \varepsilon t$, $T_2 = \varepsilon^2 t$, and $T_3 = \varepsilon^3 t$. In other words,

$$\xi_n=\xi_n(x, T_0, T_1, T_2, T_3),$$
$$\phi_n=\phi_n(x, z, T_0, T_1, T_2, T_3),$$
$$\Phi_n=\Phi_n(x, z, T_0, T_1, T_2, T_3).$$

Then, according to the differentiation rule for a function of several variables, operator $\partial/\partial t$ of taking the first time derivative takes the form

$$\frac{\partial}{\partial t}=\frac{\partial}{\partial T_0}+\varepsilon\frac{\partial}{\partial T_1}+\varepsilon^2\frac{\partial}{\partial T_2}+\varepsilon^3\frac{\partial}{\partial T_3}+O(\varepsilon^4). \tag{4}$$

Substituting (3) and (4) into (1) and (2) and equating the coefficients multiplying the terms with the same powers of ε to zero yields problems of the zeroth, first, second, third, and fourth orders of smallness.

(4) In the zeroth order of smallness, the free liquid surface remains unperturbed (and is described by the equation $z = h$), the liquid is at rest, and the electric field is uniform throughout the space,

$$\nabla\phi_0\equiv 0,\quad P_E=-\frac{E_0^2}{8\pi},\quad \nabla\Phi_0\equiv -E_0\cdot\mathbf{e}_z.$$

(5) Mathematically, the first-order subproblem is stated as

$$0<z<h:\ \Delta\phi_1=0,$$
$$h<z<\infty:\ \Delta\Phi_1=0,$$
$$z=h:\ \frac{\partial\xi_1}{\partial T_0}-\frac{\partial\phi_1}{\partial z}=0,$$
$$\rho\frac{\partial\phi_1}{\partial T_0}+\rho g\xi_1-\sigma\frac{\partial^2\xi_1}{\partial x^2}+\frac{E_0}{4\pi}\frac{\partial\Phi_1}{\partial z}=0,$$
$$\xi_1\frac{\partial\Phi_0}{\partial z}+\Phi_1=0,$$
$$z=0:\ \frac{\partial\phi_1}{\partial z}=0,$$
$$z\to\infty:\ \Phi_1\to 0.$$

The first-order subproblem is easy to solve by classical methods,

$$\xi_1=\frac{1}{2}(\zeta\exp(i\theta)+\bar{\zeta}\exp(-i\theta)),\quad \theta\equiv kx-\omega T_0,$$
$$\phi_1=\frac{i\omega}{2k}\frac{\cosh(kz)}{\sinh(kh)}(-\zeta\exp(i\theta)+\bar{\zeta}\exp(-i\theta)),$$
$$\Phi_1=\frac{E_0}{2}\exp(k(h-z))(\zeta\exp(i\theta)+\bar{\zeta}\exp(-i\theta)), \tag{5}$$

$$\omega^2 = \frac{k}{\rho}\tanh(kh)\left(\rho g + \sigma k^2 - \frac{E_0^2 k}{4\pi}\right),$$

where ω is the frequency, $\zeta = \zeta(T_1, T_2, T_3)$ is an unknown complex function of time that is found by solving the higher order problems, and the bar marks complex conjugates.

(6) The second-order problem is stated as

$$0 < z < h\colon \Delta\phi_2 = 0,$$

$$h < z < \infty\colon \Delta\Phi_2 = 0,$$

$$z = h\colon -\frac{\partial\xi_2}{\partial T_0} + \frac{\partial\phi_2}{\partial z} = \frac{\partial\xi_1}{\partial T_1} + \frac{\partial\phi_1}{\partial x}\frac{\partial\xi_1}{\partial x} - \xi_1\frac{\partial^2\phi_1}{\partial z^2},$$

$$-\rho\frac{\partial\phi_2}{\partial T_0} + \rho g\xi_2 + \sigma\frac{\partial^2\xi_2}{\partial x^2} - \frac{E_0}{4\pi}\frac{\partial\Phi_2}{\partial z}$$

$$= \rho\frac{\partial\phi_1}{\partial T_1} + \rho\xi_1\frac{\partial^2\phi_1}{\partial T_0\partial z} + \frac{1}{2}\rho\left(\frac{\partial\phi_1}{\partial x}\right)^2 + \frac{1}{2}\rho\left(\frac{\partial\phi_1}{\partial z}\right)^2$$

$$-\frac{1}{8\pi}\left(\frac{\partial\Phi_1}{\partial x}\right)^2 - \frac{1}{8\pi}\left(\frac{\partial\Phi_1}{\partial z}\right)^2 + \xi_1\frac{E_0}{4\pi}\frac{\partial^2\Phi_1}{\partial z^2},$$

$$\xi_2\frac{\partial\Phi_0}{\partial z} + \Phi_2 = -\xi_1\frac{\partial\Phi_1}{\partial z},$$

$$z = 0\colon \frac{\partial\phi_2}{\partial z} = 0,$$

$$z \longrightarrow \infty\colon \Phi_2 \longrightarrow 0.$$

Substituting first-order solutions (5) into the inhomogeneity functions, one can obtain a solution to the second-order problem,

$$\xi_2 = \frac{\omega^2}{4g}(1 - (\coth(kh))^2)\zeta\bar{\zeta}$$

$$+ \Omega(\zeta^2\exp(2i\theta) + \bar{\zeta}^2\exp(-2i\theta)),$$

$$\phi_2 = \frac{i\omega}{k}\frac{\cosh(2kz)}{\sinh(2kh)}\left(\frac{k}{4}\coth(kh) - \Omega\right)$$

$$\times(\zeta^2\exp(2i\theta) - \bar{\zeta}^2\exp(-2i\theta)), \qquad (6)$$

$$\Phi_2 = \left(\frac{E_0\omega^2}{4g}((\coth(kh))^2 - 1) + \frac{E_0 k}{2}\right)\zeta\bar{\zeta}$$

$$+ E_0\exp(2k(h-z))\left(\frac{k}{4} + \Omega\right)$$

$$\times(\zeta^2\exp(2i\theta) + \bar{\zeta}^2\exp(-2i\theta)).$$

Coefficient Ω entering in this solution will be defined below.

When seeking second-order solution (6), we used the second initial condition: vanishing of the amplitude coefficient multiplying a nonlinear correction to the first-order solution (this correction has the same, not double, argument of the hyperbolic cosine as the linear solution).

(7) In the third order of smallness, the related subproblem is stated as

$$0 < z < h\colon \Delta\phi_3 = 0,$$

$$h < z < \infty\colon \Delta\Phi_3 = 0,$$

$$z = h\colon \frac{\partial\xi_3}{\partial T_0} - \frac{\partial\phi_3}{\partial z} = -\frac{\partial\xi_2}{\partial T_1} - \frac{\partial\xi_1}{\partial T_2} - \frac{\partial\phi_2}{\partial x}\frac{\partial\xi_1}{\partial x}$$

$$-\frac{\partial\phi_1}{\partial x}\frac{\partial\xi_2}{\partial x} - \xi_1\frac{\partial^2\phi_1}{\partial x\partial z}\frac{\partial\xi_1}{\partial x}$$

$$+ \xi_2\frac{\partial^2\phi_1}{\partial z^2} + \xi_1\frac{\partial^2\phi_2}{\partial z^2} + \frac{1}{2}\xi_1^2\frac{\partial^3\phi_1}{\partial z^3},$$

$$-\rho\frac{\partial\phi_3}{\partial T_0} - \rho g\xi_3 + \sigma\frac{\partial^2\xi_3}{\partial x^2} - \frac{E_0}{4\pi}\frac{\partial\Phi_3}{\partial z}$$

$$= \rho\frac{\partial\phi_1}{\partial T_2} + \rho\frac{\partial\phi_2}{\partial T_1} + \rho\xi_1\frac{\partial^2\phi_1}{\partial T_1\partial z} + \rho\xi_1\frac{\partial^2\phi_2}{\partial T_0\partial z}$$

$$+ \rho\xi_2\frac{\partial^2\phi_1}{\partial T_0\partial z} + \frac{1}{2}\rho\xi_1^2\frac{\partial^3\phi_1}{\partial T_0\partial z^2} + \rho\frac{\partial\phi_1}{\partial x}\frac{\partial\phi_2}{\partial x}$$

$$+ \rho\xi_1\frac{\partial\phi_1}{\partial x}\frac{\partial^2\phi_1}{\partial x\partial z} + \rho\frac{\partial\phi_1}{\partial z}\frac{\partial\phi_2}{\partial z} + \rho\xi_1\frac{\partial\phi_1}{\partial z}\frac{\partial^2\phi_1}{\partial z^2}$$

$$+ \frac{3}{2}\sigma\frac{\partial^2\xi_1}{\partial x^2}\left(\frac{\partial\xi_1}{\partial x}\right)^2 - \frac{1}{4\pi}\frac{\partial\Phi_1}{\partial x}\frac{\partial\Phi_2}{\partial x} - \frac{1}{4\pi}\xi_1\frac{\partial\Phi_1}{\partial x}\frac{\partial^2\Phi_1}{\partial x\partial z}$$

$$-\frac{1}{4\pi}\frac{\partial\Phi_1}{\partial z}\frac{\partial\Phi_2}{\partial z} - \frac{1}{4\pi}\xi_1\frac{\partial\Phi_1}{\partial z}\frac{\partial^2\Phi_1}{\partial z^2} + \frac{E_0}{4\pi}\xi_1\frac{\partial^2\Phi_2}{\partial z^2}$$

$$+ \frac{E_0}{4\pi}\xi_2\frac{\partial^2\Phi_1}{\partial z^2} + \frac{E_0}{8\pi}\xi_1^2\frac{\partial^3\Phi_1}{\partial z^3},$$

$$\Phi_3 - E_0\xi_3 = -\xi_1\frac{\partial\Phi_2}{\partial z} - \xi_2\frac{\partial\Phi_1}{\partial z} - \frac{1}{2}\xi_1^2\frac{\partial^2\Phi_1}{\partial z^2},$$

$$z = 0\colon \frac{\partial\phi_3}{\partial z} = 0,$$

$$z \longrightarrow \infty\colon \Phi_3 \longrightarrow 0.$$

Substituting first- and second-order solutions (5) and (6) into the inhomogeneity functions, one arrives at a solution to the third-order subproblem performing straightforward, while tedious, mathematical transformations,

$$\xi_3 = \Psi(\zeta^3\exp(3i\theta) + \bar{\zeta}^3\exp(-3i\theta)),$$

$$\phi_3 = -\frac{\cosh(kz)}{2k\sinh(kh)}\left(\Lambda_2 - \frac{1}{2}i\Theta\right)\zeta\bar{\zeta}$$

$$\times(\zeta\exp(i\theta) - \bar{\zeta}\exp(-i\theta))$$

$$-\frac{(3i\omega\Psi + \Lambda_1)\cosh(3kz)}{3k\sinh(3kh)}(\zeta^3\exp(3i\theta) - \bar{\zeta}^3\exp(3i\theta)), \quad (7)$$

$$\Phi_3 = \Xi_2\zeta\bar{\zeta}\exp(k(h-z))(\zeta\exp(i\theta) + \bar{\zeta}\exp(i\theta))$$

$$+ \exp(3k(h-z)(E_0\Psi + \Xi_1))$$

$$\times(\zeta^3\exp(3i\theta) + \bar{\zeta}^3\exp(-3i\theta)).$$

The solution to the third-order subproblem defines function ζ as a function of time scales T_2 and T_3,

$$\zeta = \zeta_1(T_3)\exp(i\beta_0(T_3))\exp(i\Theta\zeta_1^2 T_2). \quad (8)$$

Coefficients Ψ, Λ_1, Λ_2, Ξ_1, Ξ_2, and Θ appearing in the above expressions will be defined below. Functions ζ_1 and β_0 depending only on T_3 will be determined by solving the fourth-order subproblem.

(8) The fourth-order subproblem is mathematically stated as

$$0 < z < h: \Delta\phi_4 = 0,$$

$$h < z < \infty: \Delta\Phi_4 = 0,$$

$$z = h: -\frac{\partial\xi_4}{\partial T_0} + \frac{\partial\phi_4}{\partial z} = H_{41},$$

$$-\rho\frac{\partial\phi_4}{\partial T_0} - \rho g\xi_4 + \sigma\frac{\partial^2\xi_4}{\partial x^2} - \frac{E_0}{4\pi}\frac{\partial\Phi_4}{\partial z} = H_{42},$$

$$E_0\xi_4 - \Phi_4 = H_{43},$$

$$z = 0: \frac{\partial\phi_4}{\partial z} = 0,$$

$$z \longrightarrow \infty: \Phi_4 \longrightarrow 0.$$

Awkward expressions for inhomogeneity functions H_{41}, H_{42}, and H_{43}, which are found by solving first-, second-, and third-order problems (5)–(8), are given in the Appendix.

The solution to the fourth-order problem subject to the initial condition adopted has the form

$$\xi_4 = \phi_4 = \Phi_4 = 0, \quad \zeta_1 = 1/k, \quad \beta_0 = 0.$$

This means that a solution to the general problem will not contain fourth-order corrections to the perturbation of the free surface of the liquid layer, as well as to the hydrodynamic and electrostatic potentials.

(9) A final solution to problem (1)–(2) of a capillary–gravitational periodic wave traveling over the uniformly charged equilibrium (free) surface of a conducting incompressible ideal liquid (namely, expressions for free surface perturbation $\xi(x, t)$ velocity field potentials $\phi(x, z, t)$, and electric field potential $\Phi(x, z, t)$ will be written in dimensionless variables such that $\rho = \sigma = g = 1$. In terms of such variables, the characteristic scales of the dimensional quantities are written as follows:

$$\omega_* = \left[\frac{\rho g^3}{\sigma}\right]^{1/4}, \quad k_* = \left[\frac{\rho g}{\sigma}\right]^{1/2}, \quad h_* = \left[\frac{\sigma}{\rho g}\right]^{1/4},$$

$$E_0 = (\rho\sigma g)^{1/4}, \quad a_* = \left[\frac{\sigma}{\rho g}\right]^{1/2}.$$

In the notation accepted, the solution is written in the form

$$\xi = a\cos(\theta + a^2\Theta t) + a^2\frac{\omega^2}{4}(1 - (\coth(kh))^2)$$

$$+ 2a^2\Omega\cos(2\theta + 2a^2\Theta t) + 2a^3\Psi\cos(3\theta),$$

$$\phi = \frac{a\omega}{k}\frac{\cosh(kz)}{\sinh(kh)}\sin(\theta + a^2\Theta t)$$

$$+ a^2\frac{\omega}{k}\frac{\cosh(2kz)}{\sinh(2kh)}\left(-\frac{k}{4}\coth(kh) + \Omega\right)\sin(2\theta + 2a^2\Theta t)$$

$$- a^3\frac{\coth(kz)}{k\sinh(kh)}\left(i\Lambda_2 + \frac{1}{2}\Theta\right)\sin(\theta)$$

$$- a^3\frac{2(-3\omega\Psi + i\Lambda_1)\cosh(3kz)}{3k\sinh(3kh)}\sin(3\theta), \quad (9)$$

$$\Phi = -\sqrt{4\pi W}z + a\sqrt{4\pi W}\exp(k(h-z))\cos(\theta + a^2\Theta t)$$

$$+ a^2\left(\frac{\omega^2\sqrt{\pi W}}{2}((\coth(kh))^2 - 1) + k\sqrt{\pi W}\right)$$

$$+ 4a^2\sqrt{\pi W}\exp(2k(h-z))\left(\frac{k}{4} + \Omega\right)\cos(2\theta + 2a^2\Theta t)$$

$$+ 2a^3\Xi_2\exp(k(h-z))\cos(3\theta)$$

$$+ 2a^3\exp(3k(h-z))(\sqrt{4\pi W}\Psi + \Xi_1)\cos(3\theta),$$

where frequency ω is determined from the dispersion relation

$$\omega^2 = (k + k^3 - Wk^2)\tanh(kh)$$

and

$$W = E_0^2/4\pi\sqrt{\rho g\sigma},$$

is the dimensionless Tonks–Frenkel parameter characterizing the charge stability of the free liquid surface.

In nondimensionalized form, the constant coefficients entering into the general solution take the form

$$\Omega = \frac{-4Wk^2\tanh(2kh) + 2k\tanh(kh)(1+k^2-Wk)H(kh)}{32\tanh(kh)(1+k^2-Wk) - 16\tanh(2kh)(1+4k^2-2Wk)},$$

$$H(kh) \equiv -3\tanh(2kh) + (\coth(kh))^2\tanh(2kh) + 4\coth(kh),$$

$$\Lambda_1 = \frac{3}{4}i\omega k^2\coth(2kh)\coth(kh) - 3i\omega k\Omega\coth(2kh) - i\omega k\Omega\coth(kh) - \frac{1}{8}i\omega k^2 - \frac{1}{2}i\omega k\Omega - \frac{1}{16}i\omega k^2\coth(kh), \quad (10)$$

$$\Lambda_2 = \frac{1}{4}i\omega k^2\coth(2kh)\coth(kh) - i\omega k\Omega\coth(2kh) - i\omega k\Omega\coth(kh) - \frac{1}{8}i\omega k^2 - \frac{1}{8}i\omega^3 k\coth(kh) + \frac{1}{8}i\omega^3 k(\coth(kh))^3 + \frac{1}{2}i\omega k\Omega - \frac{1}{16}i\omega k^2\coth(kh);$$

$$\Xi_1 = \frac{3}{2}k\sqrt{\pi W}\left(\frac{k}{8} + \Omega\right),$$

$$\Xi_2 = k\sqrt{\pi W}\left(\frac{k}{8} + 3\Omega + \frac{\omega^2}{4}(1-(\coth(kh))^2)\right),$$

$$\Psi = \left(\omega^2 k\coth(3kh)\left(-3k\coth(2kh)\coth(kh) + 12\Omega\coth(2kh) + 4\Omega\coth(kh) + \frac{k}{2} + 2\Omega + \frac{k}{4}\coth(kh)\right) - 18Wk^3\left(\frac{k}{8} + \Omega\right)\right. \quad (11)$$

$$+ \frac{11}{4}\omega^2 k\coth(kh) - 14k\omega\Omega + \frac{3k^5}{4} + \frac{7Wk^4}{4} + 10Wk^3\Omega + 4\omega^2 k\Omega\coth(2kh)\coth(kh)$$

$$\left. - \omega^4 k^2(\coth(kh))^2\coth(2kh)\right)/(12\omega^2\coth(3kh) - 4k - 36k^3 + 12Wk^2);$$

$$\Theta = \omega k\coth(kh)\left(\frac{k}{4}\coth(2kh)\coth(kh) - \Omega\coth(2kh) - \Omega\coth(kh) - \frac{\Omega}{8} - \frac{\omega^2}{8}\coth(kh) - \frac{k}{16}\coth(kh)\right)$$

$$+ \frac{Wk^3}{2\omega}\left(\frac{k}{8} + 3\Omega\right) + \frac{Wk^3\omega}{8}(1-(\coth(kh))^2) + k\omega\left(\frac{k}{4}\coth(kh) - \Omega\right)\coth(2kh)\coth(kh) \quad (12)$$

$$- \frac{\omega k}{8}(\omega^2 - Wk^2)((\coth(kh))^2 - 1) + \frac{3k^5}{16\omega} - \frac{Wk^3\Omega}{2\omega} + \frac{5Wk^4}{16\omega} + \frac{9\omega k^2}{16}\coth(kh) - \frac{3\Omega k}{2}.$$

(10) In the limit $h \longrightarrow \infty$, the expression for the nonlinear wave profile coincides with the solution for an infinitely deep liquid [19]; at $W \longrightarrow 0$, it transforms into the known expression for the profile of a nonlinear capillary–gravitational wave on the uncharged surface of a finite-thickness ideal liquid layer [6]. It was shown [6, 19] that the amplitude coefficients of second- and third-order corrections to a perturbation of the free surface are of resonant character both for an infinitely deep liquid and for a finite-thickness liquid layer. In the former case, the amplitude coefficient of the second-order correction increases resonantly at $k^2 \longrightarrow 1/2$, while the amplitude coefficient of the third-order correction exhibits the resonance behavior twice: at $k^2 \longrightarrow 1/2$ and $k^2 \longrightarrow 1/3$. Despite expression (9) for $\xi(x, t)$ is applicable in a wide range of wavenumbers, amplitude factors Ω and Ψ (see (10) and (11)) increase indefinitely in the neighborhoods of the resonances when

$$n\tanh(kh)(1+k^2-Wk) - \tanh(nkh)(1+n^2k^2-nWk) = 0. \quad (13)$$

Amplitude factor Ω resonates at $n = 2$, and Ψ has two resonances: at $n = 2$ and 3. This means that expression (9) applies in the neighborhood of wavenumbers k that are determined from Eq. (13), since nonlinear corrections must be small compared with first-order quantities. Figures 1a–1d show that the positions of the internal nonlinear resonances due to nonlinear interaction between gravitational and capillary waves appreciably depend on the liquid layer thickness and surface charge density (parameter W), the influence of the surface charge increasing as the liquid layer gets thinner. In thin layers ($kh \leq 1$), the positions of the internal nonlinear resonances (i.e., the values of wavenumber k at which the amplitude factor of quadratic (in small parameter) correction Ω to the wave profile indefinitely grows) depend on Tonks–Frenkel parameter W. In thick layers ($kh \gg 1$, Figs. 1c and 1d), the position of the internal nonlinear resonance of quadratic correction Ω

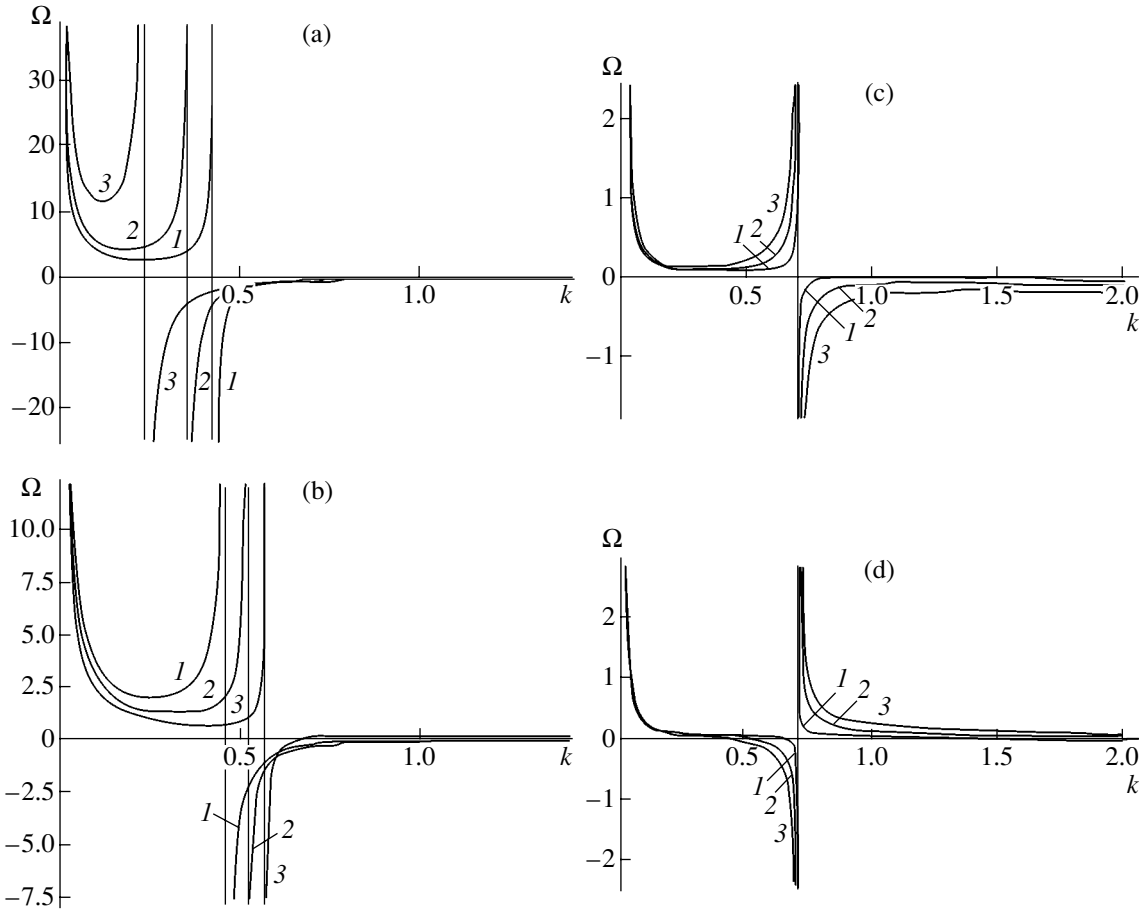

Fig. 1. Dimensionless amplitude factor Ω multiplying the quadratic (in the small parameter) correction to the wave profile vs. dimensionless wave number k calculated for various layer thickness h and Tonks–Frenkel parameters W: (a) $h = 1$, $W = (1)$ 1, (2) 0.8, and (3) 0.5; (b) $h = 1$, $W = (1)$ 1.1, (2) 1.3, and (3) 1.5; (c) $h = 5$, $W = (1)$ 1.0, (2) 0.8, and (3) 0.5; and (d) $h = 5$, $W = (1)$ 1.1, (2) 1.3, and (3) 1.5.

does not depend on W. The positions of the internal nonlinear resonances of the amplitude factor multiplying third-order correction Ψ behave in a similar way. However, Ψ varies with wavenumber k, parameter W, and layer thickness h even more appreciably. From Figs. 1a and 1b, it also follows that, when the wavenumber varies, the resonance positions shift in opposite directions at $W < 1$ and $W > 1$. With Tonks–Frenkel parameter W falling into these ranges, coefficient Ω varies with wavenumber k also in qualitatively different ways (for details of the wave liquid flow in these ranges of W, see [17, 19]).

(11) According to expression (9), the wave profile is nonstationary, because the terms of expression (9) that are linear and quadratic in the small parameter involve nonlinear frequency correction $a^2\Theta$ (dimensionless parameter Θ is given by (12)). The absolute value and sign of amplitude factor Θ depend on wavenumber k, parameter W, and layer thickness h (Fig. 2). Correction $a^2\Theta$ to the oscillation frequency of the last (third-order) term of the total solution for wave profile $\xi(x, t)$ (see (9)) changes this term by a quantity of order $O(a^5)$. However, quantities of such a high order are neglected in the problem, and so the third-order term includes unperturbed argument Θ. Eventually, the phase velocities of the waves involved in the total solution will be different. A frequency correction $\sim a^3$ that could appear in the linear term of (9) (recall that the problem is solved up to terms $\sim a^4$) is absent, just as in the case of nonlinear waves on the surface of an indefinitely deep liquid [19]. In asymptotic calculations up to a^5 [19], it is shown that frequency corrections are proportional to the small parameter squared and that frequency corrections $\sim a^2$ and $\sim a^4$ appear in calculations up to a^5.

From expression (10), it follows that the nonlinear correction to the frequency, as well as amplitude factors Ω and Ψ, has a resonance form. Dimensionless coefficient Θ, like Ω, resonantly grows in the vicinity of wavenumbers determined from Eq. (13) at $n = 2$. Figures 2a and 2b indicate that the positions of resonances of amplitude factor Θ multiplying the frequency correction appreciably depend on the layer thickness: in thin layers ($kh \le 1$), the resonance value of wavenumber k depends on the surface charge (on parameter W) (see

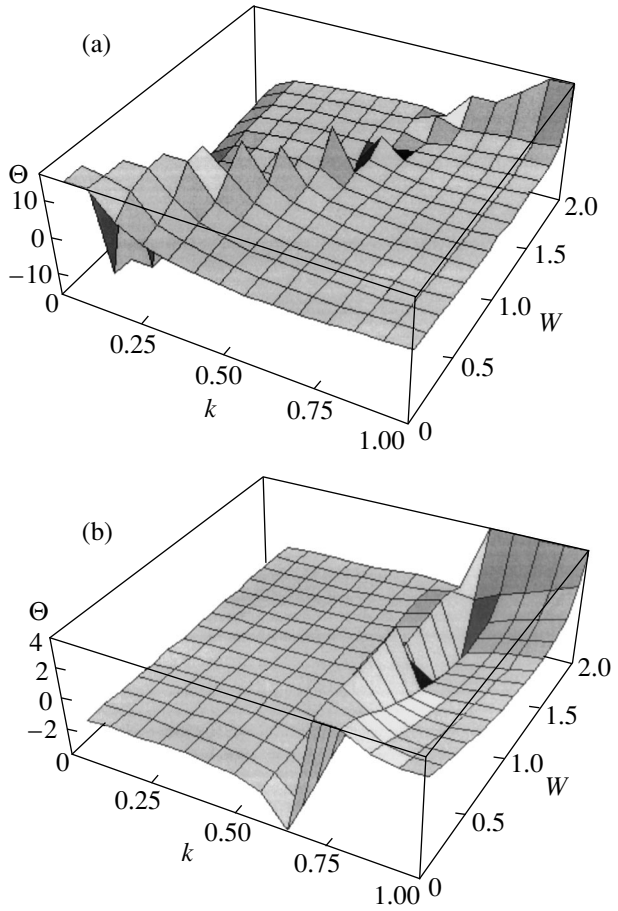

Fig. 2. Dimensionless factor Θ multiplying the nonlinear correction to the oscillation frequency vs. dimensionless wavenumber k and Tonks–Frenkel parameter W at liquid layer depth h = (a) 1 and (b) 5.

Fig. 2a); in thick layers ($kh \gg 1$, Fig. 2b), the resonance value of wavenumber k is virtually independent of the surface charge. This circumstance is of great importance for the problem considered: it means that mechanisms responsible for the nonlinear wave flow in thin and thick layers differ substantially. The dependences of the nonlinear corrections to amplitudes Ω and Ψ on wavenumber k and Tonks–Frenkel parameter W support this conclusion.

(12) The profiles of nonlinear waves on the charged surface of a finite-depth liquid (Fig. 3) differ from those of the waves on the uncharged liquid surface. That is, the presence of a surface charge changes the form of the curves describing the disturbed free surface: a high density of the surface charge increases the curvature of capillary wave crests. In addition, the profiles of periodic capillary–gravitational waves on the charged liquid surface vary with the layer thickness: the crests smooth out as the layer thickens. From Figs. 3a and 3b, it follows that an increase in the layer thickness may change the sign of the nonlinear correction to the wave profile (as is also evident from Fig. 1).

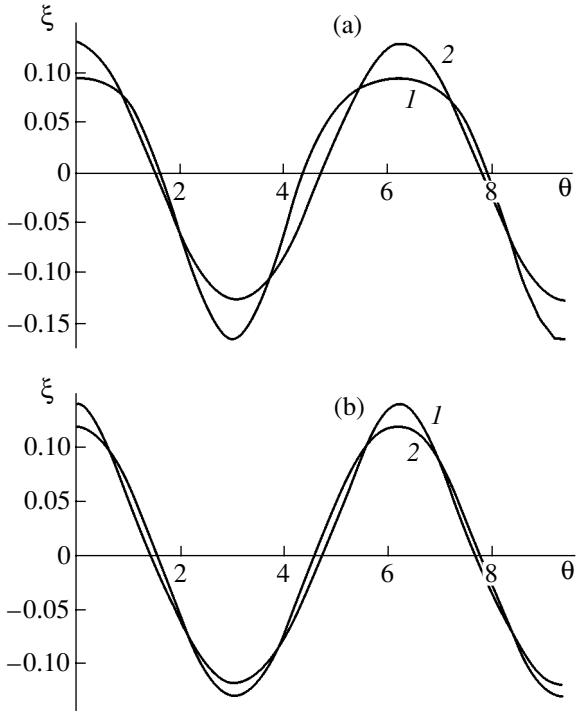

Fig. 3. Nonlinear wave profiles calculated at (*1*) k = 0.5 and W = 0 and (*2*) k = 0.5 and W = 1.8. h = (a) 1 and (b) 5.

CONCLUSIONS

Our calculation of nonlinear capillary–gravitational waves traveling over the charged free surface of an ideal finite-depth liquid layer (performed accurate to the fourth order of smallness in wave amplitude) shows that coefficients Ω and Ψ (specifying the wave profile, wave flow potential, and electrostatic field potential), as well as amplitude factor Θ multiplying the nonlinear correction to the frequency, have a resonance form. The positions of internal nonlinear resonances considerably depend on the liquid layer thickness and surface charge density, the influence of the latter increasing with decreasing layer thickness. As the layer gets thinner, the crests of periodic capillary–gravitational waves smooth out, while a high surface charge increases the curvature of capillary waves.

APPENDIX

The right-hand sides of the boundary conditions ($z = h$) to the fourth-order subproblem have the form

$$H_{41} = \frac{\partial \xi_3}{\partial T_1} + \frac{\partial \xi_2}{\partial T_2} + \frac{\partial \xi_1}{\partial T_3} + \frac{\partial \phi_3}{\partial x}\frac{\partial \xi_1}{\partial x} + \frac{\partial \phi_2}{\partial x}\frac{\partial \xi_2}{\partial x}$$

$$+ \frac{\partial \phi_1}{\partial x}\frac{\partial \xi_3}{\partial x} + \xi_2\frac{\partial^2 \phi_1}{\partial x \partial z}\frac{\partial \xi_1}{\partial x} + \xi_1\frac{\partial^2 \phi_2}{\partial x \partial z}\frac{\partial \xi_1}{\partial x}$$

$$+\frac{1}{2}\xi_1^2\frac{\partial^3\phi_1}{\partial^2 z\partial x}\frac{\partial\xi_1}{\partial x}-\xi_3\frac{\partial^2\phi_1}{\partial z^2}-\xi_2\frac{\partial^2\phi_2}{\partial z^2}$$

$$-\xi_1\frac{\partial^2\phi_3}{\partial z^2}-\frac{1}{2}\xi_1^2\frac{\partial^2\phi_2}{\partial z^2}-\xi_1\xi_2\frac{\partial^3\phi_1}{\partial z^3}-\frac{1}{6}\xi_1^3\frac{\partial^4\phi_1}{\partial z^4},$$

$$H_{42}=\rho\frac{\partial\phi_1}{\partial T_3}+\rho\frac{\partial\phi_2}{\partial T_2}+\rho\frac{\partial\phi_3}{\partial T_1}+\rho\xi_1\frac{\partial^2\phi_1}{\partial T_2\partial z}+\rho\xi_1\frac{\partial^2\phi_2}{\partial T_1\partial z}$$

$$+\rho\xi_1\frac{\partial^2\phi_3}{\partial T_0\partial z}+\rho\xi_2\frac{\partial^2\phi_1}{\partial T_1\partial z}+\rho\xi_2\frac{\partial^2\phi_2}{\partial T_0\partial z}$$

$$+\rho\xi_3\frac{\partial^2\phi_1}{\partial T_0\partial z}+\frac{1}{2}\rho\xi_1^2\frac{\partial^3\phi_1}{\partial T_1\partial z}+\frac{1}{2}\rho\xi_1^2\frac{\partial^3\phi_2}{\partial T_0\partial z^2}$$

$$+\rho\xi_1\xi_2\frac{\partial^3\phi_1}{\partial T_0\partial z^2}+\frac{1}{6}\rho\xi_1^3\frac{\partial^4\phi_1}{\partial T_0\partial z^3}+\frac{1}{2}\rho\left(\frac{\partial\phi_2}{\partial x}\right)^2$$

$$+\rho\frac{\partial\phi_1}{\partial x}\frac{\partial\phi_3}{\partial x}+\rho\xi_1\frac{\partial\phi_1}{\partial x}\frac{\partial^2\phi_2}{\partial x\partial z}+\rho\xi_1\frac{\partial\phi_2}{\partial x}\frac{\partial^2\phi_1}{\partial x\partial z}$$

$$+\rho\xi_2\frac{\partial\phi_1}{\partial x}\frac{\partial^2\phi_1}{\partial x\partial z}+\frac{1}{2}\rho\xi_1^2\left(\frac{\partial^2\phi_1}{\partial x\partial z}\right)^2$$

$$+\frac{1}{2}\rho\xi_1^2\frac{\partial\phi_1}{\partial x}\frac{\partial^3\phi_1}{\partial x\partial z^2}+\frac{1}{2}\rho\left(\frac{\partial\phi_2}{\partial z}\right)^2+\frac{1}{2}\rho\xi_1^2\left(\frac{\partial^2\phi_1}{\partial z^2}\right)^2$$

$$+\rho\frac{\partial\phi_1}{\partial z}\frac{\partial\phi_3}{\partial z}+\rho\xi_1\frac{\partial\phi_1}{\partial z}\frac{\partial^2\phi_2}{\partial z^2}+\rho\xi_1\frac{\partial\phi_2}{\partial z}\frac{\partial^2\phi_1}{\partial z^2}$$

$$+\rho\xi_2\frac{\partial\phi_1}{\partial z}\frac{\partial^2\phi_1}{\partial z^2}+\frac{1}{2}\rho\xi_1^2\frac{\partial\phi_1}{\partial z}\frac{\partial^3\phi_1}{\partial z^3}$$

$$+3\sigma\frac{\partial^2\xi_1}{\partial x^2}\frac{\partial\xi_1}{\partial x}\frac{\partial\xi_2}{\partial x}+\frac{3}{2}\sigma\frac{\partial^2\xi_2}{\partial x^2}\left(\frac{\partial\xi_1}{\partial x}\right)^2$$

$$-\frac{1}{8\pi}\left(\frac{\partial\Phi_2}{\partial x}\right)^2-\frac{1}{4\pi}\frac{\partial\Phi_1}{\partial x}\frac{\partial\Phi_3}{\partial x}-\frac{1}{4\pi}\xi_1\frac{\partial\Phi_1}{\partial x}\frac{\partial^2\Phi_2}{\partial x\partial z}$$

$$-\frac{1}{4\pi}\xi_1\frac{\partial\Phi_2}{\partial x}\frac{\partial^2\Phi_1}{\partial x\partial z}-\frac{1}{8\pi}\left(\frac{\partial\Phi_2}{\partial z}\right)^2-\frac{1}{4\pi}\xi_2\frac{\partial\Phi_1}{\partial x}\frac{\partial^2\Phi_1}{\partial x\partial z}$$

$$-\frac{1}{8\pi}\xi_1^2\frac{\partial\Phi_1}{\partial x}\frac{\partial^3\Phi_1}{\partial x\partial z^2}-\frac{1}{8\pi}\xi_1^2\left(\frac{\partial^2\Phi_1}{\partial x\partial z}\right)^2$$

$$-\frac{1}{4\pi}\frac{\partial\Phi_1}{\partial z}\frac{\partial\Phi_3}{\partial z}+\frac{E_0}{4\pi}\xi_1\frac{\partial^2\Phi_3}{\partial z^2}-\frac{1}{4\pi}\xi_1\frac{\partial\Phi_1}{\partial z}\frac{\partial^2\Phi_2}{\partial z^2}$$

$$-\frac{1}{4\pi}\xi_1\frac{\partial\Phi_2}{\partial z}\frac{\partial^2\Phi_1}{\partial z^2}+\frac{E_0}{4\pi}\xi_2\frac{\partial^2\Phi_2}{\partial z^2}-\frac{1}{4\pi}\xi_2\frac{\partial\Phi_1}{\partial z}\frac{\partial^2\Phi_1}{\partial z^2}$$

$$+\frac{E_0}{4\pi}\xi_3\frac{\partial^2\Phi_1}{\partial z^2}-\frac{1}{8\pi}\xi_1^2\left(\frac{\partial^2\Phi_1}{\partial z^2}\right)^2+\frac{E_0}{8\pi}\xi_1^2\frac{\partial^3\Phi_2}{\partial z^3}$$

$$+\frac{E_0}{4\pi}\xi_1\xi_2\frac{\partial^3\Phi_1}{\partial z^3}-\frac{1}{4\pi}\xi_1^2\frac{\partial\Phi_1}{\partial z}\frac{\partial^3\Phi_1}{\partial z^3}+\frac{E_0}{24\pi}\xi_1^3\frac{\partial^4\Phi_1}{\partial z^4},$$

$$H_{43}=\xi_1\frac{\partial\Phi_3}{\partial z}+\xi_2\frac{\partial\Phi_2}{\partial z}+\xi_3\frac{\partial\Phi_1}{\partial z}+\frac{1}{2}\xi_1^2\frac{\partial^2\Phi_2}{\partial z^2}$$

$$+\xi_1\xi_2\frac{\partial^2\Phi_1}{\partial z^2}+\frac{1}{6}\xi_1^3\frac{\partial^3\Phi_1}{\partial z^3}.$$

ACKNOWLEDGMENTS

This work was supported by the Russian Foundation for Basic Research, grant no. 03-01-00760.

REFERENCES

1. M. D. Gabovich, Usp. Fiz. Nauk **140**, 137 (1983) [Sov. Phys. Usp. **26**, 447 (1983)].
2. A. I. Grigor'ev and S. O. Shiryaeva, Izv. Ross. Akad. Nauk, Mekh. Zhidk. Gaza, No. 3, 3 (1994).
3. S. A. Kurochkina, D. F. Belonozhko, and A. I. Grigor'ev, Elektrokhim. Obrab. Met., No. 3, 26 (2003).
4. D. F. Belonozhko, A. I. Grigor'ev, A. V. Klimov, and S. A. Kurochkina, Elektrokhim. Obrab. Met., No. 4, 66 (2004).
5. A. I. Grigor'ev, S. O. Shiryaeva, V. A. Koromyslov, and D. F. Belonozhko, Zh. Tekh. Fiz. **67** (9), 12 (1997) [Tech. Phys. **42**, 877 (1997)].
6. A. H. Nayfeh, J. Fluid Mech. **40**, Part 4, 671 (1970).
7. É. L. Aromin, A. N. Ivanov, and D. Yu. Sadovnikov, Izv. Ross. Akad. Nauk, Mekh. Zhidk. Gaza, No. 4, 125 (1994).
8. A. I. Zhakin, Izv. Ross. Akad. Nauk, Mekh. Zhidk. Gaza, No. 3, 94 (1984).
9. A. Gonzalez and A. Castellanos, Phys. Rev. E **53**, 3573 (1996).
10. A. T. Il'ichev, Izv. Ross. Akad. Nauk, Mekh. Zhidk. Gaza, No. 2, 3 (2000).
11. D. H. Michael, Quarterly Appl. Math. **35**, 139 (1977).
12. Sh. K. Bhimsen, Quarterly Appl. Math. **35**, 423 (1979).
13. Rama Kant, R. K. Jindia, and S. K. Malik, Quarterly Appl. Math. **39**, 23 (1981).
14. S. K. Malik and Rama, Quarterly Appl. Math. **43**, 23 (1986).
15. N. M. Zubarev and O. V. Zubareva, Zh. Tekh. Fiz. **71** (7), 21 (2001) [Tech. Phys. **46**, 806 (2001)].
16. N. M. Zubarev, Zh. Éksp. Teor. Fiz. **116**, 1990 (1999) [JETP **89**, 1078 (1999)].

17. D. F. Belonozhko and A. I. Grigor'ev, Pis'ma Zh. Tekh. Fiz. **29** (18), 46 (2003) [Tech. Phys. Lett. **29**, 768 (2003)].
18. D. F. Belonozhko and A. I. Grigor'ev, Izv. Ross. Akad. Nauk, Mekh. Zhidk. Gaza, No. 6, 102 (2003).
19. A. V. Klimov, D. F. Belonozhko, and A. I. Grigor'ev, Zh. Tekh. Fiz. **74** (1), 32 (2004) [Tech. Phys. **49**, 30 (2004)].
20. J. H. Michell, Philos. Mag. **36**, 430 (1893).
21. J. R. Wilton, Philos. Mag. **29**, 688 (1915).
22. A. H. Nayfeh, Philos. Mag. **13**, 545 (1970).
23. A. H. Nayfeh and S. D. Hassan, J. Fluid Mech. **48**, 463 (1973).
24. D. F. Belonozhko and A. I. Grigor'ev, Zh. Tekh. Fiz. **73** (11), 37 (2003) [Tech. Phys. **48**, 1396 (2003)].
25. D. F. Belonozhko and A. I. Grigor'ev, Zh. Tekh. Fiz. **74** (3), 5 (2004) [Tech. Phys. **49**, 287 (2004)].
26. A. V. Klimov and S. A. Kurochkina, in *Proceedings of the All-Russia Scientific Conference in Honor of the 200th Anniversary of Demidov State University, Yaroslavl, 2003*, Ser. Phys., pp. 50–53.

Translated by N. Mende

Technical Physics, Vol. 50, No. 11, 2005, pp. 1444–1450. Translated from Zhurnal Tekhnicheskoĭ Fiziki, Vol. 75, No. 11, 2005, pp. 52–58.

GASES AND LIQUIDS

Effect of Small Methane and Monosilane Additives on Clustering in Pulsed Supersonic Argon Jets

A. E. Zarvin*, V. Zh. Madirbaev*, N. G. Korobeishchikov*, G. G. Gartvich*, and R. G. Sharafutdinov**

** Novosibirsk State University, ul. Pirogova 2, Novosibirsk, 630090 Russia*
e-mail: zarvin@phys.nsu.ru
*** Kutateladze Institute of Thermal Physics, Siberian Division, Russian Academy of Sciences, ul. Akademika Lavrent'eva 1, Novosibirsk, 630090 Russia*

Received March 25, 2005

Abstract—Condensation of argon–methane and argon–monosilane gas mixtures in pulsed supersonic jets is studied experimentally. The signal intensities from monomer and cluster ions are studied as functions of the stagnation pressure, and the parameters characterizing the flow–condensation transition are determined. Features of methane clustering are considered. It is shown that silicon–carbon complexes may form in the ternary mixture. © *2005 Pleiades Publishing, Inc.*

INTRODUCTION

Interest in clustering in supersonic jets of methane–monosilane mixtures with an inert diluent stems from the fact that these gases are used in plasma-chemical film deposition, hydrocarbon conversion, waste utilization, etc. [1, 2]. Considerable attention is also given to formation mechanisms of organosilicon complexes [3]. Earlier, we studied condensation in argon–monosilane mixtures [4, 5]. Along with hydrogenated silicon and argon clusters, we observed argon–silane complexes and found the conditions for their formation in the jet. It was established that condensation in an argon–monosilane jet at low stagnation pressures causes the formation of only monosilane clusters and argon atoms start depositing on these clusters with an increase in the jet density. In this work, we elaborate upon studying the initial stages of condensation in pulsed argon jets containing small molecular additives. The data for Ar + (5–10)%CH_4 and Ar + (5–10)%SiH_4 binary mixtures and a 2.5%SiH_4 + 2.5%CH_4 + Ar ternary mixture are compared with those for pure argon.

EXPERIMENTAL

Experiments were performed on the LEMPUS complex of gasdynamic benches at Novosibirsk State University [6] in the stagnation pressure range P_0 = 1–700 kPa at stagnation temperature T_0 = 295 K. As in our previous works [4–7], we employed a pulsed source making it possible to vary the density of a supersonic underexpanded jet of a given composition in wide limits. The partial concentrations of the components behind the sonic nozzle (d_* = 0.55 and/or 1 mm) were measured by the method of molecular-beam mass spectrometry [8]. Pulsed measurements were taken with a specially tailored MS-7303 quadrupole mass spectrometer. The electron energy in the ionization chamber of the mass spectrometer was set equal to 40 eV. All the measurements were performed at a fixed nozzle-to-skimmer distance (x/d = 175); therefore, the effect of skimmer interaction was ignored.

The composition of the clusters was determined from the stagnation parameters of di-, tri-, tetra-, and pentamers in the argon–methane and argon–monosilane mixtures. Data for condensation in a pulsed jet of pure argon were both obtained by new measurements and borrowed from our previous publications [9].

Figure 1 exemplifies the dependence of the mass peak amplitude for monomers in the 10%SiH_4 + 90% Ar mixture on parameter $P_0d^{0.8}$. This parameter is commonly used for generalizing results on condensation in argon. As was noted above, nozzles of two diameters were used in the experiments. Therefore, the basic parameter varying in a wide range was stagnation pressure P_0. In the mass spectrum of SiH_4, signals at m/e = 29–32 were recorded. The peak at m/e = 28 (Si^+) was omitted from analysis because of the presence of residual molecular nitrogen in the setup. It is known that the dissociative ionization cross section for SiH_2^+ is larger than that for SiH_3^+ under equilibrium conditions [10, 11]. In this work, as before [7], the spacing between the peaks due to these two ions remains nearly the same throughout the stagnation pressure range. Therefore, both the peak at m/e = 30 and that at m/e = 31 will be assigned to the monomer of monosilane.

Silicon has three stable isotopes: ^{28}Si (92.2%), ^{29}Si (4.7%), and ^{30}Si (3.0%). The peaks corresponding to masses of 32 and 33 are usually assigned to di- and tri-

1063-7842/05/5011-1444$26.00 © 2005 Pleiades Publishing, Inc.

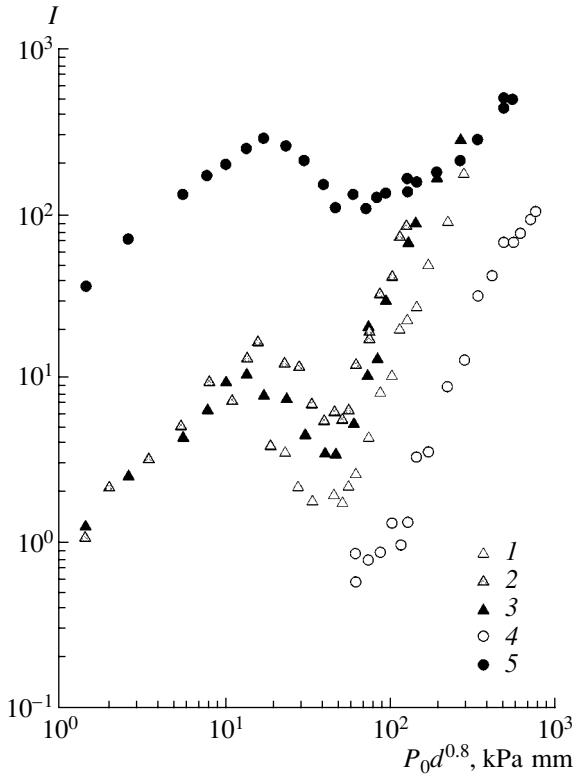

Fig. 1. Intensity of the argon and monosilane monomer signals vs. parameter $P_0d^{0.8}$ for the 90%Ar + 10%SiH_4 mixture. m/e = (*1*) 29, (*2*) 30, (*3*) 31, (*4*) 32, and (*5*) 40.

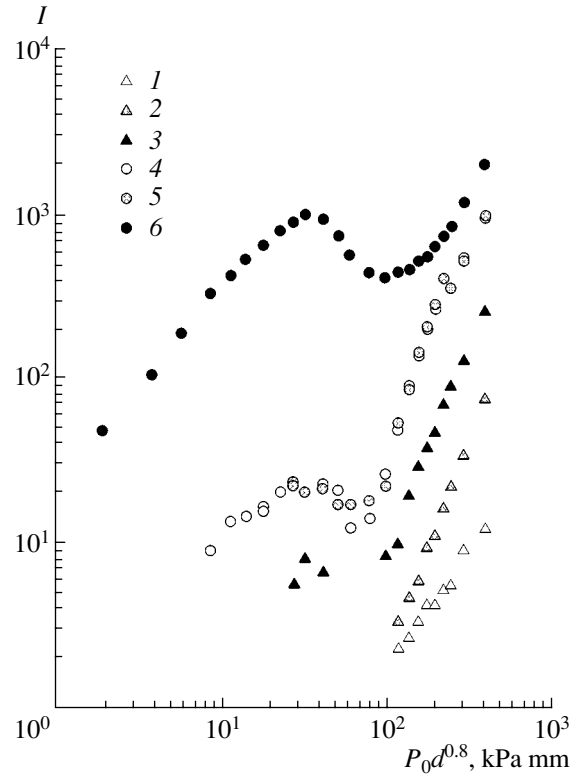

Fig. 2. Intensity of the argon and methane monomer signals vs. parameter $P_0d^{0.8}$ for the 90%Ar + 10%CH_4 mixture. m/e = (*1*) 12, (*2*) 13, (*3*) 14, (*4*) 15, (*5*) 16, and (*6*) 40.

hydrates of the heavier isotopes, respectively [12]. Since the error introduced into the ionic signal by heavier silicon isotopes (^{29}Si and ^{30}Si) is small compared with the measurement accuracy, the contribution of the heavy isotopes were not subtracted.

The same spectra for the 10%CH_4 + 90%Ar mixture are shown in Fig. 2. For methane, the peaks corresponding to CH_n^+ monomers (n = 0–4) are presented. It is easy to see that the spacing between the peaks due to CH_4^+ and CH_3^+ ions also remains almost the same throughout the range of stagnation pressures (and, accordingly, local densities at points of measurement). In what follows, CH_4^+ or CH_3^+ (m/e = 16 and 15, respectively) will be used as the methane monomer. As was expected, the peaks at m/e = 14, 13, and 12, i.e., for CH_2^+, CH^+, and C^+, are much lower. Therefore, we succeeded in detecting these signals only at high P_0. The relationship between CH_n^+ signals for two values of parameter $P_0d^{0.8}$ is given in the table. The discrepancy with the NIST data [13] is not so large that one can speak of distortion due to condensation.

The results for the monomers in the argon–methane and argon–monosilane mixtures at two component percentages (5 and 10% of the respective additive in argon) are compared in Fig. 3. For the dimers and trimers, the comparison is presented in Figs. 4a and 4b for the argon–methane and argon–monosilane mixtures, respectively. To illustrate the reproducibility of the results, Fig. 3a plots the data obtained in three experiments performed at different times with the 5% CH_4 + 95% Ar mixture (*2–4*). Clearly, the reliability of the results is high. Figure 3 also shows results obtained for pure argon under similar conditions.

CH_n^+ components detected in the mass spectrometry of methane

m/e, u	NIST	Experiment	
		$P_0^* d^{0.8}$, kPa mm	
		100	200
12	0.04	0.04	0.02
13	0.105	0.06	0.04
14	0.204	0.19	0.17
15	0.888	0.89	0.94
16	1	1	1

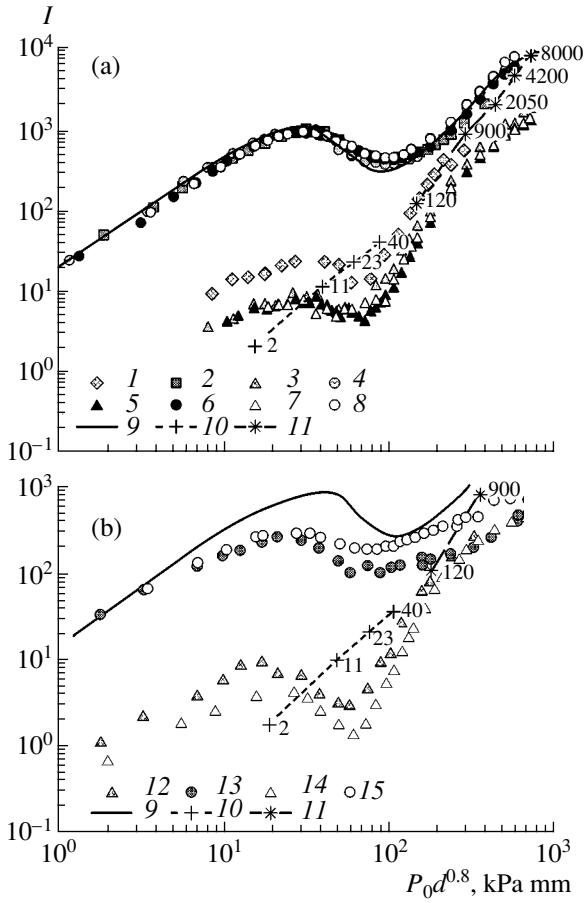

Fig. 3. Comparison of the monomer components at 5 and 10 vol % of the additives in the argon. (a) Argon–methane mixtures: *m*/*e* = (*1*) 15 (mixture *1*, 10% CH_4), (*2*) 40 (mixture *1*, 10% CH_4), (*3*) 15 (mixture *2*, 5% CH_4), (*4*) 40 (mixture *2*, 5% CH_4), (*5*) 15 (mixture *3*, 5% CH_4), (*6*) 40 (mixture *3*, 5% CH_4), (*7*) 15 (mixture *4*, 5% CH_4), (*8*) 40 (mixture *4*, 5% CH_4), (*9*) 15 (pure Ar), (*10*) N_{clust} [20], (*11*) N_{clust} [21]; (b) argon–monosilane mixtures: *m*/*e* = (*12*) 31 (mixture *5*, 10% SiH_4), (*13*) 40 (mixture *5*, 10% SiH_4), (*14*) 31 (mixture *6*, 5% SiH_4), (*15*) 40 (mixture *6*, 5% SiH_4), (*9*) 40 (pure Ar), (*10*) N_{clust} [20], and (*11*) N_{clust} [21].

Variation of the peak intensities with the stagnation pressure is common to molecular-beam measurements in the supersonic jets under condensation. The point where the monomer signal intensity versus the stagnation pressure curve deviates from linearity is usually taken for the onset of clustering (the appearance of dimers). The region near the local maximum for monomers is considered to be the region of small cluster formation. A further rise in pressure P_0 favors condensation and increases the cluster average size. Association of some of the monomers into clusters and release of the heat of condensation cause the jet to turn in the transverse direction. As a result, the gas density at the axis of the jet drops [14] and the monomer signal intensity in the molecular beam decreases. It is believed that the gas flow passes to the regime of developed condensation under such conditions [15].

Ionization of the clusters in the detector of the mass spectrometer by low-energy electrons causes their fragmentation and distorts the mass spectra [16]. Experimental [17] and theoretical [18] insights into the ionization of small Ar_n clusters (n = 9 of less) due to electron bombardment showed that, as a result of ionization of an Ar_n cluster, a positive charge is localized on the dimer and the resulting Ar_2^+–Ar_{n-2} complex disintegrates, generating Ar_2^+ dimer ions and, less probably, ions of other oligomers. Stability of the dimer is provided by its high bond energy [16]. Therefore, the sharp initial increase in the dimer peak intensity is explained by a substantial contribution of larger fragments to the signal.

As the stagnation pressure rises further, the clusters go on growing and their structure and phase state change [19]. It is likely that fragmentation of such clusters generates mainly monomer ions. Accordingly, the signals from di-, tri-, and tetramers decline, while the signal from monomers first stops decreasing and then grows. The formation stage of large clusters is characterized by a sharp increase in the monomer signal intensity and subsequently in the intensity of the signals from small clusters.

The dashed curves in Figs. 3a and 3b fit the experimental data for the argon cluster sizes, N_{clust}, taken from [20, 21]. Figures by the curves are the numerical values of the cluster sizes. Obviously, comparison of these curves with our data is valid only in the case of pure argon. The minimal stagnation pressure at which dimers can be found in a pure argon jet corresponds to an argon cluster average size equal to two, in accordance with [20]. The local maximum and minimum in the argon monomer curve correspond to an average cluster size of ≈20 and ≈100, respectively. At maximal pressure P_0 used in this study, the average size of clusters in a pure argon jet is expected to reach several thousand.

RESULTS AND DISCUSSION

Comparing the data for the methane–argon and silane–argon mixtures highlights the difference in the behavior of the monomers and clusters. It seems likely that the methane additive has no effect on the initial stage of argon condensation, unlike the monosilane additive. In particular, the Ar monomer curves for the Ar–CH_4 mixture and pure Ar virtually coincide throughout the range of parameter $P_0d^{0.8}$ (Fig. 3), while the corresponding curves for the Ar–SiH_4 mixture and pure Ar diverge considerably (Fig. 3b). The methane curve passes through a maximum at the same P_0 as the curve for the argon; in the case of monosilane, the peak shifts noticeably toward lower values of $P_0d^{0.8}$.

Monosilane clusters appear at jet densities much lower than those casing methane clustering (cf. Figs. 4a and 4b). Moreover, for small methane clusters, no extrema typical of the mixtures with monosilane are observed. However, as the stagnation pressure rises, covering the range where the monomer signal intensity grows again, the run of the curves for methane and monosilane monomers becomes almost identical. In this range, the clusters rapidly grow.

Since methane and monosilane are small additives to argon, the signals due to their monomers fade out with decreasing $P_0d^{0.8}$. The extrema in the curves for the argon and methane monomers in the binary mixture coincide, which seems to mean that small argon and methane clusters grow in parallel. We failed to detect a tangible amount of methane dimers at low let densities (low values of parameter $P_0d^{0.8}$).

In an argon–monosilane mixture, monosilane clusters form first [4, 8]. This decreases the density at the axis of the jet, and so the argon monomer signal intensity grows more slowly. Although argon clusters arise at a later stage than monosilane clusters, clustering as a whole proceeds at a higher rate.

On a further increase in parameter $P_0d^{0.8}$ and, accordingly, in the jet density, the signal intensity of both argon monomers and monomers of the additives rises abruptly for the second time (this is observed for both binary mixtures). The second abrupt increase in the monomer signal intensity is routinely explained by formation of large clusters and their disintegration due to ionization in the detector of the mass spectrometer. It is assumed that large clusters disintegrate mainly into monomers [21]. The intensity of the signal from additive monomers grows faster and even becomes equal to the argon monomer intensity in the argon–10% monosilane mixture. It is noteworthy that the curves for the additives are nearly equidistant from that for the argon. A reason for such behavior in the argon–monosilane mixture may be prevailing clustering of the additive, as a result of which the monosilane monomer signal might be expected to increase. However, as follows from our measurements, argon and methane clusters in the methane-containing mixture grow concurrently. It is likely that methane clusters in the argon–methane mixture grow faster than argon clusters. Accordingly, the intensity of the methane monomer signal in mass-spectrometric measurements grows more rapidly. On the other hand, in the monosilane-containing mixture, monosilane nuclei may be gradually covered by an argon "coat," which generates mixed fragments, such as argon–monosilane dimers and trimers [4] (Fig. 4b). The clusters formed in the methane-containing mixture may have a monoatomic structure. Certainly, other explanations cannot be ruled out, e.g., those taking into consideration complex mechanisms of disintegration of clusters with a different size, structure, and phase composition. It should also be noted that we failed to detect

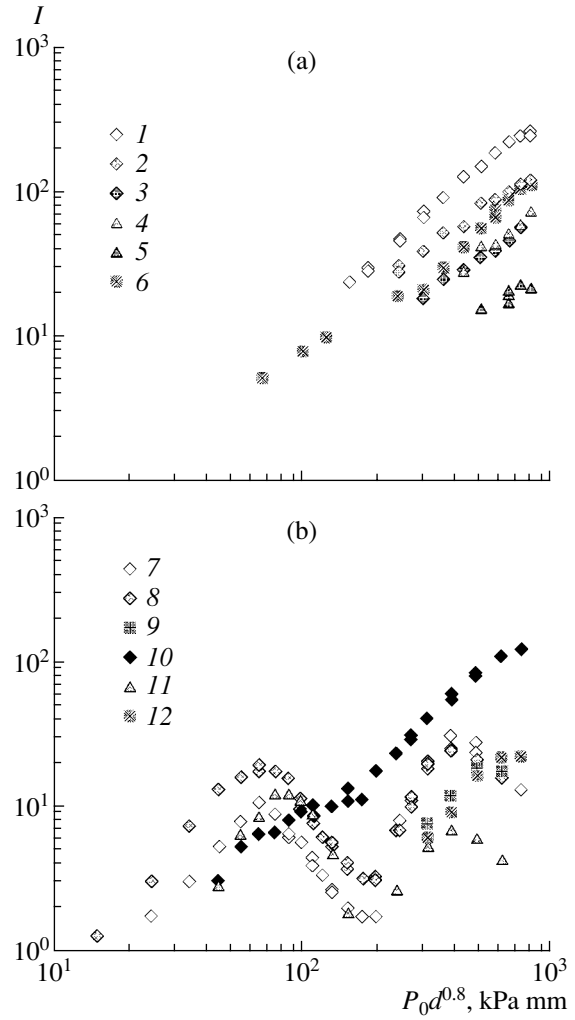

Fig. 4. Amplitudes of the cluster components in the mixtures vs. parameter $P_0d^{0.8}$. (a) 95% Ar + 5% CH_4 mixture: m/e = (*1*) 28 ($C_2H_4^+$), (*2*) 29 ($C_2H_5^+$), (*3*) 30 ($C_2H_6^+$), (*4*) 43 ($C_3H_7^+$), (*5*) 44 ($C_3H_8^+$), and (*6*) 80 (Ar_2^+); (b) 95%Ar + 5%SiH_4 mixture: m/e = (*7*) 62 ($Si_2H_6^+$), (*8*) 63 ($Si_2H_4^+$), (*9*) 70 ($ArSiH_2^+$), (*10*) 80 (Ar_2^+), (*11*) 94 ($Si_3H_{10}^+$), and (*12*) 110 ($Ar_2SiH_2^+$).

mixed clusters in the Ar–CH_4 mixture, unlike in the Ar–SiH_4 one.

The above results on the behavior of binary mixtures suggest that monosilane may also have a considerable effect on clustering in the Ar–SiH_4–CH_4 ternary mixture. Figure 5 presents the associated data for a clustered jet of the ternary mixture where methane and monosilane are small additives (2.5 vol% each) to the argon carrier. Here, as before, the relative intensities of the monomer peaks are plotted against parameter $P_0d^{0.8}$. For comparison, Fig. 5 also plots the data for the

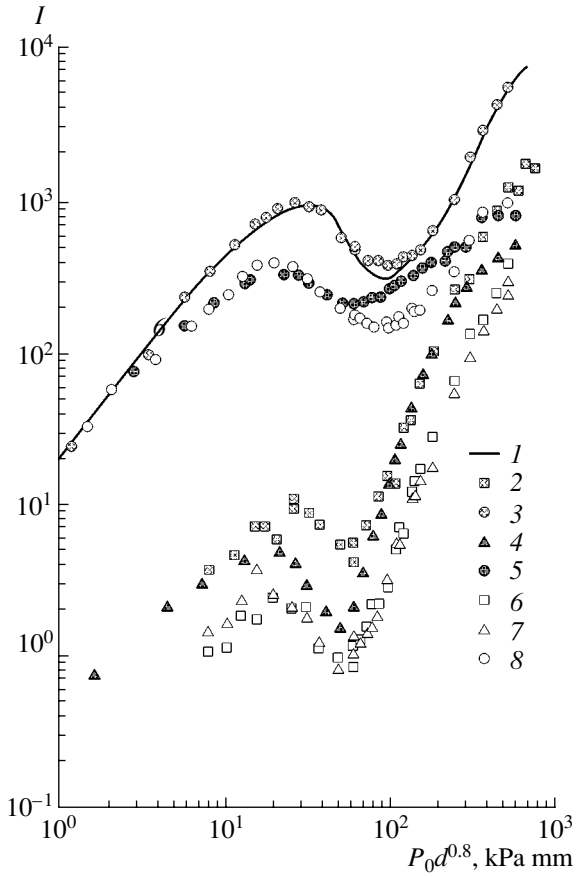

Fig. 5. Variation of the argon, methane, and monosilane monomer signals in the ternary mixture in comparison with the binary mixtures. m/e = (*1*) 40 (pure Ar), (*2*) 16 (Ar + CH_4), (*3*) 40 (Ar + CH_4), (*4*) 31 (Ar + SiH_4), (*5*) 40 (Ar + SiH_4), (*6*) 16 (Ar + CH_4 + SiH_4), (*7*) 31 (Ar + CH_4 + SiH_4), and (*8*) 40 (Ar + CH_4 + SiH_4).

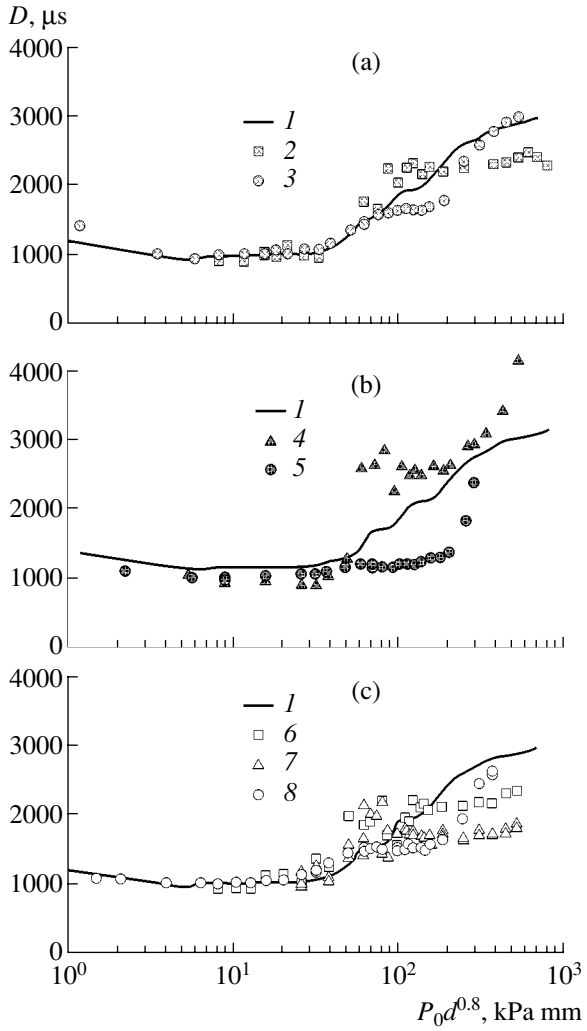

Fig. 6. Signal half-widths vs. parameter $P_0d^{0.8}$: (a) 95% Ar + 5% CH_4, (b) 95% Ar + 5% SiH_4, and (c) 95% Ar + 2.5% CH_4 + 2.5% SiH_4. m/e = (*1*) 40 (pure Ar), (*2*) 16 (Ar + CH_4), (*3*) 40 (Ar + CH_4), (*4*) 31 (Ar + SiH_4), (*5*) 40 (Ar + SiH_4), (*6*) 16 (Ar + CH_4 + SiH_4), (*7*) 31 (Ar + CH_4 + SiH_4), and (*8*) 40 (Ar + CH_4 + SiH_4).

argon monomer in pure argon (solid line) and in the mixtures (white, gray, and black circles), as well as for the monomers of methane (gray squares) and monosilane (black triangles) in the binary mixtures. As previously, the peaks at m/e = 16 and m/e = 31 are assigned to methane and monosilane, respectively. It is seen from Fig. 5 that the first argon peaks in the ternary mixture (light dots) and in the 95%Ar + 5%SiH_4 binary mixture arise at the same value of parameter $P_0d^{0.8}$, whereas the argon minimum for the ternary mixture coincides with the argon minimum in the 95%Ar + 5%CH_4 mixture. The data for methane and silane monomers are fitted (within the measurement error) by a single line, the spacing between this line and the line for the monosilane-containing binary mixture remaining the same: the extrema of these experimental lines coincide. Thus, clustering in the ternary system proceeds otherwise than in the related binary mixtures: at low jet densities (nucleation), it follows the mechanism typical of the monosilane-containing binary mixture; at higher densities (growth of clusters), it proceeds as in the methane-containing binary mixture.

Using pulsed instrumentation to generate and diagnose gas flows with condensation, one can measure not only the signal amplitude but also the rise time and half-width of the pulsed signals from monomers and small clusters of components in a mixture. It was found [22] that condensation in the flow changes these parameters. Monitoring the parameters of a pulsed jet enables one to separate out stages of condensation.

Figures 6a–6c plot half-widths D (in microseconds) of the monomer signals for the 95%Ar + 5%CH_4, 95%Ar + 5%SiH_4, and 95%Ar + 2.5%CH_4 + 2.5%SiH_4 mixtures, respectively, against $P_0d^{0.8}$. The results for pure argon are given for comparison. Here, the curves

for the mixtures deviate from that for pure argon and the data for the components diverge. Note that characteristic points in the half-width curves correlate with those in the intensity curves for the corresponding components.

An abrupt change in the half-width of the mass-spectrometric signal from only one component (especially if it is a small additive to the system) cannot be explained in terms of gas dynamics. As was mentioned above, the reason for this effect is disintegration of clusters in the detector of the mass spectrometer. We found that the half-width of the signals from small clusters changes insignificantly throughout the range of parameter $P_0d^{0.8}$. Comparing the dependences of the half-width and intensity of the signals from individual components (monomers, clusters of the additives and carrier) on $P_0d^{0.8}$ makes it possible to reveal the differences in clustering occurring in the mixtures at different stages of condensation.

The variation of the signal half-width is convenient to consider in several ranges of $P_0d^{0.8}$.

(1) At small values of $P_0d^{0.8}$, when condensation is absent in all the mixtures, the monomer signal intensities increase linearly with $P_0d^{0.8}$. Half-width D of the signals from both the argon and small additives decreases with increasing stagnation pressure only slightly, as for the case of a pure argon jet [23]. This agrees with the statement that argon, being a carrier gas, specifies the gas dynamics of the pulsed jet in all the mixtures.

(2) Early in condensation, small clusters ($n \le 20$) are detected in the jet, which means that the run of the curves becomes nonlinear and the monomer signals reach a maximum. The amplitudes of the argon monomer signals in the argon–methane mixture and in the pure argon coincide, whereas in the argon–monosilane and ternary mixtures, the argon monomer signals are lower. The half-width of the monomer signals in the mixtures, as well as in the pure argon, increases only slightly, and the value of D for monomers in the mixtures and those in the pure argon jet is the same. Hence, condensation in the argon–methane mixture starts at the same values of $P_0d^{0.8}$ as in the pure argon. However, the intensity of the argon dimer signal in this mixture is considerably lower than in the pure gas (Fig. 4a), which indicates simultaneous condensation of the argon and methane.

With monosilane added to the argon, condensation starts at lower local densities (lower values of $P_0d^{0.8}$). Small monosilane clusters appear in the flow first (Fig. 4b) and serve as centers of condensation. Monosilane clustering inhibits argon condensation. As a result, trimers and still heavier clusters of argon are absent in the jet.

Condensation in ternary mixture starts as early as in the argon–monosilane mixture, which seems to indicate monosilane-stimulated clustering in the jet.

(3) As $P_0d^{0.8}$ increases, so do the fraction of condensate and cluster mean size. At the same time, the intensity of the monomer signals in all the gas mixtures declines. Fragmentation in the pure argon leads to an increase in the monomer signal half-width in proportion to the mean size of the clusters.

In the argon–methane mixture, the signal intensities increase concurrent with a decrease in the half-width of the signals from the carrier gas and additive, indicating simultaneous condensation of both gases. The lack of signals from methane dimers and trimers may be explained by a low formation probability of small clusters.

At this stage of condensation, argon condensation in the argon–monosilane mixture ends in the formation of dimers, whereas monosilane clusters continue to grow. This is indicated, first, by the considerable drop of the additive signal intensity compared with the argon intensity (Fig. 1) and, second, by the fact that the half-width of the argon monomer signal first slightly increases and then remains constant, whereas the half-width of the monosilane monomer signal increases by a factor of 2.5 (Fig. 6b).

In the ternary mixture, the equal decrease in the monomer signal amplitudes synchronously with the increase in the half-width of the signals may be explained by jointly condensing all the components with the formation of multicomponent clusters.

(4) At the stage of developed condensation in pure gases, the mass fraction of the condensate stops growing, unlike the cluster average size. Restructuring of clusters; modification of their phase state; and, eventually, the change in the fragmentation mechanism cause the cluster signal amplitude to diminish and the monomer signal amplitude to rise.

The abrupt increase in the amplitude and half-width of the methane monomer signal in the argon–methane mixture testifies that the condensation of the additive proceeds at a higher rate than that of the carrier. As the stagnation pressure (hence, the jet density) rises, a major part of the methane turns out to be in the bound state. As a consequence, the half-width of the monomer signals does not increase, although their amplitudes continue growing. On a further increase in the density and persisting supersaturation of the medium, condensation continues owing to the argon: both the amplitude and half-width of its monomer signal increase.

In the argon–monosilane mixture, the intense condensation of the additive continues suppressing the condensation of the carrier until almost all the additive is in the bound state. As the stagnation pressure (density of the jet) increases, the intense condensation of the argon begins and argon atoms deposit on clusters consisting of monosilane molecules. Upon disintegration, such mixed clusters form argon–silane complexes [4] and the half-width of the argon monomer signal increase abruptly.

In the ternary mixture, the condensation of the carrier is also retarded compared with that in the pure argon, while to a smaller extent than in the argon–monosilane mixture. So, we can speak of concurrent condensation of all the three components. The cluster size (half-width of the monomer signals) saturates as early as in the argon–monosilane mixture. However, the half-width of the signals is considerably smaller than in the binary mixtures, which is an indication of concurrent condensation. This process is bound to form mixed organosilicon complexes. The peaks from cluster fragments with m/e = 46, 54, 69, and 87 that were found in the ternary mixture at high values of parameter $P_0d^{0.8}$ (stagnation pressure) but were absent in the binary mixtures may be identified as methane–silane fragments of large clusters.

ACKNOWLEDGMENTS

This work was supported by the Ministry of Science and Technical Policy of the Russian Federation.

REFERENCES

1. R. G. Sharafutdinov, A. V. Skrinnikov, A. V. Parakhnevich, *et al.*, J. Appl. Phys. **79**, 7274 (1996).
2. R. W. Randall, J. B. Ibbotson, and B. J. Howard, J. Chem. Phys. **100**, 7051 (1994).
3. A. Desalvo, F. Giorgis, C. F. Pirri, *et al.*, J. Appl. Phys. **81**, 7973 (1997).
4. R. G. Sharafutdinov, A. E. Zarvin, N. G. Korobeishchikov, *et al.*, Pis'ma Zh. Tekh. Fiz. **25** (21), 47 (1999) [Tech. Phys. Lett. **25**, 865 (1999)].
5. A. E. Zarvin, N. G. Korobeishchikov, V. Zh. Madirbaev, *et al.*, Zh. Tekh. Fiz. **71** (4), 141 (2001) [Tech. Phys. **46**, 503 (2001)].
6. A. E. Zarvin, N. G. Korobeishchikov, V. Zh. Madirbaev, *et al.*, Prib. Tekh. Éksp., No. 5, 64 (2000).
7. A. E. Zarvin, N. G. Korobeishchikov, V. Zh. Madirbaev, *et al.*, Teplofiz. Aeromekh. **8**, 427 (2001).
8. G. G. Gartvich, A. E. Zarvin, V. V. Kalyada, *et al.*, Prib. Tekh. Éksp., No. 5, 160 (1996).
9. N. G. Korobeĭshchikov, A. E. Zarvin, V. Zh. Madirbaev, *et al.*, Plasma Chem. Plasma Process. **25** (2005) (in press).
10. E. Krishnakumar and S. K. Srivastava, Contrib. Plasma Phys. **35**, 395 (1995).
11. R. Basner, M. Schmidt, V. Tarnovsky, *et al.*, Int. J. Mass Spectrom. Ion Phys. **171**, 83 (1997).
12. A. Ding, R. A. Cassidy, L. S. Cordis, *et al.*, J. Chem. Phys. **83**, 3426 (1985).
13. *National Institute of Standards and Technology: NIST Chemistry WebBook*, http://webbook.nist.gov/chemistry/.
14. V. Zh. Madirbaev, S. A. Palopezhentsev, V. N. Yarygin, *et al.*, in *Proceedings of the 15th International Symposium on Rarefied Gas Dynamics, Grado, 1986*, Vol. 2, pp. 179–187.
15. S. Ya. Khmel, R. G. Sharafutdinov, A. E. Belikov, *et al.*, Preprint No. 271 (Institute of Thermal Physics, Novosibirsk, 1994).
16. M. L. Aleksandrov and Yu. S. Kusner, *Gasdynamic Molecular, Ion, and Clustered Beams* (Nauka, Moscow, 1989) [in Russian].
17. U. Buck and H. Meyer, J. Chem. Phys. **84**, 4854 (1986).
18. A. Bastida, N. Halberstadt, J. A. Beswick, *et al.*, Chem. Phys. Lett. **249**, 1 (1996).
19. J. Farges, M. F. de Feraudy, B. Raoult, *et al.*, J. Chem. Phys. **84**, 3491 (1986).
20. U. Buck and R. Krohne, J. Chem. Phys. **105**, 5408 (1996).
21. R. Karnbach, M. Joppien, J. Stapelfeldt, *et al.*, Rev. Sci. Instrum. **64**, 2838 (1993).
22. A. E. Zarvin, N. G. Korobeishchikov, V. Zh. Madirbaev, *et al.*, Pis'ma Zh. Tekh. Fiz. **26** (22), 21 (2000) [Tech. Phys. Lett. **26**, 989 (2000)].
23. N. G. Korobeishchikov, A. E. Zarvin, and V. Zh. Madirbaev, Zh. Tekh. Fiz. **74** (8), 21 (2004) [Tech. Phys. **49**, 973 (2004)].

Translated by M. Lebedev

Technical Physics, Vol. 50, No. 11, 2005, pp. 1451–1457. Translated from Zhurnal Tekhnicheskoĭ Fiziki, Vol. 75, No. 11, 2005, pp. 59–64.

GAS DISCHARGES, PLASMA

Calculation of the Parameters of a High-Current Reflective Discharge with a Hot Cathode

L. A. Zjulkova, A. V. Kozyrev, and D. I. Proskurovsky

Institute of High-Current Electronics, Siberian Division, Russian Academy of Sciences, Akademicheskiĭ pr. 4, Tomsk, 634055 Russia

e-mail: kozyrev@to.hcei.tsc.ru

Received July 26, 2004

Abstract—A physical model of a self-sustaining reflective discharge is formulated based on the continuity equation for the electron flux and the equation of energy balance on the hot cathode. The model allows one to calculate the current-voltage characteristic of a high current reflective discharge with a hot cathode in a wide range of magnetic fields, discharge cell dimensions, and cathode material work functions. An advantage of the model is that it is capable of describing the ordinary operating mode of a reflective discharge with cold cathodes as a limiting case. The model predicts the existence of two discharge operating modes with thermionic electron emission on the cathode: a low-voltage mode with a high current density and a high-voltage mode with a significantly lower current density. It is shown that the low-voltage operating mode can occur in a wide range of the discharge currents, while the discharge voltage can be substantially reduced by using a cathode material with a low work function. © *2005 Pleiades Publishing, Inc.*

INTRODUCTION

The reflective discharge, also known as the Penning discharge or the Phillips discharge, is an axisymmetric low-pressure discharge operating in crossed $\mathbf{E} \times \mathbf{B}$ fields (see [1]). This type of discharge has long been used in charged particle generators [2–5]), ion pumps [6, 7], and manometers [1]. An important advantage of this discharge is the high efficiency of gas ionization in a wide range of the gas pressures, magnetic fields, and discharge cell dimensions. An analysis of the results obtained in [2–12] show that the high-voltage low-current mode of a low-pressure ($p \le 10^{-3}$ Torr) Penning discharge is of primary research interest. However, the high operating voltages make this mode of limited utility for high-purity technologies because of the erosion of the cathode material under ion bombardment. In this respect, the low-voltage mode of a reflective discharge with a hot cathode is more advantageous [2, 5, 12]. In this case, however, the discharge is non-self-sustaining and the presence of the cathode heating system significantly complicates the design of the discharge cell. Therefore, a self-sustaining reflective discharge with a self-heated cathode seems to be more promising [4, 5, 12, 13]. In this case, the heat-insulated cathode is heated due to ion bombardment rather than by an external heat source. Since this type of discharge requires intense heat release on the cathode, it can operate only at relatively high currents, which can only be provided at relatively high gas pressures. It can be expected that the structure and operating mechanism of such a discharge, which will be further referred to as a high-current reflective discharge with a hot-cathode, would substantially differ from the low-pressure Penning discharge. In recent years, sources of charged [4] and neutral [13] particles have been created based on a high-current reflective discharge with a hot cathode. Since this type of discharge can be efficiently used in advanced technologies, it is desirable to develop a general theory that would allow one to calculate the main characteristics of the discharge cell in a wide range of geometrical and electrophysical parameters.

The interrelation between the ionization and recombination processes in a discharge in crossed $\mathbf{E} \times \mathbf{B}$ fields, as well as conditions that are necessary to sustain such a discharge, is generally described by the analytic model proposed in [14]. However, since the model is one-dimensional, the results obtained in [14] cannot be directly applied to real discharge cells, which are typically axisymmetric. For some reasons, it is impossible to calculate the current-voltage (I–V) characteristic of a real reflective discharge with sufficient accuracy. First, it is rather difficult to calculate the gas ionization rate and the motion of charged particles in crossed fields. Second, although the linear model of gas ionization and charged particle drift makes it possible to fairly exactly evaluate the discharge voltage, it does not allow one to calculate the discharge current without incorporating the external circuit parameters in the model. The incorporation of these parameters makes the problem too specific, so it becomes impossible to analyze the general features of the discharge. It was shown in [13] that the introduction of a central self-heated rod electrode allows one to calculate the parameters of a real reflective discharge with sufficient accuracy. On the one

1063-7842/05/5011-1451$26.00 © 2005 Pleiades Publishing, Inc.

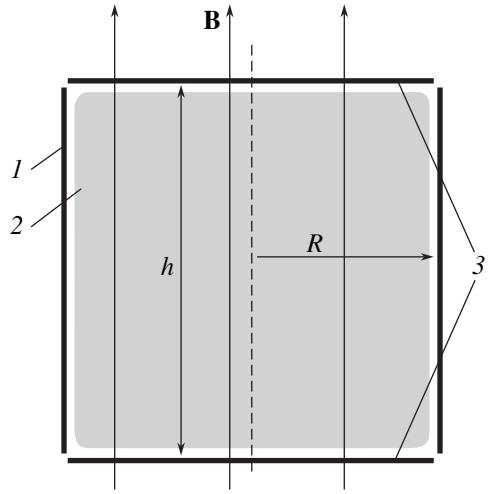

Fig. 1. Sketch of a discharge cell: (*1*) cylindrical anode, (*2*) gas-discharge plasma, and (*3*) disk cathodes.

hand, the heated element complicates the calculation of the discharge parameters and introduces a significant nonlinearity in the set of equations describing the discharge. On the other hand, however, the presence of such an element relates the theoretical model to the absolute values of the temperature and emission current of the hot element. In the present study, it is shown that the method proposed in [13] allows one to calculate the discharge parameters in crossed $\mathbf{E} \times \mathbf{B}$ fields not only when the central rod is used as a hot cathode, but also when the hot cathode is one of the disk cathodes of a reflective discharge.

PHYSICAL MODEL OF A HIGH-CURRENT REFLECTIVE DISCHARGE

Let us consider an axisymmetric Penning discharge cell (of height h) consisting of a hollow cylindrical anode of radius R and two plane-parallel disk cathodes biased by the same negative potential relative to the cathode (see Fig. 1). One of the disk cathodes is assumed to be heat-insulated; due to its strong heating, it can operate in the thermionic mode. The second disk cathode is assumed to be relatively cold, so its thermal emission current can be ignored. The discharge cell is in a uniform external magnetic field, whose field lines are parallel to the symmetry axis of the system.

The main parameters of such a discharge cell can be calculated using the following simplified discharge model.

(i) We consider only a steady-state high-current mode in which almost the entire voltage drop occurs in a thin cathode sheath. The main discharge space is occupied by a quasineutral plasma, which will be further referred to as a discharge column. The discharge column is separated from the electrodes by relatively narrow space-charge sheaths. Such a simplification of the discharge structure limits the model applicability to the case of a relatively high plasma density.

(ii) It is assumed that the plasma column is weakly ionized and the density of the neutral gas particles is independent of the discharge current. This assumption limits the charged particle density from above by a value comparable to the neutral particle density.

(iii) In the cathode sheath, the flux of fast electrons with energies approximately corresponding to the discharge voltage is formed. This electron flux transfers the energy supplied by the power source to the plasma and provides the necessary level of gas ionization in the discharge column.

(iv) Gas ionization by the thermal plasma electrons is ignored. This is justified when the discharge voltage greatly exceeds the gas ionization potential [4]. The role of the plasma electrons in this case is reduced to the transport of the electric current to the anode across the magnetic field.

(v) It is assumed that the ions in the plasma column are not magnetized and the ion current is distributed uniformly over the entire cathode surface. Moreover, the plasma nonuniformity along the height is ignored. Such an averaging over height significantly simplifies calculations and, thus, allows one to efficiently analyze the general features of the discharge.

(vi) In contrast, the electrons are assumed to be highly magnetized, so that their diffusion coefficient across the magnetic field is proportional to the transport frequency of electron–atom collisions. This approximation imposes constraints on both the gas pressure and the magnetic field.

(vii) It is assumed that the temperature of the heat-insulated cathode is determined by the power balance between the energy release due to ion bombardment and radiative heat transfer from the surface. The other channels of energy removal are disregarded.

CALCULATION OF THE DISCHARGE *I–V* CHARACTERISTIC

The discharge *I–V* characteristic can be calculated in the same way as in [13]. The flux of fast electrons j_f across the magnetic field in the discharge column is diffusive in character and is described by [14]

$$j_f(r) = -D_f \frac{dn_f(r)}{dr}. \quad (1)$$

Here, $n_f(r)$ is the radial profile of the fast electron density and D_f is the classical cross-field diffusion coefficient of fast electrons. Under the above assumptions,

this coefficient can be estimated as

$$D_f \cong \left\langle \frac{r_{Le}^2}{3\tau_a} \right\rangle \cong \left\langle \frac{2}{3\tau_i}\left(\frac{mv_f}{eB}\right)^2 \right\rangle \cong \frac{4}{3}\frac{mU_c}{e\tau_i B^2}, \quad (2)$$

where e and m are the charge and mass of an electron, B is the magnetic induction, v_f is the mean velocity of the fast electrons in the discharge column, r_{Le} is the mean electron Larmor radius, U_c is the cathode drop (approximately equal to the discharge voltage), τ_i is the mean time between ionizing collisions of the fast electrons with gas particles, and τ_a is the electron–atom collisional time.

For electrons with energies of about a few hundred electronvolts, the cross section for electron-impact ionization of atoms is comparable to the electron transport cross section; therefore, in Eq. (2), we assume $\tau_a \cong \tau_i/2$.

We consider a steady-state influx of fast electrons from the cathode surfaces into the plasma due to both ion–electron emission (γ processes) ($j_{f\gamma}$ flux) and thermionic emission (j_{ft} flux). These electrons then "disappear" due to the loss of their energy over a characteristic time τ_f. Therefore, taking into account the axial symmetry of the problem, the time-independent continuity equation in cylindrical coordinates can be written as

$$\frac{1}{r}\frac{d(rj_f(r))}{dr} = \frac{2j_{f\gamma} + j_{ft}}{h} - \frac{n_f(r)}{\tau_f}. \quad (3)$$

Physically, τ_f is the time during which a fast electron with an initial energy E_0 becomes slow, losing its energy in collisions with neutral particles and producing on average $\mu = E_0/E_i$ plasma electrons. Here, E_i is the mean energy spent on the production of one electron–ion pair, which is a characteristic value of a given gas. Let us assume that $E_0 \cong eU_c$; then, we have $\tau_f = (eU_c/E_i)\tau_i$.

In solving differential equation (3), it is convenient to introduce the characteristic diffusion length λ, which determines the distance covered by a fast electron with a characteristic kinetic energy eU_c across the magnetic field during the time τ_f,

$$\lambda(U_c, B) = \sqrt{D_f\tau_f} = \sqrt{\frac{4m}{3E_i}}\frac{U_c}{B}. \quad (4)$$

In our model, the fast-electron diffusion length λ is independent of the gas pressure [13, 14]. If we take into account that the electrons are magnetized incompletely, then the parameter λ will decrease slightly with increasing gas pressure.

Introducing the dimensionless coordinate $\rho = r/\lambda$ and substituting Eq. (1) into Eq. (3), we obtain the equation for the radial profile of the fast-electron density,

$$\frac{d^2n_f(\rho)}{d\rho^2} + \frac{1}{\rho}\frac{dn_f(\rho)}{d\rho} - n_f(\rho) = -\frac{\tau_f}{h}(2j_{f\gamma} + j_{ft}). \quad (5)$$

If we impose the following boundary conditions at the anode and the discharge axis,

$$n_f(r = R + r_{Le}) = 0, \quad \left.\frac{dn_f}{dr}\right|_{r=0} = 0, \quad (6)$$

then the solution to Eq. (5) is

$$n_f(\rho) = \frac{\tau_f}{h}(2j_{f\gamma} + j_{ft})\left(1 - \frac{I_0(\rho)}{I_0(\rho_g)}\right), \quad (7)$$

where $I_0(\rho)$ is the zero-order modified Bessel function and $\rho_g = (R + r_{Le})/\lambda$.

Let us write out the steady-state continuity equation for the flux j_s of slow electrons, assuming that they are produced only due to gas ionization by the fast electrons and are lost only on the anode,

$$\frac{1}{\rho}\frac{d(\rho j_s(\rho))}{d\rho} = (\mu + 1)\lambda\frac{n_f(\rho)}{\tau_f}. \quad (8)$$

We introduce the following notation for the radial dependences of the currents: $J_s(\rho) = 2\pi h\rho\lambda e j_s(\rho)$ is the plasma electron current, $J_{f\gamma}(\rho) = \pi\rho^2\lambda^2 e j_{f\gamma}$ is the current of the fast γ-electrons from the cathode, and $J_{ft}(\rho) = \pi\rho^2\lambda^2 e j_{ft}$ is the thermionic current of the fast electrons from the hot cathode.

Integrating Eq. (8) with allowance for the natural boundary condition $J_s(0) = 0$, we obtain the expression for the radial dependence of the plasma electron current,

$$J_s(\rho) = 2(\mu + 1)[2J_{f\gamma}(\rho) + J_{ft}(\rho)]\left[\frac{1}{2} - \frac{I_1(\rho)}{\rho I_0(\rho_g)}\right], \quad (9)$$

where $I_0(x)$ and $I_1(x)$ are the zero- and first-order modified Bessel functions, respectively. Analogously, integrating Eq. (3) in dimensionless variables with the boundary conditions $J_f(0) = 0$, we obtain the expression for the fast-electron current $J_f(\rho)$,

$$J_f(\rho) = \frac{\lambda}{h}[2J_{f\gamma}(\rho) + J_{ft}(\rho)]\frac{I_1(\rho)}{I_0(\rho_g)}. \quad (10)$$

The total electron current in the anode circuit, $J_a = J(\rho_a = R/\lambda)$, can be obtained by adding currents (9) and (10). Assuming that the ion flux onto the cathode is uniform, the net current in the cathode circuit J_c with allowance for γ-emission and thermionic emission can be written as $J_c = J_{em} + J_{ic}(1 + \gamma)$, where J_{ic} is the total current at the cathode and J_{em} is the total thermionic

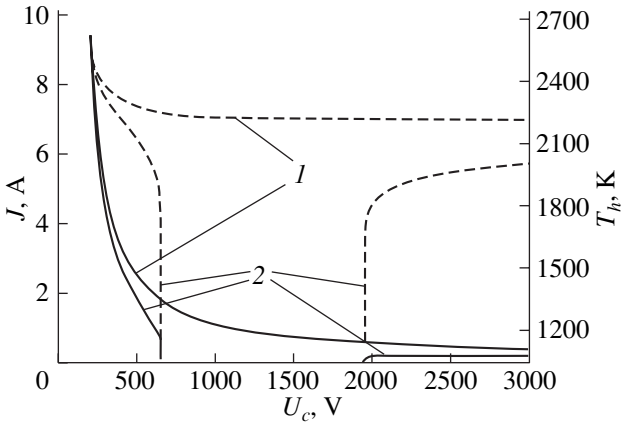

Fig. 2. Calculated parameters of a reflective discharge with a hot tungsten cathode at two different values of the magnetic induction for $h = 2$ cm, $R = 1$ cm, $\gamma = 0.1$, and $B_{cr} \sim 0.088$ T: (*1*) $B = 0.05$ T $< B_{cr}$ and (*2*) $B = 0.1$ T $> B_{cr}$. The solid lines show the *I–V* characteristics, while the dashed lines show the hot cathode temperature as a function of the discharge voltage.

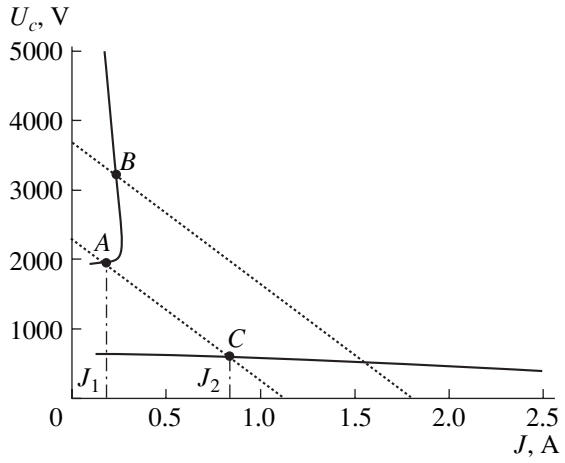

Fig. 3. Concerning the stability analysis of the operating modes of a reflective discharge with a hot tungsten cathode for $h = 2$ cm, $R = 1$ cm, $\gamma = 0.1$, and $B = 0.1$ T.

current from the hot cathode. Equating J_a to J_c, we obtain the self-sustainment condition,

$$\left[\frac{J_{em}}{J_{ic}} + \gamma\right]\left[\mu + 2\left(\frac{\lambda}{2h} - \frac{\mu + 1}{\rho_a}\right)\frac{I_1(\rho_a)}{I_0(\rho_g)}\right] = 1. \qquad (11)$$

This equation also determines the ratio of the thermionic current to the ion current at the cathode as a function of the cell size, magnetic induction, and discharge operation voltage, which enter into expression (4) for the length λ.

Assuming that thermal radiation escapes freely from the hot cathode and that the energy of the ions incident onto the hot cathode is completely dissipated in it, the power balance equation can be written as

$$P_{\text{rad}} = S_{h0}\varepsilon_T\sigma T_h^4 = 1/2eU_cJ_{ic}. \qquad (12)$$

Here, σ is the Stephan–Boltzman constant, $\varepsilon_T \approx 0.5$ is the emissivity factor of the hot cathode, and S_{h0} is the area of the hot cathode radiating surface. It is also taken into account that only one-half of the ion current reaches the hot cathode.

From Eq. (12), we find the temperature of the hot cathode,

$$T_h = \left(\frac{eU_cJ_{ic}}{2S_{h0}\varepsilon_T\sigma}\right)^{1/4}, \qquad (13)$$

and the thermionic current,

$$J_{em} = \pi R^2 A_0 T_h^2 \exp(-\varphi_h/kT_h), \qquad (14)$$

where φ_h is the work function of the hot cathode material and $A_0 \approx 100$ A/cm^2 K^2.

In fact, Eqs. (13) and (14) determine the thermionic current as a function of the ion current at the cathode. Expression (14), along with equality (11), relates these currents to one another. The solution of this set of two equations with two unknowns allows one to find both the thermionic current and the ion current at the cathode.

Having determined the total ion current at the cathode, we can find the current of γ-electrons from the cathodes, $J_{f\gamma} = \gamma J_{ic}$, and, finally, the total discharge current,

$$J_{\text{tot}} = J_{em} + (1 + \gamma)J_{ic}. \qquad (15)$$

Thus, we can find the *I–V* characteristic of a discharge cell with given parameters of the cathode material. Because of the assumptions adopted in our model, the gas density dropped out from all the above equations; therefore, the calculated *I–V* characteristic is independent of the gas pressure. Such a dependence can appear, if we account for, e.g., the relation between the mean energy E_i spent on the production of one ion-electron pair and the actual kinetics of the ionization process.

RESULTS AND DISCUSSION

Two Modes of a High-Current Reflective Discharge with a Hot Cathode

An analysis of solutions to the above set of equations shows that there is a certain critical value of the magnetic induction, B_{cr}, that determines the voltage range within which steady-state solutions for the discharge current exist. It was found that, at $B < B_{cr}$, the solution for the current exists at any voltage in the thermionic mode, while, at $B > B_{cr}$, a voltage range appears within which there are no steady-state solutions for the current (the "forbidden" zone). Figure 2 shows two typ-

ical dependences of the discharge current and hot cathode temperature on the voltage for two different ratios between B and B_{cr}. It can be seen that, at $B > B_{cr}$, the I–V characteristic consists of two branches. The first branch is characterized by high currents and low voltages, whereas the second corresponds to high voltages and substantially lower currents. Both branches, however, correspond to high cathode temperatures.

Let us analyze the stability of the two steady-state operating modes of a reflective discharge in the case of $B > B_{cr}$. The solid lines in Fig. 3 show (in the conventional electrophysics representation) the two branches of the I–V characteristic that correspond to curves *2* in Fig. 2. The load curves of the discharge power source for two values of the ballast resistance are also shown in the figure by the dashed lines. Let us first consider the load curve passing through points A and C of the I–V characteristic. It can be seen that both these points correspond to stable operating modes. Indeed, if the discharge current increases, e.g., as a result of a random fluctuation, the discharge voltage will become slightly lower than that corresponding to the I–V characteristic. In contrast, if the discharge current decreases, the voltage will be slightly higher than that required to sustain the discharge. In both cases, the current fluctuation will be suppressed and the discharge current will be stably maintained at a level corresponding to the point where the load curve intersects the I–V characteristic. The situation is, however, quite different when the intersection point of the I–V characteristic and the load curve (Fig. 3, point B) lies on the segment corresponding to a negative differential resistance of the discharge. Similar considerations show that, in this case, steady-state modes corresponding to the high-voltage branch will be unstable: a small current fluctuation would result in the discharge extinction. Therefore, on the high-voltage branch of the I–V characteristic, only those points that lie in the vicinity of the minimum operating voltage correspond to stable modes, while the entire low-voltage branch is stable.

Reflective Discharge with Cold Cathodes as a Limiting Case

The reasons for the appearance of the above forbidden zone are easier to understand by considering how the discharge current and the hot cathode temperature vary with varying discharge voltage at a given value of the magnetic induction. A specific feature of the solutions obtained is that the cathode temperature and the discharge current decrease rapidly to zero as the discharge voltage approaches the boundary of the forbidden zone. This allows one to interpret the boundaries of the forbidden zone as the ignition voltage of a Penning discharge with cold cathodes at a given value of the magnetic induction.

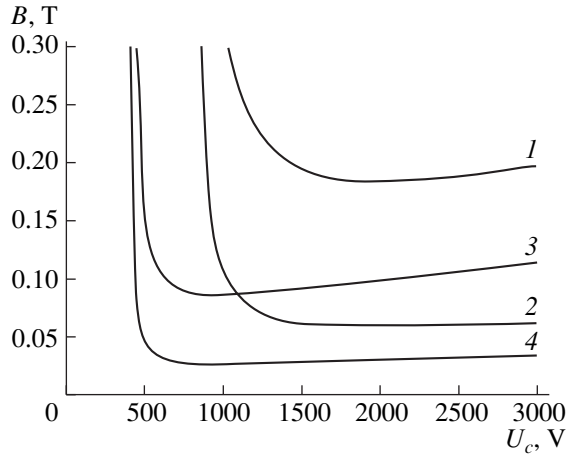

Fig. 4. Operating voltage of a reflex discharge with a cold cathode vs. magnetic induction for h = 1 cm and different values of the discharge cell radius R and the coefficient γ: (*1*, *2*) γ = 0.05 and R = 1 and 3 cm, respectively, and (*3*, *4*) γ = 0.1 and R = 1 and 3 cm, respectively.

The dependence $B(U)$ for a reflective discharge with cold cathodes can easily be obtained from Eq. (11), in which it is necessary to set $J_{em} = 0$. Figure 4 presents several examples of such curves for a given fast-electron energy required for one ionization event (E_i = 40 eV). The positions of the curves depend primarily on the discharge cell geometry and the coefficient γ. Obviously, these curves correspond to the low-current mode of a reflective discharge with cold cathodes. This mode is determined not only by the discharge processes, but also the parameters of the external circuit and power source. Similar curves characterizing the region of existence of a low-pressure Penning discharge are well known [11, 15–18]; in the one-dimensional version of a similar model, they were calculated in [14].

Low-Voltage Mode of a Reflective Discharge with a Hot Cathode

In the (B, U) plane (Fig. 4), the domain of existence of a steady-state reflective discharge with a hot cathode is bounded from above by a curve $B(U)$, whose minimum corresponds to the critical value of the magnetic induction, B_{cr}.

From I–V characteristic *1* in Fig. 2, it can be seen that, at $B < B_{cr}$, a steady-state discharge with a hot cathode can operate in a simply connected domain of voltages. This mode can be efficiently used in devices intended to operate in a wide current range [4, 13]. The I–V characteristic of a reflective discharge with a hot cathode has a negative differential resistance, which is typical of arc discharges. Figure 5 shows an example of the calculated structure of a high-current discharge with

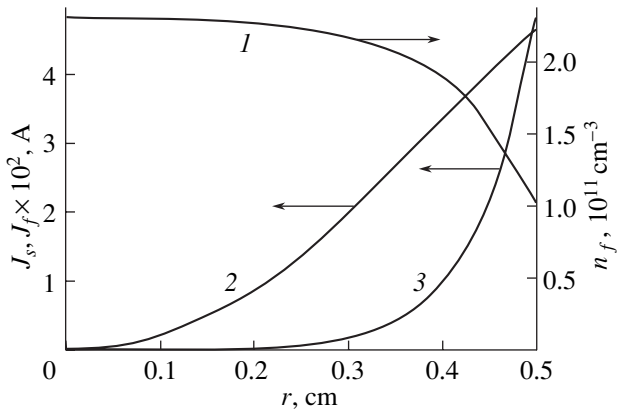

Fig. 5. Radial profiles of (*1*) the fast-electron density $n_f(r)$, (*2*) the slow-electron current $J_s(r)$, and (*3*) the fast-electron current $J_f(r)$ for U_c = 150 V, φ_h = 4.54 eV (tungsten), γ = 0.05, B = 0.08 T, h = 1 cm, and R = 0.5 cm.

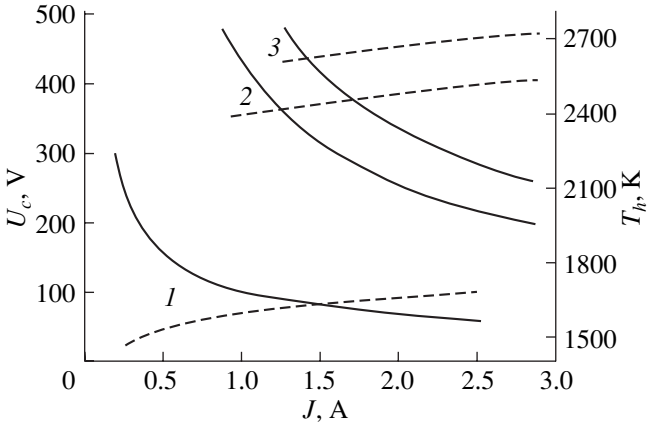

Fig. 6. Calculated *I–V* characteristics (solid lines) and the corresponding temperatures of the self-heated electrode (dashed lines) for a reflective discharge with a hot cathode made of different materials for h = 1 cm, R = 0.5 cm, and B = 0.08 T: (*1*) LaB_6 (φ_h = 2.8 eV), (*2*) W (φ_h = 4.5 eV), and (*3*) Re (φ_h = 5.0 eV).

a hot cathode: the radial distributions of the fast-electron density and the current in the electrode gap.

To illustrate the possibility of reducing the discharge voltage, Fig. 6 presents examples of the calculated *I–V* characteristics of a discharge cell with a self-heated cathode for different work functions. These characteristics indicate that the discharge voltage substantially decreases with decreasing hot-cathode work function, as was previously observed experimentally (see, e.g. [4]). A decrease in the discharge voltage below 100 V usually results in a sharp decrease in the cathode erosion rate; this extends the cathode lifetime and substantially reduces the amount of impurities emerging from the plasma source.

Applicability Limits of the Model

Let us determine the applicability limits of our model with respect to the gas pressure. Since the plasma column is assumed to be weakly ionized, the density of neutral particles should be much higher than that of charged particles. The lower estimate for the electron density can be obtained from the electron density near the anode, which in turn can be estimated from the discharge current I, the anode surface area $2\pi hR$, and the thermal velocity of plasma electrons V_{Te}. The upper estimate for the atomic density can be obtained from the condition that the electrons are magnetized. The electron–atom collision frequency ν_{ea} can be estimated from the transport collision cross section σ_{ea} and the electron thermal velocity V_{Te}. As a result, we obtain the range of gas densities within which our model is valid: $2I/\pi h\mathrm{Re}V_{Te} \ll n_a \ll eB/m\sigma_{ea}V_{Te}$. Thus, for the discharge parameters from Fig. 5, we have $4 \times 10^{11} \ll n_a \ll 2 \times 10^{17}$ cm^{-3}.

In addition, it is necessary that the thickness of the electrode sheaths be much less than the discharge cell dimensions. The cathode sheath thickness d_c can be estimated from the 3/2 law. As a result, we obtain the limitations on the cell dimensions,

$$R, h \gg d_c \cong \left(\frac{2e}{m}\right)^{1/4} \sqrt{\frac{4\varepsilon_0}{9}\frac{2\pi R^2}{I}U_c^{3/2}} \sim 5 \times 10^{-2}\ \text{cm}.$$

CONCLUSIONS

We have calculated the *I–V* characteristic of a high current reflective discharge with a hot cathode and the corresponding temperature of the self-heated electrode. The domain of existence of steady-state modes of a reflective discharge in the (B, U) plane has been determined. It is shown that, at sufficiently strong magnetic fields, two modes of a Penning discharge can exist: high-current and a high-voltage ones. At sufficiently weak magnetic fields, the reflective discharge can operate only in the thermionic mode. The model proposed allows one to optimize the design of charged- and neutral-particle plasma sources based on this type of discharge.

ACKNOWLEDGMENTS

We thank V.A. Kagadeĭ and G.E. Ozur for interesting and helpful discussions.

REFERENCES

1. F. M. Penning, Physica **4** (4), 71 (1937).
2. M. D. Gabovich, *Physics and Technology of Ion Plasma Sources* (Atomizdat, Moscow, 1972) [in Russian].
3. Yu. E. Kreĭndel', *Plasma Sources of Electrons* (Atomizdat, Moscow, 1977) [in Russian].

4. A. P. Semenov, in *Scattering Ion Beams: Generation and Application*, Ed. by G. A. Mesyats (Izd. BNTs SO RAN, Ulan-Ude, 1999) [in Russian].
5. B. Wolf, *Handbook of Ion Sources* (CRC, Boca Raton, 1995).
6. E. M. Reĭkhrudel', G. V. Smirnitskaya, and A. I. Borisenko, Radiotekh. Élektron. (Moscow) **2**, 253 (1956).
7. O. K. Kurbatov, Zh. Tekh. Fiz. **36**, 1665 (1966) [Sov. Phys. Tech. Phys. **11**, 1240 (1966)].
8. R. L. Jepsen, J. Appl. Phys. **32**, 2619 (1961).
9. W. Knauer, J. Appl. Phys. **33**, 2093 (1962).
10. Yu. Kreĭndel' and A. S. Ionov, Zh. Tekh. Fiz. **34**, 1199 (1964) [Sov. Phys. Tech. Phys. **9**, 930 (1964)].
11. E. M. Reĭkhrudel', A. V. Chernetskiĭ, V. V. Mikhnevich, *et al.*, Zh. Tekh. Fiz. **22**, 1945 (1952).
12. A. Guthrie and R. K. Wakerling, *The Characteristics of Electrical Discharges in Magnetic Fields* (McGraw-Hill, New York, 1949).
13. V. A. Kagadeĭ, A. V. Kozyrev, I. V. Osipov, and D. I. Proskurovskiy, Zh. Tekh. Fiz. **71** (3), 22 (2001) [Tech. Phys. **46**, 292 (2001)].
14. S. P. Nikulin, Zh. Tekh. Fiz. **68** (7), 56 (1998) [Tech. Phys. **43**, 795 (1998)].
15. L. A. Zjulkova, A. V. Kozyrev, and D. I. Proskurovskiy, Pis'ma Zh. Tekh. Fiz. **30** (16), 19 (2004) [Tech. Phys. Lett. **30**, 672 (2004)].
16. E. M. Reĭkhrudel' and E. P. Sheretov, Zh. Tekh. Fiz. **35**, 1255 (1965) [Sov. Phys. Tech. Phys. **10**, 972 (1965)].
17. E. M. Reĭkhrudel', G. V. Smirnitskaya, and G. A. Egiazaryan, Zh. Tekh. Fiz. **35**, 130 (1965) [Sov. Phys. Tech. Phys. **10** (1965)].
18. E. M. Oks, A. A. Chagin, and P. M. Shchanin, in *Proceedings of the 1st All-Union Workshop on Emission Plasma Electronics, Ulan-Ude, 1991*, pp. 18–23.

Translated by B. Chernyavskiĭ

Technical Physics, Vol. 50, No. 11, 2005, pp. 1458–1461. Translated from Zhurnal Tekhnicheskoĭ Fiziki, Vol. 75, No. 11, 2005, pp. 65–68.

SOLIDS

X-ray Diffraction Analysis of C_{60} Fullerene Powder and Fullerene Soot

B. M. Ginzburg, Sh. Tuĭchiev, S. Kh. Tabarov, A. A. Shepelevskiĭ, and L. A. Shibaev

Institute of Problems in Machine Science, Russian Academy of Sciences, Vasil'evskiĭ Ostrov, Bol'shoĭ pr. 61, St. Petersburg, 199178 Russia

Received June 9, 2004; in final form, October 19, 2004

Abstract—C_{60} fullerene powder and fullerene soot are examined by the method of small-angle X-ray diffraction. Small-angle diffraction patterns constructed in the Guinier coordinates make it possible to find the radii of inertia of scattering elements. The small-angle diffraction scattering findings agree well with large-angle X-ray diffraction data. © *2005 Pleiades Publishing, Inc.*

Small-angle X-ray diffraction has been widely used in studying solid disperse systems, such as powder-like soots, coals, etc. [1]. However, small-angle X-ray diffraction data should sometimes be compared with independent experimental results, since this method is well developed for only dilute systems of similar equal-size particles [2]. Here, we took advantage of the fact that the structure of C_{60} fullerene powder can also be examined by large-angle diffraction [3] and so applied both X-ray techniques to find the size of its scatterers. The soot from which the fullerene was extracted was also studied by both techniques. The results obtained with these two techniques not only correlate but also complement each other.

EXPERIMENTAL

C_{60} fullerene (of purity 99.7%) was obtained by the Krätschmer–Huffman method [4]. Large-angle diffraction studies were carried out on a DRON-2.0 diffractometer (CuK_α or CoK_α radiation) with a graphite monochromator using the Bragg–Brentano scheme. The samples were prepared by applying a drop of a C_{60} or soot suspension in ethanol on the degreased surface of cover silicate glass. After the alcohol has evaporated, a thin powder layer remained on the glass due to adhesion. The glasses with the powder were placed directly on the goniometer head, and reflection diffraction lines were recorded under room conditions. From the width of the reflections, we estimated mean size L_{hkl} of crystallites in an [*hkl*] direction by the Scherrer formula [1]. In addition, the size of crystallites along the [111] direction and parameter g_{II} of lattice paracrystalline distortions were calculated, in accordance with the Hosemann theory [5], by measuring several orders of reflection from the (111) surface,

$$(\delta S)^2 = (\delta S)_c^2 + (\delta S)_{II}^2 = \bar{1}/L_{hkl}^2 + (\pi g_{II})^4 m^4/d_{hkl}^2, \quad (1)$$

where (δS) is found by the formula

$$\bar{L}_{hkl} = K/[(2\cos\theta)/\lambda]\delta\theta \approx 1/(\delta S). \quad (2)$$

In the above formulas, $S = 2(\sin\theta)/\lambda$, λ is the X-ray radiation wavelength, K is a constant close to unity, 2θ is the scattering angle, $(\delta S)_c$ and $(\delta S)_{II}$ are the respective contributions of the grain size and lattice distortions to the width of the reflection, m is the order of reflection, and $g_{II} = (\Delta d_{hkl}/d_{hkl})$ is the relative change in interplanar spacing d_{hkl}. Formula (1) applies if $2\pi^2 g_{II}^2 m^2 \ll 1$.

Small-angle diffraction studies were performed in the transmission mode on a KRM-1 setup with slot collimation of the primary X-ray beam. The width of the beam at its base was 5'. Only Ni-filtered CuK_α radiation was used. The scattering angles were varied from 12′ to 2°. The substrate was a 7.5- to 10-μm-thick hydrated cellulose film covered by a thin layer of silicate adhesive. A thin layer of the powder was more or less uniformly distributed over its surface, and the entire composition was then rolled by a glass roller. The contribution of a reference adhesive-covered substrate to scattering was insignificant compared to the background in the scattering angle range studied.

According to the Guinier theory, the distribution of small-angle scattering intensity for X rays scattered by dilute systems of similar equal-size particles is described by the formula

$$I(S) = n^2 \exp(-4\pi^2 R_i^2 S^2/3), \quad (3)$$

where $I(S)$ is the scattering intensity, n^2 is the scattering capacity per scatterer, R_i is the radius of inertia, and S can be set equal to $2\theta/\lambda$ (because of the smallness of the scattering angle).

Formula (3) is valid if the product $R_i S$ is much smaller than unity. Taking the logarithm of (3) yields

$$\log I = \log n^2 - (4\pi^2 R_i^2 S^2/3)\log e. \quad (4)$$

1063-7842/05/5011-1458$26.00

Therefore, experimental scattering curves were first constructed in the standard coordinates (intensity versus scattering angle) and then converted to the curves in the Guinier coordinates (logarithm of intensity versus scattering angle squared). From slope α of these curves in the Guinier coordinates, the radii of inertia of scatterers were found. For CuK_α radiation,

$$R_i \approx 0.644(-\alpha)^{1/2}. \quad (5)$$

It was found experimentally [2] that, for a set of scattering particles of, e.g., two sorts each with a relatively narrow size distribution, the general distribution constructed in the Guinier coordinates has the form of a broken line with two respective linear portions.

In taking small-angle measurements, the goniometer was rotated manually and a total of 1000 counts were recorded at each fixed scattering angle; so, the relative error of intensity measurement was within 3–4%.

RESULTS AND DISCUSSION

Figure 1 shows the diffraction pattern of the C_{60} fullerene powder on the glass substrate. The reflections from the fullerene are much more intense than the scattering from the substrate, and so determination of their intensities and positions poses no difficulties. According to calculations, the interplanar spacings in the fcc and hcp lattices are nearly the same but the intensities of the corresponding reflections differ. The majority of the most intense peaks can be attributed to the $Fm\bar{3}m$ fcc lattice, which is observed at $T > 260$ K [6], and the interplanar spacing agrees with the published data [3, 6–9] accurate to 0.001–0.002 nm.

Having constructed a linear dependence of $(\delta S)^2$ on m^4 (Fig. 2) for the (111), (222), and (333) reflections by the least squares method, we find from the point of intersection of this plot with the vertical axis that $L_{111} = 18 \pm 2$ nm. The slope of this line gives $g_{II} \approx 2\%$.

The grain least size measured from the same reflections and also from the (220) reflection is 20–30 nm. Thus, grains in the as-prepared C_{60} fullerene are sufficiently perfect and 20–30 nm across, as follows from the large-angle diffraction scattering data.

It should be noted that the structure of C_{60} fullerene powders depends on the preparation technique. Korolev *et al.* [3] studied seven lots of C_{60} fullerene that differ in phase composition. They believe that fullerene powders contain, along with the crystalline phase with perfect "large" grains, fine "grains" 2–4 nm across and individual C_{60} molecules. The two additional phases show up in wide-angle X-ray diffraction patterns as halos under reflections in the interval 10°–15° and 17°–30°, respectively (for CuK_α radiation). In Fig. 1, these halos (shown as dark areas) are seen not so distinctly as in [3]. Significantly, grains 2 nm across are physically unrealistic, since the interplanar spacings in the C_{60} lattice are on the order of 1 nm (the molecular diameter exceeds 0.7 nm), so that long-range order cannot arise over a distance of 2 nm. It seems that Korolev *et al.* [3] meant clusters consisting of two to four molecules rather than grains (crystallites).

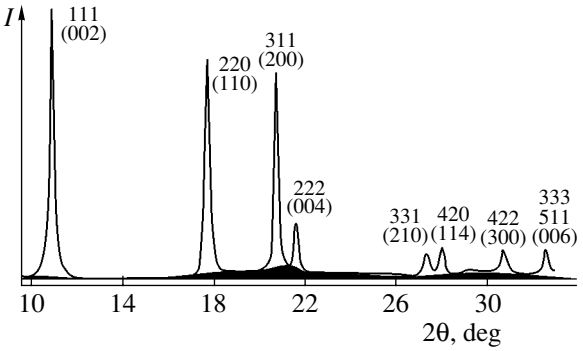

Fig. 1. Large-angle diffraction pattern taken of the C_{60} fullerene powder. Numbers above the peaks are reflection indices in the fcc and hcp (in parentheses) lattices. CuK_α radiation.

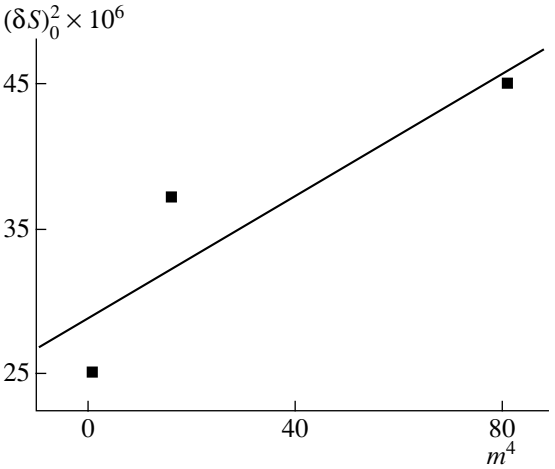

Fig. 2. $(\delta S)^2$ vs. m^4 (formula (1)) for the C_{60} fullerene powder.

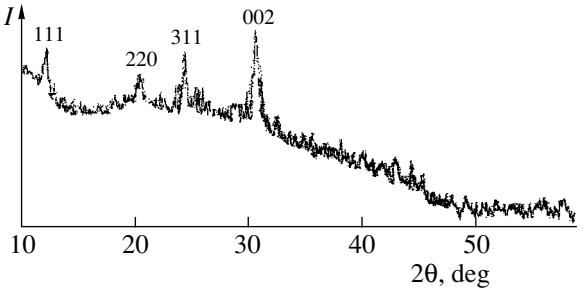

Fig. 3. Large-angle diffraction pattern taken of the fullerene soot. Reflection indices (except for (002)) correspond to the fcc lattice of fullerene C_{60}. The (002) reflection is that of graphite. CoK_α radiation.

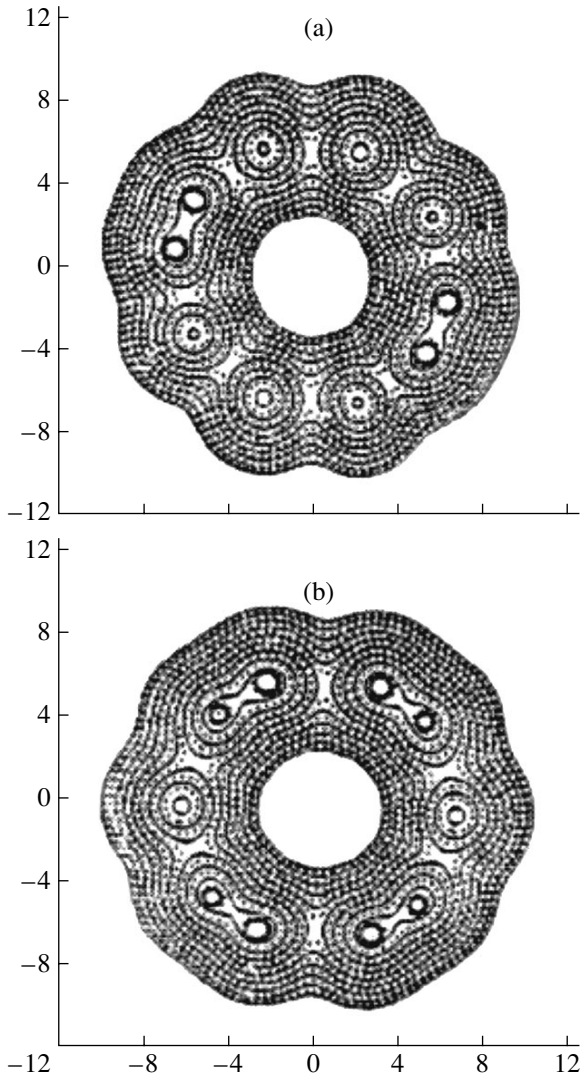

Fig. 4. Computer simulation of the electron density distribution over two central cross sections of a C_{60} fullerene molecule passing through (a) two and (b) four double bonds [10].

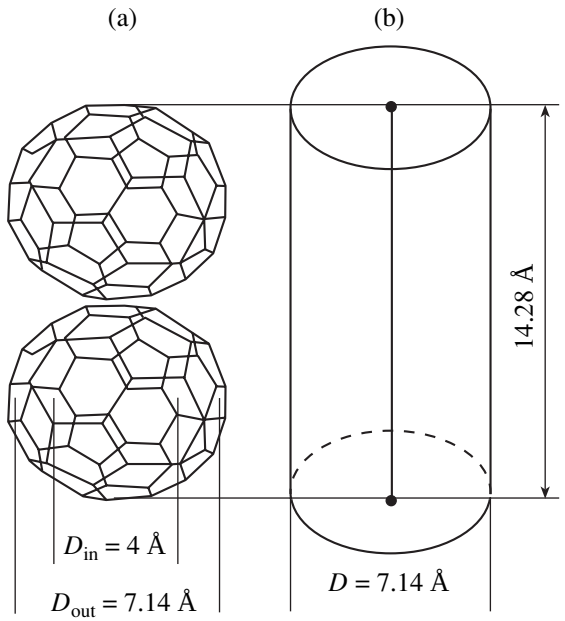

Fig. 5. (a) Cluster of two C_{60} molecules (the inner and outer diameters of the molecule are indicated) and (b) its cylindrical approximation.

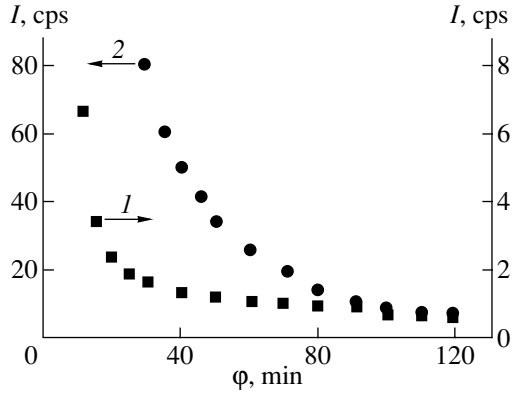

Fig. 6. Small-angle diffraction patterns taken of the C_{60} fullerene powder and fullerene soot.

In the wide-angle diffraction pattern taken of the fullerene soot (Fig. 3), only four reflections are distinctly seen, three corresponding to the fcc lattice of pure C_{60} fullerene. The fourth (most intense) reflection can be assigned to the (002) reflection from the graphite lattice. The crystallite sizes in the C_{60} fullerene and fullerene soot calculated by the Scherrer formula from the widths of the (220) and (111) reflections are ≈20 and ≈25 nm, respectively. Thus, crystallites in the fullerene powder and fullerene soot are of the same size.

Before turning to the results of small-angle measurements, we note that a C_{60} fullerene molecule has the form of a hollow truncated icosahedron with zero electron density inside (Fig. 4), as follows from experimental and analytical results [10]. The inner and outer diameters are, respectively, 0.4 and 0.714 nm (Fig. 5) [11]. With this in mind, a C_{60} fullerene molecule can be approximated by a spherical sheath with a uniformly distributed density; then, its radius of inertia equals 0.30 nm.

Figure 6 shows the small-angle diffraction patterns for the C_{60} fullerene powder; Fig. 7, the same patterns constructed in the Guinier coordinates. It is noteworthy that curves *1* and *2* have the same slope at very small angles; the radius of inertia equals 10 nm in both cases. If we assume that scattering particles are cubes with a uniform density, the edge of the cube is then 20 nm long. This value is in agreement with the large-angle diffraction data for the C_{60} crystallite size in both the powder and the soot.

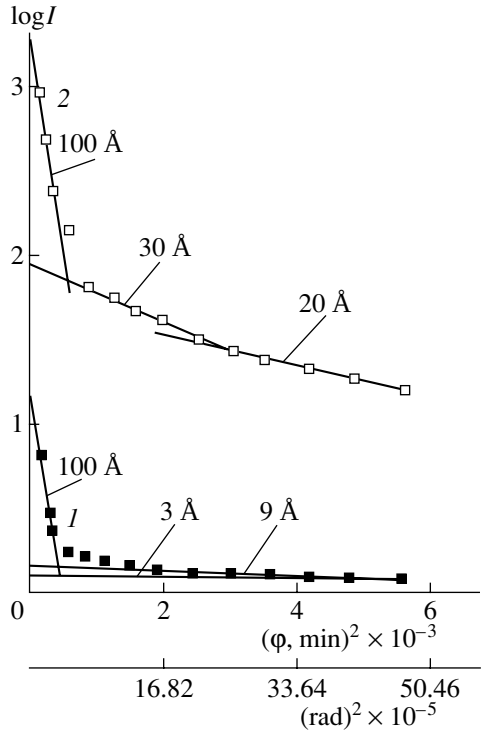

Fig. 7. The same patterns as in Fig. 6 constructed in the Guinier coordinates. Numbers by different rectilinear portions indicate the corresponding radii of inertia.

Let us now turn to the second portion of curve *1* in Fig. 7. Here, two straight lines are drawn with regard to the measurement error: their slopes give radii of inertia of ≈0.9 and ≈0.3 nm, respectively. The first value corresponds well to clusters consisting of two C_{60} molecules. In fact, let us represent such a cluster as a cylinder of height H equal to two diameters of a C_{60} molecule and radius R equal to the radius of the molecule (Fig. 5b). The relationship $R_i = (R^2/2 + H^2/3)^{1/2}$, which is valid for homogeneous cylinders, yields $R_i = 0.86$ nm, in good agreement with the experimental data. The other value corresponds to individual C_{60} molecules, a large amount of which is present in C_{60} fullerene powder prepared by the Krätschmer–Huffman method, as follows from the shape of the amorphous halo observed in large-angle diffraction patterns [3].

The second and third rectilinear portions of curve *2* in Fig. 6 correspond to fullerene soot particles with radii of inertia of 3 and 2 nm, respectively. Such values cannot as yet be assigned to any structural element.

Thus, the C_{60} fullerene powder consists of grains ≈20 nm in size, two-molecule clusters, and individual fullerene molecules. The fullerene soot also contains C_{60} grains 20–25 nm across.

ACKNOWLEDGMENTS

This work was supported by the program “Thermal and Thermal Oxidative Failure of Fullerene-Based Polymers: The Nature and Mechanisms” at the St. Petersburg Research Center.

REFERENCES

1. L. I. Kitaĭgorodskiĭ, *X-ray Diffraction Analysis of Finely Crystalline and Amorphous Solids* (GITTL, Moscow, 1952) [in Russian].
2. A. Guinier, *Théorie et Technique de la Radiocristallographie* (Dunod, Paris, 1956; Fizmatgiz, Moscow, 1961).
3. Yu. M. Korolev, V. V. Kozlov, V. M. Polikarpov, and E. M. Antipov, Vysokomol. Soedin., Ser. A **43**, 1933 (2001).
4. W. Krätschmer and D. R. Huffman, Philos. Trans. R. Soc. London, Ser. A **343** (1667), 33 (1993).
5. L. E. Alexander, *X-ray Diffraction Methods in Polymer Science* (Wiley, New York, 1969), p. 429.
6. P. A. Heyney, J. E. Fisher, A. R. McGhie, *et al.*, Phys. Rev. Lett. **66**, 2911 (1991).
7. P. A. Heyney, in *The Fullerenes*, Ed. by H. W. Kroto, J. E. Fischer, and D. E. Cox (Pergamon, London, 1993), p. 163.
8. R. M. Fleming, B. Hessen, T. Siegriest, *et al.*, in *Fullerenes: Synthesis, Properties and Chemistry of Large Carbon Clusters*, Ed. by G. S. Hammond and V. J. Kuck (ACS, Washington, 1992); J. Am. Chem. Soc. Symp. Ser. **481**, 25 (1992).
9. W. Krätschmer, L. D. Lamb, K. Fostiropolous, and D. R. Huffman, Nature **347**, 354 (1990).
10. S. V. Kozyrev and V. V. Rotkin, Fiz. Tekh. Poluprovodn. (St. Petersburg) **27**, 1409 (1993) [Semiconductors **27**, 777 (1993)].
11. A. V. Eletskiĭ and B. M. Smirnov, Usp. Fiz. Nauk **163** (2), 33 (1993) [Phys. Usp. **36**, 202 (1993)].

Translated by V. Isaakyan

Technical Physics, Vol. 50, No. 11, 2005, pp. 1462–1466. Translated from Zhurnal Tekhnicheskoĭ Fiziki, Vol. 75, No. 11, 2005, pp. 69–74.

OPTICS, QUANTUM ELECTRONICS

Generation of X-ray Radiation with a High Pulse Repetition Rate by Means of a Volume Discharge in an Open Gas Diode

V. F. Tarasenko*, S. K. Lyubutin, S. N. Rukin**, B. G. Slovikovskii**, I. D. Kostyrya*, and V. M. Orlovskii***

** Institute of High-Current Electronics, Siberian Division, Russian Academy of Sciences, Akademicheskiĭ pr. 4, Tomsk, 634055 Russia*

e-mail: VFT@loi.hcei.tsc.ru

*** Institute of Electrophysics, Ural Division, Russian Academy of Sciences, ul. Amundsena 106, Yekaterinburg, 620016 Russia*

e-mail: rukin@iep.uran.ru

Received March 11, 2005

Abstract—The subject of study is ultrashort avalanche-produced electron pulses generated in air under atmospheric pressure. The current amplitude of the pulses behind 45-μm-thick AlBe foil exceeds 100 A, and their FWHM is ≈0.2 ns. The conditions of generation of ultrashort pulses persist at repetition rates as high as 1.5 kHz. A volume discharge initiated in an open coaxial-electrode gas diode by high-voltage nanosecond pulses generates hard (>60 keV) radiation. © *2005 Pleiades Publishing, Inc.*

INTRODUCTION

Pulsed and continuous sources of X rays are being widely applied in various areas of science and technology. Usually, X-ray radiation is generated by stopping an electron beam on a target made of a heavy metal, while electron beams are produced in high-voltage (several tens of kilovolts) vacuum diodes [1]. It was reported [2–7] that ultrashort avalanche electron beams (UAEBs) were produced in gas diodes at a pressure of 1 atm or higher. Possible applications of nanosecond electrons beams were considered in [8, 9].

The UAEB offers unique properties. Upon filling a gas diode of an appropriate configuration (small dimensions and a low inductance) with atmospheric-pressure air, the beam current amplitude amounts to several hundreds of amperes and the FWHM of the pulses is no more than several hundreds of picoseconds [3–7]. Optimized UAEBs were used to initiate a volume discharge in an atmospheric-pressure CO_2 laser [8] and excite cathodoluminescence in crystals [9]. However, the early experiments on UAEB generation used single shots or a low repetition rate (no higher than 5 Hz), while advanced nanosecond high-voltage pulse generators operate in the pulsed–periodic regime with a pulse repetition rate of 1 kHz or higher [10, 11]. Specifically, a mechanism of superfast current switching in semiconductors based on tunnel–collision ionization has been implemented [11]. Terminated by a 50-Ω load, a pulser built around this effect generated pulses of amplitude 150–160 kV and duration 1.4 ns with a rate of up to 3 kHz. The pulse rise time was 200–250 ps.

The aim of this work is to study the properties of UAEBs produced in gas diodes of different configurations and also the feasibility of producing UAEBs at a high repetition rate of generating pulses. UAEBs were generated in an open gas diode with subsequent recording of X-ray radiation.

EXPERIMENTAL

The setup used in our experiments was described elsewhere [11, 12]. An overvoltage across a tunnel–collision sharpener was achieved with an SOS-diode-based short-pulse generator and intermediate sharpener [12] operating in the normal collision-ionized wave mode. The generator provided an output voltage amplitude of 220 V with a rise time of about 1 ns. A terminating tunnel–collision sharpener placed at the beginning of the transmission line generated in the line a pulse with a rise time of about 250 ps. All the circuits of the generator were filled with transformer oil. The gas diode used in the experiments (Fig. 1) was similar to the diode described in [5] and was implemented in two versions: (i) a cathode mounted on a central electrode and an anode made of foil and (ii) an open gas diode without foil, which was used to generate X-ray radiation.

We studied the parameters of the electron beam and/or X-ray radiation using three cathodes and two anodes of different configuration. Cathode 1 (*5* in Fig. 1) is a tube 6 mm in diameter made of a steel sheet 100 μm thick. Cathode 2 was a steel ball 17.4 mm in diameter. Cathode 3 was a steel ball 7 mm in diameter, which was fixed at the end of a steel tube of diameter 6 mm. Planar anode 1 (*4* in Fig. 1) was made of AlBe foil 45 μm thick. As the second anode, we used the inner metallic surface of the gas diode (*3*) to provide

1063-7842/05/5011-1462$26.00 © 2005 Pleiades Publishing, Inc.

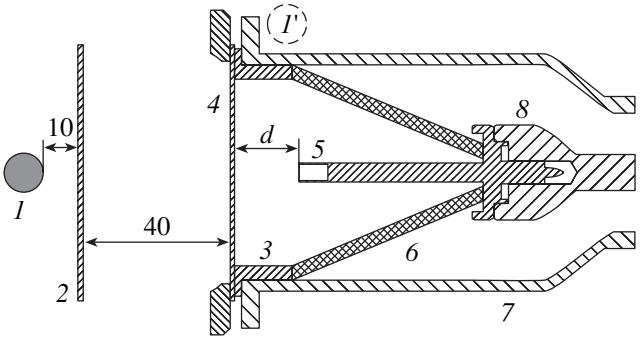

Fig. 1. Schematic of the experimental setup: (*1*, *1*') dosimeter, (*2*) additional screen, (*3*) case of gas diode (anode 2), (*4*) foil, (*5*) cathode, (*6*) gas diode insulator, (*7*) transmission line body, and (*8*) central conductor.

more efficient (compared with the foil) anode cooling at high pulse repetition rates. In the latter case, the foil was removed, so that the diode remained open.

Under conditions 1, the gas diode consisted of the planar anode and cathode 1 or 3. Here, breakdown was accomplished between the end face of the cathode and central part of the planar foil anode. The electrode gap could be varied between 5 and 16 mm. As was already noted, when the diode was open (conditions 2), the foil was removed and breakdown of the air was accomplished at a low repetition rate between the end face of the tube (cathode 1) or lateral surface of the ball (cathodes 2 and 3) and the edge of the cylindrical case of the diode. The electrodes were coaxial. The gap between the cylindrical surface of the anode and cathode 1 was equal to 21 mm; cathode 2, 15.3 mm; and cathode 3, 20.5 mm. Since the foil was absent under conditions 2, we could observe and photograph the integral glow of the discharge. Under conditions 1, we measured the beam parameters behind the foil. Under conditions 2, the electron beam was detected and its relative intensity was measured with a VICTOREEN541R dosimeter, which was placed at a distance of 5 cm from the foil normally to the axis of the transmission line of the generator (*1* in Fig. 1). In the pulse train mode, the open diode combined with the dosimeter allowed measurements at a repetition rate of pulses in a train of up to 1.5 kHz. The number of pulses per train was varied from 150 to 3000. The dosimeter used in the experiments recorded the electrons and X-ray quanta that have an energy exceeding 60 keV.

Voltage pulses were detected by capacitive voltage dividers inserted in the transmission line of the generator. Current pulses were detected with a low-inductance collector 2 cm in diameter terminated by a coaxial cable. The pulses from the divider and collector were applied to a TDS6604 digital oscilloscope with a 6-GHz transmission band and a recording rate of 20 points per nanosecond (20 GHz). The pulse rise time in the measuring system did not exceed 100 ns. The measurements were taken in the single shot mode and at a pulse repetition rate varying from 1.5 to 1500 Hz. At a rate of 100 Hz or more, the pulses were applied to the gas diode in trains.

RESULTS AND DISCUSSION

In the course of experiments, we recorded the incident and reflected voltage pulses in the transmission

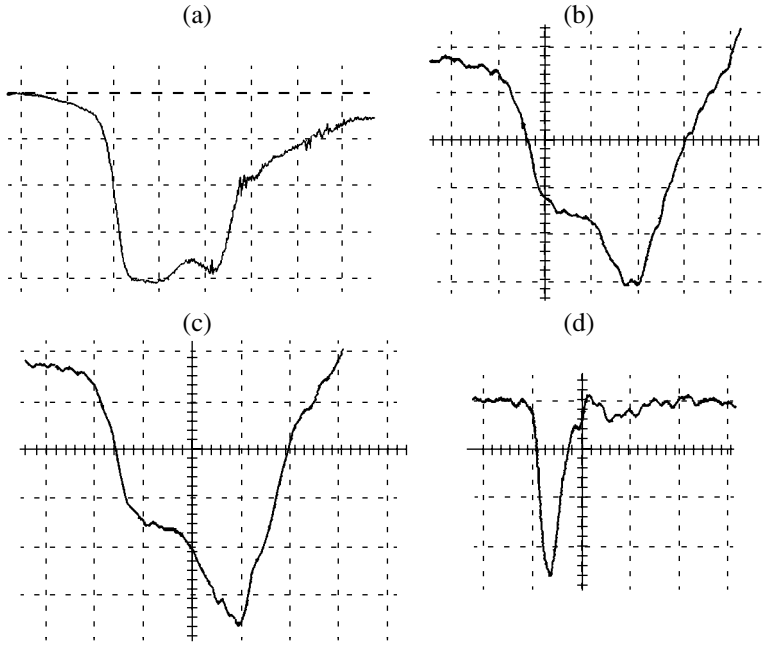

Fig. 2. Waveforms of the (a–c) voltage pulses and (d) beam electron current at a low pulse repetition rate. The horizontal scale is 0.5 ns/div, and the vertical scale is (a–c) 36 kV/div and (d) 30 A/div.

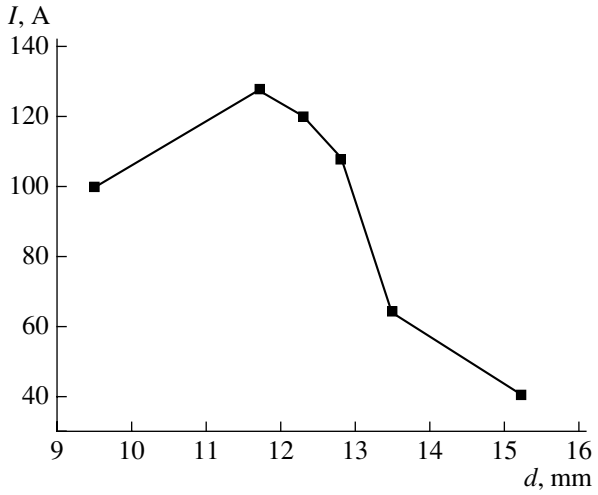

Fig. 3. UAEB amplitude vs. electrode gap width under conditions 1 (single shots, cathode 1).

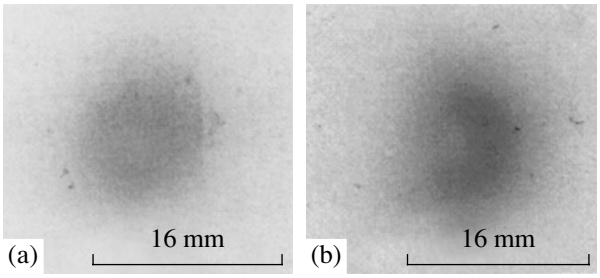

Fig. 4. UAEB autographs behind aluminum foil (a) 10 and (b) 70 mm thick (the gap width is 11.7 mm, cathode 1).

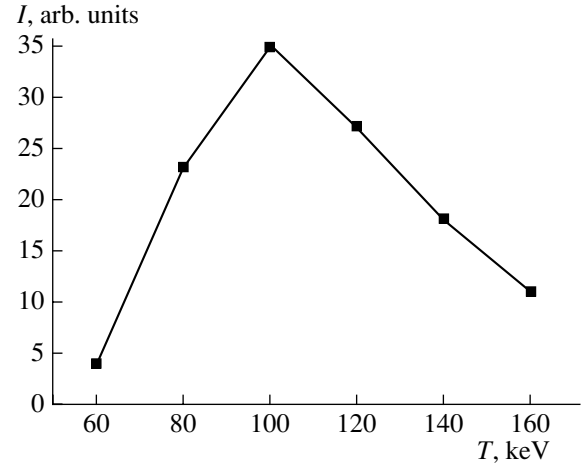

Fig. 5. Electron energy distribution in the UAEB (the gap width is 11.7 mm, cathode 1).

line, beam current waveforms behind the foil, and electron beam "autograph"; measured the X-ray exposure dose; and calculated the electron energy distribution behind the foil. Figure 2a shows the waveform of a pulse from the voltage divider placed in the transmission line of the generator. The pulse is unaffected by reflection from the gas diode due to the elongation of the transmission line. The pulse voltage and current amplitudes are, respectively, 156 kV and 3.2 kA, and the FWHM equals 1.4 ns. The voltage pulse generated by the gas diode with cathode 1 under conditions 1 is shown in Fig. 2b, and the current waveform after the foil is depicted in Fig. 2d. The incident and reflected voltage pulse amplitudes are, respectively, 134 and 55 kV, which corresponds to a maximal voltage across the gap of ≈190 kV (at this voltage, the resistance of the gas diode equals ≈120 Ω). Under optimal conditions, the UAEB amplitude (Fig. 2d) behind the foil exceeds 100 A, and the FWHM is ≈0.2 ns. The voltage pulse waveform for the open diode with cathode 1 is represented in Fig. 2c. The increase in the reflected pulse amplitude is associated with an extension of the gap and, accordingly, an increase in the gap resistance to ≈170 Ω. Remarkably, the peak in the voltage pulse waveforms (Figs. 2b and 2c) is followed by a shallow dip, which reflects a decrease in the discharge plasma resistance during the pulse. The current pulse amplitude behind the foil (cathode 1) versus gap width dependence is shown in Fig. 3. The highest current is observed at a gap width of 11.7 mm. When cathode 1 was replaced by cathode 2 in the single shot mode, the optimal gap shrinks to 7.5 mm and the electron beam current decreases by ≈30%.

Note a considerable scatter in the measured beam current amplitudes, especially under nonoptimal conditions. However, the peak amplitudes were reliably reproduced from measurement to measurement and the operating stability of the gas diode was even improved after pretraining in the pulsed–periodic regime. Here, we give the maximal amplitudes of the beam current. Figure 4 demonstrates the autographs of the electron beam behind Al foil 10 and 70 μm thick. In the latter case, the number of pulses needed to record the autograph was raised from 450 to 1350. The diameter of the autograph in the plane of the foil is about ≈16 mm. The electron energy distribution taken by the foil method is shown in Fig. 5. The distribution after the foil peaks at an electron energy near 100 keV. A substantial number of electrons had an energy above 140 keV. Narrowing of the voltage pulse front compared with the front of voltage pulses produced in the RADAN-303 accelerator [5, 6] increased the UAEB energy.

The most significant result was obtained when the open diode was studied in the pulsed–periodic regime (Fig. 6). With cathode 1 (Fig. 6a), the maximal X-ray exposure dose (within the initial 150 pulses) was observed at a pulse repetition rate of 1.5 Hz or less. As the repetition rate was raised, the exposure dose declined continuously and, eventually, the dosimeter did not detected X-ray radiation within the initial 450 pulses when the rate achieved 100 Hz. However, with a further rise in the repetition rate, X rays were detected again. The second maximum appears at a repetition rate of ≈200 Hz. When the repetition rate was increased

from 0.5 to 1.5 kHz, the X-ray exposure dose per initial 150 pulses dropped only twofold.

With cathode 2 (Fig. 6b), the minimal and maximal doses were observed t repetition rates of 1.5 Hz and ≈200 Hz, respectively. When the repetition rate was raised from 0.5 to 1.5 kHz, the X-ray exposure dose per 150 pulses decreased by no more than three times and was 1.5 times higher than with cathode 1. With cathode *3* (Fig. 6c), the maximal dose, as with cathode *1*, was observed at a repetition rate of 1.5 Hz; however, the second maximum appeared at a lower rate, ≈50 Hz. Thus, in all the three cases, X-ray radiation was generated at a high pulse repetition rate and a change in the repetition rate or cathode design influenced the exposure dose of the X-ray radiation.

With a 5-mm-thick lead screen (*2* in Fig. 1) placed before the dosimeter, X rays were not detected under all the conditions. However, when an aluminum screen 170 μm thick was mounted at the same place, the dosimeter readings changed insignificantly. With the dosimeter placed in position *1'* in Fig. 1 (i.e., behind the lateral wall of the diode and transmission line), X rays were not detected over 450 pulses.

Visual observation and photographing of the glow in the gas diode suggest that the discharge in the diode is volume and concentrates at the places where the electric field is slightly enhanced (Fig. 7). With cathode 3, the discharge is the most homogeneous (Fig. 7c) and the current partially closes to the central part of the ball. When the pulse repetition rate was low and the number of pulses per train was small, the volume discharge had the form of overlapping jets with bright spots at the end of the tube (cathode 1) [6] or on the spherical surface (cathode 2), which is at a very short distance from the anode.

When the pulse repetition rate is high and the number of pulses per train is large (more than 50), the discharge remains volume but its form changes. The discharge-occupied space between the electrodes starts expanding, and an additional volume discharge of a lower density arises between the cathode holder and inner metallic surface of the cylindrical anode. As the repetition rate and number of pulses per train grow further (1000 or more), bright channels appear in the gap.

It should be noted that the X-ray exposure doses under conditions 1 (with foil) and conditions 2 (open gas diode) with cathode 1 differed by as little as 20%; namely, they equaled 16 and 13 mR, respectively, over 150 pulses following with a rate of 1.5 Hz. In both cases, the dosimeter was at a distance of 5 cm from the foil.

Let us discuss the results obtained. When a high-voltage pulse with a subnanosecond rise time is applied to the gap, the plasma front moving from the cathode toward the anode produces a critical field near the anode and a UAEB forms [3]. The UAEB amplitude and energy depend on many factors [6], including the pulse repetition rate. X-ray radiation with a quantum energy of >60 keV is generated mainly when the electron beam stops at the anode. In this work, it is for the first time shown that the conditions for UAEB generation persist when the repetition rate of pulses, including those in a train of 150 pulses, is high (1.5 kHz).

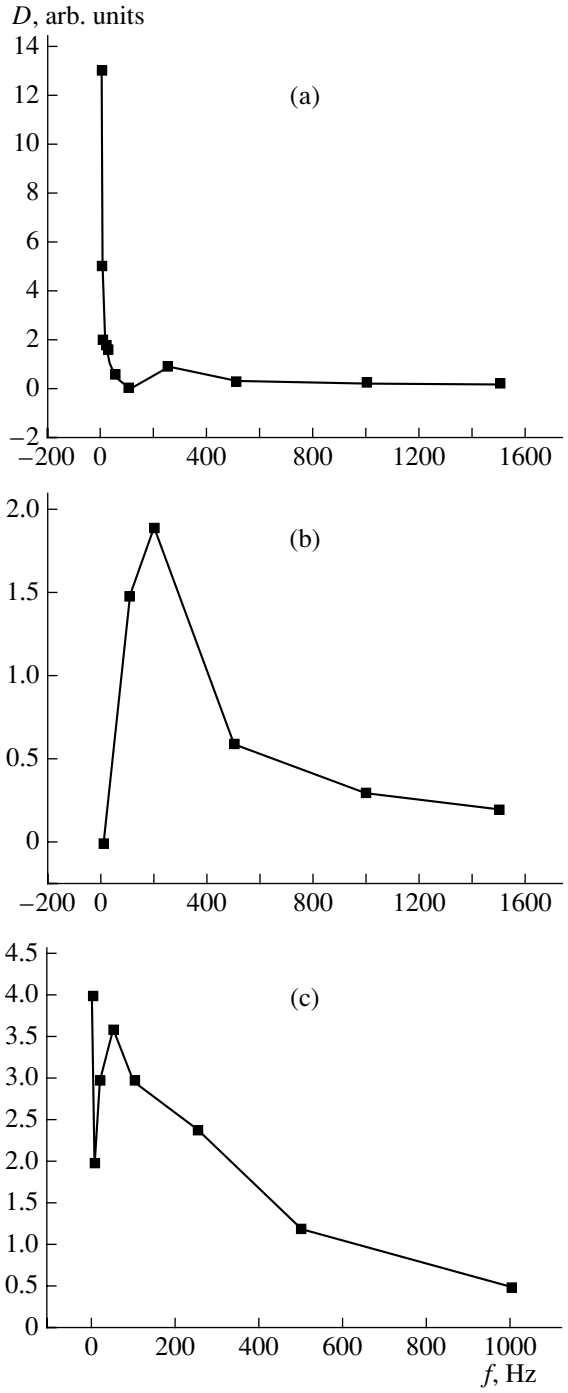

Fig. 6. X-ray exposure dose (over 150 pulses) vs. pulse repetition rate for the open gas diode with cathode (a) 1, (b) 2, and (c) 3.

The second maximum in the dependence of the exposure dose on the repetition rate is due to expansion

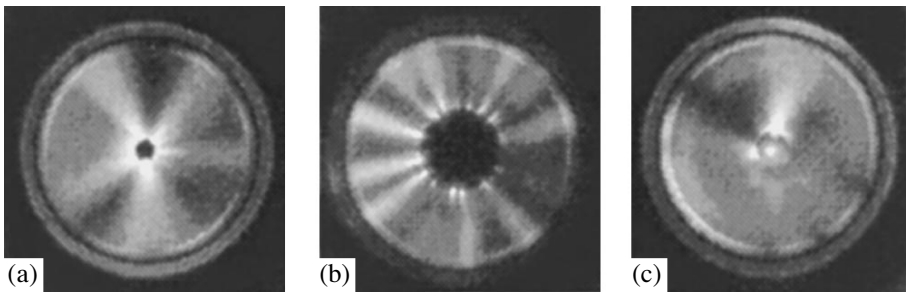

Fig. 7. Pattern of the volume discharge in the open diode with cathode (a) 1, (b) 2, and (c) 3 after one shot.

of the space occupied by the discharge. It appears that, when the repetition rate is high, the plasma has no time to recombine in the areas where the current density is the highest and the UAEB forms under worse conditions (the electric field gradient near the anode weakens). As the current density decreases as a result of the discharge area expansion toward the transmission line, the UAEB forms in areas with a lower current density and X-ray radiation is generated at high repetition rates. Although the exposure dose at repetition rates of 0.5 kHz or higher was smaller than at lower rates, the dosimeter continuously detected X-ray radiation with a quantum energy above 60 keV.

CONCLUSIONS

We studied an ultrashort avalanche electron beam produced in air under atmospheric pressure. It is shown for the first time that the conditions for UAEB generation persist at a pulse repetition rate as high as 1.5 kHz. X rays generated by electrons with an energy above 60 keV are detected if nanosecond high-voltage pulses are employed and a volume discharge is initiated in an open gas diode filled with air under atmospheric pressure. The X-ray exposure dose depends on the pulse repetition rate nonmonotonically (nonlinearly). It seems that such a nonlinear dose–rate dependence may be used to improve the stability of sharpeners operating in the pulse–periodic regime. Behind 45-μm-thick AlBe foil, the UAEB current amplitude exceeds 100 A at an FWHM of ≈0.2 ns.

ACKNOWLEDGMENTS

The authors thank V.G. Shpak for support and S.A. Shunaĭlov for assistance in conducting the experiments.

REFERENCES

1. G. A. Mesyats, *Pulsed Power* (Plenum, New York, 2004; Nauka, Moscow, 2004).
2. S. B. Alekseev, V. M. Orlovskiĭ, and V. F. Tarasenko, Pis'ma Zh. Tekh. Fiz. **29** (10), 29 (2003) [Tech. Phys. Lett. **29**, 411 (2003)].
3. V. F. Tarasenko, V. M. Orlovskiĭ, and S. A. Shunaĭlov, Izv. Vyssh. Uchebn. Zaved., Fiz., No. 3, 9 (2003).
4. V. F. Tarasenko, S. I. Yakovlenko, V. M. Orlovskiĭ, *et al.*, Pis'ma Zh. Éksp. Teor. Fiz. **77**, 737 (2003) [JETP Lett. **77**, 611 (2003)].
5. V. F. Tarasenko, V. G. Shpak, S. A. Shunaĭlov, *et al.*, Pis'ma Zh. Tekh. Fiz. **29** (21), 1 (2003) [Tech. Phys. Lett. **29**, 879 (2003)].
6. V. F. Tarasenko, V. S. Skakun, I. D. Kostyrya, *et al.*, Laser Part. Beams **22**, 75 (2004).
7. S. B. Alekseev, V. P. Gubanov, V. M. Orlovskiĭ, and V. F. Tarasenko, Pis'ma Zh. Tekh. Fiz. **30** (20), 35 (2004) [Tech. Phys. Lett. **30**, 859 (2004)].
8. S. B. Alekseev, V. M. Orlovskiĭ, and V. F. Tarasenko, Kvantovaya Élektron. (Moscow) **31**, 1059 (2003).
9. E. I. Lipatov, V. F. Tarasenko, V. M. Orlovskiĭ, *et al.*, Pis'ma Zh. Tekh. Fiz. **31** (6), 29 (2005) [Tech. Phys. Lett. **31**, 231 (2005)].
10. V. P. Gubanov, S. D. Korovin, I. V. Pegel, *et al.*, IEEE Trans. Plasma Sci. **25**, 258 (1997).
11. S. K. Lyubutin, S. N. Rukin, B. G. Slovikovskiĭ, and S. N. Tsyranov, Pis'ma Zh. Tekh. Fiz. **31** (5), 36 (2005) [Tech. Phys. Lett. **31**, 196 (2005)].
12. E. A. Alichkin, S. K. Lyubutin, A. V. Ponomarev, *et al.*, Prib. Tekh. Éksp., No. 4, 106 (2002).
13. V. F. Tarasenko and S. I. Yakovlenko, Usp. Fiz. Nauk **174**, 953 (2004) [Phys. Usp. **47**, 887 (2004)].

Translated by V. Isaakyan

Technical Physics, Vol. 50, No. 11, 2005, pp. 1467–1469. Translated from Zhurnal Tekhnicheskoĭ Fiziki, Vol. 75, No. 11, 2005, pp. 75–77.

OPTICS, QUANTUM ELECTRONICS

Excitation of UV Radiation by a Pulsed-Periodic Discharge in Xenon

D. L. Glebov, O. N. Kryutchenko, D. A. Morozov, and M. V. Chirkin

Esenin State Pedagogical University, ul. Svobody 46, Ryazan, 390000 Russia

e-mail: chirkin@rspu.ryazan.ru

Received March 23, 2005

Abstract—Optoelectrical characteristics of a pulsed-periodic discharge in xenon are investigated experimentally under conditions such that the product of the electrode gap length and the gas pressure is in the range of 4–20 Torr cm. High conversion efficiency of the energy deposited into vacuum UV radiation in a discharge sustained by 0.1-μs voltage pulses at a repetition rate of 1–10 kHz is demonstrated. It is shown that this effect is related to the fast expansion of the negative glow occurring after each discharge ignition. The conditions are determined under which the discharge is not accompanied by the heating and sputtering of the cathode. *© 2005 Pleiades Publishing, Inc.*

Pulsed-periodic discharge in xenon at pressures of 10–40 Torr was investigated in [1, 2] as a source of vacuum UV radiation in the 145- to 190-nm wavelength range. The discharge was excited in two-electrode gaps with a distance of 1–5 mm between the cathode and anode. Zn_2SiO_4 : Mn phosphor was used to convert UV radiation into visible light. It was shown that the light power efficiency increases significantly as the duration of the applied voltage pulses is reduced. At a pulse duration shorter than 0.2 μs, the light efficiency was found to be one to two orders of magnitude higher than that in the negative glow of a dc discharge. It was shown in [3] that the decrease in the duration of the voltage pulses sustaining a discharge in xenon-filled industrial gas-discharge indicator panel cells from 2 to 0.3 μs was accompanied by a twofold increase in the UV radiation intensity. However, the reason for such an efficient conversion of the deposited energy into UV radiation remains unclear.

In [4], the propagation of the negative glow boundary toward the cathode with a velocity of 10^6–2.5×10^6 cm/s was observed after discharge ignition in a Ne–Xe(10%) mixture by voltage pulses with an amplitude of 190–220 V. It is known [5] that the emission of UV radiation is caused by the processes initiated by electron-impact gas ionization near the negative glow boundary. The question naturally arises as to whether the propagation of the cathode glow boundary can lead to the production of the excited xenon atoms and dimers in a volume larger than that in a dc discharge.

In this paper, we present results of experiments on the investigation of the negative glow expansion as a mechanism for the efficient conversion of the deposited energy into UV radiation in a xenon discharge sustained by short periodic voltage pulses.

The experimental setup consisted of two identical glass cells with internal dimensions of $20 \times 20 \times 6$ mm. The inner surface of one of the cells was covered with a (Eu, Ba)$MgAl_{10}O_{17}$ phosphor. Both cells contained two parallel 20-mm-long 0.15-mm-diameter nickel–iron alloy wire electrodes separated by 3 mm. The setup was located in a vacuum chamber with a residual pressure of lower than 2×10^{-6} Torr. The xenon pressure was measured by a VDG-1 vacuometer.

Voltage pulses with an amplitude of 200–800 V, a repetition rate of 1–10 kHz, and an FWHM of 60–450 ns were supplied to the anode. The cathode was grounded through a 50-Ω measuring resistor. The voltage pulse rise time (from $0.1U_{max}$ to $0.9U_{max}$) was 40 ns and remained unchanged in the course of our experiments. The discharge voltage and current were measured by a two-channel wideband oscilloscope. The voltage pulses were supplied to the input of the oscilloscope through a frequency-independent divider. A signal proportional to the discharge current (from which the signal of the displacement current through the "cold" discharge gap was preliminary extracted) was supplied to the second input of the oscilloscope. For this purpose, the signals from resistors in the cathode circuit and an *RC*-circuit connected in series to the anode (the capacitance being chosen to be equal to that of the "cold" interelectrode gap) were supplied to the inputs of a differential amplifier.

A pulsed optoelectronic amplifier with a 2.8-cm-focal-length objective producing a twofold magnified image of the discharge gap was used as a system for recording the phosphor and discharge radiation with a spatial resolution of 0.1 mm. In the image plane, a variable-width diaphragm was installed. Immediately behind the diaphragm, an FÉU-115 optoelectronic amplifier with a 5-ns response time was located. The

1063-7842/05/5011-1467$26.00 © 2005 Pleiades Publishing, Inc.

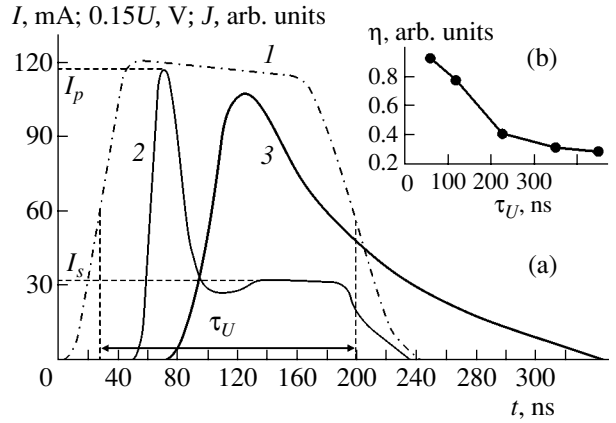

Fig. 1. Influence of the excitation duration on the characteristics of a pulsed-periodic discharge: (a) waveforms of the (*1*) voltage, (*2*) current, and (*3*) phosphor emission intensity and (b) the dependence of the light power efficiency on the voltage pulse duration.

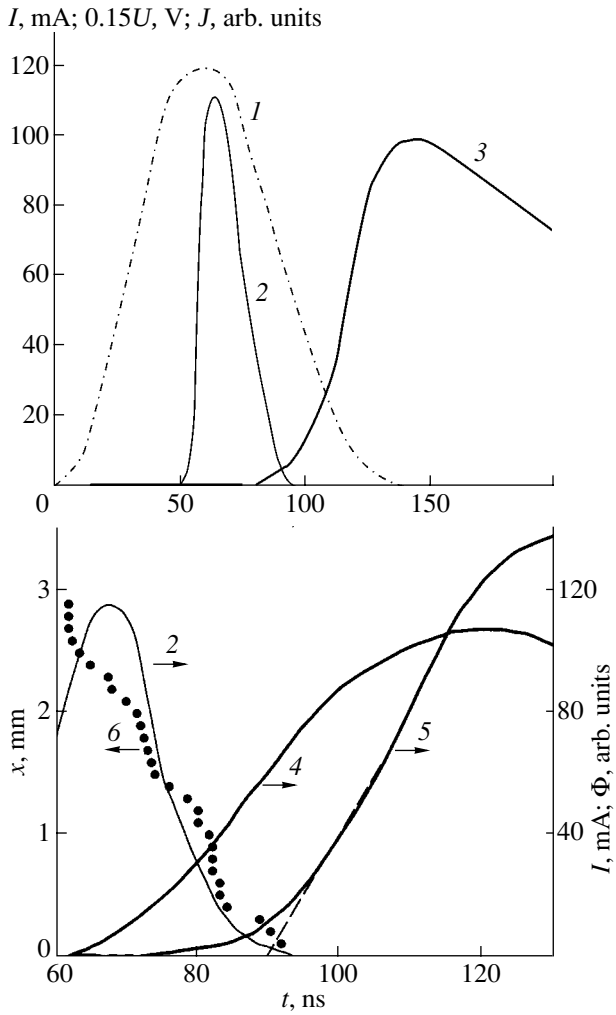

Fig. 2. Expansion of the negative glow after discharge ignition: (*1*) voltage; (*2*) current; (*3*) phosphor emission intensity; (*4, 5*) optical emission intensity from the anode and near cathode regions, respectively; and (*6*) location of the negative glow boundary.

entire system was mounted on a movable support and could be displaced in the image plane by using a micrometer screw. The light pulses were recorded by an oscilloscope with a 2-ns time resolution.

Fig. 1a shows waveforms of the voltage $U(t)$; the discharge current $I(t)$; and the anode current $J(t)$ of the optoelectronic amplifier, which is proportional to the phosphor radiation intensity. The waveforms were obtained at a 15-Torr xenon pressure and 1-kHz pulse repetition rate. At the front of the current waveform, there is a peak (with an amplitude I_p), which is followed by a rapid drop and the subsequent gradual increase with a tendency toward saturation. A steady-state discharge current of $I_s \approx 0.3I_p$ is established about 120 ns after the beginning of the discharge. The peak current I_p, the steady-state current I_s, and the amplitude of the phosphor radiation pulse depend slightly on the voltage pulse duration. An increase in the latter results only in a longer quasi-steady stage of the discharge current.

As a quantitative criterion of the conversion efficiency of the energy deposited in a discharge into UV radiation, we used the light power efficiency η,

$$\eta = \frac{\int_0^T J(t)dt}{\int_0^T U(t)I(t)dt}, \quad (1)$$

where T is the pulse repetition period.

Figure 1b shows the dependence of the light power efficiency η on the voltage pulse duration τ_U at a constant repetition period. The maximum efficiency was achieved at a voltage pulse duration below 100 ns, which was insufficient for the formation of a quasi-steady discharge. In this case, the conversion efficiency of the deposited energy into UV radiation was four times higher than that in the case of $\tau_U > 300$ ns, when an anomalous glow discharge was primarily in a quasi-steady state. Hence, UV sources in xenon are produced with the maximum efficiency due to the processes that occur when the negative glow appears, which is accompanied by a characteristic peak in the current waveform.

Figure 2 shows waveforms obtained in the case of short voltage pulses ($\tau_U \approx 70$ ns) with a repetition rate of 1 kHz. In addition to the waveforms of the voltage, current, and phosphor radiation intensity, optical radiation signals from the anode and cathode regions of the cell not covered with phosphor are also shown. In order to determine the dependence of the time at which radiation appears at a distance x between the center of the recording region and the cathode, the optical system was displaced from the anode toward the cathode through 0.1-mm steps. The results of measurements of the glow boundary propagation are presented in Fig. 2 by circles. The negative glow expands toward the cath-

ode with a velocity of ~10^7 cm/s, which is two orders of magnitude larger than the drift velocity of xenon ions under the conditions of our experiments. An increase in the voltage pulse amplitude or a decrease in the xenon pressure is accompanied by an exponential increase in the propagation velocity of the glow boundary.

A comparison between the propagation velocity of the glow boundary and the peak amplitude of the current I_p, as well as the coincidence in time of the current peak and the glow expansion, allows us to interpret the current flowing through the cathode region when the glow appears as a displacement current caused by the contraction of the region between the cathode and the negative glow. When the pulse repetition period is less than 50 μs, a plateau appears at the front of the waveform. As the repetition period decreases, the height of the plateau increases and the time delay between the voltage and current pulses decreases to zero. The peak at the front of the current pulse, which is characteristic of the negative glow expansion mode, disappears at a pulse repetition rate above 25 kHz. Investigation of the spatial distribution of the discharge optical radiation shows that, at short repetition periods ($T < 40$ μs), the aforementioned expansion of the negative glow is absent. At the same time, the phosphor radiation intensity decreases substantially: at a repetition rate of 100 kHz, it is five times lower than that at a 10-kHz repetition rate. Similar results were obtained when the xenon pressure was increased to 70 Torr.

The high conversion efficiency of the deposited energy into UV radiation in the negative glow expansion mode is confirmed by the following experiment. First, a pulsed-periodic discharge with a repetition rate of 10 kHz and, then, a dc discharge were ignited in the same cell. The discharge conditions were chosen such that the average light flux emitted by the phosphor was the same in both cases. The difference in the conversion efficiencies was evaluated by comparing the average power deposited in the pulsed-periodic discharge,

$$\langle P \rangle = \frac{1}{T}\int_0^T U(t)I(t)dt, \qquad (2)$$

and the power P_{DC} deposited in the dc discharge. A comparison of the results presented in the table shows

Table

Xenon pressure, Torr	Pulsed-periodic discharge, τ_U = 100 ns			DC discharge		
	I_p, mA	U_{max}, V	$\langle P \rangle$, mW	I_{DC}, mA	U_{DC}, V	P_{DC}, W
15	34	675	4	5.45	235	1.28
30	54	675	6	5.7	219	1.25

that the efficiency of the UV glow excitation in a pulsed-periodic discharge is two orders of magnitude higher than that in a dc discharge.

Thus, in a pulsed-periodic discharge in xenon under conditions such that each ignition is accompanied by the propagation of the negative glow boundary toward the cathode with a velocity of 10^7 cm/s, the excitation efficiency of UV radiation is much higher than in a dc discharge. When utilizing this effect, it is desirable to limit the duration of the voltage pulses by the time at which the glow approaches the cathode (100 ns under our experimental conditions). In this mode, the discharge is not accompanied by the heating and intense sputtering of the cathode. The results obtained open the way to creating efficient gas-discharge sources of vacuum UV radiation without utilizing cathodes with a protective (e.g., mercury) coating.

REFERENCES

1. S. Mikoschiba, S. Schinada, and S. Shirai, J. Appl. Phys. **58**, 3720 (1985).
2. Y. Okamoto and M. Fukushima, Jpn. J. Appl. Phys. **26**, 1100 (1987).
3. A. E. Chizhikov, Izv. Ross. Akad. Nauk, Ser. Fiz. **62**, 2034 (1998).
4. R. Ganter, Th. Callegari, J. Ouyang, *et al.*, in *Proceedings of the 15th International Symposium on Plasma Chemistry, Orlean, 2001*, Vol. 2, pp. 1335–1340.
5. G. N. Gerasimov, B. E. Krylov, A. V. Loginov, and S. A. Shchukin, Usp. Fiz. Nauk **162**, 123 (1992) [Sov. Phys. Usp. **35**, 400 (1992)].

Translated by B. Chernyavskiĭ

Technical Physics, Vol. 50, No. 11, 2005, pp. 1470–1473. Translated from Zhurnal Tekhnicheskoĭ Fiziki, Vol. 75, No. 11, 2005, pp. 78–80.

RADIOPHYSICS

Conditions for the Onset of Superradiance Regime in a Relativistic Electron Bunch

V. V. Porkhaev, N. V. Zavialov, V. T. Punin, A. V. Telnov, and Yu. A. Khokhlov†

Institute of Nuclear and Radiation Physics, Russian Federal Nuclear Center–All-Russia Research Institute of Experimental Physics, Sarov, Nizhni Novgorod oblast, 607190 Russia

e-mail: porkhaev@expd.vniief.ru

Received October 14, 2003

Abstract—Problems associated with the formation of coherent oscillations of an ensemble of classical oscillators and their superradiance instability are considered. The dispersion properties of an electron bunch and the conditions for the generation of nonequilibrium radiation are determined in the quasi-steady anharmonic oscillator approximation. © *2005 Pleiades Publishing, Inc.*

In an early paper [1], Ginzburg proposed a method for converting the kinetic energy of relativistic beams of charged particles into electromagnetic radiation. The method is based on the oscillations of charges in the field of an external wave (in the undulator field). The first undulator source—a free electron laser (FEL)—for producing coherent optical light was build in the middle of the 1970s [2]. At present, FELs are capable of generating light over a broad spectral range (see, e.g., [3]).

Problems concerning the radiative instability of classical oscillators and their interaction with electromagnetic fields were studied in quite a number of papers (see, e.g., [4] and the literature cited therein). Since the active medium in an FEL is a relativistic electron bunch, the formation of the field of stimulated radiations is a necessary condition for the generation of laser light. By its very nature, the field of stimulated radiations is nonequilibrium with respect to the energy of electron oscillations in the undulator field; it is generated as a result of the energy exchange between a nonequilibrium electromagnetic wave (primary radiation) and oscillating electrons (oscillators). In theoretical papers, the presence of the field of nonequilibrium radiations in an ensemble of oscillators is attributed to random processes [5, 6], to the presence of an external source [7, 8], or to such a width of the energy distribution of the beam electrons at which the oscillators can efficiently exchange their energy via radiative transfer [9–11]. Kurilko and Ognivenko [12] obtained the following condition for the generation of stimulated (collective) radiation in a relativistic electron beam: $N \gg 1$, where N is the number of electrons in a bunch with a size equal to the bremsstrahlung wavelength in a frame of reference associated with the guiding center of the bunch.

The objective of the present paper is to determine the possibility, as well as the conditions, for the onset of the superradiance instability (the superradiance regime) of a relativistic electron bunch in an undulator whose parameters are optimal for the generation of the lowest radiation mode. By the superradiance instability we mean the generation of nonequilibrium radiation in an electron gas due to the random fluctuations of the radiation field that are amplified by the energy exchange between this field and the oscillating electrons.

Let us consider the generation of electromagnetic radiation by a relativistic electron bunch ($v_e \approx c$) with a space charge density g that moves along the z axis in the destabilizing undulator field $\mathbf{H}(z) = \mathbf{q}_H H_0 f(z)$, where $\mathbf{q}_H$ is a unit vector in the direction of the field $\mathbf{H}(z)$ and $f(z)$ is a periodic function of z. We assume that $\mathbf{v}_e \perp \mathbf{H}(z)$ and that the electron bunch is a closed equilibrium system in which the individual electrons can exchange energy with a radiation field of any nature. We describe the electron energy distribution in the bunch by the function $F(\gamma)$ (with γ being the relativistic factor) such that $\Delta\gamma \ll \gamma_c$ (where γ_c is the most probable electron energy for a given distribution and $\Delta\gamma$ is the distribution width) under the additional assumptions that there are no Coulomb interactions between the electrons, electron losses are absent, and the parameters of the undulator and of the electron injector are optimal for the generation of the lowest bremsstrahlung mode.

In the field of the force $\mathbf{F}_L(z) = e\mathbf{v}_e \times \mathbf{H}(z)/c$, each bunch electron moves along the vector $\mathbf{q}_L = \mathbf{q}_v \times \mathbf{q}_H$ (where $\mathbf{q}_L$ and $\mathbf{q}_v$ are unit vectors in the directions of the force $\mathbf{F}_L(z)$ and the velocity $\mathbf{v}_e$) in "its own" potential well (the electron gas is magnetized in the z direction).

† Deceased.

1063-7842/05/5011-1470$26.00 © 2005 Pleiades Publishing, Inc.

This is why, for virtually any value of the space charge density, we can ignore the effects associated with the fine structure of the electron bunch and thereby can describe the processes in terms of classical electrodynamics and field theory.

We consider the dynamics of an individual electron in the frame of reference associated with its guiding center (in what follows, this frame of reference will be denoted by K'). In the frame K', the plane wave of the undulator field is described by the expression $\mathbf{H}(t) = \mathbf{q}_H H_0 \xi(t)$, where $\xi(t)$ is a bounded function with the period T_u. The field strength of bremsstrahlung from a point charge, $\mathbf{E}_{Bs}(t)$, is generally related to the field potentials $\mathbf{A}(t)$ and φ by the relationship $\mathbf{E}_{Bs}(t) = -d\mathbf{A}(t)/(cdt) - \nabla\varphi$. Since the scalar potential φ possesses central symmetry in the frame K' and since the vector potential is given by the expression $\mathbf{A}(t) = e\mathbf{v}_L(t)/(cR - \mathbf{v}_L(t)\mathbf{R})$ (where $\mathbf{v}_L$ is the velocity acquired by the electron under the action of the force $\mathbf{F}_L$ and $\mathbf{R}$ is the position vector from the origin of the frame K' to the observation point), the oscillating vectors $\mathbf{E}_{Bs}(t)$ and $\mathbf{H}(t)$ are mutually orthogonal and have the same phase. In this case, the bunch electrons move in the crossed fields $\mathbf{E}$ and $\mathbf{H}$ and, in the z direction, the dielectric constant of the electron gas is real (there are no free charges in the direction of the vector $\mathbf{q}_L$). Hence, for a transverse wave propagating along the z axis, the magnetized electron gas behaves as a dielectric [13].

Let there be an ensemble of N_a oscillators near the ith electron within a volume V_a whose dimensions are determined by the radiation wavelength, and let the oscillators interact with the field E_i of the radiation emitted by the electron. In turn, the dynamics of the ith electron is influenced by the radiation field of the ensemble of oscillators. We turn to the quasi-steady anharmonic oscillator approximation and assume that the parameters of the system under consideration do not vary during the period T_u. In this case, we can describe the system by using the Bush theorem of the conservation of the angular moment of an electron in the case of radiative interaction in the bunches of oscillators [14]. In the generation regime, each electron of the bunch simultaneously emits its own bremsstrahlung and amplifies the radiation that is nonequilibrium with respect to the energy of its oscillations in the undulator field. The field strength of the bremsstrahlung emitted by the electron is described by the relationship $E_{bs\,i} = (2gDr_e^2\gamma_i H_0^2/3)^{1/2}$ [15]. We take the limit $\Delta\gamma \ll \gamma_c$ and assume that the initial oscillations performed by oscillators are incoherent to see that the averaged (over the volume V_a) intensity of the bremsstrahlung emitted by an ensemble of $N_a$oscillators is directly proportional to the sum $\sum_i E_{Bsi}^2$. The number N_a can be determined from the synchronization condition in the frame K': $\omega_c' \Delta t = \pi$, where ω_c' is the most probable bremsstrahlung frequency for a given distribution $F(\gamma)$. In this case, the ensemble of oscillators in question is within a volume bounded by a spherical surface of radius $R_S = \lambda_c'/2$ and we have $N_a = gV_a = g\pi D^3/(6\gamma_c^3)$.

SPONTANEOUS RADIATION REGIME

In the laboratory frame of reference, the intensity of the radiation emitted by an electron bunch is the sum of the intensity of spontaneous emissions from the electrons, I_{sp}, in the undulator field and the intensities of stimulated emission from each of the electrons, I_{st}, in the radiation field of an ensemble of N_a neighboring oscillators. In this case, the total intensity of the lowest radiation mode generated in a unit volume of the electron bunch is equal to [15]

$$I_{\text{tot}}(\gamma_i) = I_{sp} + I_{st} = \frac{2e^4 g}{3m^2c^3}(H_0^2\gamma_i^2 + E_{Bs}^2 N_a \sin^2 \Delta\omega_i' t), \quad (1)$$

where $\Delta\omega_i' = \omega_i' - \omega_c'$ is the characteristic frequency of the electron injector.

The field strength E_{Bs} of the spontaneous emission from an ensemble of N_a oscillators is related to the intensity $I_a = I_{sp}N_a/(4\pi)$ by the formula $E_{Bs}^2 = gDI_{sp}/(c\gamma)$, so we have

$$\frac{E_{Bs}^2}{H_0^2} = \frac{2}{3}D\gamma g r_e^2, \quad (2)$$

where D is the undulator period and $r_e = e^2/m_e c^2$ is the classical radius of an electron.

It follows from relationship (1) that the function $I_{\text{tot}}(\gamma)$ is nonmonotonic and has an optimum value at the point at which the following equality (obtained with allowance for formula (2)) is satisfied:

$$\frac{\omega_p^2}{\omega_i'^2} = \frac{\sqrt{6}}{\sqrt{\pi}\sin(\omega_i' - \omega_c')t}, \quad (3)$$

where $\omega_p^2 = 4\pi g e^2/m_e$ is the Langmuir frequency of the electron gas.

In terms of the equations for electron dynamics in the field $H(t)$ of a plane wave, the function $F(\gamma)$ describes the frequency and width of the spectral line of the bremsstrahlung emitted by an electron. However, radiative energy exchange is collective in nature and is largely governed by such parameters of the medium as the width $\Delta\omega'$ of the spectral line of radiation from a wave packet and the temporal energy-exchange parameter Δt. Consequently, in the frame K', the quantity $\Delta\omega_i' = |\omega_i' - \omega_c'|$ in formulas (1) and (3) should, first of all, satisfy the uncertainty relation $\Delta\omega'\Delta t = \pi$, i.e., $\Delta\omega' =$

$\pi c/r_a n(\omega_c')$, where r_a is the mean distance between the electrons and $n(\omega_c')$ is the refractive index of an electron gas at the frequency ω_c' that is most probable for a given distribution $F(\gamma)$. Since $\Delta\omega' = \omega_c'\Delta\gamma/\gamma_c$, we see that $r_a^{\min} = \pi c\gamma_c/(\omega_c' n(\omega_c')\Delta\gamma) = D/(2\Delta\gamma)$, so, in the limit $r_a \longrightarrow r_a^{\min} = \lambda'/2 = D/(2\gamma_c)$, we obtain $\Delta\omega' \longrightarrow \omega_c'$. Hence, for $r_a \le \lambda'/2 < R_S$ and $\Delta\gamma \ll \gamma_c$, we have $\Delta\omega' \gg \Delta\omega_i'$, which means that the shape of the distribution function $F(\gamma)$ has essentially no effect on the width of the spectral line characteristic of the radiative energy exchange between the electrons in the bunch. From relationship (3) we thus readily find the minimum value of the refractive index of the electron gas for a transverse radiation wave with the frequency ω_i' propagating along the z axis:

$$n_z^{\min}(\omega_i') = \sqrt{1 + \frac{\omega_p^2}{\omega_i'^2}} = 1.54.$$

The dispersion properties of the medium govern its response to an electromagnetic perturbation. From formula (3) it follows that, along the undulator axis, the magnetized electron gas is completely opaque to the bremsstrahlung at the frequency ω_c' that is most probable for a given distribution $F(\gamma)$. In such a medium, for $\omega_p > \omega_i'$, the field E_{Bs} is attenuated due to its resonant interaction with the particles of the medium and falls off to zero at a distance of about $\sim\lambda_c'$ [16]. The electrons absorb the energy of the field E_{Bs} and reemit it, the phase difference between the emitted electromagnetic wave and the field E_{Bs} being $\pi/2$. The result is the formation of the field of nonequilibrium radiations E_{pr} in an ensemble of oscillators. Since there are no other mechanisms whereby the energy of the field E_{Bs} is dissipated, for a monoenergetic electron bunch we can set $E_{pr}(\omega_c') \approx E_{Bs}$; note that, in this case, the fields E_{Bs} and E_{pr} have the same direction and are polarized to the same extent. The minimum value of the refractive index, $n_z^{\min} = 1.54$, determines the condition for the existence of the field E_{pr} and for the transition of an ensemble of oscillators to the superradiance regime, specifically, the condition $g_{tr} \ge \sqrt{6}\gamma_c^2/\sqrt{\pi}D^2 r_e$ for the space charge density of the bunch.

SUPERRADIANCE REGIME

The radiative energy exchange between the electrons in the bunch gives rise to the field of the coherent oscillations performed by oscillators, whose radiation intensity is directly proportional to

$$E_{Bs\,SR}^2 = \left(\sum_{i=1}^{N_{\rm coh}} E_{Bs\,i}\right), \quad (4)$$

where $N_{\rm coh} = g_{SR}V_{\rm coh}$, with g_{SR} being the space charge density in the superradiance regime and $V_{\rm coh}$ being the volume of the region in which the field of coherent oscillations executed by oscillators has been formed.

However, for $r_a \sim \lambda'/2$, the spectral range characteristic of the radiative energy exchange broadens and we have $\lambda_c' \sim \Delta\lambda'$. As a result, the radiative energy exchange becomes far less efficient; so, within the volume V_a, binary interactions between the oscillators are most probable. In this case, the region of coherent oscillations is a spherical layer of radius $r_0 = \lambda'/2$ and thickness $\delta = \Delta\lambda'$. At $\Delta\gamma \ll \gamma_c$, the volume of the layer is equal to $V_{\rm coh} = \pi D^3\Delta\gamma/(2\gamma^4)$ and we have $N_{\rm coh} = 3\Delta\gamma N_a/\gamma_c$. For $\gamma_i = \gamma_c$, relationship (1) reads

$$I_{\rm tot}(\gamma_c) = I_{sp} + I_{st} = \frac{2e^4 g}{3m^2c^3}(H_0^2\gamma_c^2 + E_{Bs}^2 N_{\rm coh}^2). \quad (5)$$

From relationship (5) we can easily determine the electron energy that is optimal for superradiance from the active medium of an FEL. With allowance for formula (2), this energy is equal to $\gamma_c^{\rm opt} = (2\pi^2 D^7 g^3 r_e^2 \Delta\gamma^2/3)^{1/9}$. From this it follows that the optimal condition for the generation of coherent radiation by an electron bunch in the superradiance regime is $g_{SR} = (3\gamma_c^9/2\pi^2 D^7 r_e^2 \Delta\gamma^6)^{1/3}$. At this value of the space charge density of the bunch, we have $\omega_p \ll \omega_c'$ and, moreover, $g_{SR}/g_{tr} = (r_e/\sqrt{96\pi}\lambda'\Delta\gamma^2)^{1/3} \ll 1$. For the superradiance regime, we can readily obtain the dispersion of an electron gas magnetized in the z direction:

$$n_{SR}(\omega') = \sqrt{1 + \left(\frac{9N_a}{4\pi^3 N_{\rm coh}^2}\right)^{1/2}} \le 1.13.$$

Hence, the transition of the active medium of an FEL to the superradiance regime is a threshold process whose characteristic parameter is the frequency of Langmuir oscillations of the electron gas. The measure of the threshold level can be the refractive index of the medium, $n_z \ge 1.54$, at which the frequency of Langmuir oscillations of the electron gas is comparable to the frequency of electron oscillations in the undulator field. Under such conditions, the active medium of the laser generates radiation that is nonequilibrium with respect to the energy of electron oscillations in the undulator field and the field of coherent oscillations of an ensemble of oscillators forms. In the superradiance regime, the optimum value of the space charge density of an electron bunch is $n_z \le 1.13$.

REFERENCES

1. V. L. Ginzburg, Izv. Akad. Nauk SSSR, Ser. Fiz. **11**, 165 (1947).
2. D. A. G. Deacon, L. R. Elias, J. M. J. Madeys, *et al.*, Phys. Rev. Lett. **38**, 892 (1977).
3. *Proceedings of the 23rd International Free Electron Laser Conference and the 8th FEL Users Workshop, Darmstadt, 2001*; Nucl. Instrum. Methods Phys. Res. A **483**, 1 (2002).
4. M. V. Fedorov, Usp. Fiz. Nauk **135**, 213 (1981) [Sov. Phys. Usp. **24**, 801 (1981)].
5. A. V. Gaponov, Zh. Éksp. Teor. Fiz. **39**, 326 (1960) [Sov. Phys. JETP **12**, 232 (1960)].
6. A. V. Gaponov, M. I. Petelin, and V. K. Yulpatov, Izv. Vyssh. Uchebn. Zaved., Radiofiz. **10**, 1414 (1967).
7. A. M. Kondratenko and E. L. Saldin, Zh. Tekh. Fiz. **51**, 1633 (1981) [Sov. Phys. Tech. Phys. **26**, 937 (1981)].
8. A. A. Kolomenskiĭ and A. N. Lebedev, Kvantovaya Élektron. (Moscow) **5**, 1543 (1978).
9. A. G. Bonch-Osmolovskiĭ, S. N. Dolya, and K. A. Reshetnikova, Zh. Tekh. Fiz. **53**, 1055 (1983) [Sov. Phys. Tech. Phys. **28**, 639 (1983)].
10. V. I. Kurilko and Yu. V. Tkach, Usp. Fiz. Nauk **165**, 241 (1995) [Phys. Usp. **38**, 231 (1995)].
11. N. S. Ginzburg, Pis'ma Zh. Tekh. Fiz. **14**, 440 (1988) [Sov. Tech. Phys. Lett. **14**, 197 (1988)].
12. V. I. Kurilko and V. V. Ognivenko, Dokl. Akad. Nauk **335**, 437 (1994) [Phys. Dokl. **39**, 214 (1994)].
13. I. E. Tamm, *The Principles of the Theory of Electricity* (Nauka, Moscow, 1976) [in Russian].
14. L. G. Lomize and N. N. Sveshnikova, Pis'ma Zh. Tekh. Fiz. **5**, 611 (1979) [Sov. Tech. Phys. Lett. **5**, 250 (1979)].
15. L. D. Landau and E. M. Lifshitz, *Course of Theoretical Physics*, Vol. 2: *The Classical Theory of Fields* (Nauka, Moscow, 1988; Pergamon, Oxford, 1975).
16. L. Spitzer, *Physics of Fully Ionized Gases* (Interscience Publ., New York, 1962; Mir, Moscow, 1965).

Translated by O. Khadin

Technical Physics, Vol. 50, No. 11, 2005, pp. 1474–1478. Translated from Zhurnal Tekhnicheskoĭ Fiziki, Vol. 75, No. 11, 2005, pp. 81–85.

RADIOPHYSICS

Interference of Co- and Counterpropagating Waveguide Modes in a Planar Structure

Yu. N. Kuznetsov and D. I. Sementsov

Ulyanovsk State University, Ulyanovsk, 432700 Russia

e-mail: sementsovdi@ulsu.ru

Received November 12, 2004

Abstract—Interference between inhomogeneous waves in a planar waveguide placed in a perfectly conducting environment is studied. It is shown that the interference flux of copropagating waveguide *TM* modes behaves like counterpropagating homogeneous volume waves. The longitudinal and transverse components of the interference fluxes of co- and counterpropagating waves in the general case result from interference between both the active and reactive components of the field. The interference flux of waveguide modes may also be observed when the partial fluxes of the modes equal zero. © *2005 Pleiades Publishing, Inc.*

INTRODUCTION

Interest in wave phenomena occurring in media with complex and/or negative material parameters, namely, ε and μ [1–5], is largely associated with the problem of redistributing energy fluxes when an electromagnetic wave leaves an absorbing medium for a transparent one [4, 5]. This problem is intimately related to the effect of decreased absorption in thin metal films due to interference between counterpropagating waves. This interference was called "tunnel" [6–8], because the wavevectors of waves traveling in a highly absorbing medium have an imaginary part. It was shown [9] that interfering reactive components of wave fields generate interference fluxes (IFs) even in those directions where the initial waves do not necessarily transfer the energy. In the available publications, tunnel interference is analyzed mostly for the case of homogeneous waves passing through a layer in the normal direction. However, interference has a significant effect on propagation of inhomogeneous waves in various guiding structures. It was shown [10] that the structure and direction of the IF in the case of inhomogeneous co- and counterpropagating waves exhibit intriguing features that are absent when homogeneous waves interfere. The most important guiding structure is a planar waveguide, which can support both volume [11] and surface [12] inhomogeneous waves (modes). The type of wave propagation in a waveguide depends on the material of its layers and on the type of propagating mode. Interference between inhomogeneous waves is easiest to analyze by the example of modes propagating in a waveguide consisting of a planar dielectric layer sandwiched in ideal conductors, which are barriers for the waveguide mode field. With such a structure, one can derive fairly simple analytical expressions for the mode fields and gain insight into interference between inhomogeneous volume modes in a guiding structure. In this work, we consider interference between *TM* modes copropagating and counterpropagating in the waveguide mentioned above and analyze the effect of the active and reactive components of the energy flux in the structure.

WAVEGUIDE MODE FIELDS AND ENERGY FLUXES

Consider a planar waveguiding layer of thickness d and permittivity ε sandwiched in ideal conductors (the top layer and substrate). The interfaces coincide with the planes $x = 0$ and $x = d$. Let *TM* waveguide modes, which are the subject of analysis here, propagate in the positive z direction. With regard to the boundary conditions for these modes, the solutions to the Maxwell equations inside the layer can be written as follows:

$$H_{ny} = H_0 \cos q_n x \exp[i(\omega t - \beta_n z)],$$
$$E_{nx} = \frac{\beta_n}{k_0 \varepsilon} H_{ny}, \quad E_{nz} = \frac{i}{k_0 \varepsilon} \frac{\partial H_{ny}}{\partial x}, \tag{1}$$

where n is the mode order, $k_0 = \omega/c$, ω is the frequency, and c is the speed of light in free space.

The propagation constant and transverse wavenumber of the modes are given by $\beta_n = (k_0^2 \varepsilon\mu - q_n^2)^{1/2}$ and $q_n = \pi n/d$, respectively. Permittivity ε and permeability μ of the waveguiding layer are generally frequency-dependent complex quantities. The projections of the energy flux density for the *TM* mode are expressed as

$$S_{nz} = \frac{c}{8\pi} \mathrm{Re}(E_{nx} H_{ny}^*)$$
$$= \frac{c}{8\pi k_0} \mathrm{Re}\left(\frac{\beta_n}{\varepsilon}\right) H_0^2 \cos^2 q_n x \exp(2\mathrm{Im}\beta_n z), \tag{2}$$

1063-7842/05/5011-1474$26.00

$$S_{nx} = -\frac{c}{8\pi}\mathrm{Re}(E_{nz}H_{ny}^*)$$
$$= -\frac{cq_n}{16\pi k_0}\frac{\mathrm{Im}\varepsilon}{\varepsilon\varepsilon^*}H_0^2\sin 2q_n x\exp(2\mathrm{Im}\beta_n z). \quad (3)$$

The energy flux projection onto the z axis is defined by the wave field active components: it is proportional to the real part of factor β_n/ε, which relates field components E_{nx} and H_{ny}. If β_n and ε are real, these field components are in phase. The energy flux projection onto the x axis depends on the wave field reactive components: it is proportional to the imaginary part of ε. This component of the energy flux changes sign at points $x_l = \pi l/2q_n$. At real ε, field components H_{ny} and E_{nz} are shifted in phase by $\pi/2$; accordingly, the flux in the x direction is absent. It also follows from (2) that, when ε is real and negative, flux component S_{nz} and propagation constant β_n have opposite signs and so one can speak of backward waves [3]. For the mode propagation constant to be real in this case, it is necessary that the conditions $\varepsilon < 0$ and $\mu < 0$ be met simultaneously.

The role of flux component S_{nx}, which appears when $\mathrm{Im}\varepsilon \neq 0$, can be clarified by analyzing an expression for the thermal power released by a waveguide mode in a unit volume of a lossy medium,

$$Q_n = \frac{\omega}{8\pi}[\mathrm{Im}\varepsilon(E_{nz}E_{nz}^* + E_{nx}E_{nx}^* + \mathrm{Im}\mu H_{ny}H_{ny}^*]$$
$$= Q_{nz} + Q_{nx} + Q_{ny}, \quad (4)$$

where $Q_{n\alpha}$ is the partial heat release due to a particular field component.

From the above relationships, it follows that energy flux component S_{nx} is responsible for heat release component Q_{nz}, which is associated with field component E_{nz}. At each point, this component of the energy flux is directed toward the nearest maximum of Q_{nz}, the maxima of Q_{nz} being localized at points $x_l = (2l + 1)\pi/2q_n$. Flux component S_{nz} is responsible for heat release component $Q_{nx} + Q_{ny}$, which is associated with field components E_{nx} and H_{ny}. The maxima of S_{nz} and $Q_{nx} + Q_{ny}$ are localized at points $x_l = l\pi/q_n$. Figure 1 shows the distributions of energy flux components S_{nz} and S_{nx} across the waveguiding layer for the waveguide mode $n = 2$ (curves *1* and *2*, respectively, in the upper part of Fig. 1), as well as of heat release components Q_{nx} and Q_{nx} (curves *1* and *2*, respectively, in the lower part) for this mode ($Q_{ny} = 0$ at $\mathrm{Im}\mu = 0$). Hereafter, we take $\varepsilon = 2–10^{-5}i$, $\mu = 1$, and $\omega = 3 \times 10^{15}$ s^{-1}. Thus, in a dissipative planar waveguide, the x component of the energy flux provides energy transfer from the nodes to antinodes (the regions of intense heat release) of a standing wave along the x axis, which arises even if a single mode propagates in the waveguide. This flux component is nonzero even if the wave cannot propagate, i.e., when β_n is imaginary, but vanishes in a nondissipative medium. The run of S_{nx} with the structure parameters and x coordinate suggests that this dependence is of interference character.

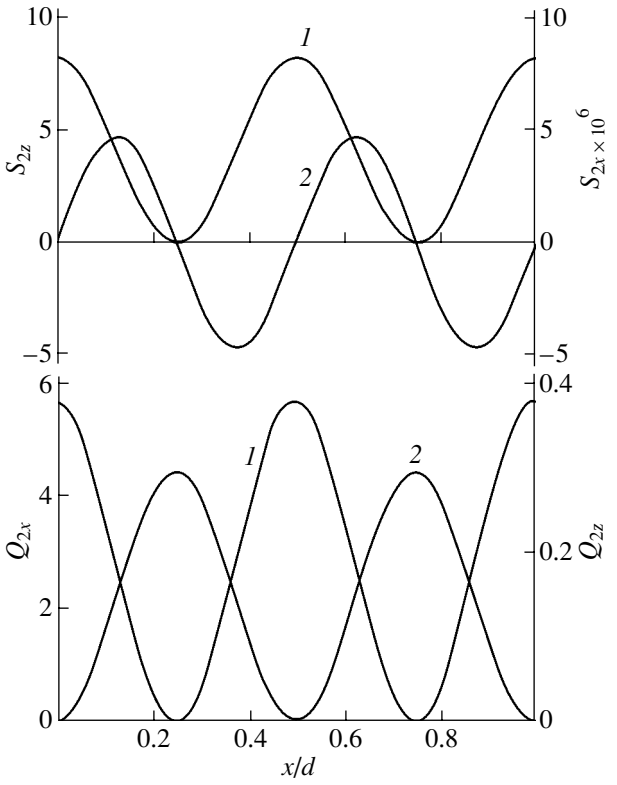

Fig. 1. Distribution of the longitudinal and transverse components of the flux and of the heat release components for the mode $n = 2$ across the thickness of the waveguide.

INTERFERENCE BETWEEN COPROPAGATING MODES

Let two waveguide modes propagating in the positive z direction be shifted in phase by φ in the plane $z = 0$. For one of these modes (subscript a), field components H_{ay}, E_{ax}, and E_{az} are given by Eqs. (1), where H_0 should be replaced by H_{0a}; n, by n_a; β_n, by β_a; and q_n, by q_a. The magnetic component of the field of the other wave (subscript b) is given by

$$H_{by} = H_{0b}\cos q_b x\exp[i(\omega t - \beta_b z - \varphi)]; \quad (5)$$

for electric components E_{bx} and E_{bz}, Eqs. (1) remain valid.

For the total field, the time-averaged energy flux density can be represented (according to the principle of superposition of fields) as a sum of the flux densities for individual modes and IFs,

$$S_z = \frac{c}{8\pi}\mathrm{Re}[(E_{ax} + E_{bx})(H_{ay}^* + H_{by}^*)] = S_{az} + S_{bz} + S_z^{\mathrm{int}},$$
$$S_x = -\frac{c}{8\pi}\mathrm{Re}[(E_{az} + E_{bz})(H_{ay}^* + H_{by}^*)] = S_{ax} + S_{bx} + S_x^{\mathrm{int}}. \quad (6)$$

Here, the flux components for each of the modes are given by relationships (2) and (3), where H_0 should be replaced by H_{0a} or H_{0b}; n, by n_a or n_b; β_n, by β_a or β_b; and q_n, by q_a or q_b. The IF components are expressed as

$$S_z^{\text{int}} = \frac{c}{8\pi}\text{Re}(E_{ax}H_{by}^* + E_{bx}H_{ay}^*)$$

$$= \frac{c}{8\pi k_0}H_{0a}H_{0b}\cos q_a x\cos q_b x\exp(\text{Im}2\beta z) \quad (7)$$

$$\times[\text{Re}(2\beta/\varepsilon)\cos(\text{Re}\Delta\beta z - \varphi) + \text{Im}(\Delta\beta/\varepsilon)\sin(\text{Re}\Delta\beta z - \varphi)],$$

$$S_x^{\text{int}} = -\frac{c}{8\pi}\text{Re}(E_{az}H_{by}^* + E_{bz}H_{ay}^*)$$

$$= -\frac{c}{16\pi k_0\varepsilon\varepsilon^*}H_{0a}H_{0b}\exp(\text{Im}2\beta z) \quad (8)$$

$$\times[\text{Im}\varepsilon(2q\sin\Delta qx + \Delta q\sin 2qx)\cos(\text{Re}\Delta\beta z - \varphi) + \text{Re}\varepsilon(2q\sin\Delta qx + \Delta q\sin 2qx)\sin(\text{Re}\Delta\beta z - \varphi)],$$

where $\beta_a + \beta_b = 2\beta$, $\beta_a - \beta_b = \Delta\beta$, $q_a + q_b = 2q$, and $q_a - q_b = \Delta q$.

From (7), it follows that the z component of the IF for identical modes ($n_a = n_b$) is associated with interference between homogeneous waves, i.e., between the active components, which depend on x and z in the same way as the single wave flux. For modes with different indices ($n_a \neq n_b$), the IF acquires a z component due to interference between the reactive components. For homogeneous waves, this component is present when counterpropagating waves interfere and is absent when interference between copropagating ones takes place. In this case, the active and reactive components exhibit a similar dependence on x and, along with the damping, similar (phase-shifted by $\pi/2$) slowly oscillating dependences on z (with a period, which is the reciprocal of $\text{Re}\Delta\beta$).

Note that, if β and β/ε are purely imaginary (for example, when mode numbers n_a and n_b differ significantly or the real part of the permittivity is negative), the waveguide modes cannot propagate and their x components equal zero. However, the z component of the IF is other than zero in this case,

$$S_z^{\text{int}} = -\frac{c}{8\pi k_0}H_{0a}H_{0b}\cos q_a x\cos q_b x \times \text{Im}(\Delta\beta/\varepsilon)\exp(\text{Im}2\beta z)\sin\varphi. \quad (9)$$

From (9), it follows that, depending on φ, the IF may be either codirected with both modes (the cocurrent IF) or counterdirected with both modes (the countercurrent IF of copropagating modes). In the case of volume homogeneous waves, such effects are absent for copropagating waves and arise only when counterpropagating waves interfere.

For identical modes, the IF x component is equal to the flux of either of the modes. This shows up in the presence of only the reactive component, which depends on x and z in the same way as the single mode flux. In the case of various modes, the IF acquires an active (x) component, which is present even if the fluxes of individual modes in a given direction are absent (ε is real). In this case, the active and reactive components, along with the damping, exhibit similar (phase-shifted by $\pi/2$) slowly oscillating (with a period, which is the reciprocal of $\text{Re}\Delta\beta$) dependences on z and somewhat differing periodic dependences on x. Figure 2a shows the components of total energy flux S_z at $z = 0$ (curve *1*), as well as components S_z^{int} and S_x^{int} of the IF (curves *2* and *3*), across the guiding layer for copropagating modes $n_a = 2$ and $n_b = 1$ of equal amplitude at $\varphi = \pi/3$ and $L = 1$ cm. Figure 2b demonstrates the variation of the envelopes of the component distributions along the waveguide. It is seen that component S_z^{int} is comparable in amplitude to total flux S_z in this direction. When modes are weakly absorbed, the flux along the x axis is almost completely an interference flux; therefore, the curve for $S_x(x)$ is omitted in Fig. 2: it nearly completely coincides with the curve for $S_x^{\text{int}}(x)$ on the scale selected. This is because the x components of the single mode fluxes have only a small reactive component, which is proportional to $\text{Im}\varepsilon$, while the x component of

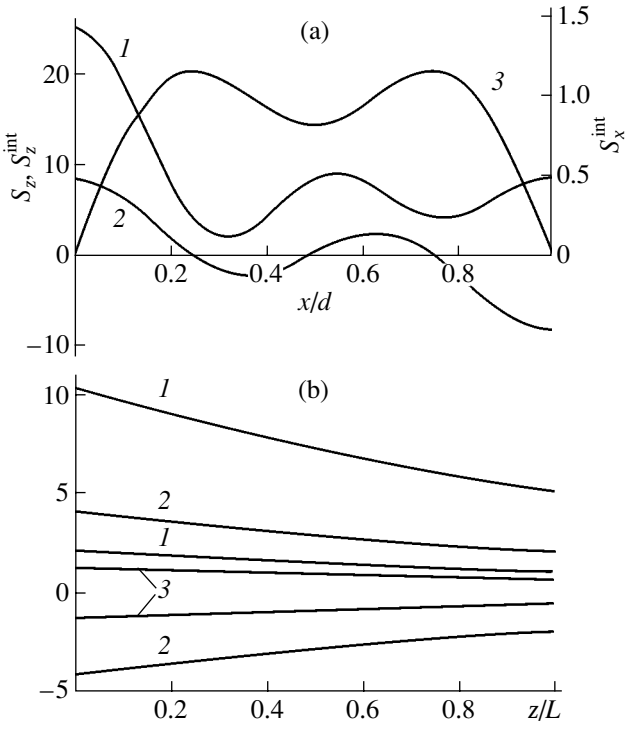

Fig. 2. Distribution of (a) the components of the total and interference fluxes for copropagating modes $n_a = 2$ and $n_b = 1$ along the thickness of the waveguide and (b) the envelopes of the components along the waveguide.

the IF has a large active component, which is proportional to $\mathrm{Re}\varepsilon$. As follows from (7) and (8), the coordinate dependence of the IF z component is always defined by the product of the independent functions of z and x. When absorption is weak, the same is true for the IF x component (except for copropagating modes of the same order with the zero phase shift).

INTERFERENCE OF COUNTERPROPAGATING MODES

Consider two *TM* modes propagating along the z axis toward each other. Let they have phase difference φ in the planes $z = -L$ and $z = L$. For the mode propagating in the positive z direction, the magnetic component of the field is written as

$$H_{ay} = H_{0a}\cos q_a x \exp[i(\omega t - \beta_a z - \beta_a L)] \quad (10)$$

and the electric components are defined by Eqs. (1). For the flux components of this mode, we have

$$S_{az} = \frac{c}{8\pi k_0}\mathrm{Re}\left(\frac{\beta_a}{\varepsilon}\right)H_{0a}^2\cos^2 q_a x \exp[2\mathrm{Im}\beta_a(z+L)],$$
$$S_{ax} = -\frac{cq_a}{16\pi k_0}\frac{\mathrm{Im}\varepsilon}{\varepsilon\varepsilon^*}H_{0a}^2\sin 2q_a x \exp[2\mathrm{Im}\beta_a(z+L)]. \quad (11)$$

With regard to a phase difference, the field components of the counterpropagating mode obey the following relationships:

$$H_{by} = H_{0b}\cos q_b x \exp[i(\omega t + \beta_b z - \beta_b L + \varphi)],$$
$$E_{bx} = -\frac{\beta_b}{k_0\varepsilon}H_{by}, \quad E_{bz} = \frac{i}{k_0\varepsilon}\frac{\partial H_y}{\partial x}. \quad (12)$$

The energy flux components for this mode are given by

$$S_{bz} = -\frac{c}{8\pi k_0}\mathrm{Re}\left(\frac{\beta_b}{\varepsilon}\right)H_{0b}^2\cos^2 q_b x \times \exp[-2\mathrm{Im}\beta_b(z-L)],$$
$$S_{bx} = -\frac{cq_b}{16\pi k_0}\frac{\mathrm{Im}\varepsilon}{\varepsilon\varepsilon^*}H_{0b}^2\sin 2q_b x \times \exp[-2\mathrm{Im}\beta_b(z-L)]. \quad (13)$$

As for copropagating modes, the time-averaged energy flux density for the total field can be represented as a sum of the single mode fluxes and the IF. According to (7) and (8), the IF components for counterpropagating waves are given by

$$S_z^{\mathrm{int}} = \frac{c}{8\pi k_0}H_{0a}H_{0b}\cos q_a x \cos q_b x \exp[\mathrm{Im}(\Delta\beta z + 2\beta L)] \times \left\{\mathrm{Re}\left(\frac{\beta_a}{\varepsilon}\right)\cos[\mathrm{Re}(2\beta z - \Delta\beta L) - \varphi] - \mathrm{Re}\left(\frac{\beta_b}{\varepsilon}\right)\cos[\mathrm{Re}(2\beta z + \Delta\beta L) - \varphi] + \mathrm{Im}\left(\frac{\beta_a}{\varepsilon}\right)\sin[\mathrm{Re}(2\beta z - \Delta\beta L) - \varphi] + \mathrm{Im}\left(\frac{\beta_b}{\varepsilon}\right)\sin[\mathrm{Re}(2\beta z + \Delta\beta L) - \varphi]\right\}, \quad (14)$$

$$S_x^{\mathrm{int}} = -\frac{c}{16\pi k_0\varepsilon\varepsilon^*}H_{0a}H_{0b}\exp[\mathrm{Im}(\Delta\beta z + 2\beta L)] \times \{\mathrm{Im}\varepsilon(2q\sin 2qx + \Delta q\sin\Delta qx) \times \cos[\mathrm{Re}(2\beta z - \Delta\beta L) + \varphi] + \mathrm{Re}\varepsilon(\Delta q\sin 2qx + 2q\sin\Delta qx) \times \sin[\mathrm{Re}(2\beta z + \Delta\beta L) + \varphi]\}. \quad (15)$$

If the modes are identical, the z component of the IF contains only the reactive component, which oscillates along the z axis and depends on x in the same way as the single mode flux, as follows from (14). At different modes, the IF has also an active z component. The active and reactive components exhibit the same periodic dependence on x, the same damping (at $\mathrm{Im}\beta_a \neq \mathrm{Im}\beta_b$), and slightly different oscillating dependences on z (with an oscillation period proportional to $(\mathrm{Re}\,2\beta)^{-1}$). Unlike the IF for copropagating waves and individual waves, the damping of the IF for counterpropagating waves is weak, since it depends on the difference between the imaginary parts of the mode propagation constants. When $\mathrm{Im}\beta_a = \mathrm{Im}\beta_b$, the IF of counterpropagating waves becomes undamped.

If β and β/ε are purely imaginary, the z components of the single mode fluxes vanish, while the z component of the IF is other than zero for different modes,

$$S_z^{\mathrm{int}} = -\frac{c}{8\pi k_0}\mathrm{Im}\left(\frac{2\beta}{\varepsilon}\right)H_{0a}H_{0b}\cos q_a x \cos q_b x \times \exp[\mathrm{Im}(\Delta\beta z + 2\beta L)]\sin\varphi. \quad (16)$$

Depending on phase difference φ, this component may propagate in both the positive and negative direction along the z axis. It differs from the corresponding flux of homogeneous waves in that it weakly decays along the z axis when $\mathrm{Im}\beta_a \neq \mathrm{Im}\beta_b$. For the same modes, the z dependence is absent and the flux becomes undamped.

For identical counterpropagating modes, the x and z components of the IF are purely reactive, oscillate along the z axis, and depend on x in the same way as the single mode flux. When the modes differ, the IF takes an active component along the x axis, which persists even when the single mode fluxes in this direction are absent (ε is real). In this case, the active and reactive components exhibit the same damping (at $\mathrm{Im}\beta_a \neq \mathrm{Im}\beta_b$) along the z axis, the same (phase-shifted by $\pi/2$)

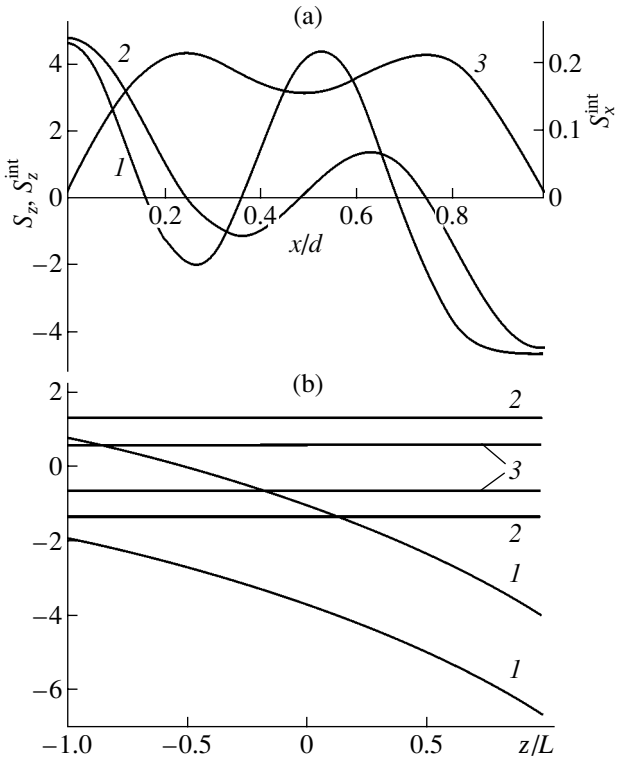

Fig. 3. Distribution of (a) the components of the total and interference fluxes for counterpropagating modes $n_a = 2$ and $n_b = 1$ along the thickness of the waveguide and (b) the envelopes of the components along the waveguide.

oscillating dependence on z (with an oscillation period proportional to $(\mathrm{Re}2\beta)^{-1}$), and slightly different periodic dependences on x. Figure 3a shows the components of total energy flux S_z (curve *1*), as well as components S_z^{int} and S_x^{int} of the IF (curves *2* and *3*), across the guiding layer at $z = 0$ for counterpropagating modes $n_a = 2$ and $n_b = 1$ at $\varphi = \pi/3$ and $L = 1$ cm. Figure 3b demonstrates the variation of the envelopes of the component distributions along the waveguide at $x/d = 0.2$. In this case of different modes, the flux along the x axis is an almost totally interference flux for the same reason as in the case of copropagating waves. From (14) and (15), it follows that, when absorption is weak, the IF reactive component is small and can be neglected. Therefore, its coordinate dependence is defined by the product of the independent functions of z and x.

CONCLUSIONS

Thus, the interference fluxes of different modes propagating in a planar waveguide differ in properties from the same fluxes of homogeneous waves. For different waveguide modes, both the longitudinal and transverse components of the interference flux consist of two parts, one associated with interference between the reactive components of the field and the other with interference between the active components. For homogeneous waves, each of the projections of the interference flux is either purely active or purely reactive. Different copropagating waves exhibit energy interference effects inherent in only counterpropagating homogeneous waves. These features of interference fluxes may be helpful in designing and applying waveguides and integrated optical devices.

REFERENCES

1. V. G. Veselago, Usp. Fiz. Nauk **173**, 790 (2003) [Phys. Usp. **46**, 764 (2003)].
2. D. R. Smith, J. Padilla Willie, D. C. Vier, *et al.*, Phys. Rev. Lett. **84**, 4184 (2000).
3. V. V. Shevchenko, Radiotekh. Élektron. (Moscow) **48**, 1202 (2003).
4. I. M. Minkov, Opt. Spektrosk. **58**, 466 (1985) [Opt. Spectrosc. **58**, 280 (1985)].
5. A. A. Romanenko and A. B. Sotskiĭ, Zh. Tekh. Fiz. **68** (4), 68 (1998) [Tech. Phys. **43**, 427 (1998)].
6. V. V. Sidorenkov and V. V. Tolmachev, Pis'ma Zh. Tekh. Fiz. **16** (20), 5 (1990) [Sov. Tech. Phys. Lett. **16**, 91 (1990)].
7. S. A. Afanas'ev, V. V. Efimov, and D. I. Sementsov, Pis'ma Zh. Tekh. Fiz. **19** (22), 84 (1993) [Tech. Phys. Lett. **19**, 733 (1993)].
8. S. A. Afanas'ev and D. I. Sementsov, Zh. Tekh. Fiz. **67** (10), 77 (1997) [Tech. Phys. **42**, 1181 (1997)].
9. A. A. Kolokolov and G. V. Skrotskiĭ, Usp. Fiz. Nauk **162**, 165 (1992) [Sov. Phys. Usp. **35**, 1089 (1992)].
10. Yu. N. Kuznetsov and D. I. Sementsov, Opt. Spektrosk. **97**, 647 (2004) [Opt. Spectrosc. **97**, 614 (2004)].
11. M. K. Barnoski, *Introduction to Integrated Optics* (Plenum, New York, 1974; Mir, Moscow, 1977), pp. 47–59.
12. J. J. Burke, G. I. Stegeman, and T. Tamir, Phys. Rev. B **33**, 5186 (1986).

Translated by V. Isaakyan

Technical Physics, Vol. 50, No. 11, 2005, pp. 1479–1484. Translated from Zhurnal Tekhnicheskoĭ Fiziki, Vol. 75, No. 11, 2005, pp. 86–91.

RADIOPHYSICS

Electric- and Magnetic-Field Strengths in the Fresnel Zone of a Microradiator Formed by an Electric and a Magnetic Dipole

O. G. Vendik and I. A. Pakhomov

St. Petersburg Institute of Electrical Engineering, St. Petersburg, 197376 Russia

Received April 12, 2005

Abstract—The propagation of electric and magnetic fields and of the Poynting vector in the near zone (Fresnel zone) of an electric dipole, a loop, and a dipole–loop pair is considered. The dimensions of all radiators are much smaller than the radiation wavelength. It is shown that the ideas of the field distribution (polar diagram) in the far zone cannot be applied to the properties of the field in the Fresnel zone. The radiated-power fraction that is absorbed by an object whose electrodynamic properties are close to those of biological media is found at a distance from the radiator to the absorbing object on the order of several millimeters. *© 2005 Pleiades Publishing, Inc.*

In recent years, considerable attention has been given to studying fields in the near zone (Fresnel zone) of a radiating dipole [2], especially antennas whose dimensions are much smaller than the radiation wavelength [3]. This is due, in particular, to the development of antennas for mobile telephones [4], since the user of a mobile telephone is in the near zone of the ultrahigh-frequency radiator entering into the composition of the telephone apparatus. The distribution of electric and magnetic fields in the Fresnel zone differs substantially from the field distribution in the far zone (Fraunhofer zone [1]), the latter being described by the polar diagram of an antenna. Therefore, the field distribution in the Fresnel zone of a radiator whose dimensions are smaller than the radiation wavelength requires a dedicated study.

A radiator such that all of its dimensions are much smaller than the radiation wavelength will be referred to here as a microradiator. For a microradiator, one can consider an individual dipole or a loop. Of particular interest is a device combining a small dipole and a small loop. Such a combination makes it possible to obtain directed radiation without using superdirectivity effects [3]. In the far zone of radiation, a combination of a dipole and a loop ensures a polar diagram in the form of a cardioid featuring zero radiation in the direction of the main ray of the antenna being considered [5]. It is of particular interest to clarify the question of how the strengths of the electric and magnetic fields of such a pair of radiators change in the near zone (Fresnel zone).

STRENGTHS OF THE ELECTRIC AND MAGNETIC FIELDS OF A MICRORADIATOR IN SPHERICAL COORDINATES

Let us consider an electric dipole of length $l \ll \lambda$ and a circular loop of radius $a \gg \lambda$. Figure 1 shows the arrangement of the radiators with respect to the chosen coordinate frame [5]. We would like to emphasize that, traditionally, fields generated by a loop are determined for a loop lying in the *xy* plane. In our case, the loop lies in the *yz* plane. By using known relations for going over from the radiating current to the vector potential and the field-strength vectors [6], we obtain the strengths of the

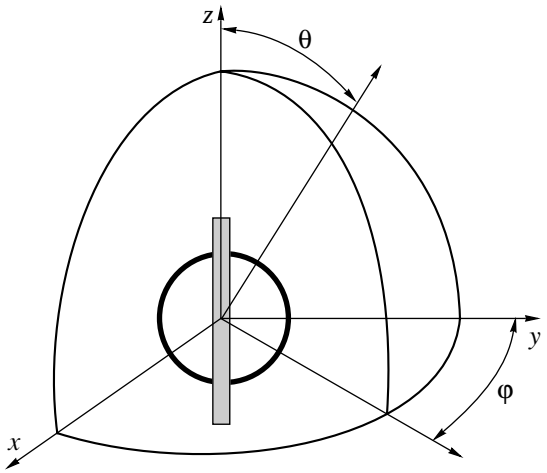

Fig. 1. Dipole and loop (microradiator elements) in spherical coordinates.

1063-7842/05/5011-1479$26.00 © 2005 Pleiades Publishing, Inc.

Microradiator type

Coefficients used		Microradiator type
$A = \sqrt{2}$	$B = 0$	Loop
$A = 0$	$B = \sqrt{2}$	Dipole
$A = 1$	$B = 1$	Loop–dipole pair

magnetic and electric fields of an electric dipole aligned with the *z* axis and a loop lying in the *yz* plane.

For an electric dipole of length *l*, we have

$$H_\varphi(\theta, r) = I_{\text{dip}}\frac{ikl\sin\theta}{4\pi r}\left(1+\frac{1}{ikr}\right)e^{-ikr},$$

$$H_\theta(\theta, r) = 0, \quad H_r(\theta, r) = 0, \tag{1}$$

$$E_r(\theta, r) = Z_0 I_{\text{dip}}\frac{l\cos\theta}{2\pi r^2}\left(1+\frac{1}{ikr}\right)e^{-ikr},$$

$$E_\theta(\theta, r) = Z_0 I_{\text{dip}}\frac{ikl\sin\theta}{4\pi r}\left(1+\frac{1}{ikr}-\frac{1}{(kr)^2}\right)e^{-ikr}, \tag{2}$$

$$E_\varphi(\theta, r) = 0.$$

For a magnetic dipole represented by a loop of radius *a*, the results are

$$H_\varphi(\varphi, \theta, r) = I_{\text{loop}}\frac{a^2\sin\varphi}{4r^3}(-1+k^2r^2-ikr)e^{-ikr},$$

$$H_\theta(\varphi, \theta, r) = I_{\text{loop}}\frac{a^2\cos\varphi\cos\theta}{4r^3}(1-k^2r^2+ikr)e^{-ikr}, \tag{3}$$

$$H_r(\varphi, \theta, r) = 0,$$

$$E_\theta(\varphi, \theta, r) = Z_0 I_{\text{loop}}\frac{(ka)^2}{4r}\left(1+\frac{1}{ikr}\right)\sin\varphi e^{-ikr},$$

$$E(\varphi, \theta, r) = Z_0 I_{\text{loop}}\frac{-(ka)^2}{4r}\left(1+\frac{1}{ikr}\right)\cos\varphi\cos\theta e^{-ikr}, \tag{4}$$

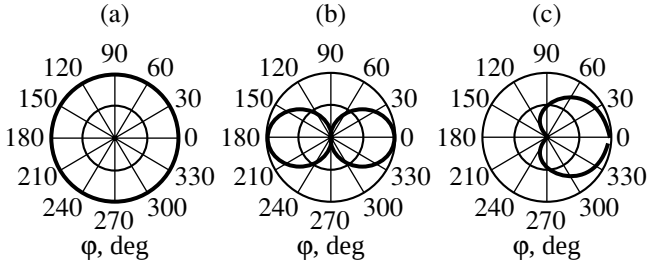

Fig. 2. Polar diagrams in the far region for microradiators of three types: (a) dipole, (b) loop, and (c) dipole–loop pair.

$$E_r(\varphi, \theta, r) = 0.$$

Here, we have used the following notation: *r* is the distance between the center of radiation and the point of observation and i_{dip} and I_{loop} are the currents in the dipole and the loop, respectively. The wave number is

$$k = \frac{2\pi}{\lambda}, \tag{5}$$

where λ is the wavelength in a free space.

Let us find the sum of the fields radiated by the dipole and the loop arranged in such a way that their phase centers coincide and that the phase difference between the dipole and loop currents is 90°. We have

$$E_\theta(\varphi, \theta, r) = Z_0\frac{1}{r}\left[A\rho\left(1+\frac{1}{ikr}\right)\cos\varphi + B\rho\left(1+\frac{1}{ikr}-\frac{1}{(kr)^2}\right)\sin\theta\right]e^{-ikr}, \tag{6}$$

$$E_\varphi(\varphi, \theta, r) = \frac{1}{r}\left[A\rho\left(1+\frac{1}{ikr}\right)\sin\varphi\cos\theta\right]e^{-ikr}, \tag{7}$$

$$H_\theta(\varphi, \theta, r) = -\frac{1}{r}\left[A\rho\left(1+\frac{1}{ikr}-\frac{1}{(kr)^2}\right)\times\sin\varphi\cos\theta\right]e^{-ikr}, \tag{8}$$

$$H_\varphi(\varphi, \theta, r) = \frac{1}{r}\left[A\rho\left(1+\frac{1}{ikr}-\frac{1}{(kr)^2}\right)\cos\varphi + B\rho\left(1+\frac{1}{ikr}\right)\sin\theta\right]e^{-ikr}. \tag{9}$$

Here, we have used the following notation:

$$A\rho = I_{\text{loop}}\frac{(ka)^2}{4}, \quad B\rho = I_{\text{dip}}\frac{kl}{4\pi}. \tag{10}$$

We note that the factors $A\rho$ and $B\rho$ have the dimensions of a current. The table gives the sets of coefficients *A* and *B* for various microradiator types.

If the value of $\rho = 0.01779$ A is chosen, the total active power radiated by each of the aforementioned radiator is 1 W. The polar diagrams of each of the microradiators in the far zone ($kr \gg 1$) are shown in Fig. 2 for the equatorial plane ($\theta = \pi/2$).

COMPLEX FLUX OF THE POYNTING VECTOR THROUGH A SPHERICAL SURFACE SURROUNDING A MICRORADIATOR

Let us consider the flux of the Poynting vector through a sphere of radius *r* surrounding a microradia-

tor occurring in a free space. We have

$$P_0(r) = \int_0^{2\pi}\int_0^{\pi}[E_\theta(\varphi, \theta, r)H_\varphi^*(\varphi, \theta, r) - E_\varphi(\varphi, \theta, r)H_\theta^*(\varphi, \theta, r)]r^2\sin\theta d\theta d\varphi, \quad (11)$$

where asterisks denote complex conjugation. The dependence of the real and imaginary parts of the Poynting vector flux on the radius r is shown in Fig. 3 according to formula (11). We note that $\mathrm{Re}[P_0(r)]$ is formally a function of r, but, in fact, it does not depend on r. This is a consequence of the energy-conservation law and confirms the validity of the analytic expressions for $E_\theta(\varphi, \theta, r)$ and $H_\varphi(\varphi, \theta, r)$. For $kr < 0.1$, the imaginary part of the Poynting flux vector, $\mathrm{Im}[P_0(r)]$, for an individual dipole or an individual loop exceeds its real part; as one approaches the center of radiation, the former may exceed the latter by several orders of magnitude. This suggests that a large amount of pulsed electromagnetic-field energy is accumulated in the antenna whose dimensions are much smaller than the radiation wavelength. At the same time, the imaginary part of the Poynting flux vector, $\mathrm{Im}[P_0(r)]$, for $kr < 0.1$ in the case of a dipole–loop pair is close to zero. This is likely to indicate that the reactive energies of the dipole and the loop compensate each other.

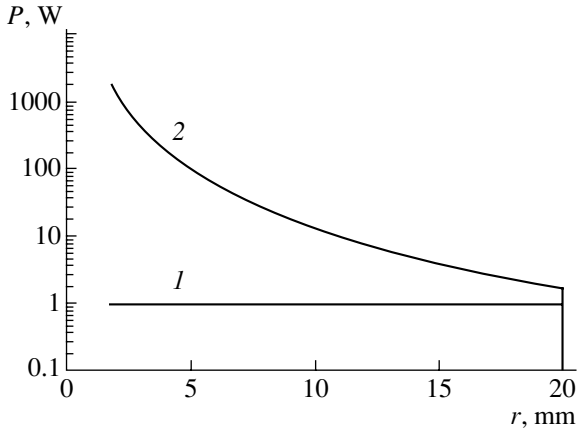

Fig. 3. Dependence of the (*1*) real and (*2*) imaginary parts of the Poynting vector flux on the distance r to the radiator center. The imaginary part of the flux is positive for the loop, but it is negative for the dipole. The respective two dependences coincide in magnitude. For the dipole–loop pair, the imaginary part of the Poynting vector flux does not exceed 0.01 W in magnitude.

DISSIPATION OF ELECTROMAGNETIC ENERGY BY AN ABSORBING OBJECT IN THE MICRORADIATOR FRESNEL ZONE

Let us consider the dissipation of electromagnetic energy by an absorbing object that has the shape of a sphere and is placed in the Fresnel zone of the microradiator being considered (see Fig. 4a). The absorbing object covers the radiation flux within the cone of opening angle 4α, where

$$\alpha = \frac{1}{2}\arcsin\left(\frac{R}{R+r}\right). \quad (12)$$

Here, R is the radius of the absorbing ball, while r is the distance from the center of the radiator to the surface of the ball.

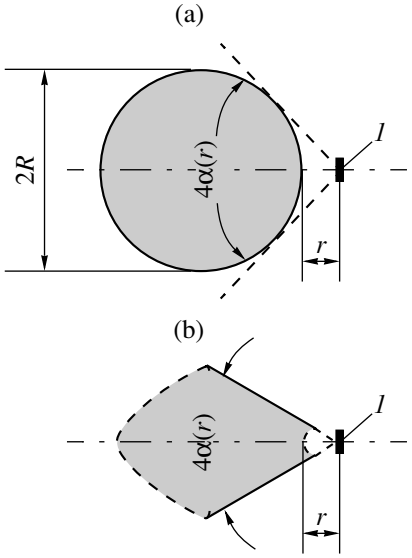

Fig. 4. (a) Arrangement of the (*1*) microradiator and an absorbing element near it and (b) simplified scheme of this arrangement for calculating the absorbed power.

For the sake of definiteness, we assume that the relative magnetic permeability of the ball is $\mu_r = 1$ and that its dielectric characteristics at a frequency of 1–2 GHz correspond to the values of $\varepsilon_m \cong 50$ and $\sigma_m \cong 1$ $(\Omega\ \mathrm{m})^{-1}$. The chosen parameters correspond to the properties of biological objects [7]. In order to simplify the evaluation of relevant integrals, we will calculate the absorption by using a simplified scheme that is illustrated in Fig. 4b. In isolating the central part of the cone, we have considered that, in the external part of the cone the lines of force of the spherical wave radiated by the microradiator are orthogonal to the surface of the absorbing ball and are strongly weakened at the dielectric characteristics specified above. In the central part of the cone, the lines of force of the spherical wave are tangential to the surface of the ball and are therefore continuous at the interface of the free space and the absorbing ball.

For $kr \ll 1$, the interaction of the electric field with the absorbing object is of a quasistatic character. In view of this, it would be illegitimate to consider the presence of incident and reflected waves in spherical coordinates at a distance from the radiator center much shorter than the radiation wavelength. We now consider a sphere of radius r surrounding the microradiator. At the surface of the sphere, one can introduce the charac-

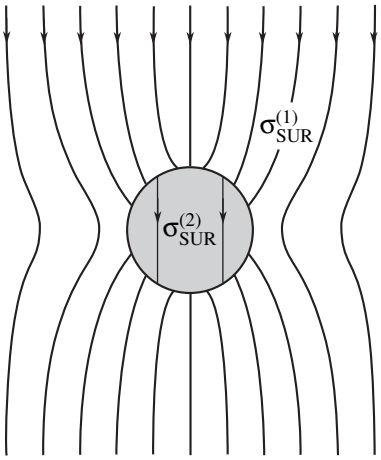

Fig. 5. Distribution of the lines of force of the electric field on a planar conducting surface having conductivity $\sigma_{SUR}^{(1)}$ and containing an inserted disk of conductivity $\sigma_{SUR}^{(2)}$.

teristic impedance Z_{fresn} in the Fresnel zone as the ratio of $E_\theta(\varphi, \theta, r)$ to $H_\varphi(\varphi, \theta, r)$ at a specific small distance r and arbitrary angles φ and θ [2]. For $kr < 1$, the characteristic impedance Z_{fresn} becomes a pure imaginary quantity whose modulus may exceed Z_0 substantially. Upon averaging, we can set $Z_{fresn} = 2Z_0$ with an acceptable degree of accuracy. We assume that, in accordance with Fig. 4b, the cone of opening angle 4α cuts, from the sphere surrounding the microradiator, a spherical segment whose surface impedance is determined by the properties of the absorbing object,

$$Z_{SUR} = \sqrt{\frac{i\omega\mu_0}{\sigma_m + i\omega\varepsilon_0\varepsilon_m}}, \quad (13)$$

where ε_0 and μ_0 are, respectively, the electric permittivity of the free space and its magnetic permeability and σ_m and ε_m are, respectively, the conductivity and the relative dielectric permittivity of the absorbing-object material.

Let us consider the question of how the lines of force of magnetic and electric fields penetrate into an absorbing object. Within the cone of opening angle 4α, the lines of force of the magnetic field are tangential to the surface of the object; from this and from the known boundary conditions, it follows that, at the surface of the object, they generate a surface current that is numerically equal to the magnetic-field strength. Further, the irradiated ball surface, which is singled out by the cone of opening angle 4α, will be considered as a conducting segment surrounded by a weakly conducting medium. In the quasistatic approximation, the electric field causes a polarization of this segment, this leading to the weakening of the field strength at its surface. To an acceptable degree of precision, we can assume that the spherical segment cut by the cone of opening angle 4α can be replaced by a plane disk. Figure 5 displays the distribution of the lines of force of the electric field on a plane conducting surface having the conductivity $\sigma_{SUR}^{(1)}$ and containing an inserted disk of conductivity $\sigma_{SUR}^{(2)}$. By solving Laplace's equation [8], one can show that the field strength in the disk plane is uniform and is given by

$$E_{in} = \frac{2E_{out}}{1 + \sigma_{SUR}^{(2)}/\sigma_{SUR}^{(1)}}. \quad (14)$$

The above considerations make it possible to calculate the power that is absorbed by an absorbing object situated near a microradiator. We have

$$P_{abs}(\varphi_0, \theta_0, r) = \frac{\pi}{4}\int_{\varphi_0-\alpha}^{\varphi_0+\alpha}\int_{\theta_0-\alpha}^{\theta_0+\alpha} S(\varphi, \theta, r)\sin\theta d\theta d\varphi, \quad (15)$$

where

$$S(\varphi, \theta, r) = \frac{|H_\theta(\varphi, \theta, r)|^2 + |H_\varphi(\varphi, \theta, r)|^2}{2}\mathrm{Re}(Z_{SUR}) + \frac{|2E_\theta(\varphi, \theta, r)|^2 + |2E_\varphi(\varphi, \theta, r)|^2}{2\left|1 + \frac{2Z_0}{Z_{SUR}}\right|^2}\mathrm{Re}(Z_{SUR});$$

φ_0 and θ_0 are the angles that, in the system of spherical coordinates introduced above, determine the direction from the center of the microradiator to the irradiated segment of the absorbing object; and the factor $\pi/4$ reflects the ratio of the area of the circle used in the model to the area of the square specified by the limits of integration in (15).

We will now find the ratio of the power absorbed by the absorbing object to the total power radiated by the microradiator as a function of the distance between the radiator center and the surface of the absorbing object. We have

$$\kappa(\varphi_0, \theta_0, r) = \frac{P_{abs}(\varphi_0, \theta_0, r)}{\mathrm{Re}[P_0(r)] + P_{abs}(\varphi_0, \theta_0, r)}. \quad (16)$$

The parameter $\kappa(\varphi_0, \theta_0, r)$ is known as the specific absorption coefficient. We note that, at a small distance from the microradiator to the absorbing-object surface, it may turn out that $P_{abs}(\varphi_0, \theta_0, r) > \mathrm{Re}[P_0(r)]$. In this case, the microradiator radiation resistance will grow owing to a strong coupling to the absorbing object.

Figure 6 shows the specific absorption coefficient as a function of the distance between the microradiator and the absorbing-object surface at $\theta_0 = \pi/2$ for three microradiator types considered here. For a dipole–loop pair, the specific absorption coefficient is given for two directions corresponding to the maximum and the zero of the relevant cardioid ($\varphi_0 = 0$ and π, respectively).

From the graph in Fig. 6, one can see that, at the distance between the radiator center and the absorbing-object surface on the order of 1–3 mm, the bulk of the radiated power goes to the absorbing object. With increasing distance, the absorption decreases sharply, falling below 1% even at a distance as small as 10 mm. In [9], the relative power absorbed by a phantom mimicking the head of a human being was measured at a frequency of 1800 MHz, the distance from the radiator center to the outer surface of the absorbing object being taken to be 4.7 mm [7]. The measurement showed that the experimental phantom absorbs 24% of the total radiated power. The point corresponding to this measurement is shown in Fig. 6.

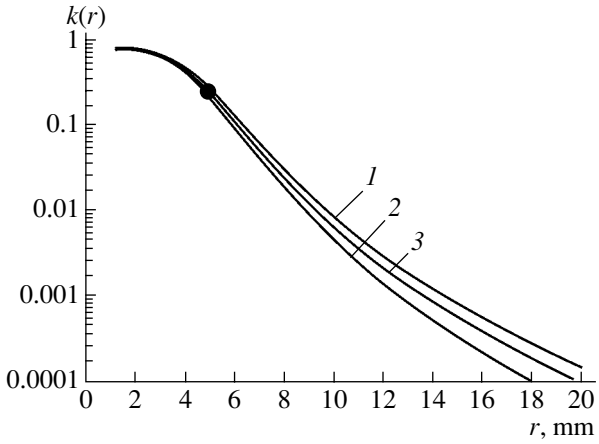

Fig. 6. Specific absorption coefficient as a function of the distance between the microradiator and the absorbing-object surface at $\theta_0 = \pi/2$ for three microradiator types considered in the present study: a dipole–loop pair at $\varphi_0 = (1)$ 0 and (*2*) π and (*3*) a dipole or a loop. The point represents an experimental result.

DISCUSSION OF THE RESULTS AND CONCLUSIONS

We will now proceed to discuss some special features of the distribution of electric and magnetic fields in the near zone of microradiators. First of all, we will consider the dependence of the electric- and magnetic-field strengths on the azimuthal angle φ_0 in the equatorial plane $\theta_0 = \pi/2$ of a dipole–loop pair. In order to obtain an integrated characteristic of the dependence being discussed, it is convenient to consider the angular dependence of the specific absorption coefficient at various distances between the microradiator center and the absorbing-object surface. Figure 7 shows $\kappa(\varphi_0, \theta_0, r)$ as a function of φ_0 at $\theta_0 = \pi/2$ for three different distances. At $r = \lambda/2$, $\kappa(\varphi_0, \theta_0, r)$ is the square of the function describing the cardioid—that is, it replicates the polar diagram of the microradiator in the far zone. At $r = \lambda/8$, the ratio of $\kappa(0, \theta_0, r)$ to $\kappa(\pi, \theta_0, r)$ is approximately equal to 3, while, at $r = \lambda/15$, this ratio is close to unity. The diagrams in Fig. 7 show how strong the distribution of the field in the near zone of a microradiator differs from the respective distribution in its far zone. For a single dipole or a single loop, the ratio of $\kappa(0, \theta_0, r)$ to $\kappa(\pi, \theta_0, r)$ is equal to unity at any value of *r*. Thus, we see that, for $r \le \lambda/15$, the fraction of the power absorbed in the absorbing object takes the same value for a loop, a dipole, and a dipole–loop pair, although the polar diagram of the pair in the far zone has the form of a cardioid. At first glance, it therefore seems that, in what is concerned with the absorption of the power of ultrahigh-frequency radiation in a closely lying absorbing object, a dipole–loop pair does not have advantages over a single dipole or a single loop. However, we note that the gain factor for a dipole or a loop such that either has dimensions much smaller than the radiation wavelength is $G = 1.5$, while the gain factor for a dipole–loop pair is $G = 3$ [4, 5]. This means that, if the microradiators used generate identical field strengths in the far zone, the absorbed power in the absorbing object is two times smaller in case of a dipole–loop pair than in the case of a single loop or a single dipole.

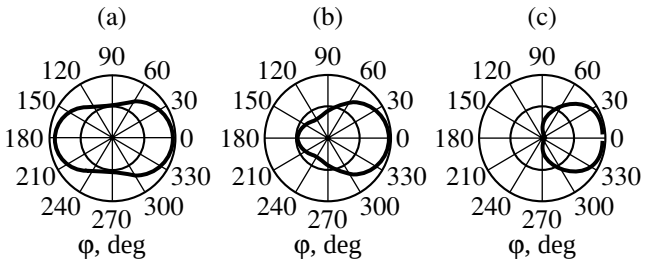

Fig. 7. Dependence of $\kappa(\varphi_0, \theta_0, r)$ on φ_0 at $\theta_0 = \pi/2$ for $r =$ (a) $\lambda/15$, (b) $\lambda/8$, and (c) $\lambda/2$.

We would like to emphasize that the imaginary part of the Poynting vector flux through a sphere surrounding a microradiator grows extremely fast as the radius of the sphere decreases. It can be shown that, for a single dipole or a single loop, the ratio of the imaginary and real parts of the Poynting vector flux determines the quality factor of the radiator being considered. By way of example, we indicate that, for a loop of radius $a =$ 10 mm, the radiation resistance at a frequency of 2 GHz is 6 Ω [6], while its reactive resistance under the same conditions is about 150 Ω, which corresponds to a quality factor of $Q = 25$. From Fig. 3b, we find that, at $r =$ 10 mm, $\mathrm{Im}[P_0(r)] \cong 15$, while $\mathrm{Re}[P_0(r)] = 1$. Thus, we see that, if *r* is equal to the radiator size ($r = a$), then the ratio of $\mathrm{Im}[P_0(r)]$ to $\mathrm{Re}[P_0(r)]$ is on the same order of magnitude as the microradiator quality factor. The distinction between these quantities can be explained by the fact that part of the reactive energy is stored in the field components $E_r(\theta, r)$ and $H_r(\theta, r)$, which do not take part in the formation of the Poynting vector flux. The explanation for the extreme smallness of the imaginary part of the Poynting vector flux for a microradia-

tor in the form of a dipole–loop pair is expected to be much more involved. The absence of the imaginary part of the flux does not mean that the radiator quality factor is close to zero. The point is that the imaginary part of the flux vanishes in the case of the exact equality of the amplitudes of the currents in the dipole and in the loop ($A = B$ in our case). Only at a fixed frequency is it possible to ensure the equality of the amplitudes of the currents in the reactive loads, a dipole and a loop, by means of corresponding matching devices. In other words, the problem of the quality factor for the system in question becomes dependent on the characteristic of the frequency dependence of the dipole and loop supply circuits.

We have considered special features of the distribution of the electric and magnetic fields in the Fresnel zone of microradiators represented by a dipole, a loop, or a dipole–loop air, whose polar diagram in the far zone has the form of a cardioid. The main conclusion is that the ideas of the field distribution (polar diagram) in the far zone cannot be applied to the properties of the fields in the Fresnel zone. For the radiators considered here, the special features of the Fresnel zone manifest themselves within a sphere of radius $\lambda/8$, naturally in the case where the dimensions of the radiators do not exceed the radius of this sphere. If a microradiator is situated within a distance of several millimeters from the surface of an absorbing object whose electrodynamic properties are close to those of biological media, the fraction of the absorbed power (specific absorption coefficient) at a frequency of 1–2 GHz can be as high as 20–30%.

REFERENCES

1. L. A. Vaĭnshteĭn, *Electromagnetic Waves* (Sov. Radio, Moscow, 1957) [in Russian].
2. S. Laybros and P. F. Combes, IEEE Antennas Propag. Mag. **46**, 53 (2004).
3. O. G. Vendik and M. D. Parnes, *Electronically Scanned Antennas* (*Introduction to Theory*), Ed. by L. D. Bakhrakh (Sains Press, Moscow, 2002) [in Russian].
4. K. Fujimoto and J. R. James, *Mobile Antenna System Handbook* (Artech House, Boston, 2004).
5. A. Z. Fradin, *Antenna-Feeder Devices* (Svyaz', Moscow, 1977) [in Russian].
6. C. A. Balanis, *Advanced Engineering Electromagnetics* (Wiley, New York, 1989).
7. M. Y. Kanda, M. G. Douglas, E. D. Mendivil, *et al.*, IEEE Trans. Microwave Theory Tech. **52**, 2013 (2004).
8. J. A. Stratton, *Electromagnetic Theory* (McGraw-Hill, New York, 1941; Gostekhizdat, Moscow, 1948).
9. A. Hadjem, D. Lautry, Ch. Dale, *et al.*, IEEE Trans. Microwave Theory Tech. **53**, 4 (2005).

Translated by A. Isaakyan

Technical Physics, Vol. 50, No. 11, 2005, pp. 1485–1489. Translated from Zhurnal Tekhnicheskoĭ Fiziki, Vol. 75, No. 11, 2005, pp. 92–96.

SURFACE, ELECTRON AND ION EMISSION

Energy Distribution of Electrons Field-Emitted from Carbon Nanoemitters

V. M. Lobanov

Bashkir State Agricultural University, Ufa, 450001 Bashkortostan, Russia

e-mail: bgau@soros.bashedu.ru

Received December 8, 2004

Abstract—The height of an extra low-energy maximum in the energy distribution of electrons tunneling from crystalline carbon fibers and carbon nanotubes is studied as a function of emitter heating and emitter rotation relative to the energy analyzer axis. The relationships found are related to emission from electron states on the surface of the reconstructed nanocrystals and nanotubes. © *2005 Pleiades Publishing, Inc.*

INTRODUCTION

In the previous works [1, 2], we described the phenomena of spontaneous (current-related) thermofield reconstruction (CTFR) and induced thermofield reconstruction (ITFR) of an carbon nanocrystal emitting in an electric field of appropriate (autoemission) sign. The essence of the former is that the anode voltage and field-emission probe current from an emitting carbon nanocrystal may be increased to a certain threshold over which the probe current sharply drops (roughly by one order of magnitude) and the field-emitted electron energy distribution (FEED) exhibits an extra low-energy maximum shifted by 0.45–0.50 eV toward lower energies relative to the main one. Heating of the emitter to ≈1000 K recovers the FEED and restores the probe current [1].

The latter phenomenon is typical of field emitters made of metals and semiconductors. In this case, heating of the nanocrystalline emitter subjected to a voltage of autoemission sign causes reconstruction of its tip and shifts the total current–voltage characteristic. Further heating almost restores the initial position of the characteristic, since the emitter slightly blunts. In our previous experiments [2], upon heating the nanocrystalline carbon emitter, as well as upon CTFR [1], the field-emission probe current decreased by one order of magnitude, the current–voltage characteristic shifted down, and the FEED exhibited an extra maximum shifted by 0.45–0.50 eV toward lower energies relative to the main one. A further smooth rise in the field-emission current to some threshold value led to the spontaneous restoration of the probe current–voltage characteristic and FEED. The position of the characteristic and the energy distribution did not change after this procedure had been repeated many times.

The decrease in the probe current after ITFR and CTFR was explained by the effect of surface electron states (SESs) of type I arising near the Fermi level and producing an additional barrier and also of SESs of type II, which lie 0.45–0.50 eV below the Fermi level and are responsible for the extra low-energy peak in the FEED.

Such assumptions are based on the results of studying SESs on tungsten, silicon, and germanium emitters [3–5]. It was found that the density of SESs and the height of the extra low-energy peak in the FEED, which is produced by the electrons emitted from the SESs, are extremely sensitive to emitter heat treatment. It was also established that the height of the extra maximum depends on the angle between an emitter face probed and the axis of an energy analyzer. Analytical calculations of the extra maximum for electrons emitted from the (100)W face are in good agreement with experimental data on the assumption that the SES energy distribution is Gaussian [6].

In this work, we check the hypothesis of the presence of SESs on the emitting surface of reconstructed carbon nanocrystals and nanotubes. The second goal of this study is to see how the height of the extra low-energy maximum depends on the emitter heating and angular position of the emitter relative to axis of an energy analyzer. The objects of investigation are VMN-RK crystalline carbon fibers annealed at 900°C and carbon nanotubes applied on W foil by electrophoresis.

EXPERIMENTAL

A fiber ≈1 mm long was attached to a narrow strip cut of tantalum foil by Aquadag (the strip was welded to a tungsten bow), dried, and heated in a vacuum at ≈1000 K. The field cathode thus produced was introduced through a lock into a USU-4 ultra-high-vacuum chamber equipped with a field electron microprojector and an electrostatic energy-dispersion analyzer, the secondary emission multiplier of which operated in the electron count mode.

1063-7842/05/5011-1485$26.00 © 2005 Pleiades Publishing, Inc.

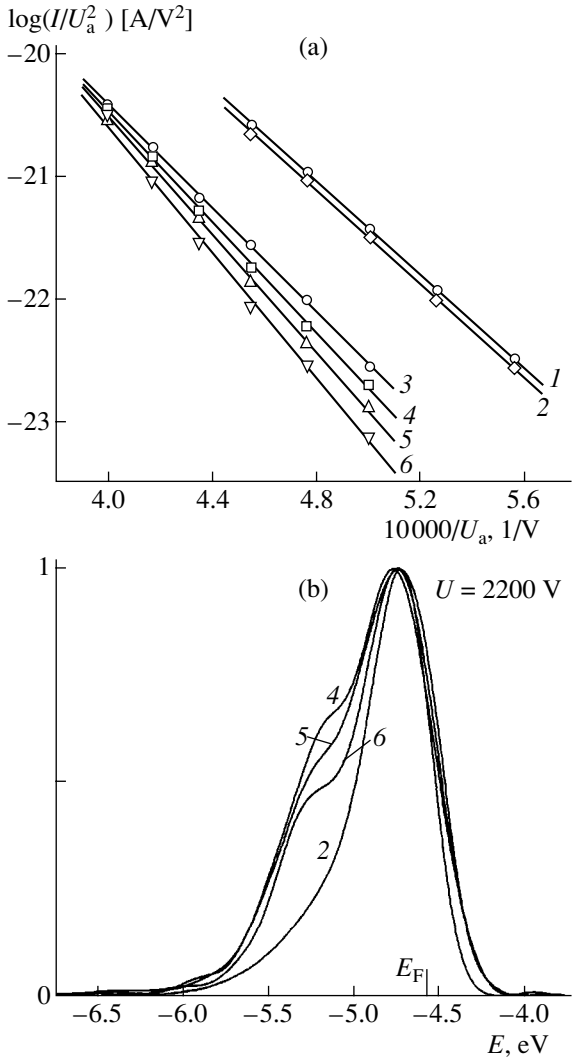

Fig. 1. (a) *I–V* characteristics of the carbon fiber: (*1*) after stripping off the surface layer by the current pulse; (*2*) after 10-min heating; (*3*) after rapid rise in the emitter current to 5 μA; and (*4–6*) after 10-, 20, and 30-min heating of the reconstructed nanocrystal, respectively. (b) Energy distribution of electrons emitted from the carbon nanocrystal: (*2*) after stripping off the surface layer by the current pulse and 10-min heating and (*4–6*) after 10-, 20, and 30-min heating of the reconstructed nanocrystal, respectively.

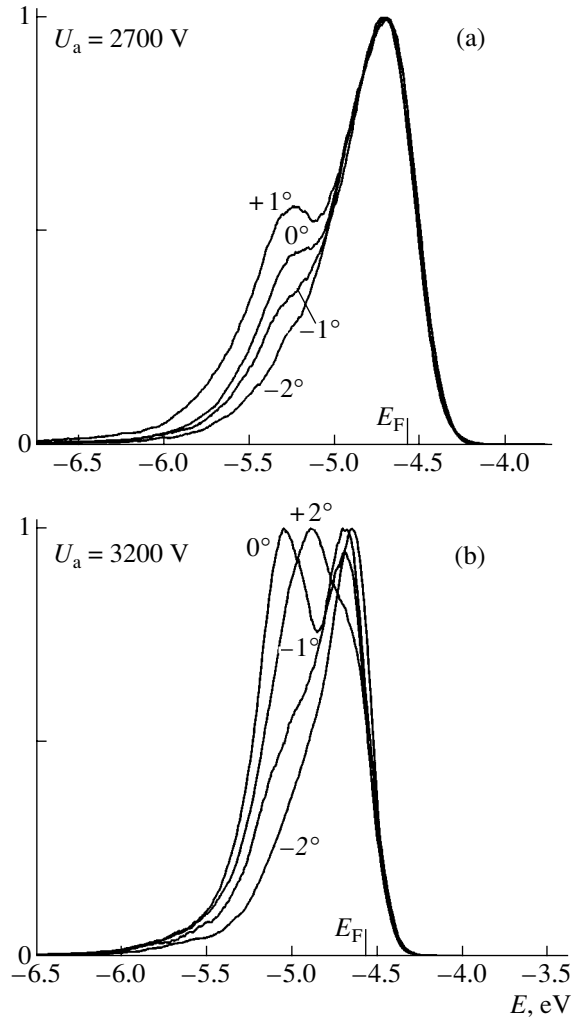

Fig. 2. Height of the extra maximum in the FEED vs. emitter angular position relative to the analyzer for the (a) first and (b) second sample of the reconstructed nanocrystal.

After locking, the cathode (emitter) was "formed" under a rough vacuum by raising the total emission current to 150 μA. Such a procedure allows nanocrystals to emerge on the emitting surface via removal (sputtering) of amorphous carbon under the action of residual gas ions [7]. Then, in an ultrahigh vacuum, the emitting layer on the fiber surface was stripped off several times by ponderomotive forces arising when a current pulse of ≈130 μA was applied until the emission image, a single spot at the center of the projector screen, appeared. This spot was directed to the probing diaphragm of the analyzer. The emitting surface of the samples was cleaned by heating the tungsten bow to 1000 K. The same heating was used to activate SESs. The FEED was measured with the technique described in [8]. The probe current–voltage characteristics were constructed based on the values of the electron current passing through the energy analyzer and corresponding anode voltages U_a.

Electron emission from carbon nanotubes was observed at the edge of a 2.0×0.5-mm curved strip cut of the W foil. The strip was welded to a supporting nickel tube, rinsed in ethanol, dried in the lock chamber, and introduced into the vacuum chamber. Once the entire vacuum chamber had been heated and the pressure in the chamber had been decreased to 5×10^{-10} Torr or lower, a voltage was applied to a ballast resistor between the high-voltage supply and emitter and the carbon nanotubes were heated by the Joule heat due to the emission current. CTFR of the nanotube region probed was also carried out after applying a voltage to the ballast resistor.

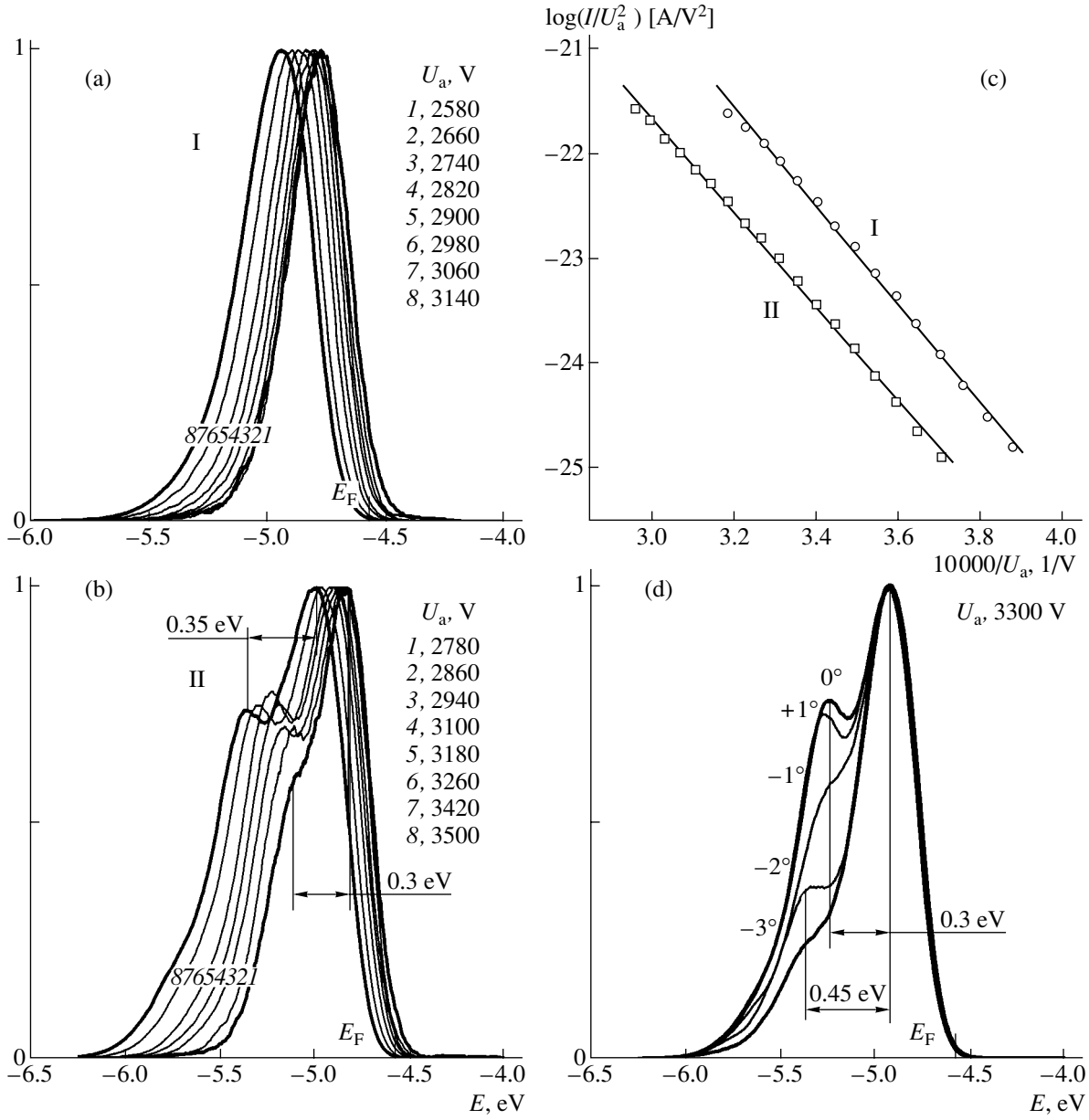

Fig. 3. (a) Initial energy distributions of electrons field-emitted from the carbon nanotubes, (b) energy distributions of electrons field-emitted from the nanotubes subjected to current-related thermofield reconstruction, (c) probe *I–V* characteristics of the nanotubes (*1*) before and (*2*) after current-related thermofield reconstruction, and (d) the height of the extra maximum in the FEED vs. emitter angular position relative to the analyzer for the reconstructed nanotube.

RESULTS AND DISCUSSION

After the surface layer of the emitter had been stripped off in an ultrahigh vacuum, the *I–V* characteristic of the nanocrystal was measured by scanning the FEED (Fig. 1a, curve *1*). Within 10 min of subsequent heating of the emitter at 1000 K, the emitter image stopped flickering and the FEED was measured again. The energy distributions had one maximum (Fig. 1b), and its FWHM increased from 0.30 to 0.45 eV as the anode voltage was raised from 1800 to 2500 V. The *I–V* characteristic of the heated sample is represented by curve *2* in Fig. 1a. The fact that curves *1* and *2* run close together suggests that stripping the surface layer off in an ultrahigh vacuum does make the emitting surface of the nanocrystal pure.

CTFR was accomplished by increasing the anode voltage in several steps for a short time, after which the energy distribution of electrons emitted from the region probed was checked. An extra low-energy peak in the distribution, which is shifted by 0.45–0.50 eV toward lower energies relative to the main one, appeared after the total emitter current reached a value of 5 μA. By scanning the FEED in the anode voltage range from

2000 to 2600 V, *I–V* characteristic *3* (Fig. 1a) was taken. This curve demonstrates that the emission current from the carbon nanocrystal decreased by one order of magnitude. Then, the emitter was heated to 1000 K and kept at this temperature for 10 min three times, and the FEED was taken after each heating. The measurements made at U_a = 2200 V (Fig. 1b) show that the extra low-energy maximum lowers after each heating and the energy interval between the maxima expands from 0.4 to 0.5 eV. The related *I–V* characteristics are presented in Fig. 1a.

Using an arm with four degrees of freedom, the emitter was rotated in the horizontal plane by +1°, –1°, and –2° (the initial position is 0°). Angles –2° and +1° correspond to the left- and right-hand edges of the emission spot from the nanocrystal. The FEEDs shown in Fig. 2a indicate that the height of the extra maximum depends on the angular position of the emitter relative to the energy analyzer with the interval between the maxima remaining constant.

The dependence of the extra peak height in the FEED taken of the reconstructed carbon nanocrystal on the emitter heating and emitter rotation was checked on the second sample of the same carbon fiber. To reconstruct the nanocrystal, the total emission current was increased to 5 μA and simultaneously the sample was heated to ≈1500 K by applying a voltage to the bow for a short time. In this case, too, the extra peak height changes when the emitter is heated to T = 1000 K and depends on the emitter rotation relative to the energy analyzer. When the emitter is rotated, the interval between the main and extra maxima changed by 0.3–0.4 eV (Fig. 2b).

In another series of experiments, we studied the carbon nanotubes applied on the W foil by electrophoresis. Examination of the nanotubes in a JEM 100S transmission electron microscope showed that they are closed and have semispherical tops.

After the vacuum chamber and emitting nanotubes had been warmed by Joule heat, the emission pattern represented a number of aligned oval spots. One stably emitting spot was directed to the probing aperture of the energy analyzer, and the FEEDs were measured in the anode voltage range from 2580 to 3140 V. The measured distributions are seen to be narrow and have a single peak (Fig. 3a). As the anode voltage rises, the distribution shits toward lower energies and its FWHM increases from 0.30 to 0.35 eV. The current–voltage characteristic (curve I in Fig. 3c) is linear. The carbon nanotube probed was categorized as "metallic."

To carry out the CTFR of the area probed, the anode voltage was raised in steps until the total emission current sharply dropped from 420 to 350 nA. Subsequent scanning revealed an extra low-energy peak in the FEED. As the anode voltage increases from 2700 to 3380 V, the extra peak slightly grows and the interval between the maxima expands from 0.3 to 0.4 eV (Fig. 3b). The voltage dependence of the probe current (curve II in Fig. 3c) indicates a decrease in the emission current by one order of magnitude, i.e., that the probed area of the nanotube has been reconstructed. Figure 3d plots the relative height of the extra maximum versus the emitter rotation relative to the energy analyzer in the angular range from –3° to +1°. Under rotation, the interval between the maxima varies within 0.3–0.5 eV.

A total of five emission spots from three foils with nanotubes were studied. As the anode voltage increased, the FEED shifted toward lower energies in proportion to either the probe current (metallic properties of the nanotubes) or the anode voltage (semiconductor properties). Unlike nanocrystalline carbon fibers, all the nanotubes were reconstructed at an emission current from one hundred to several hundreds of nanoamperes. This confirms the compelling fact that heat removal from the nanotube top is inferior to that from a nanocrystalline carbon fiber.

Thus, our study demonstrated that the height of an extra low-energy maximum in the energy distribution of electrons field-emitted from carbon nanocrystals and nanotubes depends on the emitter heating and emitter angular position relative to the energy analyzer. This is consistent with the assumption that the electrons involved in the distribution are emitted from states on the field emitter surface.

CONCLUSIONS

We studied VMN-RK nanocrystalline carbon fiber annealed at 900°C. The nanocrystals were reconstructed by raising the total emission current to 5 μA and heating them at ≈1500 K. As a result, their emission current decreased by one order of magnitude and an extra low-energy peak appeared in the FEED, whose energy position is 0.45–0.50 eV below the position of the main maximum. The FEED taken of the reconstructed nanocrystals suggests that the height of the extra peak depends on the heat treatment conditions. As the heating duration grows, the peak lowers, indicating the possibility of recovering the normal energy distribution of electrons emitted from the carbon nanocrystal.

Another subject of investigation was carbon nanotubes with semispherical tops. It was found that they are prone to current-related thermofield reconstruction: when the anode voltage reaches some threshold, the emission current from the nanotube top drops by nearly one order of magnitude and an extra low-energy peak appears, whose energy position is 0.45–0.50 eV below the position of the main maximum.

The FEEDs taken of reconstructed samples upon rotating about the energy analyzer axis show that the height of the extra maximum depends on the angular position of the emitting nanocrystals and nanotubes. This counts in favor of the assumption that the extra maximum is due to the electrons emitted from surface states of the reconstructed samples.

From the dependences of the extra low-energy maximum on the heating duration and emitter angular position relative to the analyzer, the interval between the extra and main peaks in the FEED is estimated as 0.3–0.5 eV for the samples of both types.

ACKNOWLEDGMENTS

The author is indebted to prof. E.P. Sheshin for submitting carbon fibers and foils with carbon nanotubes.

REFERENCES

1. V. M. Lobanov, Yu. M. Yumaguzin, and R. Z. Bakhtizin, Poverkhnost, No. 8, 53 (2000).
2. V. M. Lobanov and Yu. M. Yumaguzin, Pis'ma Zh. Tekh. Fiz. **28** (1), 3 (2002) [Tech. Phys. Lett. **28**, 1 (2002)].
3. F. G. Allen and G. M. Gobelli, Phys. Rev. **127**, 150 (1962).
4. A. A. Dadykin, Candidate's Dissertation (Kiev, 1990).
5. W. B. Shepherd and W. T. Peria, Surf. Sci. **38**, 461 (1973).
6. J. W. Gadzuk and E. W. Plummer, Rev. Mod. Phys. **45**, 487 (1973).
7. B. V. Bondarenko, E. S. Bakanova, A. Yu. Cherepanov, *et al.*, Radiotekh. Élektron. (Moscow) **30**, 2234 (1985).
8. R. Z. Bakhtizin, V. M. Lobanov, and Yu. M. Yumaguzin, Prib. Tekh. Éksp., No. 4, 247 (1987).

Translated by V. Isaakyan

Technical Physics, Vol. 50, No. 11, 2005, pp. 1490–1496. Translated from Zhurnal Tekhnicheskoĭ Fiziki, Vol. 75, No. 11, 2005, pp. 97–104.

SURFACE, ELECTRON AND ION EMISSION

Ion Transport Mechanism in Solid Electrolyte Films on Lithium

A. V. Churikov

Chernyshevsky State University, Saratov, 410012 Russia

e-mail: churikovav@info.sgu.ru

Received February 9, 2004

Abstract—The rate of Li^+ ion transport in an insulating solid electrolyte film on the Li metal surface versus electric field (<10^7 V/cm) and temperature (in the range 238–343 K) is studied. The dependences found in this work are shown to reflect structural disorder in the electrolyte film material. Disorder causes a spread in the site-to-site hopping length and time. © *2005 Pleiades Publishing, Inc.*

The transport properties of dielectric ion-conducting films covering the metallic lithium surface are of great practical interest, since Li–film–solution structures are used in lithium cells with a nonaqueous electrolyte [1]. The chemical composition of a solid electrolyte film on lithium is rather complex and depends on the composition of a surrounding solution. The thickness of the film varies between 10^{-7} and 10^{-5} cm, its ionic conductivity ranges between 10^{-9} and 10^{-6} $(\Omega\ \mathrm{cm})^{-1}$, and its electron conductivity is less than 10^{-12} $(\Omega\ \mathrm{cm})^{-1}$. Even at the early stage of investigation it was found that electrical processes in Li–film–solution structures are described well in terms of the concept of carrier injection into the surface layer, which increases its ionic conductivity under a voltage [2, 3]. In this work, the author elaborates upon the model mechanism of ion transport in solid electrolyte films on lithium and contrasts theoretical results with experimental data.

EXPERIMENTAL DATA

Experiments were carried out with hermetically sealed cells assembled in dry argon. The cells contained a lithium electrode to be tested, a small amount of an electrolyte, and polarizing and measuring electrodes. A solid electrolyte layer was formed on the surface of the lithium electrode by keeping it in the electrolyte for 1 month. As electrolytes, we used concentrated solutions of $LiClO_4$ in propylene carbonate (PC) and butyrolactone (BA), where a film consisting of lithium carbonate Li_2CO_3 and lithium oxide Li_2O forms, and solutions of $LiBF_4$ in BA, which produce a film consisting of lithium oxide Li_2O and lithium fluoride LiF. Measurements were taken in the temperature range from –35 to 70°C with a temperature control accuracy of 0.1°C. To protect the surface films from damage, the electrode tested was polarized by short direct current pulses of amplitude from 10^{-8} to 10^{-2} A. The same technique was applied to determine the thickness of the films, which was found to vary between 5 and 40 nm in our case. The current pulse minimum width needed to complete the transient and establish a constant potential jump varied within 0.5 and 10 ms.

For all the samples, the results were qualitatively similar. To illustrate the generality of the approach being developed, we present the results for films of different compositions. Figure 1 plots typical j–V curves (j is the current density) in the log–log coordinates. The final results did not depend on the current sense. No hysteresis was found in heating–cooling cycles, as well

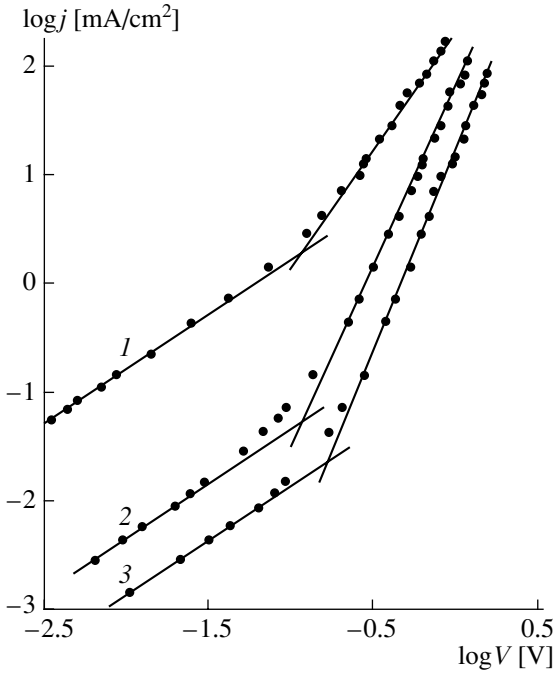

Fig. 1. Current–voltage characteristics of the Li–film–solution structures at a temperature of (*1*) 30, (*2*) –18, (*3*) –27°C (the $LiBF_4$–BA electrolyte).

1063-7842/05/5011-1490$26.00 © 2005 Pleiades Publishing, Inc.

as in taking the j–V curve in the forward and backward directions. In the general case, an ohmic dependence $j \sim V$, observed at low V, changes to a power-type dependence $j \sim V^n$ at high voltages, with exponent n smoothly varying with temperature. Such behavior is characteristic of injection currents [4]. General current density j is a sum of ohmic current $j_\Omega = \sigma_i V/L$ and injection current j_{inj},

$$j = j_\Omega + j_{inj}. \quad (1)$$

The temperature dependence of ionic conductivity σ_i is of activation character with constant energy of activation ω_i,

$$\sigma_i = \frac{\sigma_0}{T}\exp\left(-\frac{\omega_i}{kT}\right), \quad (2)$$

where k is the Boltzmann constant, T is the absolute temperature, and coefficient σ_0 depends on the sample's history.

For the films obtained in the $LiClO_4$–PC, $LiClO_4$–BA, and $LiBF_4$–BA solutions, the measured activation energies were close to each other, namely, 0.59 ± 0.03, 0.58 ± 0.05, and 0.54 ± 0.05 eV, respectively (hereafter, the confidence intervals are given with a 95% probability).

Thus, injection current j_{inj} can be viewed as an increase of the total current over the ohmic (conduction) current. When the j–V curves are represented in the coordinates $\log j_{inj} - \log V$ (Fig. 2), the injection current is seen to strictly follow the power-type dependence $j_{inj} \sim V^n$. The form and temperature run of the j–V curves are nearly the same for all the samples, despite the chemical composition of the surface films is different. This suggests that a mechanism of charge transfer in solid electrolyte films does not depend on their composition and structure.

THEORETICAL

Consider current passage through a thin homogeneous insulating layer of low ionic conductivity that is sandwiched between high-conductivity materials (the situation meeting experimental conditions). The steady-state profiles of electric field strength ξ and the concentrations of intrinsic, n_0, and injected, n_{inj}, carriers (bearing a charge of +1 as Li^+ ions) in a film of thickness L along coordinate x ($0 \le x \le L$) satisfy the Poisson and continuity equations. In the 1D case, these equations have the form [4]

$$\frac{d\xi}{dx} = \frac{qn_{inj}}{\varepsilon\varepsilon_0}, \quad (3)$$

$$j = q\xi(\mu_\Omega n_0 + \mu_{inj} n_{inj}), \quad (4)$$

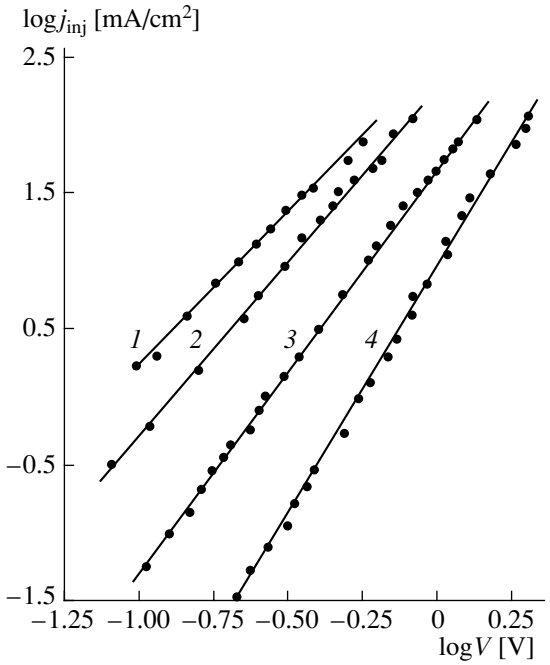

Fig. 2. Injection current–voltage characteristics of the Li–film–solution structures at a temperature of (*1*) 40, (*2*) 25, (*3*) 0, and (*4*) –27°C (the $LiClO_4$–BA electrolyte).

where q is the absolute charge of carriers, μ_Ω and μ_{inj} are the respective mobilities of intrinsic and injected carriers, and $\varepsilon\varepsilon_0$ is the permittivity of the film material.

Let us integrate the set of Eqs. (3) and (4) on the assumption that the film is kept under constant potential V and the boundary $x = 0$ infinitely long injects carriers (then, $\xi(0) = 0$), which all have the same mobility in the film ($\mu_\Omega = \mu_{inj} = \mu$). The result of integration coincides with experimentally observed dependence (1),

$$j = \frac{qn_0\mu V}{L} + \frac{\mu\varepsilon\varepsilon_0\xi_L^2}{2L} = j_\Omega + j_{inj}, \quad (5)$$

where ξ_L is the field strength at the absorbing boundary $x = L$.

Since $\sigma_i = q\mu n_0$ and $\xi_L \approx V\sqrt{2}/L$ [4], formula (5) can be recast as

$$j \approx \frac{\sigma_i V}{L} + \frac{\mu\varepsilon\varepsilon_0 V^2}{L^3}. \quad (6)$$

Expression (6) meets the experimental dependences (Fig. 1) at only one temperature when $n = 2$. The reason for such a discrepancy seems to be the following. Equation (4) implies that carriers of a given sort have the same mobility, i.e., when subjected to an electric field, are transferred through a given layer for the same time. This assumption works well for single crystals but turns out to be inadequate for the surface layer covering the lithium surface. This surface layer incorporates various

components, which form very rapidly; hence, the structure of the layer is heavily disordered. A specific feature of disordered solids is a wide spectrum of times of elementary events, which characterizes many of their time-dependent properties [5]. This feature is unrelated to details of the atomic or molecular structure of solids and therefore specifies their general behavior. Disorder gives rise to a special type of transport when the transport rate becomes a fractional-power function of time, frequency, distance, or voltage, the exponent being continuously dependent on both material properties and experimental conditions [5–18]. Based on the experimental temperature dependence of the rate of charge transport through the films on lithium, one can suppose that such anomalous transport in a strong electric field takes place in our case too.

Let us derive an expression for the voltage dependence of the injection current in a solid film with intrinsic conductivity using the notion of transition time τ. The current density is generally given by

$$j = q\bar{n}\bar{v} = q\bar{n}L/\tau, \quad (7)$$

where $\bar{n}$ and $\bar{v}$ are the mean concentration and drift velocity of charge carriers.

The numerator of (7), $q\bar{n}L$, is the total charge of mobile carriers per unit surface area of the film. Then, τ is the time of transit of carriers from one boundary of the sample to the other. Under the ohmic conditions, the concentration is uniformly distributed across the film and equals intrinsic concentration n_0; hence, $j_\Omega = qn_0L/\tau_\Omega$. A similar formula holds for the injection current, injected charge $q\bar{n}_{inj}L$ confined in the film being related to the voltage across the sample by the formula for a plane capacitor whose capacitance is roughly equal to the geometric capacitance of the film; that is, $j_{inj} = qn_{inj}L/\tau_{inj} \approx \varepsilon\varepsilon_0 V/L\tau_{inj}$.

According to (1), the total current is a sum of these two components,

$$j \approx \frac{qn_0L}{\tau_\Omega} + \frac{\varepsilon\varepsilon_0 V}{\tau_{inj}L}. \quad (8)$$

A more exact expression can be obtained by solving the set of Eqs. (3) and (4). Since the time it takes for particles of sort i to transit through a layer of thickness L is given by

$$\tau_i = \frac{1}{\mu_i}\int_0^{\xi_L}\frac{1}{\xi}\frac{dx}{d\xi}d\xi, \quad (9)$$

the transit time for intrinsic carriers is

$$\tau_\Omega = \frac{1}{j}\left(qn_0L + \frac{\varepsilon\varepsilon_0\xi_L\mu_{inj}}{\mu_\Omega}\right) \quad (10)$$

and that for injected carriers is

$$\tau_{inj} = \frac{1}{j}\left(\frac{qn_0L\mu_\Omega}{\mu_{inj}} + \varepsilon\varepsilon_0\xi_L\right). \quad (11)$$

Combining (10) and (11) yields

$$j = \frac{qn_0L}{\tau_\Omega} + \frac{\varepsilon\varepsilon_0\xi_L}{\tau_{inj}}. \quad (12)$$

In final expression (12), mobility in explicit form is lacking. The difference between Eqs. (8) and (12) is minor, because ξ_L closely approximates the electric field mean strength.

For charged particles migrating in a disordered solid, the functional dependence $\tau = f(V, L, T)$ may both coincide with and differ appreciably from this dependence in an ordered crystal lattice [5–7]. Charge transport may be both normal and anomalous, depending on the material and experimental conditions. The difference between them shows up most vividly in experiments on determining the transition time [5–13]. In the case of normal (Gaussian) transport, τ linearly depends on ratio L/ξ,

$$\tau = L/\xi\mu; \quad (13)$$

that is, carriers possess a certain mobility.

In the case of anomalous (dispersion) transport, a train of charge carriers is characterized by a large dispersion (on the order of the sample's thickness) and the transit time becomes a nonlinear function of L/ξ: $\tau \sim (L/\xi)^{1/\alpha}$, where $0 < \alpha < 1$. The notion of drift mobility loses the physical meaning: this parameter calculated from the transit time turns out to be dependent on the sample thickness instead of being dependent on the material properties [6, 7]. Experiments aimed at determining the transit time in various disordered materials show that normal and anomalous transports may be observed in the same material at different temperatures [5–10].

The theoretical models accounting for anomalous transport exploit the assumption that disordered materials feature a spread in the spacings between neighboring localized sites and/or a spread in potential barriers separating these sites. Accordingly, there appears a wide variety of times of elementary events accompanying the charge motion in a disordered material [15–18]. In the multiple sticking model, charge transfer proceeds through multiple capture of carries by and their escape from localized centers. If the crystal lattice is disordered, sticking centers (levels) will be distributed over energy. For the level exponential occupation, the j–V curve is given by

$$j \sim V^{1+1/\alpha}/L^{1+2\alpha}, \quad (14)$$

where

$$\alpha = T/T_t, \quad (15)$$

that is, exponent n is equal to $n = 1 + T_t/T$, where T_t is the distribution parameter [4, 14–17].

Another model, the model of stochastic transport, considers the charge motion as a random hopping process, when even small fluctuations of the hopping length cause a wide spread in hopping times; in other words, the hopping time distribution is due to hopping length fluctuations rather than to hopping energy fluctuations [6]. According to the theory of stochastic transport, the transport can be considered as a sequence of hops from site to site (a site may be a defect, localized center, etc.). If the sites are equally spaced (the hopping lengths are the same), the hopping frequency has certain value ν. If, however, distance r between neighboring sites that are accessible for a hopping carrier varies about some mean value r_0, the hopping frequency will tangibly depend on the site spacing: $\nu(r) \sim \exp(-r/R_{\text{eff}})$, where R_{eff} is the effective radius of localized centers. Calculation of the group velocity of carriers hopping in an electric field between randomly distributed centers results in the following expression for the transition time:

$$\tau = \frac{c}{\nu_0}\left(\frac{L}{\dot{l}(\xi)}\right)^{1/\alpha}\exp\left(\frac{\omega_0}{kT}\right), \tag{16}$$

where

$$\alpha = \left(\frac{R_{\text{eff}}}{r_0}\right)^3\left[\ln(\nu_0\tau) - \frac{\omega_0}{kT}\right]^2, \tag{17}$$

c is a factor on the order of unity ($c = 0.92$ at $\alpha = 0.5$); ω_0 is the mean potential barrier between sites; ν_0 is the hopping frequency; and $\dot{l}(\xi)$ is the mean group displacement in the direction of the electric fields per hop, which is proportional to ξ [6].

The proportionality coefficient can be found based on the fact that, in going from anomalous transport to normal one ($\alpha = 1$), expression (16) is bound to transform into (13), where the mobility depends on the microscopic parameters of transport [19],

$$\mu = \frac{qr_0^2\nu}{kT}\exp\left(-\frac{\omega_0}{kT}\right). \tag{18}$$

Hence, $\dot{l} = qr_0^2\xi/kT$ and we arrive at an expression for the transition time,

$$\tau = \frac{c}{\nu_0}\left(\frac{LkT}{qr_0^2\xi}\right)^{1/\alpha}\exp\left(\frac{\omega_0}{kT}\right). \tag{19}$$

Associated numerical factors on the order of unity, which depend on the number of nearest neighboring sites and correlation effects [19], are embodied in ν_0. Next, assuming that $c \approx 1$ and $\xi \approx V/L$, we substitute expression (19) for τ_{inj} into (8) to obtain an expression for the injection current (accurate to a factor on the order of unity) in a disordered solid for the case of anomalous transport when hopping is characterized by one value, ω_0, of the potential barrier,

$$j_{\text{inj}} \approx \nu_0\varepsilon\varepsilon_0\frac{V}{L}\left(\frac{qr_0^2V}{kTL^2}\right)^{1/\alpha}\exp\left(-\frac{\omega_0}{kT}\right). \tag{20}$$

While the models of multiple capture and stochastic transfer are based on different assumptions, they use an identical mathematical formalism [5, 14–17]. The physical patterns are also the same. In turns out in both cases that particles in a disordered solid travel over a distributed network of unequal paths. Some of the particles cross the sample fairly rapidly (short routes), while others stay in the sample for long, moving through widely spaced sites (longer hopping times). As the voltage across the sample rises, progressively wider spaced sites (requiring increasingly longer hopping times) become involved in the transport process. Such a situation may be viewed as a change in the relationship between the free charge and trapped (fixed) charge or as a change in the mean effective mobility of carriers. Eventually, the effective mobility becomes dependent on the electric field strength and sample thickness. The difference in the expressions for α (formulas (15) and (17)) reflects different model assumptions. The theory is helpful when intrinsic and injected carries are dissimilar in nature and migrate with different velocities but independently and without recombination (which may occur, for example, when the electron current coexists with the intrinsic ionic conductivity).

THEORY VERSUS EXPERIMENT

The form and temperature run of the current–voltage curves for total current j and injection current j_{inj} (Figs. 1 and 2) suggest that anomalous transport of carriers in the disordered solid films on lithium. Let us see whether the temperature variation of exponent n in the dependence $j_{\text{inj}} \sim V^n$ correlates with the theoretical predictions. Both models give $n = 1 + 1/\alpha$. However, in the model of multiple capture, parameter α is given by formula (15), which yields a straight line issuing from the origin in the coordinates $(n - 1) - T^{-1}$, while in the stochastic transport model, formula (17) for α is linearized in the coordinates $(n - 1)^{-0.5} - T^{-1}$ (see Fig. 3a). The temperature run of exponent n in the dependence $j_{\text{inj}} \sim V^n$ satisfied Eq. (17) and did not satisfy Eq. (15) for all the samples studied.

Now let us check whether the temperature variation of the current–voltage curves agrees with the general behavior predicted by the stochastic transport theory. Expressions (2) and (20) suggest that the current depends on T^{-1} exponentially and effective activation energy $\omega_j = -kd(\ln j)/d(T^{-1})$ does not depend on the voltage in the intrinsic conductivity range of the film, remaining equal to $\omega_\Omega = -kd(\ln\sigma_i)/d(T^{-1})$. As the voltage grows, ω_j is bound to change from ω_Ω to the effec-

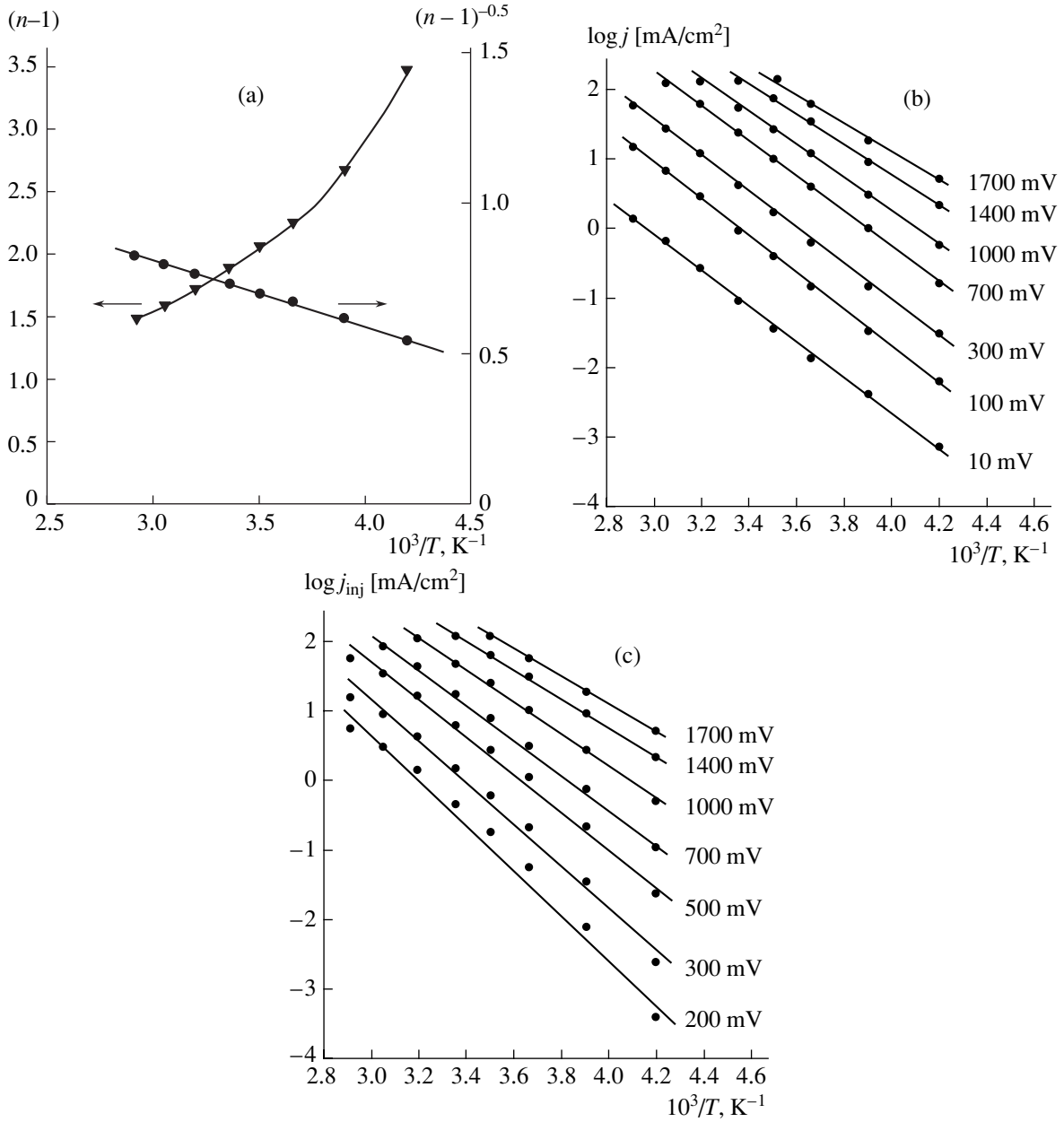

Fig. 3. Temperature dependences of (a) exponent n in the relationship $j_{inj} \sim V^n$, (b) the logarithm of total current j, and (c) the logarithm of injection current j_{inj} (the $LiClO_4$–PC electrolyte).

tive activation energy of the injection current, $\omega_{inj} = -kd(\ln j_{inj})/d(T^{-1})$. According to (17) and (20),

$$\omega_{inj} = \omega_0\left[1 - 2\left(\frac{R_{eff}}{r_0\alpha}\right)^{3/2}\ln\left(\frac{qr_0^2V}{kTL^2}\right)\right] - \frac{kT}{\alpha}. \qquad (21)$$

Experimental dependences $\log j - T^{-1}$ and $\log j_{inj} - T^{-1}$ for different voltages are shown in Figs. 3b and 3c. The slope of the straight lines in Fig. 3b remains constant in the intrinsic ionic conductivity range and changes markedly with increasing V, approaching the slope of the current in Fig. 3c. From Eq. (21), it follows that effective activation energy ω_{inj} depends on mean potential barrier ω_0 being overcome in the hopping process and, at the same time, is a complicated function of α, T, and V, remaining constant only in a narrow V-dependent temperature range. Under our experimental conditions, the voltage across the sample was varied significantly while T and α only slightly.

The voltage dependence of the effective activation energy is shown in Fig. 4. For all the samples, ω_{inj} is a linear function of the potential in accordance with (21).

The slopes of the curves $(n-1)^{-1/2} = a_1 - b_1/T$ (Fig. 3a) and $\omega_{inj} = a_2 - b_2 \ln V$ (Fig. 4) are interrelated and, as follows from (17) and (21), must correlate in view of the equality $2kb_1 b_2^{-1} \langle 1/\alpha \rangle^{3/2} = 1$, in which the mean value of $\langle 1/\alpha \rangle = \langle n-1 \rangle$ in the temperature range under study should be taken. Our measurements on lithium-based ion-conducting films gave $2kb_1 b_2^{-1} (1/\alpha)^{3/2} = 1.00 \pm 0.05$.

Thus, one can state both qualitative and quantitative agreement between equations derived from the theory of stochastic transport in a disordered solid and experimental data for the field and temperature effect on the rate of carrier transport through a solid electrolyte film on lithium. This allows us to find transport microscopic parameters ω_0, r_0, R_{eff}, and ν_0 as follows. Let

$$W_{inj} = j_{inj} \Big/ \left(\frac{q r_0^2 V}{kTL^2} \right)^{1/\alpha} \frac{V}{L}. \qquad (22)$$

Then, (20) can be recast as

$$\ln W_{inj} = \ln(\nu_0 \varepsilon \varepsilon_0) - \omega_0 / kT, \qquad (23)$$

where ν_0 contains the numerical factor on the order of unity. According to (23), all values of variable W_{inj}, having the dimension of conductivity, are the same at a given temperature and all the experimental j_{inj}–V curves must be fitted by the same straight line in the coordinates $\ln W_{inj}$–T^{-1} provided that hopping is characterized by one potential barrier ω_0. In calculations, parameters ε, L, and τ are assumed to be given. We introduce a trial value of r_0, calculate a set of W_{inj} by (22), and, based on this set, find optimal values of coefficients ν_0 and ω_0 by (23). Using Eq. (17), R_{eff} and τ are found from known coefficients a_1 and b_1. Then, we compare the calculated value of τ with the given one, change r_0 toward the desired (given) value of τ, and repeat the procedure again and again until these two values of τ coincide.

Figure 5 plots $\ln W_{inj}$ against T^{-1} at the final sage of calculation. The slope corresponds to potential barrier mean height $\omega_0 = 0.22$ eV. All pairs j_{inj}–V measured at one temperature give, as was expected, the same value of W_{inj}. The plot is almost a straight line but may curve if the temperature range is considerably extended. Therefore, the assumption that one value of the potential barrier for hopping particles prevails in the films can be adopted only as a first approximation.

Processing of the whole data array results in the following. The potential barrier has a smallest spread from sample to sample: the mean value of this parameter is $\omega_0 = 0.24 \pm 0.035$ eV. The spread in the calculated values of parameters R_{eff} and r_0 is much larger; however, ratio R_{eff}/r_0 appearing in the analytical equations is nearly the same for most of the samples, 0.245 ± 0.045.

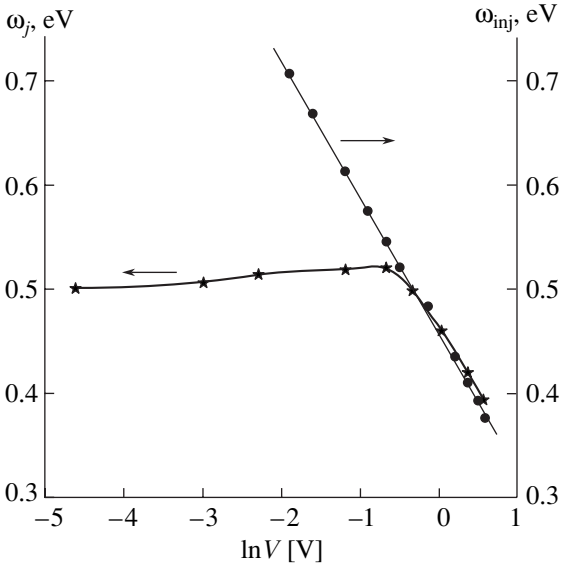

Fig. 4. Activation energies of the total current, ω_j, and injection current, ω_{inj}, vs. the logarithm of the voltage.

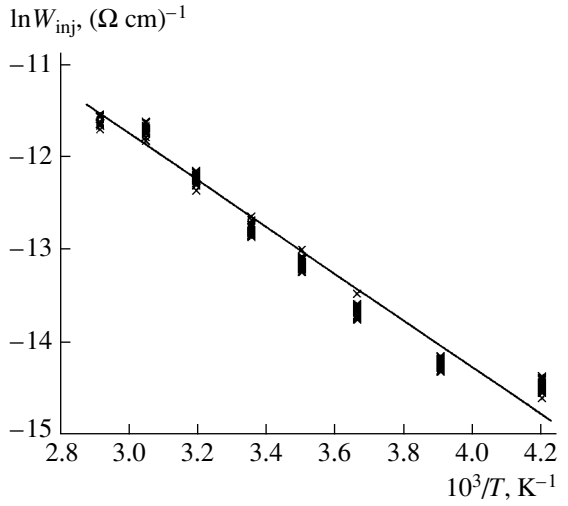

Fig. 5. $\ln W_{inj}$ vs. T^{-1}.

The logarithm of the hopping frequency is $\log \nu_0 = 10.5 \pm 0.7$ [s^{-1}].

The parameters were calculated for $\varepsilon = 8.9$ (the permittivity of Li_2O as the basic component of the film) and $\tau = 1$ ms (the approximate duration of the transient at $V = 1$ V). It is of interest to mention how the calculated parameters vary with ε and τ. A change in ε causes a proportional change in L, r_0, and R_{eff}, with all other parameters remaining the same. When τ changes by one order of magnitude, ν_0 changes two to four times and ω_0, r_0, and R_{eff} by 5–25%.

Combining Eqs. (1), (2), and (20), we can write a general expression for the j–V characteristic of Li–

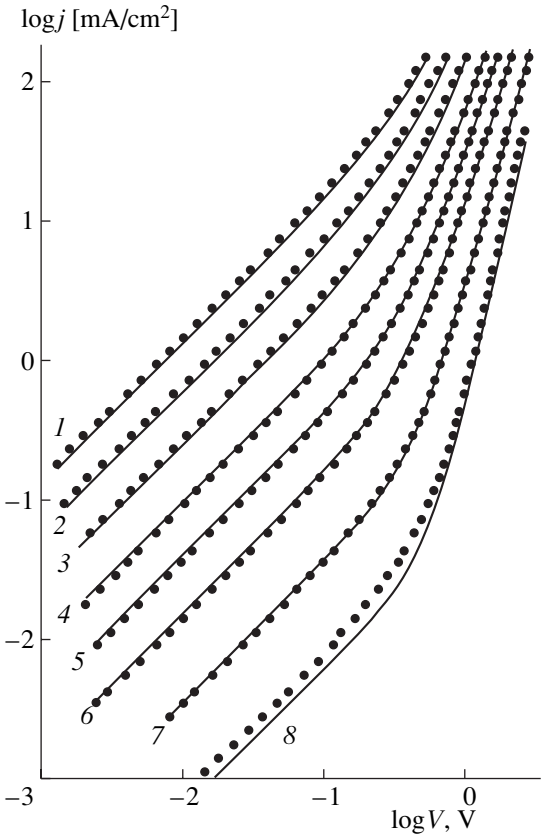

Fig. 6. Experimental j–V characteristics (circles) vs. analytical curves (continuous lines) for the Li–film–solution structure (the $LiClO_4$–PC electrolyte) at L = 7.90 nm, σ_0 = 2614 $(\Omega\ \text{cm})^{-1}$ K, ω_i = 0.5357 eV, ω_0 = 0.2125 eV, R_{eff}= 0.080 nm, r_0 = 0.404 nm, and $\nu_0 = 1.521 \times 10^{10}$ s^{-1}. The temperature is (*1*) 70, (*2*) 55, (*3*) 40, (*4*) 25, (*5*) 12.5, (*6*) 0, (*7*) –17, and (*8*) –35°C.

film–solution structures in a wide ranges of current, voltage, and temperature,

$$j = \frac{V}{L}\left[\frac{\sigma_0}{T}\exp\left(-\frac{\omega_i}{kT}\right) + \nu_0\varepsilon\varepsilon_0\left(\frac{qr_0^2V}{kTL^2}\right)^{1/\alpha}\exp\left(-\frac{\omega_0}{kT}\right)\right], \quad (24)$$

where dimensionless parameter α is given by (17).

As the temperature grows, so does α, and, at $\alpha \approx 1$, Eq. (24) passes into Eq. (6) for normal transport.

The validity of the calculations was checked by the inverse procedure, i.e., by calculating the j–V curves using the parameters found. For the same set of transport microscopic parameters, the experimental curves and analytical ones calculated by Eq. (24) coincide throughout the ranges of current, voltage, and temperature, as follows from Fig. 6. The small divergence of the ohmic portions can be eliminated by taking into account the variation of activation energy ω_i with temperature. The model suggested in this work provides a general approach to solid-state lithium-based structures the electric properties of which are controlled by surface ion-conducting layers.

CONCLUSIONS

The field and temperature dependences of the Li^+ ion transport rate in solid electrolyte films on lithium have provided an insight into a transport mechanism in such films. An ion transport model is suggested that includes the effect of injection current and material disorder. This model is shown to provide a good fit to the experimental data.

ACKNOWLEDGMENTS

This work was supported by the Russian Foundation for Basic Research (grant no. 02-03-32642) and the Federal Agency for Education of the Russian Federation (grant nos. A04-2.11-17 and UR.05.01.035).

REFERENCES

1. A. N. Dey, Thin Solid Films **43**, 131 (1977).
2. E. S. Nimon, A. V. Churikov, A. A. Senotov, *et al.*, Fiz. Tverd. Tela (Leningrad) **31**, 278 (1989) [Sov. Phys. Solid State **31**, 879 (1989)].
3. Yu. Ya. Gurevich, A. L. L'vov, E. S. Nimon, and Yu. J. Kharkats, Fiz. Tverd. Tela (St. Petersburg) **35**, 1536 (1993) [Phys. Solid State **35**, 775 (1993)].
4. M. Lampert and P. Mark, *Current Injection in Solids* (Academic, New York, 1970; Mir, Moscow, 1973).
5. G. Pfister and H. Scher, Adv. Phys. **27**, 747 (1978).
6. H. Scher and E. Montroll, Phys. Rev. B **12**, 2455 (1975).
7. N. F. Mott and E. A. Davis, *Electronic Processes in Non-Crystalline Materials* (Clarendon, Oxford, 1971; Mir, Moscow, 1982), Vol. 1.
8. G. Pfister, Phys. Rev. Lett. **36**, 271 (1976).
9. B. T. Kolomiets, E. A. Lebedev, and L. P. Kazakova, Fiz. Tekh. Poluprovodn. (Leningrad) **12**, 1771 (1978) [Sov. Phys. Semicond. **12**, 1049 (1978)].
10. S. D. Shutov, M. A. Iovu, and M. S. Iovu, Fiz. Tekh. Poluprovodn. (Leningrad) **13**, 956 (1979) [Sov. Phys. Semicond. **13**, 559 (1979)].
11. V. I. Arkhipov, E. A. Lebedev, and A. I. Rudenko, Fiz. Tekh. Poluprovodn. (Leningrad) **15**, 712 (1981) [Sov. Phys. Semicond. **15**, 405 (1981)].
12. G. Pfister, Philos. Mag. **36**, 1147 (1977).
13. G. Pfister, S. Grammatica, and J. Mort, Phys. Rev. Lett. **37**, 1360 (1976).
14. F. W. Schmidlin, Philos. Mag. B **41**, 535 (1980).
15. F. W. Schmidlin, Solid State Commun. **22**, 451 (1977).
16. J. Noolandi, Solid State Commun. **24**, 477 (1977).
17. M. Pollak, Philos. Mag. **36**, 1157 (1977).
18. J. Bisquert and G. Garcia-Belmonte, Élektrokhimiya **40**, 396 (2004) [Russ. J. Electrochem. **40**, 352 (2004)].
19. J. R. Manning, *Diffusion Kinetics for Atoms in Crystals* (Van Nostrand, New York, 1968; Mir, Moscow, 1971).

Translated by V. Isaakyan

Technical Physics, Vol. 50, No. 11, 2005, pp. 1497–1503. Translated from Zhurnal Tekhnicheskoĭ Fiziki, Vol. 75, No. 11, 2005, pp. 105–111.

EXPERIMENTAL INSTRUMENTS AND TECHNIQUES

Massive, Thick-Film, and Thin-Film $La_{0.6}Sr_{0.3}Mn_{1.1-x}Fe_xO_{3\pm\delta}$ Magnetoresistive Ceramics: Structure and Properties

V. P. Pashchenko[1,2], Yu. F. Revenko[1], A. V. Pashchenko[1], V. K. Prokopenko[1], A. A. Shemyakov[1], V. A. Turchenko[1], N. I. Nosanov[1], V. I. Volkov[2], V. M. Ishchuk[3], I. N. Chukanova[3], A. I. Bazhin[4], and V. V. Pashchenko[4]

[1] *Donetsk Physicotechnical Institute, National Academy of Sciences of Ukraine, Donetsk, 83114 Ukraine*
e-mail: pashchen@pashchen.fti.ac.donetsk.ua
[2] *Reaktivélktron Research Center, National Academy of Sciences of Ukraine, Donetsk, 83096 Ukraine*
[3] *Institute of Single Crystals, National Academy of Sciences of Ukraine, Kharkov, 61042 Ukraine*
[4] *Donetsk State University, Universitetskaya ul. 24, Donetsk, 83055 Ukraine*
e-mail: bazhin@dongu.donetsk.ua
Received November 26, 2004

Abstract—Magnetoresistive ceramic and thick- and thin-film $La_{0.6}Sr_{0.3}Mn_{1.1-x}Fe_xO_{3\pm\delta}$ ($x = 0$, 0.04) samples are studied by X-ray diffraction, ^{55}Mn nuclear magnetic resonance (NMR), resistivity measurements, and magnetic measurements. Their rhombohedrally distorted ($R\bar{3}c$) perovskite structure is found to contain anion and cation vacancies and nanocluster defects. Their broad asymmetric ^{55}Mn NMR spectra support high-frequency electron–hole exchange between Mn^{3+} and Mn^{4+} and the fact that their environments are different due to a high defect concentration and high structural inhomogeneity. Iron doping and an increase in the annealing temperature result in a decrease in the temperatures of the metal–semiconductor and ferromagnet–paramagnet phase transitions and an increase in the magnetoresistive effect (MRE). The low-field MRE in the low-temperature region (~100 K) in the ceramics and thick film is explained by tunneling in crystallite boundaries. An analysis of the effect of iron and the annealing temperature on the activation energy confirms the conclusion regarding a defect system of the perovskite structure and the presence of several mechanisms of activation processes. © *2005 Pleiades Publishing, Inc.*

INTRODUCTION

Among numerous compositions of the manganite–lanthanum perovskites $La^{3+}_{1-x}A^{2+}_xMn^{3+}_{1-x}Mn^{4+}_xO^{2-}_{3\pm\delta}$ (where A^{2+} is Ca^{2+}, Sr^{2+}, Ba^{2+}, or Pb^{2+}) [1–5], the most promising compositions from the scientific and applied points of view are strontium-doped manganites [6–8]. These compositions are characterized by the maximum peak temperatures T_p of the magnetoresistive effect (MRE) occurring near the temperatures of the metal–semiconductor (T_{ms}) and ferromagnet–paramagnet (T_C) phase transitions. Scientific and applied interest in these materials is warmed by the fact that the unique relation between electrical and magnetic phenomena near these phase transitions [9–11] is still a mystery and also by possible application of the manganite–lanthanum perovskites in transducers and sensors.

In most works, ceramic [12, 13] or thin-film [14, 15] stoichiometric manganite samples were investigated. In [16, 17], we showed that the most promising compositions should contain excess hyperstoichiometric manganese with respect to the *A*-sublattice cations of the perovskite structure. Therefore, it is interesting to compare the structure and properties of ceramic and thick- and thin-film nonstoichiometric manganite–lanthanum perovskites with excess manganese, whose structural, resistive, and magnetic features are also controversial.

EXPERIMENTAL

The $La_{0.6}Sr_{0.3}Mn_{1.1-x}Fe_xO_{3\pm\delta}$ samples were prepared from a mixture of the powders $La(OH)_3$ (*C*63/*m*, $a = 6.537$ Å, $c = 3.865$ Å) and $SrCO_3$ (*Pnma*, $a = 5.107$ Å, $b = 8.414$ Å, $c = 6.029$ Å) and the analytical-grade manganese oxides Mn_3O_4 ($I4_1/amd$, $a = 5.76$ Å, $c = 9.44$ Å) produced in Belgium or at the Dnepropetrovsk chemicals plant (in the latter case, the oxide contains an iron impurity). Due to the presence of the iron impurity, the composition of the second batch of manganite–lanthanum perovskites corresponded to the molar formula $La_{0.6}Sr_{0.3}Mn_{1.06}Fe_{0.4}O_{3\pm\delta}$. We chose this manganese-containing raw material to check the possibility of using less scarce and cheaper raw materials for the production of magnetoresistive transducers. The samples of both batches were sintered at 1000°C for 22 h.

The ceramic samples (samples *C*) ($d = 10$ mm, $h = 3$ mm), including targets ($d = 25$ mm, $h = 6$ mm) for

Table 1. Structure type, lattice parameter, magnetic ordering temperature T_C, metal–semiconductor phase transition temperature T_{ms}, MRE peak temperature T_p, and magnetoresistive effect *MR* in a magnetic field *H* for the ceramic (*C*), thick–film (*F*), and thin–film (*f*) $La_{0.6}Sr_{0.3}Mn_{1-x}Fe_xO_3$ samples

Sample	x	Structural data			T_C, K	ΔT_C, K	T_{ms}, K	$T_p(H)$, K	*MR* (T, H = 2 kOe), %	
		type	a, Å	α					T = 100 K	$T = T_p$
C 1250	0	$R\bar{3}c$	7.745	90.32°	343	269–362	366	357 (2 kOe)	8.1	1.3
C 1350	0	$R\bar{3}c$	7.744	90.31°	357	313–370	–	357 (2 kOe)	10.5	2.3
C 1500	0	$R\bar{3}c$	7.742	90.30°	355	342–370	348	352 (2 kOe)	9.5	1.0
F 1250	0	$R\bar{3}c$	7.749	90.29°	345	312–356	367	358 (2 kOe)	8.3	1.3
C 1250	0.04	$R\bar{3}c$	7.766	90.33°	320	257–352	250	330 (5 kOe)	8.5	1.2
F 1250	0.04	$R\bar{3}c$	7.751	90.30°	327	260–355	250	330 (5 kOe)	8.5	6.0
f	0.04	Pseudo cubic	3.870	–	–	–	245	175 (2 kOe) 209 (5 kOe)	4.5	6.2

laser sputtering, were sintered from compacts at 1250°C for 22 h, 1350°C for 3.5 h, and 1500°C for 3 h. The thick polycrystalline films (samples *F*) were prepared using masks: a paste was applied onto an aluminum-oxide substrate containing 94–95% Al_2O_3, 2.5% SiO_2, 1.96% MnO, and 0.48% Cr_2O_3. This paste was baked at 1250°C.

The thin (~2000 Å) single-crystal $La_{0.6}Sr_{0.3}Mn_{1.06}Fe_{0.4}O_{3\pm\delta}$ films (samples *f*) were fabricated by laser sputtering of the ceramic target of the second batch onto a single-crystal $LaAlO_3$ substrate with a pseudocubic structure (a = 3.787 Å) and the (400) crystallographic surface orientation.

The samples were studied by the following methods. (i) X-ray diffraction (on a DRON-3 diffractometer using Cu radiation) was used to determine the phase compositions of the samples (with an error of 3%) and the type and parameters of perovskite crystal lattice (with an error of 0.1%). (ii) The four-probe method was used to determine the electrical resistivity ρ and the relative resistance $R = R_{T,H}/R_{273\,K,0}$ (with an error of 0.5%) over a wide temperature range (77–450 K). (iii) A magnetic method was used to find the temperature dependence of the relative differential magnetic susceptibility χ_{ac} (with an error of 3%). (iv) ^{55}Mn NMR using the spin–echo technique was performed at a temperature of 77 K to determine the resonance spectral frequency (with an error of 0.1%), the magnetic and valence states of the manganese ions, and the difference between their environments in the ceramic samples. (v) A magnetoresistive method was used to determine the magnetoresistive effect $MR = (\rho_0 - \rho_H)/\rho_0$, where ρ_0 is the resistivity (or the relative resistance) at H = 0 and ρ_H is the resistivity in a magnetic field H = 2 or 5 kOe.

RESULTS AND DISCUSSION

The X-ray diffraction data demonstrate that, unlike the $La_{0.6}Sr_{0.2}Mn_{1.2}O_{3\pm\delta}$ samples studied earlier [18], the $La_{0.6}Sr_{0.3}Mn_{1.1-x}Fe_xO_{3\pm\delta}$ samples of both compositions (x = 0 and 0.04) are virtually single-phase and consist of a perovskite-like rhombohedral distorted ($R\bar{3}c$) structure. Table 1 gives the lattice parameters a and α; the phase transition temperatures T_{ms}, T_C, and T_p; and the magnetoresistive effects of the ceramic and thick-film samples of the first ($La_{0.6}Sr_{0.3}Mn_{1.1}O_{3\pm\delta}$) and second ($La_{0.6}Sr_{0.3}Mn_{1.06}Fe_{0.04}O_{3\pm\delta}$) compositions. The differences in the lattice parameters and the phase transition temperatures for the compositions with x = 0 and 0.04 are related to the effect of iron, whose ionic radius is large, and these differences between the ceramic and film are related to different values of their oxygen nonstoichiometry δ [19]. The low T_{ms} and T_p temperatures of the samples of the iron-containing batch are caused by Fe ions located in octahedral positions; they disturb the Mn^{3+}–Mn^{4+} interaction, which agrees with [20].

To reveal the role of iron in the formation of the structure and properties of the $La_{0.6}Sr_{0.3}Mn_{1.1-x}Fe_xO_{3\pm\delta}$ (x = 0, 0.04) ceramic samples, we performed ^{55}Mn NMR studies. Figure 1 shows the ^{55}Mn NMR spectra of the ceramic samples with x = 0 and 0.04. A comparison of these spectra by making allowance for the mechanism of defect formation [16], valence states, and their distribution allowed us to find their molar formulas (see Table 2). Computer decomposition and analysis of the ^{55}Mn NMR spectrum of the ceramic sample shown in Fig. 1 demonstrate that the average frequency for the composition with x = 0 is $\bar{F}_1$ = 378.3 ± 0.3 MHz and that for x = 0.04 is $\bar{F}_2$ = 375.2 ± 0.3 MHz. A lower resonance frequency in the

broader spectrum of the iron-doped sample indicates its higher nanoinhomogeneity.

It is interesting to analyze the effect of the annealing temperature of the ceramic samples on their relative differential magnetic susceptibility χ_{ac} and the T_C determined from these data (Fig. 2). The character of the $\chi_{ac}(T)$ temperature dependences in Fig. 2 indicates ferromagnetic ordering of the samples below the Curie temperature T_C. The T_C temperature was determined from the position of an inflection point in the $\chi_{ac}(T)$ in the region of ferromagnetic ordering; that is,

$$\left|\frac{\partial\chi_{ac}(T)}{\partial T}\right|_{T=T_C} = \max,$$

which corresponds to the maximum rate of ordering of the magnetic moment under the action of a measuring field $h = 0.1$ Oe with a modulation frequency of 600 Hz. The width ΔT_C of the magnetic phase transition corresponds to the temperature range from the maximum magnetic susceptibility in the $\chi_{ac}(T)$ dependences to the temperature of transition into a paramagnetic state ($\chi_{ac} \approx 0$). According to Table 1, an increase in the sintering temperature of the ceramics from 1250 to 1350 and 1500°C results in an increase in T_C and a decrease in T_{ms}. This behavior is thought to be due to different effects of the oxygen nonstoichiometry and the defect concentration on the magnetic and resistive properties. The effect of anion vacancies on the decrease in T_{ms} can explain its lowest value (T_{ms} = 245 K) for the incompletely oxidized thin laser film, whose crystal lattice became pseudocubic because of a high concentration of anion vacancies (Table 1). The decrease in ΔT_C with increasing sintering temperature (Table 1) is related to a decrease in the inhomogeneity, which is caused by the clustering of excess manganese. As was shown in [16], this manganese substantially increases the magnetoresistive effect in the self-doped manganite $La_{1-x}Mn_{1+x}O_3$ and the doped manganites $(La_{0.8}Sr_{0.2})_{1-x}Mn_{1+x}O_3$ [18] and $(La_{0.7}Ca_{0.3})_{1-x}Mn_{1+x}O_3$ [21], which are nearest to our composition. The neutron diffraction studies of the samples of the batch with $x = 0.1$ [22] supported their single-phase state. In this case, in the presence of hyperstoichiometric manganese, the perovskite structure contains mesoscopic cluster nanodefects [16, 23, 24].

The effect of the sintering temperature on the resistivity and the metal–semiconductor phase transition temperature T_{ms} of the $La_{0.6}Sr_{0.3}Mn_{1.1}O_{3\pm\delta}$ ceramics and thin film is illustrated in Fig. 3. An increase in the sintering temperature is seen to decrease T_{ms}, and this decrease is more substantial as compared to the decrease in T_C (see Table 1). A comparison of the phase transition temperatures T_{ms}, T_p, and T_C allowed us to draw an interesting conclusion: the MRE peak temperature T_p is located between T_{ms} and T_C. The T_{ms} temperatures of the ceramics (366 K) and the thick film (367 K) sintered at 1250°C are virtually the same (Fig. 3). A lower T_{ms} value in the ceramics sintered at a higher temperature (1500°C) is caused by higher oxygen nonstoichiometry, i.e., by a higher concentration of anion vacancies.

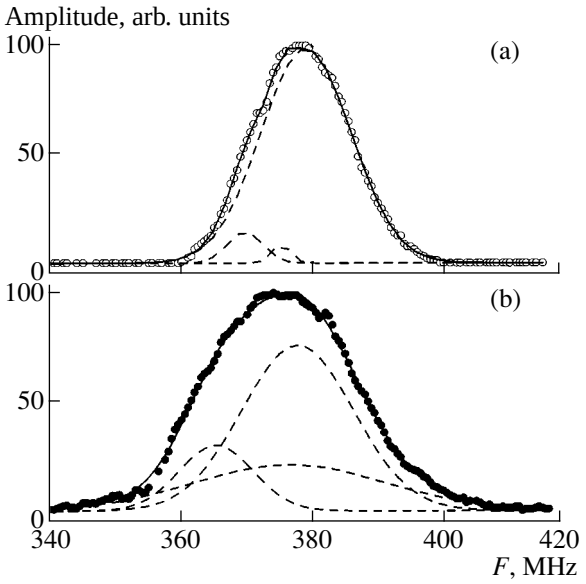

Fig. 1. ^{55}Mn NMR spectra of the $La_{0.6}Sr_{0.3}Mn_{1.1-x}Fe_xO_{3\pm\sigma}$ samples with x = (a) 0 and (b) 0.04 sintered at 1250°C.

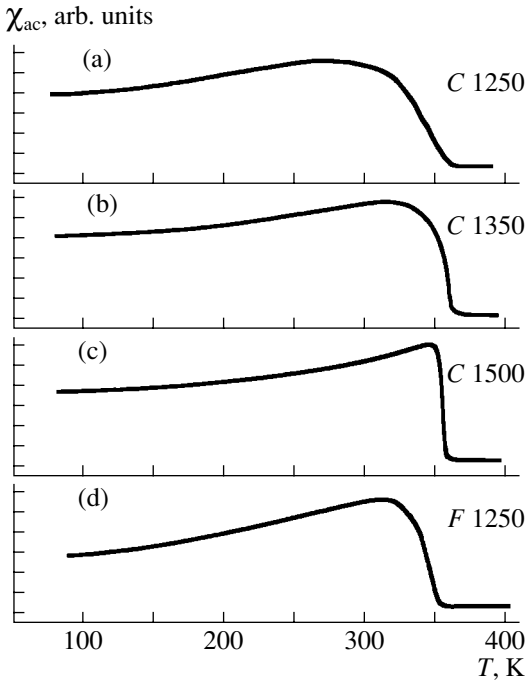

Fig. 2. Temperature dependences of the relative differential magnetic susceptibility χ_{ac} of the ceramic $La_{0.6}Sr_{0.3}Mn_{1.1}O_3$ samples sintered at (a) 1250, (b) 1350, and (c) 1500°C and of (d) the $La_{0.6}Sr_{0.3}Mn_{1.1}O_3$ thick film annealed at T = 1250°C.

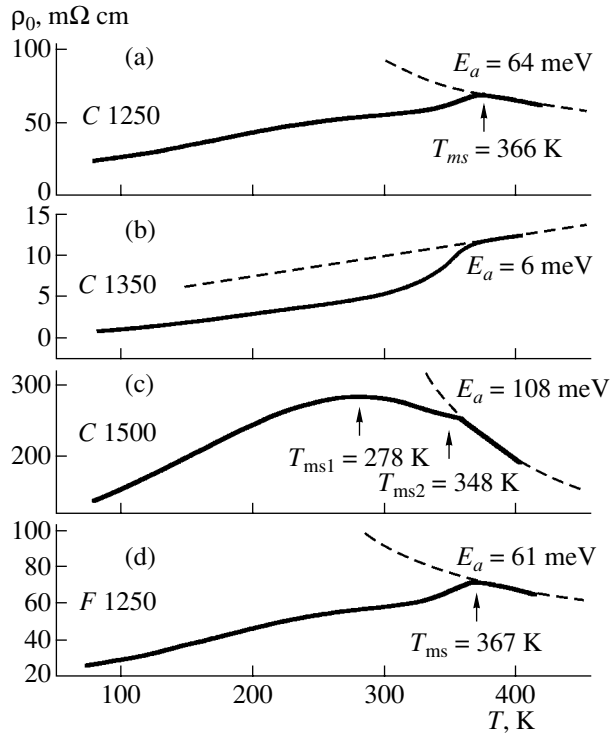

Fig. 3. Temperature dependences of the resistivity ρ_0 of the ceramic $La_{0.6}Sr_{0.3}Mn_{1.1}O_3$ samples sintered at (a) 1250, (b) 1350, and (c) 1500°C and of (d) the $La_{0.6}Sr_{0.3}Mn_{1.1}O_3$ thick film annealed at T = 1250°C. The dashed lines show the $\rho(T)$ dependences with the corresponding values of E_a.

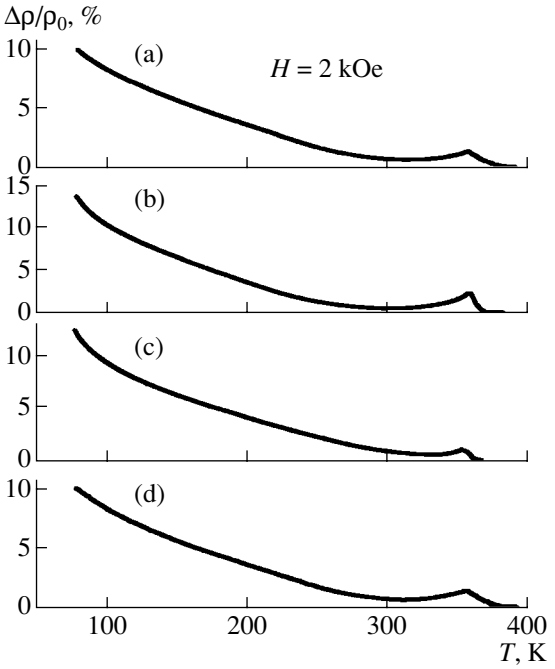

Fig. 4. Temperature dependences of the MRE of the ceramic $La_{0.6}Sr_{0.3}Mn_{1.1}O_3$ samples sintered at (a) 1250, (b) 1350, and (c) 1500°C and of (d) the $La_{0.6}Sr_{0.3}Mn_{1.1}O_3$ thick film annealed at T = 1250°C.

The temperature dependences of the magnetoresistive effect in the ceramic samples sintered at various temperatures and in the thick film are illustrated in Fig. 4. It is seen that the magnitudes of MRE near T_{ms} and T_p for the ceramics and thick film are similar and they depend relatively weakly on the sintering temperature.

Interestingly, the MREs at 77–100 K in both ceramics and thick film are significantly (a few times) higher than those at T_p (Table 1). Since the nature of the MRE in the low-temperature region is related to a tunneling effect in crystallite (grain) boundaries, its magnitude $\Delta\rho/\rho_0$ should depend on the crystallite size, which, in turn, is a function of the sintering temperature and duration. We are planning to determine the crystallite size and to study its effect on the MRE in the low-temperature region to reveal the nature of this phenomenon, which has not been observed in single crystals [25, 26], including thin-film single crystals [27, 28].

We fabricated and studied thin-film laser-sputtered samples only for the second system, which contained an iron impurity. Figure 5 shows the temperature dependences of the relative resistance and MRE of the iron-doped (*C*) and thick-film (*F*) samples prepared at 1250°C and of the thin (*f*) laser films $La_{0.6}Sr_{0.3}Mn_{1.06}Fe_{0.04}O_{3\pm\delta}$. As compared to the first system, the Fe impurity is seen to decrease T_{ms} of the ceramic and thick-film samples (the decrease in the latter sample is greater). The low phase transition temperature T_{ms} of the laser film is related to both the effect of Fe and higher oxygen nonstoichiometry, i.e., to a higher concentration of anion vacancies in the lattice of the incompletely oxidized laser film. It should be noted that Fe doping leads to a substantial decrease in T_{ms} and T_p. The thick-film and Fe-doped thin-film samples have higher MRE magnitudes as compared to the impurity-free $La_{0.6}Sr_{0.3}Mn_{1.1}O_{3\pm\delta}$ samples. The low-temperature MRE in the iron-doped ceramic and thick-film $La_{0.6}Sr_{0.3}Mn_{1.06}Fe_{0.04}O_{3\pm\delta}$ samples is slightly suppressed as compared to the first system (Figs. 4, 6).

The model that is most widely used to describe the kinetic properties of rare-earth manganites and other magnetic semiconductors having colossal magnetoresistive effect is the model of phase separation [9, 10]. Phase separation on a microscopic level is related to the formation of localized charge states (polarons, magnetic polarons, ferrons) due to a strong effect of electron–phonon interaction, high degree of polarization in a crystal, and a high defect concentration in its crystal lattice because of the presence of point defects (anion and cation vacancies) and clusters. In this case, the physical foundation of galvanomagnetic phenomena is the kinetic theory of low-mobility semiconductors [29, 30]. Large-scale phase separation is caused by the formation of conducting ferromagnetic (FM) regions

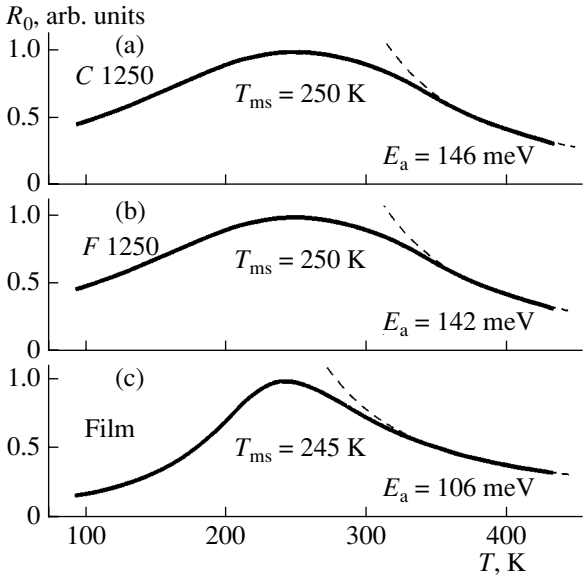

Fig. 5. Temperature dependences of the relative resistances R_0 of the (a) ceramic, (b) thick-film, and (c) thin-film $La_{0.6}Sr_{0.3}Mn_{1.06}Fe_{0.04}O_3$ samples in a zero magnetic field. The dashed lines show diffusion processes with the corresponding values of E_a.

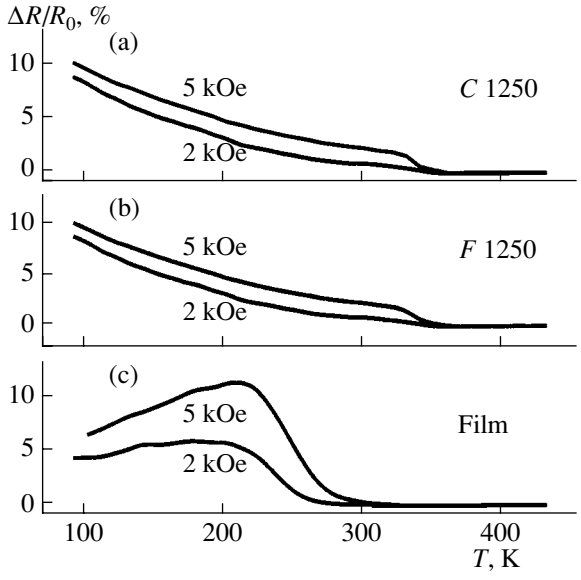

Fig. 6. Temperature dependences of the magnetoresistive effect $\Delta R/R_0$ of the (a) ceramic, (b) thick-film, and (c) thin-film $La_{0.6}Sr_{0.3}Mn_{1.06}Fe_{0.04}O_3$ samples in magnetic fields of 2 and 5 kOe.

(drops) inside a dielectric matrix. Such large-scale phase separation in the spin system of a low-doped $La_{1-x}Sr_xMnO_3$ ($x = 0.07$) manganite single crystal was detected by studying elastic neutron scattering [31]. It was related to the formation of ≈200-Å ferromagnetic regions spaced ≈420 Å apart. The appearance of conducting regions separated by dielectric leads to a significant role of tunneling effects. As the FM drops grow and the distance between them decreases, percolation processes become important. They are related to charge transfer via conduction electrons overcoming energy barriers at the boundaries of FM drops rather than via tunneling or diffusion of magnetic polarons through a crystal. This mechanism begins to operate when the interdrop distance becomes shorter than the tunneling length. For the case of small-scale phase separation, this mechanism begins to operate when the magnetic-polaron (ferron) size is comparable with the lattice parameter. It is characteristic that the temperature dependences of the resistivity for these three processes have the same shape. The only difference consists in the fact that, upon tunneling and in the percolation model, the activation energy has the Coulomb nature of interaction and it is equal to half the height of the energy barrier that must be overcome to ensure charge transfer from one phase-separated region to another [32].

Therefore, data on activation energy E_a are important to reveal the effect of lattice defects, including both point and cluster defects, on the electrical and magnetic properties of semiconductor materials [33]. The classical theory of magnetic semiconductors [34] includes three main mechanisms for an activation process: (1) the activation energy caused by local-potential fluctuations due to defects (impurities, vacancies), (2) the activation energy caused by electron–phonon interaction, and (3) the activation energy caused by *p–f* and/or *p–d* exchange. To make the physical picture of the processes that occur in rare-earth manganites more complete, these three mechanisms should be complemented by the effect of tunneling in intercrystallite regions in the ceramic samples and the effect of tunneling related to spin transfer from one ferromagnetic drop to another for large-scale phase separation.

It is known that, in a paramagnetic region ($T > T_C$), the temperature dependences of the resistivities of manganite–lanthanum perovskites can be described with a good accuracy by an activation process of the diffusion type [33, 34]:

$$\rho = \frac{kT}{ne^2D}\exp\left[\frac{E_a}{kT}\right], \qquad (1)$$

where $D = a^2\nu$ is the diffusion coefficient, e is the charge, and n is the charge concentration.

In this case, charge transfer occurs via jumps between localized states spaced a apart at a frequency ν.

Table 2 gives the values of E_a determined from the temperature dependences of the resistivity (for $x = 0$) and the relative resistance (for $x = 0.04$). The curves calculated by Eq. (1) are shown in Figs. 3 and 5 for each sample as dashed lines. As is seen from Table 2, iron doping increases E_a over the whole temperature range of the paramagnetic state. The activation energy is mainly contributed by the first mechanism. The activa-

Table 2. Molar formulas of the defect structure and the activation energy E_a of the ceramic (*C*), thick-film (*F*), and thin-film (*f*) manganite-lanthanum perovskites $La_{0.6}Sr_{0.3}Mn_{1.1-x}Fe_xO_{3\pm\delta}$ (x = 0, 0.04)

Sample	x	E_a, meV	Molar formulas of the clustered perovskite structure
C 1250	0	64	$\{La^{3+}_{0.57}Sr^{2+}_{0.29}V^{(c)}_{0.10}\}_A[Mn^{3+}_{0.67}Mn^{4+}_{0.29}]_B(Mn^{2+}_{0.04}Mn^{4+}_{0.04})_{c1}O^{2-}_{2.85}V^{(a)}_{0.15}$
C 1350	0	6	
C 1500	0	108	
F 1250	0	61	
C 1250	0.04	146	$\{La^{3+}_{0.57}Sr^{2+}_{0.29}V^{(c)}_{0.10}\}_A[Mn^{3+}_{0.63}Mn^{4+}_{0.29}Fe^{3+}_{0.04}]_B(Mn^{2+}_{0.04}Mn^{4+}_{0.04})_{c1}O^{2-}_{2.85}V^{(a)}_{0.15}$
F 1250	0.04	142	
f	0.04	106	

tion energies of the ceramic (*C* 1250) and thick-film (*F* 1250) samples with the same iron content are virtually the same. The lower E_a energy of the thin-film (*f*) sample with x = 0.04 can be explained by the absence of the contribution of tunneling effects in intercrystallite regions to the activation energy. The nonmonotonic character of the dependence of E_a on the annealing temperature for the ceramic samples with x = 0 is of particular interest. The low value (E_a = 6 meV) of sample *C* 1350 with x = 0 (Table 2), a metallic character of its $\rho_0(T)$ dependence (Fig. 3), and its resistivity (which is an order of magnitude lower than those of *C* 1250 and *C* 1500) indicate an optimum defect structure, a more uniform defect distribution, and an optimum crystallite size (which results in a decrease in the fraction of intercrystallite regions in the samples sintered at 1350°C) in this sample. It is also of interest that this sample features the maximum values of MRE in both the high-temperature region (at T_p) and at T = 100 K (Table 1).

An increase in the activation energy upon iron doping indicates the breaking (weakening) of the electron–hole exchange in manganese–oxygen (exchange) and manganese–manganese (superexchange) bonds due to a higher degree of electron localization near trivalent iron ions. Tunneling effects should play a specific role in MRE [32], which is evidenced by the character of the $MR \sim H^2/T^5$ dependences shown in Fig. 6 for samples *C* 1250 and *F* 1250 with x = 0.04, namely, by the absence of a peak near T_p at H = 2 kOe. For this class of manganites, a magnetic field of ≈2 kOe is close to the saturation field at which the magnetic moments of domains in the film samples and the magnetic moments of crystallites in the ceramic samples are arranged along the applied field. As follows from Fig. 6, the main mechanism of the appearance of MRE at $H \approx 2$ kOe in the ceramic samples is tunneling in grain boundaries, and the presence of a peak in $MR(T)$ for the thin-film sample indicates the predominant role of the effect of spin fluctuations near T_C on the scattering mechanism of charge carriers, whose contribution decreases as a magnetic field is applied.

Thus, in contrast to classic magnetic semiconductors with a giant magnetoresistive effect [36], in rare-earth manganites one has to take into account all types of interactions that have magnetic, lattice, and tunneling characters. Their contributions change depending on the composition, annealing temperature, size, and type of samples.

CONCLUSIONS

We studied ceramic, thick- and thin-film samples of manganite–lanthanum–strontium perovskites $La_{0.6}Sr_{0.3}Mn_{1.1-x}Fe_xO_3$ (x = 0, 0.04) by X-ray diffraction, resistivity measurements, magnetic measurements, ^{55}Mn NMR, and magnetoresistive measurements and established the following.

(1) All the samples have a rhombohedrally distorted perovskite structure, and its lattice parameters depend on the composition, sintering temperature, oxygen nonstoichiometry, concentration of anion vacancies, and the Mn^{3+}/Mn^{4+} ratio of the samples.

(2) The change in the metal–semiconductor phase transition temperature T_{ms}, the increase in the Curie temperature T_C, and the decrease in the temperature range ΔT_C of transition into a magnetically ordered state with increasing annealing temperature of the ceramic samples can also be explained by changes in the oxygen nonstoichiometry and in the Mn^{3+}/Mn^{4+} ratio and by different effects of defects on the magnetic and resistive properties.

(3) The iron-containing samples have lower phase transition temperatures T_{ms} and T_C and higher magnitudes of MRE.

(4) Relatively high magnitudes of the low-field MRE of the ceramic and thick-film samples at T = 77–100 K are accounted for by tunneling in grain (crystallite) boundaries.

(5) Analysis of the ^{55}Mn NMR spectra of the ceramic samples with x = 0 and 0.04 confirmed high-frequency electron–hole exchange between Mn^{3+} and Mn^{4+} and the conclusion concerning a high defect con-

centration in the crystal lattice, which contains anion and cation vacancies and nanocluster defects.

(6) The MRE is maximum in the iron-doped film samples.

(7) Analysis of the effects of the sintering temperature of the ceramic samples and an iron impurity on the activation energy and the temperature dependences of the resistivity and MRE showed that magnetic, lattice, and tunneling interactions coexist in the magnetoresistive manganite–lanthanum perovskites.

ACKNOWLEDGMENTS

This work was supported in part by the UNTTs, project no UZB-136J.

REFERENCES

1. I. O. Troyanchuk, S. V. Trukhanov, H. Szymczak, *et al.*, Zh. Éksp. Teor. Fiz. **120**, 183 (2001) [JETP **93**, 161 (2001)].
2. S. I. Khartsev, P. Johnsson, and A. M. Grishin, J. Appl. Phys. **87**, 2394 (2000).
3. P. Mandal and B. Ghosh, Phys. Rev. B **68**, 014422 (2003).
4. N. V. Volkov, G. A. Petrakovskiĭ, V. N. Vasil'ev, and K. A. Sablina, Fiz. Tverd. Tela (St. Petersburg) **44**, 1290 (2002) [Phys. Solid State **44**, 1350 (2002)].
5. G. De Marzi, Z. V. Popovic, A. Cantarero, *et al.*, Phys. Rev. B **68**, 064302 (2003).
6. T. Akimoto, Y. Maruyama, Y. Moritomo, *et al.*, Phys. Rev. B **57**, R5594 (1998).
7. Young Suk Cho, Jion Seok Hwang-Bo, Yeon Hee Kin, *et al.*, J. Magn. Magn. Mater. **226–230**, 754 (2001).
8. A. I. Tovstolytkin, A. N. Pogorelyi, I. V. Lemnenko, *et al.*, Fiz. Tverd. Tela (St. Petersburg) **45**, 1857 (2003) [Phys. Solid State **45**, 1952 (2003)].
9. E. L. Nagaev, Usp. Fiz. Nauk **166**, 833 (1996) [Phys. Usp. **39**, 781 (1996)].
10. M. Yu. Kagan and K. I. Kugel', Usp. Fiz. Nauk **171**, 577 (2001) [Phys. Usp. **44**, 553 (2001)].
11. M. C. Sancher, G. Subias, G. Garsia, *et al.*, Phys. Rev. Lett. **90**, 045503 (2003).
12. R. F. C. Marques, J. Z. Jafelicci, C. O. Paiva-Santos, *et al.*, J. Magn. Magn. Mater. **226–230**, 812 (2001).
13. Guo-meng Zhao, K. Condez, H. Keller, *et al.*, Phys. Rev. B **60**, 11914 (1999).
14. H. Vincent, M. Audiez, S. Pignard, *et al.*, J. Magn. Magn. Mater. **226–230**, 768 (2001).
15. S. S. Kucherenko, V. P. Pashchenko, P. I. Polyakov, *et al.*, Fiz. Nizk. Temp. **27**, 761 (2001) [Low Temp. Phys. **27**, 559 (2001)].
16. V. P. Pashchenko, S. I. Khartsev, O. P. Cherenkov, *et al.*, Neorg. Mater. **35**, 1509 (1999).
17. V. P. D'yakonov, V. P. Pashchenko, E. E. Zubov, *et al.*, Fiz. Tverd. Tela (St. Petersburg) **45**, 870 (2003) [Phys. Solid State **45**, 914 (2003)].
18. V. T. Dovgiĭ, A. I. Linnik, V. P. Pashchenko, *et al.*, Pis'ma Zh. Tekh. Fiz. **29** (14), 81 (2003) [Tech. Phys. Lett. **29**, 610 (2003)].
19. V. P. Pashchenko, S. S. Kucherenko, P. I. Polyakov, *et al.*, Fiz. Nizk. Temp. **27**, 1010 (2001) [Low Temp. Phys. **27**, 1010 (2001)].
20. I. V. Medvedeva, K. Bärner, G. H. Rao, *et al.*, Physica B **292**, 250 (2000).
21. V. P. Pashchenko, V. K. Prokopenko, A. A. Shemyakov, *et al.*, Metallofiz. Noveishie Tekhnol. **22** (12), 18 (2000).
22. W. Bazela, V. Dyakonov, V. Pashchenko, *et al.*, Phys. Status Solidi B **236**, 458 (2003).
23. E. Zubov, V. P. Dyakonov, and H. Szymczak, Zh. Éksp. Teor. Fiz. **122**, 1268 (2002) [JETP **95**, 1044 (2002)].
24. V. P. Paschenko, G. Kakazei, A. A. Shemyakov, *et al.*, Fiz. Nizk. Temp. **30**, 403 (2004) [Low Temp. Phys. **30**, 299 (2004)].
25. N. V. Volkov, G. A. Petrakovskiĭ, V. N. Vasil'ev, *et al.*, Fiz. Tverd. Tela (St. Petersburg) **44**, 1290 (2002) [Phys. Solid State **44**, 1350 (2002)].
26. Yu. F. Popov, A. M. Kadomtseva, G. P. Vorob'ev, *et al.*, Fiz. Tverd. Tela (St. Petersburg) **46**, 1214 (2004) [Phys. Solid State **46**, 1252 (2004)].
27. G. J. Chen, Y. H. Chang, and H. W. Hsu, J. Magn. Magn. Mater. **219**, 317 (2000).
28. V. G. Prokhorov, G. G. Kaminsky, V. A. Komashko, *et al.*, Fiz. Nizk. Temp. **29**, 885 (2003) [Low Temp. Phys. **29**, 663 (2003)].
29. I. G. Lang and Yu. A. Firsov, Zh. Éksp. Teor. Fiz. **43**, 1843 (1962) [Sov. Phys. JETP **16**, 1301 (1962)].
30. Yu. A. Firsov, Fiz. Tverd. Tela (Leningrad) **5**, 2149 (1963) [Sov. Phys. Solid State **5**, 1566 (1963)].
31. S. F. Dubinin, V. E. Arkhipov, S. G. Teploukhov, and V. D. Darkhomenko, Fiz. Tverd. Tela (St. Petersburg) **45**, 2192 (2003) [Phys. Solid State **45**, 2147 (2003)].
32. K. I. Kugel', A. L. Rakhmanov, A. O. Sboichakov, *et al.*, Zh. Éksp. Teor. Fiz. **125**, 648 (2004) [JETP **98**, 572 (2004)].
33. N. F. Mott, Adv. Phys. **50**, 865 (2001).
34. S. Methfessel and D. Mattis, *Magnetic Semiconductors* (Springer, Heidelberg, 1968; Mir, Moscow, 1972).
35. J. M. D. Coey, M. Virets, and S. von Molnar, Adv. Phys. **48**, 167 (1999).
36. S. von Molnar and S. Methfessel, J. Appl. Phys. **38**, 959 (1967).

Translated by K. Shakhlevich

Technical Physics, Vol. 50, No. 11, 2005, pp. 1504–1510. Translated from Zhurnal Tekhnicheskoĭ Fiziki, Vol. 75, No. 11, 2005, pp. 112–119.

EXPERIMENTAL INSTRUMENTS AND TECHNIQUES

Growth of Carbon Nanotubes from Ring Carbon Clusters

N. I. Alekseev and G. A. Dyuzhev

Ioffe Physicotechnical Institute, Russian Academy of Sciences, Politekhnicheskaya ul. 26, St. Petersburg, 194021 Russia

e-mail: NIalekseyev@ilip.itc.etu.ru, aleks@mail.ioffe.ru

Received August 3, 2004

Abstract—The possibility of growing single-wall carbon nanotubes from ring carbon clusters that appear at a certain stage of cooling carbon vapor is discussed. Such a technique could allow one to grow single-wall nanotubes without introducing a macroscopic amount of a catalyst and to retain nanotubes open during their growth. An analysis performed using semiempirical quantum-chemical methods shows that, when catalyst atoms interact with the edge of an already formed nanotube surface, the bonds of these atoms with carbon tend to occupy positions normal to the generatrix of the nanotube. This situation is natural for transition-metal atoms, since they favor the destruction of pentagonal cycles at the edge of the surface. The destruction mechanism consists in the fact that pentagons incorporate carbon atoms from the outside and become hexagons. The dependence of this tendency on the type of catalyst atom is considered. © *2005 Pleiades Publishing, Inc.*

INTRODUCTION

In any event, the modern processes of producing carbon nanotubes (NTs) are related to the mechanism of carbon precipitation from the melt supersaturated by carbon (the vapor–liquid–drop (VLD) mechanism). In the processes of chemical decomposition of carboniferous substances, this mechanism is realized intentionally, and it is realized spontaneously in arc-discharge and laser methods. The unavoidable disadvantage of these methods is the presence of macroquantities of a metal in the final product, at least, at one of the tube ends. In some cases, such metallic particles can be used for practical purposes (e.g., for magnetic data storage [1]); in most other cases, they are removed, which is accompanied by loss or damage of a huge number of tubes.

Therefore, methods of NT growth that are not based on the VLD mechanism are attractive. One of the alternatives is CVD of small carbon fragments on large substrate-free carbon clusters, e.g., rings [2, 3]. In [2, 3], this growth was described qualitatively, and the authors of [4] tried to quantitatively describe it, but as applied to a rather large well-shaped nanotube cage.

The idea of [2, 3] consists in the following: gas-phase molecules of a metal carbide Me_nC_m (e.g., CoC_2) attach to doubly bound carbon atoms at the edge of an already formed nanotube surface and form the next layer (circle) of hexagons (Fig. 1a). However, pentagons can easily form under these conditions. The possible mechanisms of their destruction or blocking were studied in [4] (the Lee–Tomanek scooter mechanism). In the Lee–Tomanek mechanism, a catalyst atom temporarily substitutes for a deficient carbon atom and waits for the arrival of another carbon atom to be displaced by it. When simulating this process, the authors of [4] assumed that a significant portion of an NT was assembled; therefore, the description is independent of the type (microparticle on a substrate or a ring) of nucleation centers for nanotube growth. For the mechanism to operate, an NT must be open from at least one end. Then, if NTs grow from rings according to this mechanism and if the whole catalyst is supplied to the atomic phase, NTs are open from both sides. This is important for practical growing of NTs, since there is

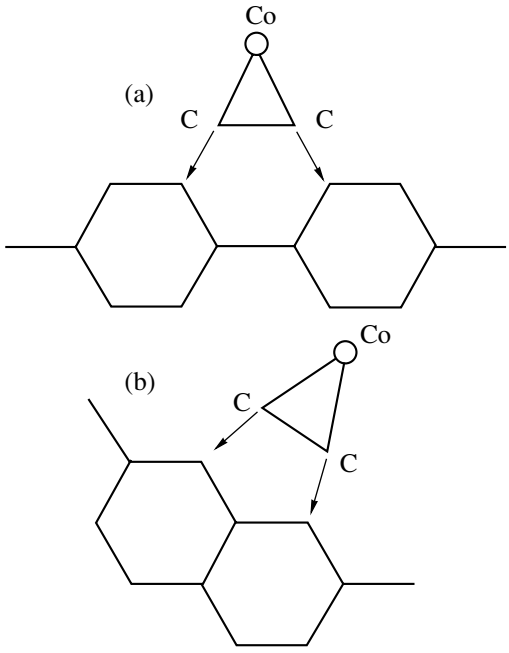

Fig. 1. Nucleation of (a) a pentagon and (b) a hexagon when an MeC_2 molecule is trapped by the edge of an NT surface (the circles stand for metallic (Co) atoms).

1063-7842/05/5011-1504$26.00 © 2005 Pleiades Publishing, Inc.

no longer need to remove lumps of amorphous carbon and solidified drops of catalytic metal.

The initial stage of NT growth, namely, the fixation of the first hexagons to a ring is only declared in [2, 3] and is ignored in [4]. Moreover, those authors did not discuss the sensitivity of this mechanism to the choice of catalyst, which manifests itself obviously in experiments, and conditions for the mechanism of NT growth from rings to be actualized.

The simulation [5] of the mechanisms of fullerene formation indicates that ring carbon clusters without foreign noncarbon atoms cannot be nucleation centers for fullerenes. The situation changes in the presence of a catalyst, and the effect of a catalyst can be of two kinds. (1) In the initial stage of assembling, catalytic atoms fix hexagons to a ring; then, for a large number of hexagons, these atoms also fix pentagons, providing the growth of a fullerene molecule. (2) Catalytic atoms fix hexagons in the course of assembling and block the appearance of pentagons, as in the scooter mechanism of [4].

In the former case, fullerene growth can be stimulated, and, in the latter, the growth of single-wall NTs can be stimulated. Any general considerations cannot prohibit the possibility of experimental conditions under which both cases can be realized.

In this work, we aimed at studying the dependence of the reactions used to assemble NTs on the type of catalytic atoms and at estimating the interval of external conditions required for nanotube growth.

Hereafter, a catalyst is taken to be any noncarbon atom (it is designated by symbol *Me* (metal)) even in the case if, in contrast to iron group metal atoms or platinoids, it has no catalytic properties with respect to NT growth.

For studies, we used the AM1 and PM1 quantum-chemical methods for carbon clusters that included third period element atoms (Ca, As, Si) and atoms of elements of the first complete period (Zn, Ga, Ge, As, Se). These methods give sufficiently reliable configurations and characteristics for clusters containing carbon atoms, and we used their results without any modifications.

The configurations of carbon compounds with elements of the first long period (Mg, Sc, …, Zn) were studied semiquantitatively by the ZINDO-I method of a HYPERCHEM 6.3 package. The ZINDO-I method gives reasonable lengths and energies for metallic element–carbon bonds. However, for purely carbon molecules and large carbon fragments in carbon–metal clusters, this method gives strongly distorted configurations and wrong binding energies. Therefore, for configurations with a large number of carbon atoms and several metal atoms, their forms and energies were estimated as follows. The configuration of a carbon cage with elements Zn, …, As located at the sites of metal *Me* was calculated by the PM3 method; then, these Zn, …, As atoms were replaced by *Me* atoms and optimization was performed by ZINDO only with respect to the *Me*-atom positions for a fixed carbon cage. The binding energy E of the configuration obtained was estimated in terms of molecular mechanics from the relation

$$E - E_0^{\mathrm{AM1}} = E^{\mathrm{ZINDO}} - E_0^{\mathrm{ZINDO}};$$

whence, we have

$$E = E^{\mathrm{ZINDO}} + (E_0^{\mathrm{AM1}} - E_0^{\mathrm{ZINDO}}). \quad (1)$$

In Eq. (1), E^{ZINDO} is the binding energy calculated by ZINDO; E_0^{AM1} and E_0^{ZINDO} are the binding energies of the cluster carbon cage calculated by PM3 and ZINDO, respectively. For the calculation of E_0^{ZINDO}, optimization was not carried out and a ready configuration was used. The difference $E_0^{\mathrm{AM1}} - E_0^{\mathrm{ZINDO}}$ can be named as a defect of the ZINDO method. The use of Eq. (1) implies that metal atoms weakly deform the structure of the carbon cage calculated by PM3 and that the metal-atom positions with respect to the carbon cage is well determined by ZINDO.

The difference in the binding energies between two configurations with the same atoms can be calculated by ZINDO without the manipulation described above. It is important that results in both cases agree with each other.

The criterion of adequacy of the dependences calculated was their (at least approximate) retention when metal atoms were replaced by the elements calculated by PM3 (i.e., Zn, Ga, Ge, etc.). Unfortunately, the only element that can be calculated by both methods (AM1 and PM3) is zinc.

THE INITIAL STAGE OF NANOTUBE GROWTH—FIXATION OF A HEXAGON TO A RING

The quantum-chemical simulation shows that, in the absence of a catalyst, the embedding of the C_2 molecule into a ring and the formation of a hexagon (Fig. 2) are possible and energetically favorable. However, the dissolution of the C_2 molecule in the ring, which is accompanied by an increase in its size by two atoms (or three atoms in the case of the C_3 molecule) is much more favorable (by about 1.5–2 eV).

The situation changes in the presence of a catalyst of the Zn–Ga type. For example, when the ZnC_2 molecule forms a hexagon, the energy decrement is 1.5 eV greater than that in the case of its dissolution in the ring. The same result remains qualitatively the same for "real" catalysts, such as Fe, Co, and Ni.

When a sufficient number of hexagons forms in the ring, the atoms of both hexagons and retained ring sections take part in further reactions of entrapment of carbon fragments from the outside (Fig. 3). Both pentagons ($A \longrightarrow B$) and hexagons ($F \longrightarrow D$) can form

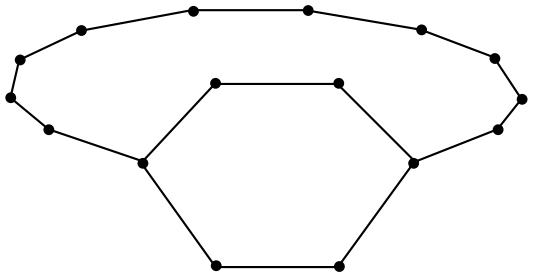

Fig. 2. Ring carbon cluster with a hexagon—the nucleation center of a nanotube in the mechanism proposed.

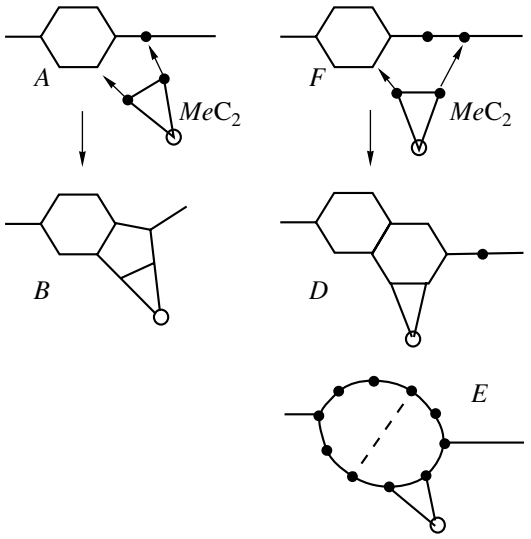

Fig. 3. Possible cases of the attachment of the C_2 molecule to the hexagon–ring section joint.

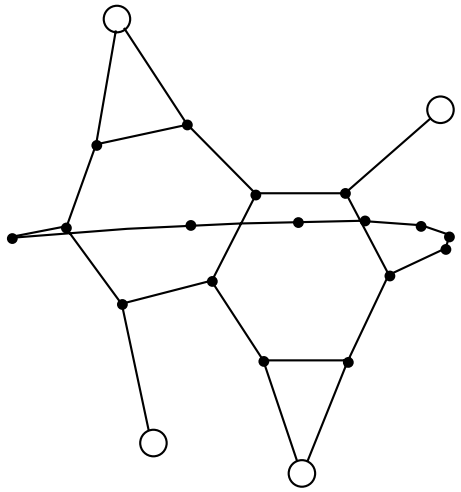

Fig. 4. Isomer with two hexagons and four zinc atoms (circles) located approximately in the surface formed by the generatrix of the nanotube ("planar" isomer).

under these conditions. The simulation demonstrates that, in both cases, the appearing configuration with two polygons is stable if a pentagon or a hexagon is fixed by at least two catalyst atoms. Otherwise, the common bond of two polygons breaks and the process of assembling a nanotube terminates ($D \longrightarrow E$).

Further simulation shows that clusters having two polygons and several catalyst atoms can have several isomers, depending on the type of the catalyst atoms. Along with the isomers where catalyst atoms are approximately located as the continuation of the generatrix of the nanotube surface (hereafter, they are called "planar," Fig. 4), there appear isomers where catalyst atoms are located at almost the maximal distance away from the surface formed by the generatrix. During optimization, catalyst atoms, which have at least one free valence, find additional bonds with carbon atoms that were not taken into account in the initial configuration. Hereafter, such isomers are called "inverted." The orientation in Fig. 5 is chosen so that both hexagons are virtually invisible and that the position of catalyst atoms (circles) is most clearly visible. Among the four Zn catalyst atoms, only the bond of atom *1* with the nearest angular carbon atom is located at a rather acute angle with respect to the nanotube axis.

Obviously, this inverted isomer does favor NT growth. On the one hand, the angular carbon atoms, which have only two neighboring carbon atoms, are rather stable due to bonds with metal atoms. On the other hand, the bonds of the catalyst atoms are saturated and do not trap carbon atoms coming from the outside to the edge of the growing nanotube. On the contrary, planar isomers cannot transform into an NT, since the saturated bonds of the catalyst atoms trap the flux of carbon fragments from the outside and form chaotic structures.

The energies of the inverted and planar isomers were compared using the elements Zn, Ga, Ge, As, and Se within the framework of the PM3 method.

In the case of As, there is only an inverted specific configuration: all As atoms are beyond the surface formed by the generatrix; however, each As atom is bound to only one angular carbon atom. When going along the period from right to left (As $\longrightarrow$ Ga $\longrightarrow$ Zn, etc.), we constructed various isomers, in which some catalyst atoms occupy the planar positions and others occupy the inverted positions. Figure 6 shows the difference ΔE in the absolute values of the binding energies of the planar and inverted isomers as a function of the catalyst-atom position in the periodic table (the first complete period). It is seen that the planar isomers are more favorable to the right of zinc (Fig. 6, curve *3*). For Ga, however, the planar isomer does not exist, and it only generates the inverted isomer. For Zn, the advantage of the planar isomer is almost zero.

When going to real catalyst atoms (where an appearing configuration cannot be completely optimized by quantum-chemical methods), we used the procedure described above: catalyst atoms were located in all configurations considered above at the sites of Zn, …, As atoms, and the configuration of a carbon cage was taken to be unchanged. Then, for each configuration of the

carbon cage, we optimized the positions of only catalyst atoms by ZINDO. As a result, we determined a conventionally optimum configuration and, then, the most conventionally optimum configuration among all the carbon-cage configurations; in all cases, the binding energy was calculated by both methods described above. The difference in the binding energies between the optimum planar and optimum inverted configurations is shown in Fig. 6 (curve *1*). Curve *2* corresponds to the energy difference calculated by ZINDO without additional computation. The advantage of the inverted configuration is obvious.

This situation is natural for atoms of the transition triad, where the valence can be different (change by one), the bonds of valence *p* and *s* electrons are weak, the *d*-electron correction to the valence is uncertain, and a large number of atomic bonds compensate for prominent atomic positions. Different catalyst-atom configurations are spatially closer than those in the planar configuration, and their displacements should be easier. However, it is natural that, within the framework of this dependence, the competition between the number of catalyst-atom bonds and the distorted valence angles along the period can be very nontrivial.

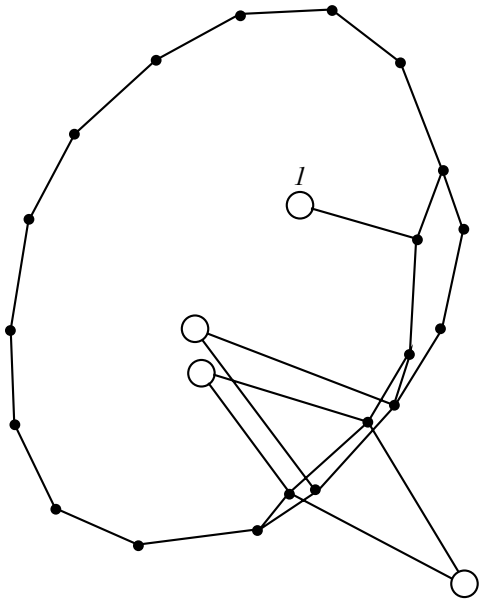

Fig. 5. Isomer with two hexagons and four zinc atoms (circles) whose bonds are almost orthogonal to the surface formed by the generatrix of the nanotube ("inverted" isomer).

CAN A CATALYST GIVE AN IMPETUS TO FULLERENE GROWTH?

The effect of a catalyst on the initiation of NT growth described above can be successfully realized if hexagon formation is more favorable than pentagon formation in the stage of coalescence of islands appearing along the radius of the initial ring. Figure 7 shows the difference δE_{ph} in the energies of the configurations with a pentagon or a hexagon attached to the first hexagon (Fig. 3, configurations *B* and *D*, respectively). As above, we assumed that there are no other hexagons along the radius of the ring. We compared optimum configurations at different numbers of catalyst atoms.

As is seen from Fig. 7, the binding energies of the configurations with a pentagon or a hexagon are virtually equal in the cases of As and Ge. Pentagons are favorable in the cases of Ga and Zn; in the case of Zn, they are less favorable than in the case of Ga. However, for Zn, the planar isomer is more favorable, which prohibits the growth of both fullerenes and nanotubes, since there is no place for a coming carbon atom. Gallium, which has the only inverted configuration with a hexagon or a pentagon, can have catalytic properties. However, this might be a purely computation effect.

As going to real catalysts, pentagons become less favorable than hexagons. This means that a catalyst moves a ring carbon cluster toward nanotubes rather than fullerenes. It is interesting that this tendency depends only weakly on the number of catalyst atoms (three or four).

This result shows that it is impossible to use well-known catalysts to stimulate fullerene growth when using not only atoms of the iron group but also platinoids, which cannot be simulated by quantum-chemical methods.

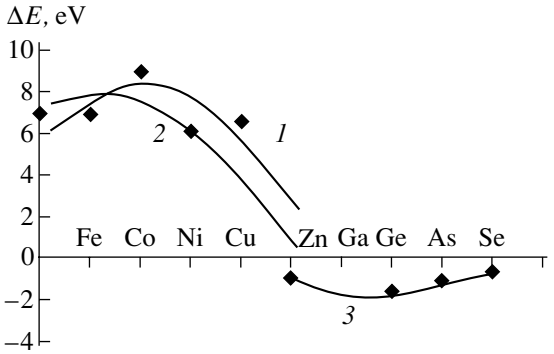

Fig. 6. The difference ΔE in the absolute values of the binding energies of the planar and inverted isomers as a function of the catalyst-atom position in the periodic table (the first complete period). Configurations with two hexagons and four catalyst atoms. (*1*) ZINDO with additional computation (smoothed curve plotted by points), (*2*) ZINDO without additional computation (calculated points are not shown), and (*3*) the PM3 method.

MECHANISMS OF SUBSTITUTING A HEXAGON FOR PENTAGON IN THE CASE OF A LARGE ASSEMBLED NANOTUBE FRAGMENT

Figure 8 shows a fragment of the edge of a large growing carbon NT (the edge is located on the top of each picture, and the formed nanotube "body" is shown at the bottom). If a pentagon forms during the reaction

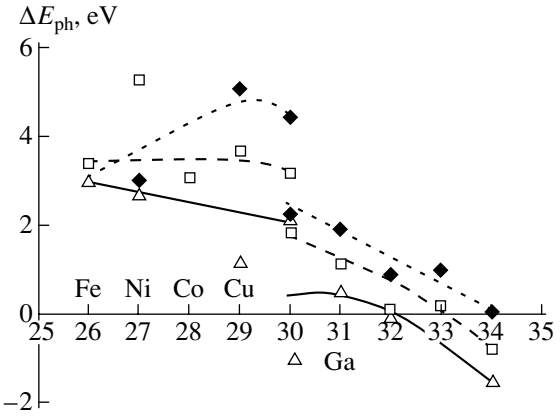

Fig. 7. The difference δE_{ph} in the absolute values of the energies of the configurations with two hexagons and a pentagon placed at the site of one of the hexagons (Fig. 3, configurations *B* and *D*) as a function of the catalyst-atom position in the periodic table. Solid (△), dashed (□), and dotted (◆) curves are plotted for two, three, and four catalyst atoms, respectively.

of attachment of a carbon molecule to the edge (Fig. 8, *A*), two basic directions of further reactions are possible for trapping the next C_2 molecule.

(A) The extreme carbon atom (atom *1*) attached to the pentagon of the C_2 molecule (Fig. 8, *B*) fixes the nearest carbon at the edge of the surface (Fig. 8, *D*) to form a hexagon. The earlier appeared pentagon is fixed in this case.

(B) The carbon atom nearest to the fragment (atom *2*) occupies a place in the bridge of a pentagon and complements it to form a hexagon (Fig. 8, *C*). The pentagon is destroyed.

In the absence of a catalyst, version *A* is more energetically favorable, and version *B* is favorable in the presence of a metallic catalyst. This result is obtained by using both molecular-dynamics simulation and ZINDO. It can be explained by the fact that the energetically unfavorable existence of the prominent carbon atom (Fig. 8, atom *1* in *D*') is partly compensated due to the saturation of the bonds of this atom by catalyst atoms. On the other hand, there is no energy increment induced by pentagonal cycles and the related surface curvature.

The behavior of the difference in the total binding-energy increment as a function of the element ordinal number for this reaction approximately corresponds to Fig. 7. Thus, well-known catalysts are seen to be preferable. Another argument for the well-known catalysts

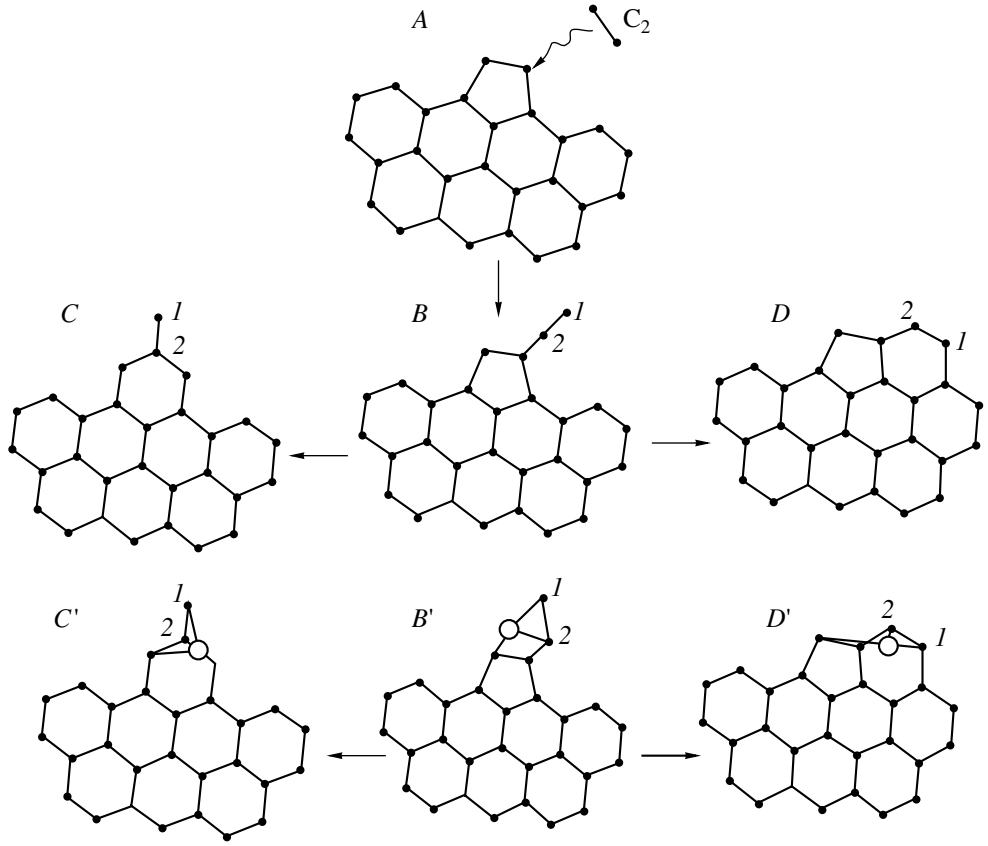

Fig. 8. Possible ways for the formation of a pentagonal cycle at the edge of the surface of a growing nanotube upon trapping the C_2 molecule. The ways $B \longrightarrow C$, $B \longrightarrow D$ show the evolution of the edge of the surface without catalyst atoms. The ways $B' \longrightarrow C'$, $B' \longrightarrow D'$ show the evolution with catalyst atoms (circles).

consists in the following. The substitution of a hexagon for a pentagon should be accompanied by the rupture of the carbon–catalyst bond, and the energy of this bond is substantially lower for the well-known catalysts (Fig. 9).

The basic mechanism of pentagon destruction is analogous to the mechanism of [4], and it is realized under the following additional conditions: (i) catalytic atoms fixing an NT edge occupy the inverted positions and (ii) the total concentrations of carbon (in the form of atoms, the C_2 and C_3 molecules, and a Me_nC_m carbide) and catalyst (in the form of atoms and molecules of the same carbide) are intimately related.

The first condition is met by the proper choice of a catalyst. Moreover, this condition specifies the upper boundary of a carbon flux. Indeed, catalyst atoms that occupy positions in the continuation of the generatrix of the nanotube (as in the case of the planar configuration) and break the following assembling of the nanotube appear in the case when a new layer (circle) of hexagons has formed on the NT edge and when the catalyst atoms fixed to the previous layer have not moved to the edge. If the angular carbon atoms on the edge interact with surrounding carbon atoms from the vapor within the time it takes for this motion to occur, the pentagons have no time to be fixed by the catalyst atoms and become embedded in the growing surface. A fullerene cap appears, and the nanotube growth ceases. Therefore, a necessary condition for assembling nanotubes is a strong degree of rarefaction of the carbon vapor.

On the other hand, the catalytic vapor should also be rarefied; otherwise, nanotube growth is blocked by catalyst atoms.

The maximum allowable concentrations of carbon (N_2) and catalyst (N_{Me}) atoms can be estimated from the relations

$$(\sigma N_2 V_T)^{-1} > \tau_j, \quad (\sigma N_{Me} V_T)^{-1} > \tau_j, \qquad (2)$$

where τ_j is the time of jumping of the inverted catalyst atoms to newly appearing angular carbon atoms at the edge of the nanotube surface and σ is the average cross section of trapping small fragments by the edge of the surface (carbon and metal atoms that enter into the compositions of carbon clusters and Me_nC_m clusters also included in N_2 and N_{Me}).

FORMULATION OF AN EXPERIMENT TO GROW NANOTUBES FROM CARBON CLUSTERS

If the quantum-chemical results correspond to the real situation, nanotube growth from rings can be realized in the framework of an arc-discharge method. However, the formation of a discharge should differ from that used for nanotube growth from supersaturated drops.

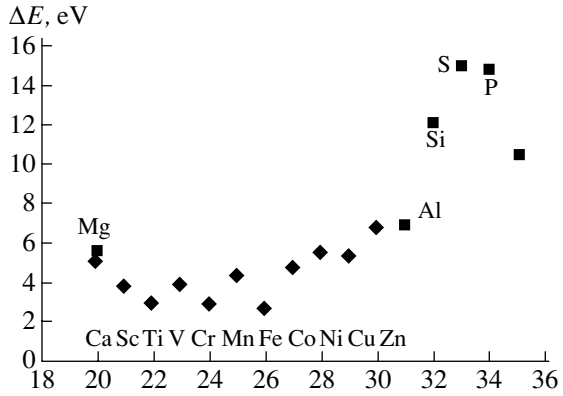

Fig. 9. The binding energy of a carbon atom with an atom from the first complete period (as well as with Mg, Al, Si, S, and P atoms).

(i) First, nucleation centers (rings) must appear. To this end, the number of metal atoms in the early stages of nucleation (atoms ⟶ chains ⟶ rings) should be minimum, so that rings rather than nuclei for carbon–metal drops appear. The allowable concentration of metal atoms in the region of generation of carbon rings from chains is determined by the condition that the ratio of the concentration N_C' of chains "loaded" by metal atoms to the concentration of "pure" chains is low. On the order of magnitude, the equilibrium N_C'/N_C ratio is

$$\frac{N_C'}{N_C} \sim N_K \left(\frac{h^2}{2\pi m_K T}\right)^{3/2} \left(\frac{T}{h\langle\nu\rangle}\right)^3 \exp\left(\frac{\delta E}{T}\right), \qquad (3)$$

where $\delta E \sim 1.3$–1.7 eV is the decrease in the total binding energy caused by the attachment of a carbon cluster to a catalyst atom, N_K is the metal-atom concentration, $(T/h\langle\nu\rangle)^3$ is the ratio of the vibrational partition functions of the loaded and pure chains, and $\langle\nu\rangle$ is the average vibration frequency in the chain considered as a system of harmonic oscillators.

At $T = 0.2$ eV, the upper boundary of the metal-atom concentration is estimated to be 10^{18} cm^{-3}. As the temperature decreases, this requirement becomes more stringent. However, in any case, this condition does not look too stringent.

(ii) When moving to the region of a dense metallic vapor and NT growth, formed ring carbon clusters must not be destroyed; that is, the temperature of this region has to be low.

From this standpoint, a steady-state low-temperature glow discharge or periphery area in a metallic target evaporated by laser radiation is optimum. The first version is preferred, since it provides controlled evaporation of nanotubes on a substrate in the strong electric field of a near-electrode layer.

(iii) Thus, the conditions of growing NTs from a gas phase are, to a certain degree, conflicting with the conditions of growing NTs from a carbon–metal drop

supersaturated by carbon. In the latter case, drops should first be formed and deposited onto a substrate surface. In the case of growing from rings, nanotubes grow before deposition on the surface. They should be deposited on a substrate as a finished product, and this process creates additional difficulties.

(iv) Our consideration demonstrates that single-wall carbon nanotubes can grow from rings only in the presence of a catalyst. Attempts to simulate the process that only involves carbon atoms or small carbon molecules were made in the initial stage of investigation of nanotubes [6] and later (e.g., see [7]); however, no experimental evidence of this process has been obtained.

CONCLUSIONS

(1) In the initial stage of growth of carbon NTs and ring clusters, the role of catalyst atoms consists in blocking the "dissolution" of small carbon fragments in a ring.

(2) When the edge of a formed nanotube surface interacts with catalyst (*Me*) atoms, the *Me*–C bonds of these atoms tend to occupy positions that are normal to the generatrix of the nanotube. This situation is natural for transition-metal atoms, which favor the destruction of pentagonal cycles at the edge of the surface via the incorporation of carbon atoms from the outside; thus, they become hexagons.

(3) During normal nanotube growth, the "inverted" catalyst atoms have time to move to the edge of the surface to follow newly attached carbon atoms (radicals). When the influx of catalyst atoms is sufficiently high, NT growth ceases, since the edge has no time to be annealed: the bonds of carbon atoms supplied to the edge of the nanotube are immediately "blocked" by catalyst atoms, which occupy both the inverted configurations and the configurations on the surface formed by the generatrix. On the other hand, the inverted catalyst atoms that are already bound to the nanotube have no time to reach the edge of the nanotube to follow carbon atoms; therefore, they fill the inside of the tube.

(4) When the influx of carbon atoms is sufficiently high, a catalyst has no time to manifest itself, and the nanotube is closed by a pentagonal cap.

Thus, the formation of an NT with open ends requires a very accurate combination of external conditions, namely, the concentrations of catalyst and carbon atoms and the temperature.

REFERENCES

1. Li De-Chang, Dai Liming, Huang Shaoming, *et al.*, Chem. Phys. Lett. **316**, 349 (2000).
2. Ching-Hwa-Kiang and W. A. Goddard, Phys. Rev. Lett. **76**, 2515 (1996).
3. Ching-Hwa-Kiang, J. Chem. Phys. **113**, 4763 (2000).
4. Lee Young Hee, Kim Seong Go, and Tomanek David, Phys. Rev. Lett. **78**, 2393 (1997).
5. N. I. Alekseev and G. A. Dyuzhev, Zh. Tekh. Fiz. **71** (5), 67 (2001) [Tech. Phys. **46**, 573 (2001)].
6. C. J. Brabec, A. Maiti, C. Roland, and J. Bernhols, Chem. Phys. Lett. **236**, 150 (1995).
7. Wen Zhao Ming, Yuan Xia Yue, Chen Ma Yu, and Yan Li Su, Chin. Phys. Lett. **18**, 82 (2001).

Translated by K. Shakhlevich

Technical Physics, Vol. 50, No. 11, 2005, pp. 1511–1512. Translated from Zhurnal Tekhnicheskoĭ Fiziki, Vol. 75, No. 11, 2005, pp. 120–121.

SHORT COMMUNICATIONS

Edge Apodization of Crystal-like Structures

E. A. Nelin

Kiev Polytechnical Institute, National Technical University of Ukraine, ul. Peremogi 37, Kiev, 03056 Ukraine

e-mail: ye_nelin@rtf.ntu-kpi.kiev.ua

Received November 12, 2004

Abstract—It is suggested that the selectivity of crystal-like structures (semiconductor superlattices, photonic crystals, and phononic crystals) be raised by apodization of their edges. The transmission and reflection coefficients illustrating the efficiency of this approach are presented. © *2005 Pleiades Publishing, Inc.*

Artificial periodic structures similar in properties to natural crystals have been extensively developed in recent years. These structures form a basis for advanced integrated signal processing devices, most of which have nanometer dimensions. Of crystal-like structures (CSs), semiconductor superlattices, where electrons behave as de Broglie waves; photonic crystals for electromagnetic waves; and phononic crystals for elastic waves have become the subject of special interest. In crystals and CSs, constructive interference between reflected waves results in forbidden frequency bands where waves cannot propagate (gaps for electrons, photons, and phonons). Such frequency filtering allows one to control wave propagation in CSs and, hence, greatly extends the potential for signal processing.

CS-based devices are being put into mass production. Commercial fiber waveguides built around photonic crystals offer unique properties [1]. Synthetic opals show great promise as optical photonic crystals [2]. High-frequency one-dimensional phononic crystals for surface acoustic waves that are made in the form of periodically arranged relatively deep grooves on the substrate surface make it possible to improve the performance of acoustoelectron devices [3].

High selectivity is a critical issue for good CS-based devices. This parameter of multielement structures can be raised by apodization, i.e., by changing the amplitudes and phases of locally excited or reflected waves. In [4], amplitude apodization of rf photonic crystals as models of more complicated optical photonic crystals has been considered.

In this work, the author suggests an effective way of edge amplitude apodization for CSs. Both constructively and technologically, such a local apodization is much simpler than standard apodization distributed over the structure.

In CSs, reflection of waves is due to the fact that different CS regions have different wave properties, which are characterized by wave impedances. Impedance ratio $r_Z = Z_1/Z_2$, where Z_1 and Z_2 are the impedances of CS regions, specifies local reflection coefficient $r = (r_Z - 1)(r_Z + 1)$. Quantity r_Z and the arrangement of local reflectors define the CS spectral characteristics [5]. Local reflectors over a CS period are responsible for frequency response $h(F)$ of the reflection coefficient of the period, where $F = f/f_0$ and f_0 is the mean frequency of the first forbidden band. Function $h(F)$ defines the oscillation damping of the reflection (R) and transmission (T) coefficients in allowable bands of the material.

Figure 1a illustrates a correspondence between curves $R(F)$ and $h(F)$ for a standard (nonapodized) CS. Local reflectors of opposite polarity are arranged in time half-period. The value $r_Z = 2.8$ for photonic crystals is the boundary of the optical contrast necessary to complete the forbidden band for photons [6].

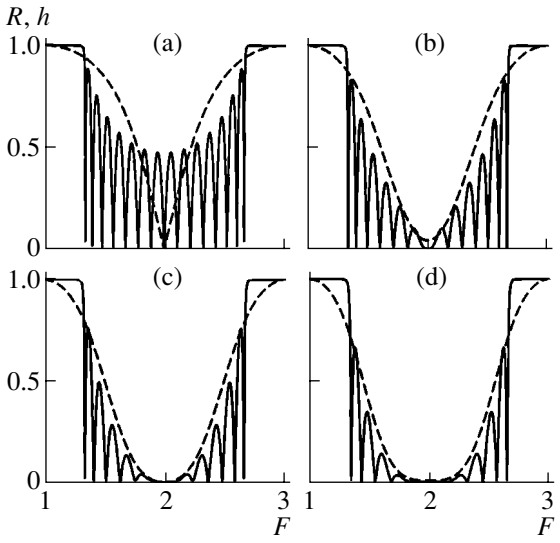

Fig. 1. Frequency dependences of reflection coefficient R for a 1D CS (continuous lines) and reflection coefficient h for an equivalent reflector of a period (dashed lines). (a) Nonapodized CS and (b–d) edge apodization versions s_2–s_4. The number of layers is 15, and $r_Z = 2.8$.

1063-7842/05/5011-1511$26.00

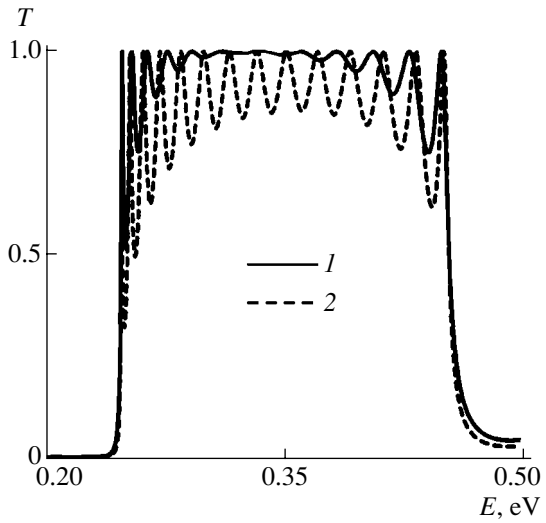

Fig. 2. Transmission coefficient T of the $Al_xGa_{1-x}As/GaAs$ superlattice vs. electron energy E (*1*) for edge apodization version s_4 and (*2*) without apodization.

The decay of sidelobes in the $R(F)$ curve depends on exponent n of the characteristics $h(F) = \varphi^n(F)$. The value $n = 1$ corresponds to the case considered above, where a reflector of a period is composed of two local reflectors in antiphase. We designate the structure of such a period reflector as $s_1 = \{r; -r\}$. For $n > 1$, a period reflector is bound to have a more complicated structure. Let each of the local reflectors be replaced by a resonator. Then, we obtain the structure $s_2 = \{r/2; -r; r/2\}$, which corresponds to $n \approx 2$. Compared with the initial structure, here only the reflection coefficients of the two edge local reflectors are changed (0.5r). The factor multiplying the reflection coefficient is the weight coefficient of a local reflector. A structure with $n \approx 3$, s_3, is formed by two structures $s_2/2$ of opposite polarity, which are arranged in time half-period. Their weight coefficients measured from the CS edges are 0.25 and 0.75. For $n \approx 4$, a reflector of a half-period with the structure $s_4 = \{r/8; -3r/8. 3r/8; -r/8\}$ is needed. In this case, the weight coefficients for edge local reflectors equal 0.125, 0.5, and 0.875.

Figures 1b–1d show the efficiency of CS edge apodization versions s_2–s_4. It is seen that edge apodization greatly improves the CS selectivity.

Transmission coefficient T of a CS is given by $T = \sqrt{1 - R^2}$. In highly selective allowable bands of a CS, where $R \ll 1$, $T \approx 1 - R^2/2$. Thus, the oscillation damping of the transmission coefficient depends on function $\varphi^{2n}(F)$ with an exponent twice as large as that appearing in the related function for the reflection coefficient. According to the model of equivalent reflectors [5], $\varphi(F) = |\sin(\pi F/2)|$.

Figure 2 plots the energy dependence of the transmission coefficient for an $Al_xGa_{1-x}As/GaAs$ superlattice where the thickness of the layers equals, respectively, 10 and 15 lattice constants of GaAs in the [100] direction (2.82665 Å [7]). The number of barriers is 15, and the barrier height is $V = 0.2$ eV. The effective electron mass in the barrier is $m_1 = (0.0665 + 0.0835x)m_0$ [8]; in the well, $m_2 = 0.0665m_0$. Here, m_0 is the mass of an electron at rest and V and x are related as $V = 0.7731x$ [9]. Since the electron wave impedance depends on energy, $Z \sim \sqrt{E - V}$ [10], the apodization procedure was carried out for the mean energy (0.36 eV) of the allowable energy band. Edge apodization substantially improves the efficiency of electron passage over a barrier.

CSs were simulated with the model [1], which is appropriate for wave structures, including CSs, of different complexity.

Edge apodization makes it possible to considerably raise the CS selectivity and still does not complicate the design, which is of great importance for advanced CS-based devices.

REFERENCES

1. www.blazephotonics.com; www.crystal-fibre.com.
2. V. G. Golubev, V. A. Kosobukin, D. A. Kurdyumov, *et al.*, Fiz. Tekh. Poluprovodn. (St. Petersburg) **35**, 710 (2001) [Semiconductors **35**, 680 (2001)].
3. L. Dhar and J. A. Rogers, Appl. Phys. Lett. **77**, 1402 (2000).
4. M. J. Erro, M. A. G. Laso, T. Lopetegi, *et al.*, Fiber Integr. Opt. **19**, 311 (2000).
5. E. A. Nelin, Zh. Tekh. Fiz. **74** (11), 70 (2004) [Tech. Phys. **49**, 1464 (2004)].
6. K. Busch and S. John, Phys. Rev. E **58**, 3896 (1998).
7. T. K. Gaylord, E. N. Glytsis, and K. F. Brennan, J. Appl. Phys. **65**, 2535 (1989).
8. K. Nakamura, A. Shimizu, K. Fujii, *et al.*, IEEE J. Quantum Electron. **28**, 1670 (1992).
9. D. W. Wilson, E. N. Glytsis, and T. K. Gaylord, IEEE J. Quantum Electron. **29**, 1364 (1993).
10. A. N. Khondker, M. R. Khan, and A. F. M. Anwar, J. Appl. Phys. **63**, 5191 (1988).
11. C. Christopoulos, *The Transmission-Line Modeling Method: TLM* (IEEE, Piscataway, 1995).

Translated by V. Isaakyan

Technical Physics, Vol. 50, No. 11, 2005, pp. 1513–1514. Translated from Zhurnal Tekhnicheskoĭ Fiziki, Vol. 75, No. 11, 2005, pp. 122–123.

SHORT COMMUNICATIONS

Semiinsulating Layers of Cadmium Telluride

V. P. Makhniĭ

Fed'kovich National University, ul. Kotsyubinskogo 2, Chernovtsy, 58012 Ukraine

e-mail: oe-dpt@chnu.cv.ua

Received November 15, 2004

Abstract—Tin diffusion into cadmium telluride substrates having different types and values of conductivity is used to fabricate layers with a resistivity of ~10^{10} Ω cm at 300 K. © *2005 Pleiades Publishing, Inc.*

A unique combination of the physical and chemical properties of cadmium telluride makes it promising for ionizing radiation detectors operating near room temperature [1]. One of the most challenging problems in this field is to grow crystals and/or films having a near-intrinsic conductivity. This problem is usually solved by doping of growing cadmium telluride by chlorine. In this way, CdTe crystals with resistivity $\rho = 10^8$–10^9 Ω cm at 300 K can be obtained [2]. A higher resistivity ($\rho \approx 5 \times 10^9$ Ω cm) can be reached when CdTe⟨Cl⟩ samples are additionally compensated by copper atoms [3]. The main disadvantage of the material thus produced is a severe degradation of its electrical performance at temperatures above 100°C. Such temperatures are typical in creating ohmic, including low-temperature indium, contacts. Moreover, high-resistivity samples require that measurements be taken at high temperatures. Note that, to one degree or another, the degradation shows up in both CdTe⟨Cl⟩ crystals and crystals doped by Cl or Cu. In this work, the author reports the fabrication of high-resistivity cadmium telluride layers with a high long-term and temperature stability and present their basic electrophysical properties.

Starting 4 × 4 × 1-mm substrates were cut from Bridgman-grown bulk cadmium telluride crystals. The type and value of conductivity were varied during growth by doping with In or Cl impurities and by deviation from stoichiometry. Diffusion layers were obtained by annealing the substrates in the saturated tin vapor at 650–950°C. Annealing was performed in a sealed quartz ampoule evacuated to 10^{-4} Torr with a charge and a substrate at the opposite ends. Before being placed into the ampoule, the substrate was mechanically polished and then chemically etched in a $K_2Cr_2O_7 : HNO_3 : H_2O = 2 : 5 : 10$ solution with subsequent rinsing in deionized water [3, 4]. Indium contacts to the samples had symmetric linear *I–V* characteristics in the voltage range 0.1–100 V. The resistivity was measured by the two-point probe method in the temperature range 300–450 K, and energy position *E* of electrically active centers was found from the ρ(*T*) dependence.

The values of ρ listed in the table were measured at 300 K; subscripts 0 and *T* designate the parameters of the starting and annealed substrates, respectively, which were averaged over five samples in each batch of crystals.

The lack of data on the diffusion coefficient of Sn in CdTe may introduce a high error in ρ measurements, since the diffusion layer thickness is not known exactly. Therefore, electrophysical measurements were taken from the samples where Sn atoms diffused through the whole substrate. At the annealing temperatures used, through diffusion is accomplished in ≈4 h [3]. Finding the diffusion coefficient of tin in cadmium telluride, which is an independent and complicated task, especially with regard to point intrinsic and impurity defects, is beyond the scope of this work.

As follows from the tabulated data, the activation energies for all the samples are virtually the same, irrespective of the parameters of the starting crystals. This indicates that the conductivity of the CdTe⟨Sn⟩ substrates is specified by the same deep center. This center is likely to be a complex including a Sn atom and an intrinsic defect, since E_T is independent of the nature and composition of the dopant. The tendency of ρ_T to increase with ρ_0 can be explained by a higher purity of the as-prepared high-resistivity crystals compared with the low-ohmic (doped) crystals.

Electrophysical properties of cadmium telluride crystals

Conductivity type	Dopant	ρ_0, Ω cm	ρ_T, Ω cm	E_0, eV	E_T, eV
n	In	10^{10}	10^{10}	–	0.75
n	Absent	10	10^{10}	0.04	0.76
n	»	10^3	2×10^{10}	0.1	0.75
n	»	10^8	4×10^{10}	0.58	0.76
p	»	10^7	4×10^{10}	0.65	0.76

1063-7842/05/5011-1513$26.00

Thus, obtaining CdTe⟨Sn⟩ diffusion layers with a near-intrinsic conductivity is quite feasible. Note that the conductivity of the diffusion layers is independent of the type and value of the conductivities of the as-prepared crystals and of the intrinsic and impurity defect composition in them. By varying the process parameters, e.g., the diffusion time, one can easily control the layer thickness. Finally, all the CdTe⟨Sn⟩ samples demonstrate a long-term and temperature stability: their electrophysical performance does not change after one-year storage under normal conditions and after thermal cycling in the range 300–450 K. Such properties of the material make it promising for designing resistive and barrier detectors of different types.

REFERENCES

1. D. V. Korbutyak, S. V. Mel'nichuk, S. V. Korbut, and M. M. Borisik, *Cadmium Telluride: Impurity- and Defect-Related States and Detectability* (Ivan Fedoriv, Kiev, 2000) [in Ukrainian].
2. M. Hage-Ali and P. Siffert, Nucl. Instrum. Methods Phys. Res. A **322**, 313 (1992).
3. M. V. Demid, Candidate's Dissertation (Chernovtsy, 2000).
4. V. P. Makhnii and M. V. Demid, Ukr. Patent No. 62650A, Byull. Izobret. No. 12 (2003).

Translated by K. Shakhlevich

Technical Physics, Vol. 50, No. 11, 2005, pp. 1515–1517. Translated from Zhurnal Tekhnicheskoĭ Fiziki, Vol. 75, No. 11, 2005, pp. 124–126.

SHORT COMMUNICATIONS

Distribution of the Electromagnetic Field of a High-Frequency Capacitive Filamentary Discharge Operating at Atmospheric Pressure

Yu. Yu. Lutsenko

Tomsk Polytechnical University, Tomsk, 634050 Russia

e-mail: tpu@tpu.ru

Received December 15, 2004

Abstract—Results are presented from measurements of the electromagnetic field of a high-frequency capacitive discharge operating in air and argon at atmospheric pressure. The experimental results are compared to those obtained for a high-frequency torch discharge. © *2005 Pleiades Publishing, Inc.*

In [1], a model of a high-frequency torch discharge was proposed according to which the discharge operates at the expense of dissipation of a symmetric surface transverse magnetic (TM) wave propagating along the discharge channel. It was assumed that the amplitude of the electromagnetic wave decreases exponentially along the channel. In order to explain the processes occurring in a high-frequency capacitive discharge, it was proposed in [2] to consider the propagation of two TM waves (direct and reflected ones) along the discharge channel. The measurements of the electromagnetic field of a high-frequency torch discharge [3] demonstrated the presence of the field components characteristic of a surface TM wave and the absence of the field dissipation along the discharge channel. In order to interpret these results, it was supposed that both a direct and a reflected TM wave were present in the torch discharge channel, which was then confirmed experimentally in [4].

The similarity between torch and capacitive discharges allows one to use a similar approach in describing them. However, there is a discrepancy between the estimated parameters of these discharges in different studies. Therefore, in the present study, we performed measurements of the electromagnetic field of a high-frequency capacitive discharge and compared them to those of a high-frequency torch discharge.

In our measurements, we used capacitive and inductive probes that could be displaced in the radial and axial directions relative to the discharge channel. Figure 1 shows a schematic of the experimental setup. A copper rod 1 mm in diameter and 3–5 mm in length was used as a capacitive probe. Three copper wire loops wound on a 10-mm-diameter Teflon cylinder were used as an inductive probe. The probe signals were fed to an oscilloscope or phase-meter, depending on the type of the measured quantity.

The discharge was excited in a 36-mm-diameter cylindrical quartz chamber enclosed by 70-mm-diameter ring electrodes located at a distance of 200 mm from one another. The electromagnetic field frequency was 35.5 MHz, and the discharge power was varied from 1.5 to 2.0 kW.

The measurements showed that four components of the electromagnetic field are present in the near zone of a high-frequency capacitive discharge: the axial and radial components of the magnetic field (H_φ and H_r) and the radial and axial components of the electric field (E_r and E_z). The presence of a magnetic field component was established by rotating the inductive loop in the corresponding plane relative to the discharge channel. Figure 2 shows the radial profile of the ratio H_φ/H_r. Measurements of the ratio H_φ/H_r showed that, without discharge ignition, there was only the radial component of the magnetic field. With a discharge, the ratio H_φ/H_r increased as the inductive probe approached the discharge zone (see Fig. 2). This indicates that the field

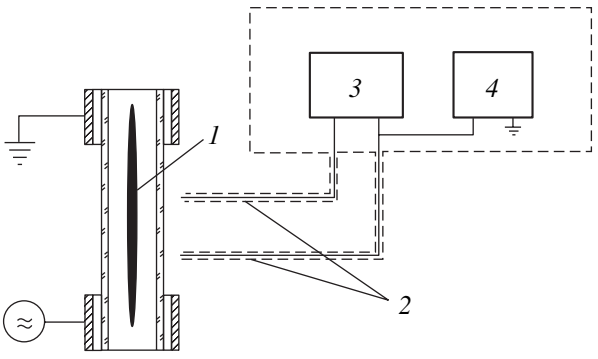

Fig. 1. Schematic of the experimental setup: (*1*) discharge, (*2*) probes, (*3*) measuring instrument, and (*4*) reference signal generator.

1063-7842/05/5011-1515$26.00

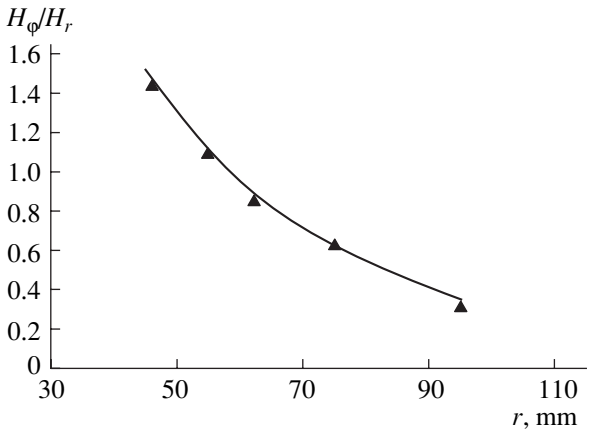

Fig. 2. Radial profile of the ratio H_φ/H_r at z = 100 mm.

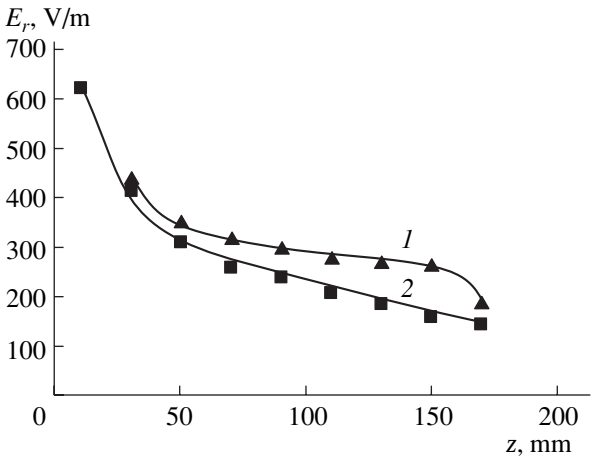

Fig. 3. Axial profiles of the radial component of the electric field of a high-frequency capacitive discharge in air for r = (*1*) 30 and (*2*) 50 mm.

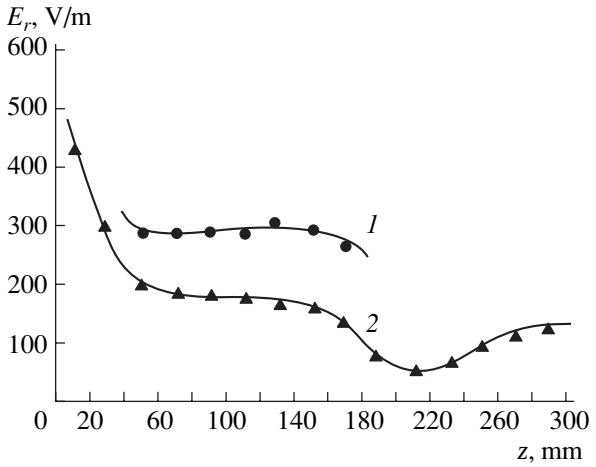

Fig. 4. Axial profiles of the radial component of the electric field of a high-frequency capacitive discharge in argon for r = (*1*) 30 and (*2*) 50 mm.

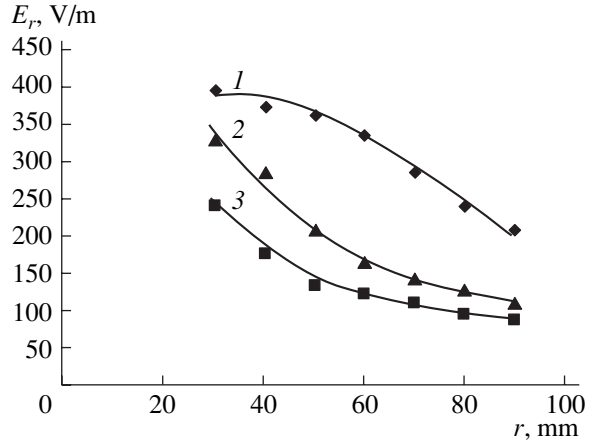

Fig. 5. Radial profiles of the radial component of the electric field of a high-frequency capacitive discharge in air for z = (*1*) 30, (*2*) 110, and (*3*) 170 mm.

components characteristic of a symmetric TM wave are predominant near the discharge channel (r = 1.5–2.0 mm).

Figures 3 and 4 show the axial profiles of the radial component of the electric field of high-frequency capacitive discharges in air and argon, respectively. The axial profiles of the other field components are similar in shape. The axial coordinate is counted from the upper edge of the high-frequency electrode. It can be seen from Figs. 3 and 4 that three zones can be distinguished in the axial profiles of the field components. The first zone is located near the high-frequency electrode, where the field amplitude decreases rapidly along the discharge axis. The length of this zone is comparable to the radius of the high-frequency electrode. It is this zone in which a surface TM wave forms. In a high-frequency torch discharge, the formation zone of a surface TM wave is practically absent. This is related to the torch discharge electrode being a cylindrical conductor along which a surface TM wave propagates. In a capacitive discharge, the surface TM wave is excited by a ring electrode, whose electromagnetic field contains the radial component of the magnetic field.

The formation zone of the surface TM wave is followed by a region where the field amplitude changes insignificantly. The axial distribution of the field components in this region can be represented as a superposition of two electromagnetic waves: a wave excited by the high-frequency electrode and that reflected from the grounded electrode. The closer to the discharge axis, the flatter the axial profile of the field amplitude. In the axial region, the field amplitude varies only slightly. This is especially pronounced in an argon discharge. Moreover, in the case of an argon discharge, a slight growth of the field amplitude along the discharge axis is observed as the discharge power is increased. This

can be explained by the higher conductivity of argon plasma [5] compared to that of air plasma: in an argon discharge, the dissipation of an electromagnetic wave propagating along the discharge axis is lower and the contribution of the reflected electromagnetic wave in the field distribution is larger.

The third region in the axial distribution of the field components is characterized by a drop in the field amplitude near the grounded electrode due to its shielding effect. The grounded electrode has little effect on the discharge operation as a whole. In air, the decrease in the field amplitude caused by the grounded electrode results in the termination of the discharge channel. On the other hand, this effect is absent in an argon discharge. Presumably, the electromagnetic wave is reflected from the end of the discharge channel rather than from the grounded electrode.

Figure 5 shows the radial profiles of the radial component of the electric field of a high-frequency capacitive discharge in air. As in the case of a high-frequency torch discharge [3], this profile, except for the zone adjacent to the high-frequency electrode (curve *1*), can be described by a Hankel function (curves *2* and *3*).

Similarly, the axial distributions of the phases of the field components in a capacitive discharge differ from those in a torch discharge [3] only in the initial segment of the discharge channel.

Therefore, the spatial distribution of the electromagnetic field of a high-frequency capacitive discharge is similar to that of a high-frequency torch discharge, except for the zone adjacent to the high-frequency electrode. Our measurements indicate that the field amplitude near the channel of a capacitive discharge, where the energy of the surface TM wave is localized, varies significantly along the discharge axis. Therefore, the torch and capacitive discharges can be described in a similar way. A certain difference in the electrodynamic properties of the torch and capacitive discharges can be associated with the termination of the channel of the latter by the grounded electrode. This in turn causes certain changes in the axial distribution of the discharge parameters.

REFERENCES

1. A. V. Kachanov, E. S. Trekhov, and E. P. Fetisov, Zh. Tekh. Fiz. **40**, 340 (1970) [Sov. Phys. Tech. Phys. **15**, 248 (1970)].
2. A. V. Zvyagintsev, R. V. Mitin, and K. K. Pryadkin, Zh. Tekh. Fiz. **45**, 278 (1975) [Sov. Phys. Tech. Phys. **20**, 177 (1975)].
3. I. A. Tikhomirov and Yu. Yu. Lutsenko, Zh. Tekh. Fiz. **59** (11), 128 (1989) [Sov. Phys. Tech. Phys. **34**, 1307 (1989)].
4. A. Ya. Khal'yaste, in *Proceedings of the 4th All-Union Conference on Physics of Gas Discharge, Makhachkala, 1988*, Chap. 1, pp. 135–136.
5. J. Janca, Czech. J. Phys., Sect. B, No. 9, 780 (1967).

Translated by B. Chernyavskiĭ

Technical Physics, Vol. 50, No. 11, 2005, pp. 1518–1519. Translated from Zhurnal Tekhnicheskoĭ Fiziki, Vol. 75, No. 11, 2005, pp. 127–128.

SHORT COMMUNICATIONS

Mathematical Simulations of the Development of the Ion Hose Instability of a Relativistic Electron Beam in a Plasma Channel with a Varying Density

A. G. Zelensky and E. K. Kolesnikov

Smirnov Research Institute of Mathematics and Mechanics, St. Petersburg State University, St. Petersburg, 198904 Russia

e-mail: zel_alex@e-mails.ru; Kolesnikov_evg@mail.ru

Received December 21, 2004

Abstract—The effect of different parameters of a plasma channel with an increasing or a decreasing density on the onset and behavior of the ion hose instability is investigated using the distributed-mass model. © *2005 Pleiades Publishing, Inc.*

At present, investigations are being carried out on application of relativistic electron beams (REBs) in various areas of science and engineering, such as the development of new types of charged particle accelerators, the solution of the controlled thermonuclear fusion problem, the development of high-power sources of electromagnetic radiation (including free electron lasers), and space research.

Particular attention is paid to the problem of transporting REBs in gas–plasma media by means of an artificial plasma channel produced by ionizing the neutral component of the background gas by UV radiation from an auxiliary laser [1, 2].

It is well-known that, when the duration of the beam pulse is comparable to the characteristic bounce period of the ions of the plasma channel in the potential well of the beam, the evolution of the beam–channel system is governed by the common dynamics of the relativistic beam electrons and channel ions. Both theory and experiment show that, in such circumstances, conditions in the beam–channel system may become favorable for the onset of various instabilities, the most dangerous of which is the ion hose instability (IHI) [3–8].

The propagation of an REB in a gas–plasma medium is described by very complicated equations and thus can be studied analytically only in a few special cases. This is why numerical simulations (along with experiments) play a key role in the relevant studies.

In our earlier paper [9], we investigated the dynamics of the development of the IHI of an REB propagating along a plasma channel in the form of a sequence of straight channels. In [10], we studied the characteristic features of the development of the IHI of an REB in a plasma channel with periodic density variations.

In the present paper, we analyze the dynamics of the IHI of an REB propagating in a plasma channel with an exponentially increasing (or decreasing) density.

We simulated the development of IHI by using the distributed-mass model, which was developed in [11, 12] and was implemented in [3] in order to study the guiding of a beam along a conventional uniform ion channel having a radius larger than the beam radius.

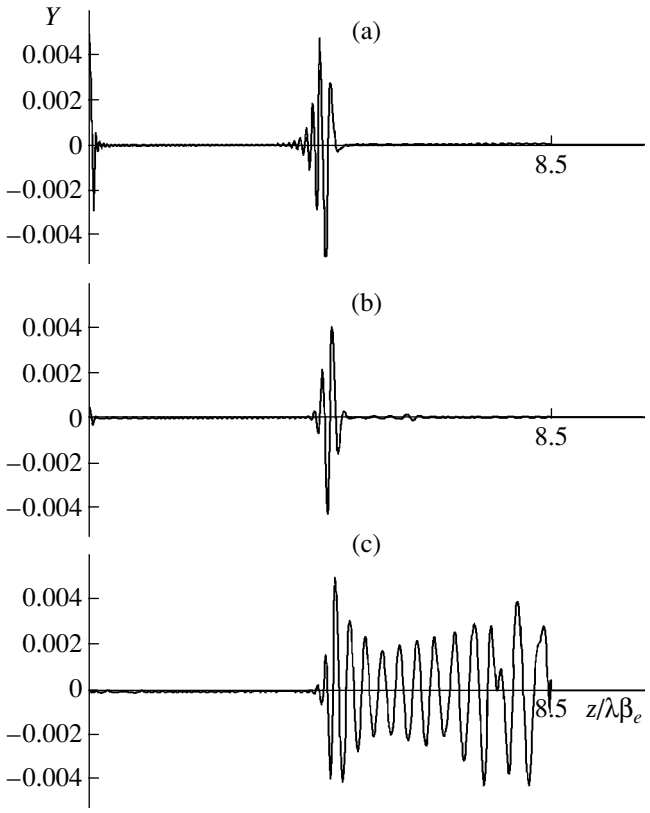

Fig. 1. Time evolutions of the coordinate Y of the centroids of the beam segments at the distances x = (a) $0.12\lambda_{\beta i}$, (b) $0.63\lambda_{\beta i}$, and (c) $1.25\lambda_{\beta i}$ from the beam front in a plasma channel with an exponentially decreasing density.

1063-7842/05/5011-1518$26.00

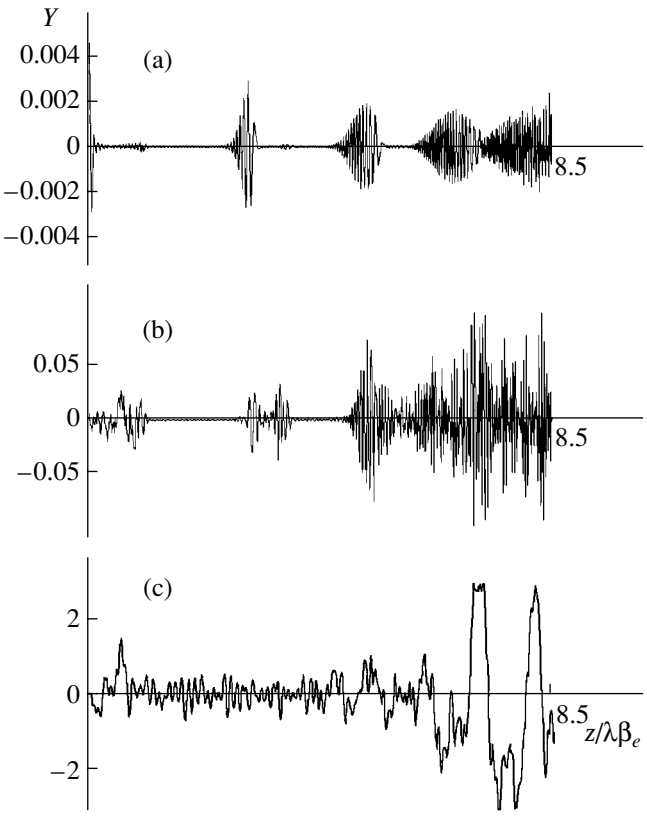

Fig. 2. Time evolutions of the sccoordinate Y of the centroids of the beam segments at the distances x = (a) $0.12\lambda_{\beta i}$, (b) $0.63\lambda_{\beta i}$, and (c) $1.25\lambda_{\beta i}$ from the beam front in a plasma channel with an exponentially increasing density.

The characteristic features of the development of the IHI of an REB in a plasma channel with a decreasing density are illustrated in Fig. 1, which shows the results of computations of the time evolution of the transverse coordinate Y of the centroids of three fixed beam segments located at different distances from the beam front, $x = 0.12$, 0.63, and $1.25\lambda_{\beta i}$ (where $\lambda_{\beta i}$ is the wavelength of oscillations of the channel ions about the beam). The total beam length was $2\lambda_{\beta i}$, and the longitudinal scale on which the density in the plasma channel decreases was $5800\lambda_{\beta i}$. The radial profiles of the beam electron density and the density of the channel ions were both assumed to be Gaussian. The characteristic radii of the beam and the ion channel were assumed to be the same.

From Fig. 1 we see that, in each of the three beam segments, the transverse oscillations of an REB grow in amplitude. As in the case of propagation of an REB in a uniform channel, the IHI is of a convective nature. The instability develops fairly slowly and thereby does not hinder the beam propagation over distances on the order of $30\lambda_{\beta e}$.

The results of numerical simulations of the development of the IHI of an REB in a plasma channel with an increasing density are illustrated in Fig. 2. From this figure it is clear that, in the case in question, the transverse oscillations of electrons in the three beam segments grow in amplitude at a significantly faster rate than in the previous case, with the result that the beam can be guided over shorter distances, on the order of $10\lambda_{\beta e}$.

REFERENCES

1. W. E. Martin *et al.*, Phys. Rev. Lett. **54**, 685 (1985).
2. G. J. Caporaso *et al.*, Phys. Rev. Lett. **57**, 1591 (1986).
3. H. L. Buchanan, Phys. Fluids **30**, 221 (1987).
4. R. E. Lipinsky, J. R. Smith, and I. R. Shokair, Phys. Fluids B **2**, 2764 (1990).
5. K. J. O'Brien, J. Appl. Phys. **65**, 9 (1989).
6. R. F. Fernsler, S. P. Slinker, M. Lampe, *et al.*, Phys. Plasmas **2**, 4338 (1995).
7. E. K. Kolesnikov and A. S. Manuĭlov, Zh. Tekh. Fiz. **70** (5), 68 (2000) [Tech. Phys. **45**, 591 (2000)].
8. V. B. Vladyko and Yu. V. Rudyak, Fiz. Plazmy **17**, 623 (1991) [Sov. J. Plasma Phys. **17**, 366 (1991)].
9. A. G. Zelenskiĭ and E. K. Kolesnikov, Zh. Tekh. Fiz. **65** (5), 188 (1995) [Tech. Phys. **40**, 507 (1995)].
10. A. G. Zelenskiĭ and E. K. Kolesnikov, Zh. Tekh. Fiz. **73** (12), 71 (2003) [Tech. Phys. **48**, 1570 (2003)].
11. E. P. Lee, Phys. Fluids **21**, 1327 (1978).
12. E. J. Lauer, R. J. Briggs, T. J. Fessenden, *et al.*, Phys. Fluids **21**, 1344 (1978).

Translated by O. Khadin

Technical Physics, Vol. 50, No. 11, 2005, pp. 1520–1521. Translated from Zhurnal Tekhnicheskoĭ Fiziki, Vol. 75, No. 11, 2005, p. 129.

SHORT COMMUNICATIONS

On Stabilization of a Perfectly Conducting Compressible Plasma Jet Flow

V. G. Kirtskhaliya and I. A. Zhvaniya†

Sukhumi Physicotechnical Institute, Sukhumi, Abkhazia, 384914 Georgia

e-mail: sipt@myoffice.ge

Received February 10, 2005

Abstract—It follows from an earlier work of the authors that taking into account plasma compressibility may stabilize the flow of plane and cylindrical plasma jets under certain conditions. Subsequent analysis and numerical calculation have shown that such conditions are unfeasible. Thus, compressibility destabilizes a plasma jet.

In [1], it was shown that the dispersion relation for the natural oscillation of an ideally conducting slightly compressible plasma jet has the form

$$[\nu G(\delta)(1+\varepsilon)+1]\xi^2 - 2a\xi + a^2 - \nu G(\delta)(1+\varepsilon)b_1^2 - b_2^2 = 0, \quad (1)$$

where ε is a small quantity that includes the effect of compressibility on the stability of the jet and the run of function $G(\delta)$ depends on the jet configuration: for a plane jet, $G(\delta) = \tanh\delta$ monotonically grows from 0 to 1; for a cylindrical jet, $G(\delta, \xi) = I_0(\delta)K_1(\delta)/I_1(\delta)K_0(\delta)$ monotonically decays from ∞ to 1 when δ varies from 0 to ∞.

The critical velocity of the jet above which the jet becomes unstable is found by equating the determinant of this equation to zero [1]. The effect of compressibility on jet stability depends on the sign of difference Δa_{cr}^2 between the squares of the critical velocities of compressible and incompressible ($\varepsilon = 0$) jets,

$$\Delta a_{cr}^2 = \frac{\nu b_1^2[G^2(\delta) - \beta^2]}{G(\delta)}\varepsilon, \quad (2)$$

where $\beta = b_2/\nu b_1$ is the parameter that specifies flow conditions that are optimal in terms of MHD stability versus jet configuration.

It is seen that the sign of Δa_{cr}^2, which depends on the signs of $[G^2(\delta) - \beta^2]$ and ε, may be positive under certain conditions. This means that compressibility has a stabilizing effect.

Subsequent calculations showed, however, that such conditions are unfeasible: having found an explicit expression for ε by formulas in [1], we obtain

$$\Delta a_{cr}^2 = -\frac{1}{2}\frac{\nu b_1^4[G(\delta) + \nu\beta^2]^2}{[\nu G(\delta) + 1]} \times \left[\frac{\nu^2 G^2(\delta)}{\mu_2^2} + \frac{1}{\nu G(\delta)\mu_1^2}\left(1 - \frac{2\delta}{\sinh 2\delta}\right)\right] \quad (3)$$

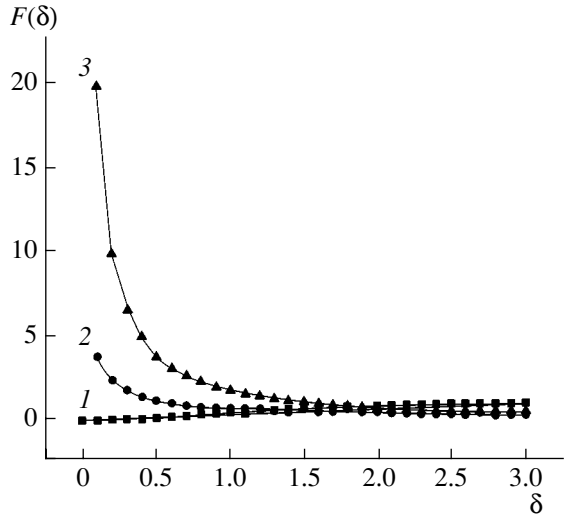

Figure. (1) $F(\delta) = 1 - \frac{2\delta}{\sinh 2\delta}$, (2) $F(\delta) = \frac{K_1(\delta)}{K_0(\delta)} - \frac{K_0(\delta)}{K_1(\delta)}$, and (3) $F(\delta) = \frac{I_0(\delta)}{I_1(\delta)} - \frac{I_1(\delta)}{I_0(\delta)}$.

† Deceased.

1063-7842/05/5011-1520$26.00 © 2005 Pleiades Publishing, Inc.

for a plane jet and

$$\Delta a_{cr}^2 = -\frac{\nu b_1^4 [G(\delta) + \nu\beta^2]^2}{[\nu G(\delta) + 1]} \left\{ \frac{\nu^2 G^2(\delta)}{\mu_2^2} \left[1 + \frac{\delta}{2} \left(\frac{K_1(\delta)}{K_0(\delta)} - \frac{K_0(\delta)}{K_1(\delta)} \right) \right] + \frac{1}{\nu G(\delta)\mu_1^2} \left[1 + \frac{\delta}{2} \left(\frac{I_0(\delta)}{I_1(\delta)} - \frac{I_1(\delta)}{I_0(\delta)} \right) \right] \right\} \quad (4)$$

for a cylindrical jet.

Since the functions plotted in the figure are positive, one can argue that the right-hand sides of (3) and (4) are negative throughout the range of δ. Hence, compressibility destabilizes a plasma jet of any configuration under any flow conditions.

REFERENCES

1. I. A. Zhvaniya, V. G. Kirtskhaliya, and A. A. Rukhadze, Zh. Tekh. Fiz. **74** (11), 132 (2004) [Tech. Phys. **49**, 1525 (2004)].

Translated by V. Isaakyan

Technical Physics, Vol. 50, No. 11, 2005, pp. 1522–1524. Translated from Zhurnal Tekhnicheskoĭ Fiziki, Vol. 75, No. 11, 2005, pp. 130–132.

SHORT COMMUNICATIONS

Thermal Radiation from Nanoparticles

Yu. V. Martynenko and L. I. Ognev

Institute for Nuclear Fusion, Russian Research Centre Kurchatov Institute, pl. Kurchatova 1, Moscow, 123182 Russia

e-mail: martyn@nfi.kiae.ru

Received March 11, 2005

Abstract—A simple and universal criterion of the efficiency of energy loss by thermal radiation is obtained for the class of small conducting particles, including, in addition to metals and graphite, the majority of carbides of metals important for practical applications, such as tungsten and titanium carbides. © *2005 Pleiades Publishing, Inc.*

In recent years, the volume of investigations and developments in the realms of nanotechnologies, nanomaterials, and nanosystems has been growing vigorously worldwide [1]. The production and application of nanopowders, which are used in metallurgy, microelectronics, and the food industry, are one of the important lines in nanotechnologies. The production of nanopowders and their use frequently involves heating nanoparticles to high temperatures, in which case one naturally expects intense thermal radiation.

At the same time, there is presently great interest in dust plasmas [2] and dust in thermonuclear facilities [3], where micro- and nanoparticles are heated to high temperatures, so that loss by radiation may play a significant role in the energy balance of particles.

In calculating the energy balance of nanoparticles, it is illegitimate to employ the Stefan–Boltzmann law for the radiation from a black ball, since this law yields strongly overestimated results at particle dimensions smaller than the radiation wavelength. The energy loss of atomic clusters by radiation was discussed in a review article of Smirnov [4].

In order to calculate the energy loss of a small body, one can employ the Kirchhoff law for equilibrium thermal radiation [5]. The thermal radiation from a body of temperature T in the circular-frequency interval $d\omega$ is

$$dT(\omega) = 4\pi c\sigma(\omega)\frac{\hbar\omega^3}{4\pi^3c^3\left(e^{\frac{\hbar\omega}{kT}}-1\right)}d\omega, \qquad (1)$$

where $\sigma(\omega)$ is the effective absorption cross section at a frequency ω, c is the speed of light, T is the temperature, and k is the Boltzmann constant.

Following [5], we can express the cross section for radiation absorption by a ball of volume V in terms of the electric permittivity α_e'' and the magnetic permeability α_m'' normalized to the volume. As a result, we arrive at

$$\sigma(\omega) = \frac{4\pi\omega}{c}(\alpha_e'' + \alpha_m'')V. \qquad (2)$$

In the case of conducting bodies, the magnetic component is dominant, and it is precisely this component that will be taken into account below for this reason.

Although general dependences of the absorption cross section on particle parameters could not be obtained [6] within Mie theory, which provides the most consistent approach to the scattering and absorption of electromagnetic radiation on small particles, an approximate method based on taking into account the radiation penetration depth into a medium can be employed in the case of conducting spheres [5]. Within this approach, the magnetic permeability for a sphere of radius r_0 depends on the dimensionless parameter (r_0/δ), where $\delta = c/(2\pi\sigma\omega)^{1/2}$ is the radiation penetration depth in a conductor, as

$$\alpha_m'' = -\frac{9\delta^2}{16\pi r_0^2}\left[1 - \frac{r_0}{\delta}\frac{\sinh(2r_0/\delta) - \sin(2r_0/\delta)}{\cosh(2r_0/\delta) - \cos(2r_0/\delta)}\right]. \qquad (3)$$

At small values of the radius ($r_0/\delta \ll 1$; this condition is also realized at low frequencies), one can use the approximation

$$\alpha_m'' = \frac{1}{20\pi}\left(\frac{r_0^2}{\delta^2}\right) = \frac{r_0^2\sigma\omega}{10c^2}. \qquad (4)$$

The respective approximation at large values of the particle radius ($r_0/\delta \gg 1$; this condition is also realized at high frequencies) is

$$\alpha_m'' = \frac{9\delta^2}{16\pi r_0^2} = \frac{9c}{16\pi r_0\sqrt{2\pi\sigma\omega}}, \qquad (5)$$

where σ is the static conductivity of the material used. The dependences specified by Eqs. (3)–(5) are depicted

1063-7842/05/5011-1522$26.00

in Fig. 1. Upon substituting high-energy approximation (5) into the integral of (1) for the radiation, the particle radius r_0 drops out from the final expression, in just the same way as in the case of blackbody radiation.

By introducing the dimensionless parameter p,

$$p = \frac{r_0}{c}\sqrt{\frac{2\pi\sigma kT}{\hbar}}, \quad (6)$$

which takes into account the conductivity of matter, its temperature, and the particle radius, and performing integration with respect to the frequency, we can go over from expression (1) to

$$I = \frac{16}{3}\frac{T^5 r_0^3}{c^3\hbar^4}J(p). \quad (7)$$

The dependence of the integral $J(p)$ on the dimensionless parameter p, which is defined in (6),

$$J(p) = \int_0^\infty \alpha_m''(p\sqrt{x})\frac{x^4 dx}{e^x - 1}, \quad (8)$$

is illustrated in Fig. 2. In (8), we have employed the dimensionless variable $x = \hbar\omega/kT$. It should be noted that $J(p) \sim 1/p$ for $p \gg 1$, which corresponds to the case of high temperatures or large particle radii, and that $J(p) \sim p^2$ for $p \ll 1$. In the latter case, the quadratic asymptotic behavior reflects a high-power dependence of the normalized cross section $\sigma(\omega)/(\pi r_0^2)$ on the small radii of spherical particles; this dependence also follows from calculations within Mie theory [6].

For the sake of clarity, it is convenient to normalize the expression for the intensity of thermal radiation to the intensity of blackbody radiation:

$$\frac{I}{I_b} = \frac{80kT}{\pi^3 c\hbar}r_0 J(p). \quad (9)$$

In view of the aforementioned asymptotic behavior $J(p) \sim 1/p$, the normalized intensity (emissivity) in the case of large particles is independent of the radius and depends only slightly on temperature. The surviving temperature dependence is explained by the inaccuracy of the above model of radiation absorption by conducting balls at high temperatures.

The dependence of the normalized emissivity (degree of blackness) I/I_b on the particle radius r_0 at the temperatures of T = 1773, 1273, and 773 K for copper microparticles is shown in Fig. 3 with allowance for the temperature dependence of the conductivity of matter [7]. Similar results for graphite microparticles at the temperatures of T= 2773, 2273, 1273, and 773 K are given in Fig. 4.

The dependence of the emissivity normalized to the blackbody emissivity, I/I_b (degree of blackness), on the size of spherical particles reflects the cubic dependence of the normalized absorption cross section on the radius

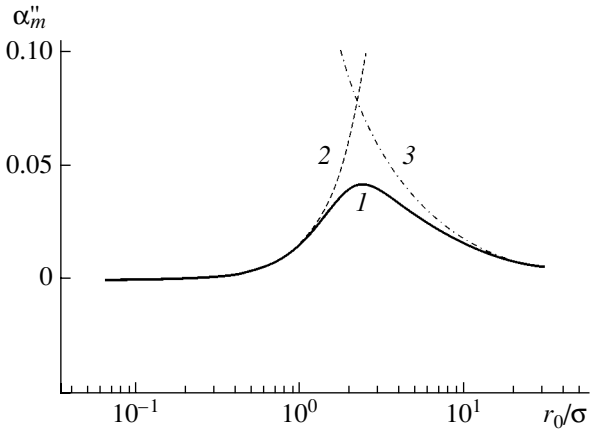

Fig. 1. Dependence of the imaginary part α_m'' of the magnetic permeability normalized to the volume on the dimensionless parameter (r_0/δ) (*1*) in the case of the exact formula and in the cases of the (*2*) low-frequency ($r_0/\delta \ll 1$) and (*3*) high-frequency ($r_0/\delta \gg 1$) approximations.

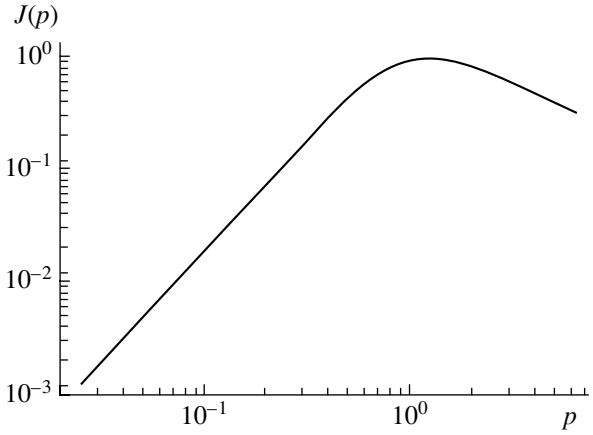

Fig. 2. Dependence of the integral $J(p)$ with respect to the radiation frequency on the dimensionless parameter $p = (r_0/c)(2\pi\sigma kT/\hbar)^{1/2}$.

for nanoparticles; with increasing particle size, this dependence approaches a constant value that agrees with values quoted in reference books. For molten copper of temperature in the range 1100–1300°C, the degree of blackness is from 0.13 to 0.15 [8], this being in good agreement with the results of the calculations for particles of radius in excess of 1 μm (Fig. 3). For graphite at a temperature of 500°C, the degree of blackness is 0.71 [9], which is in accord with the results of the calculations within the chosen model of radiating conducting balls. The exaggerated results on the radiation from graphite at high temperatures should be attributed to the inaccuracy of the model. The model used is valid in the region of radiation frequencies at which $\omega/(2\pi) \ll \sigma$. At high frequencies, the normalized cross section that is derived for the absorption on a

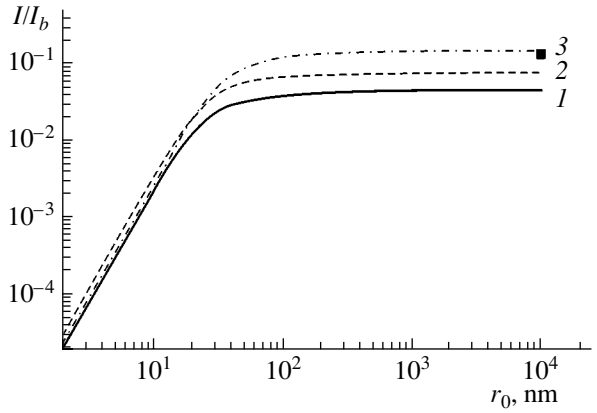

Fig. 3. Normalized emissivity of copper particles at the temperatures of (*1*) 773, (*2*) 1273, and (*3*) 1773 K.

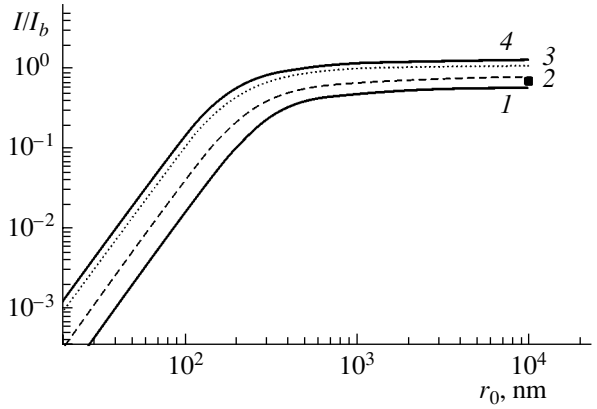

Fig. 4. Normalized emissivity of graphite particles at the temperatures of (*1*) 773, (*2*) 1273, (*3*) 2273, and (*4*) 2773 K.

spherical particle by using the asymptotic expression (5) can be recast into the form $\sigma(\omega)/(\pi r_0^2) = 3[\omega/(2\pi\sigma)]^{1/2}$. In a more accurate model of radiation absorption by a conducting medium, the respective asymptotic expression additionally involves terms of order $\omega/(2\pi\sigma)$ [6]; in the case being considered, the inclusion of these terms would lead to an improvement of the agreement with experimental data at large radii of particles at high temperatures. It should be noted that the condition of applicability of the approach used is well satisfied in the case of metal carbides, which is of importance for practice.

In either of the above examples, we see from Figs. 3 and 4 that, with decreasing particle size, the emissivity of particles for $p \le 1$ falls substantially short of that predicted by the Stefan–Boltzmann law. Thus, the dimensionless parameter $p = (r_0/c)(2\pi\sigma kT/\hbar)^{1/2}$ characterizes the emissivity of small conducting particles as a function of their dimensions and conductivity.

We note that, albeit being small in relation to blackbody radiation, radiation from nanoparticles exceeds radiation from the same amount of a gas and can therefore be used as a source of light [4].

In the case of dielectric particles, it is hardly possible to construct a rather simple dependence of the radiation-absorption cross section on the radius of a spherical particle. However, some results obtained on the basis of Mie theory for the scattering and absorption of an electromagnetic wave by absorbing spherical particles [6] suggest that the absorption cross section changes only slightly for wavelength values satisfying the condition $2\pi\lambda(n-1)/r_0 \le 6$, where n is the refraction index of matter. Since, according to the Wien displacement law [8], the maximum of the thermal-radiation spectrum at elevated temperatures corresponds to the wavelength $\lambda_{max} = B/T$, a significant decrease in the emissivity of dielectric particles should be expected for particles of radius in the region $r_0 \le (n-1)B/T$.

CONCLUSIONS

The efficiency of the energy loss of hot conducting particles, including, in addition to metals and graphite, the majority of metal carbides important for applications, such as tungsten and titanium carbides, which possess a high electrical conductivity [10], depends greatly on their dimensions. For dimensions smaller than the wavelength at the maximum of the thermal-radiation spectrum, the efficiency of losses by radiation depends both on the temperature T and on the conductivity σ of the particle material. The universal criterion $p = (r_0/c)(2\pi\sigma kT/\hbar)^{1/2} > 1$ makes it possible to determine the applicability range of the Stefan–Boltzmann law for losses by radiation as the radius of a conducting particle decreases to dimensions of $r_0 \le \lambda_{max} = B/T$.

REFERENCES

1. A. V. Gusev, Usp. Fiz. Nauk **168**, 55 (1998) [Phys. Usp. **41**, 49 (1998)].
2. V. E. Fortov, A. G. Khrapak, and I. T. Yakubov, *Physics of Nonideal Plasmas* (Fizmatlit, Moscow, 2004; World Sci. Publ., London, 1999).
3. J. Winter and V. N. Tsytovich, Usp. Fiz. Nauk **168**, 899 (1998) [Phys. Usp. **41**, 815 (1998)].
4. B. M. Smirnov, Usp. Fiz. Nauk **167**, 1169 (1997) [Phys. Usp. **40**, 1117 (1997)].
5. L. D. Landau and E. M. Lifshitz, *Course of Theoretical Physics*, Vol. 8: *Electrodynamics of Continuous Media* (Nauka, Moscow, 1982; Pergamon, New York, 1984).
6. M. Born and E. Wolf, *Principles of Optics*, 4th ed. (Pergamon, Oxford, 1969; Nauka, Moscow, 1970).
7. *Tables of Physical Quantities*, Ed. by I. K. Kikoin (Atomizdat, Moscow, 1976) [in Russian].
8. A. G. Blokh, *Fundamentals of Heat Exchange by Radiation* (Gosenergoizdat, Moscow, 1962) [in Russian].
9. *Emissivity of Specific Materials*, http://www.colcparmer.com/techinfo/.
10. *Handbook of the Physicochemical Properties of the Elements*, Ed. by G. V. Samsonov (Metallurgiya, Moscow, 1976; Plenum, New York, 1968), Chap. 1.

Translated by A. Isaakyan

Technical Physics, Vol. 50, No. 11, 2005, pp. 1525–1527. Translated from Zhurnal Tekhnicheskoĭ Fiziki, Vol. 75, No. 11, 2005, pp. 133–135.

SHORT COMMUNICATIONS

Long-Range Effect of Light on the Microhardness of Annealed Molybdenum Foils

D. I. Tetelbaum, E. V. Kuril'chik, and Yu. A. Mendeleva

Physicotechnical Research Institute, Lobachevsky State University, pr. Gagarina 23/3, Nizhni Novgorod, 603950 Russia

e-mail: Tetelbaum@phys.unn.ru

Received March 14, 2005

Abstract—It is shown that, when irradiated by light on one side, both as-prepared samples of molybdenum foil and those annealed in the temperature range 75–900°C change their microhardness on the other (nonirradiated) side. Annealing influences the relative variation in the microhardness under the action of a single irradiation and multiple irradiations, the changes being dependent on the annealing temperature. Recrystallization annealing increases the relative change in the microhardness and makes the microhardness variation under irradiation–relaxation cycling regular, whereas low-temperature annealing breaks this regularity. The results demonstrate that the state of defects in the initial state of the metal is of crucial importance in the phenomenon. © *2005 Pleiades Publishing, Inc.*

In [1–4], we found a new effect: a change in microhardness H of one side of a metal foil upon irradiation of the other side by light. This effect was qualitatively explained by the fact that photoelectrons trapped in a native oxide (NO) film that is present on the foil generate deformation waves under the action of Coulomb forces that appear as a result of violation of local electroneutrality near the traps. Having penetrated into the metal, the waves modify the defect subsystem and, thereby, change H. Krivelevich [5] proposed a phenomenological theory of transformation in systems with more than one local minimum of the free energy that applies in our case (if the effect of deformation waves is taken into account). He showed that an energy flux incident on such a system may cause a long-range change of the "switching wave" type in its structure and properties. This theory implies a relation between the amount and character of the effect, on the one hand, and the initial state of the system, on the other. The state of the system (foil) can be changed by annealing. Relevant experiments are necessary to uncover the mechanism behind this phenomenon. In particular, it was found that light does not affect the state of the NO-free surface; therefore, it is necessary to see what the role is of the metal structure itself in this effect.

The effect is characterized by relaxation of H after irradiation. Sometimes, the microhardness recovers to the initial (or close to initial) value and changes again upon repeat irradiation. If the defect system in the metal is important, the variation of H at irradiation–relaxation cycling (photocycling) can be expected to depend on the state of the defect system.

In this work, molybdenum foils are used to study how annealing influences (i) H variation under irradiation and (ii) the reproducibility of this variation at photocycling.

We experimented with 50-μm-thick rolled molybdenum foils. According to X-ray diffraction data, the foils were textured and had an average grain size of more than 1 μm. Illumination was accomplished by a 20-W incandescent lamp with the filament 5 cm distant from the foil. The foils were annealed in air ($T_{ann} \le 150$°C) and in a dried nitrogen flow ($T_{ann} \ge 200$°C) for 30 min. Despite the protective atmosphere, we could not avoid additional oxidation. After each annealing, the oxide was removed in HCl and irradiation was carried out after the time (2 h or longer) it takes for a new NO layer

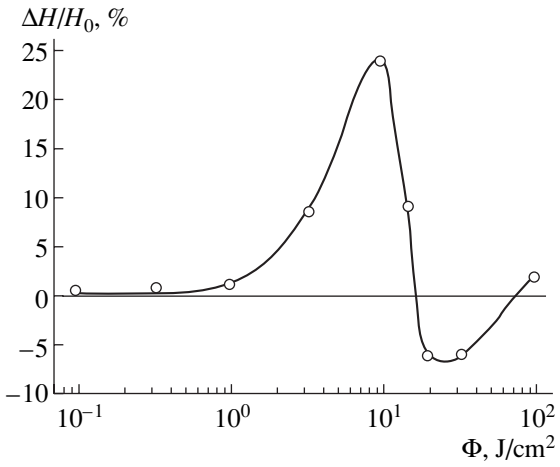

Fig. 1. Dose dependence of the relative change in the microhardness.

1063-7842/05/5011-1525$26.00 © 2005 Pleiades Publishing, Inc.

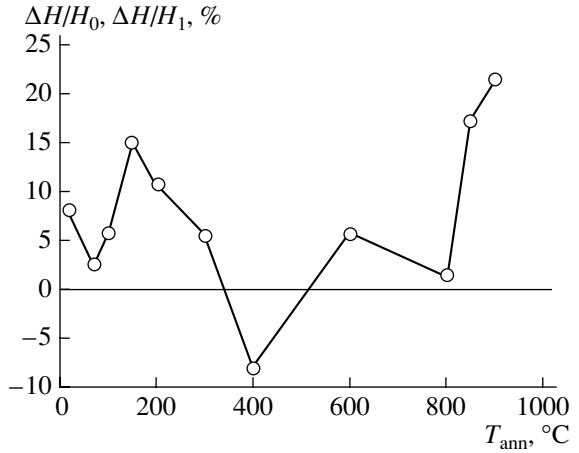

Fig. 2. Relative changes in the microhardness of the as-prepared foils, $\Delta H/H_0$, and of the foils annealed at different temperatures, $\Delta H/H_1$. The first circle refers to $\Delta H/H_0$; the others, to $\Delta H/H_1$. H_0 is the microhardness of the as-prepared foil, and H_1 is the that of the annealed foil.

to grow. With such a procedure, we exclude annealing-induced transformations in the oxide.

The microhardness was measured with a PMT-3 device at an indentation load of 50 g. The load chosen after recording an *H*–load curve was a tradeoff between a high accuracy of *H* measurement (deep indentation) and a smaller amount of the effect (a thicker layer being probed) at high loads. The results were averaged over five indentations, and the diagonals of the indentations were measured twice. Based on the estimation of systematic and random errors, a change in *H* exceeding 4% of the initial value was considered significant.

Figure 1 shows the dose dependence of the relative change in *H* on the rear side of the foil (within the limits of experimental error, no changes in *H* on the front (irradiated) side were detected). When calculating the dose (energy density), we assumed that the radiation power equals 50% of the total power. Two features are noteworthy: the nonmonotonic run of the dose dependence and the trend of the *H* change to zero at high doses. Both features were observed and discussed earlier for permalloy-79 [1–4]. The behavior of *H* in Mo demonstrates that these features are not accidental (the reasons for such behavior are beyond the scope of this work). The data in Fig. 1 were used to choose the dose for further experiments.

After the as-prepared foils had been annealed, their microhardnesses changed. The range of annealing temperatures can be divided into three subranges: in the first subrange (to T_{ann} = 150°C), *H* increases; in the second subrange (150–850°C), it virtually returns to the initial value; and in the third subrange (above 850°C), the microhardness drops below the initial value. The behavior of *H* indicates that the metal structure changes. The range of decreasing *H* (above 850°C) corresponds to temperatures of ~$0.4T_m$, where T_m is the

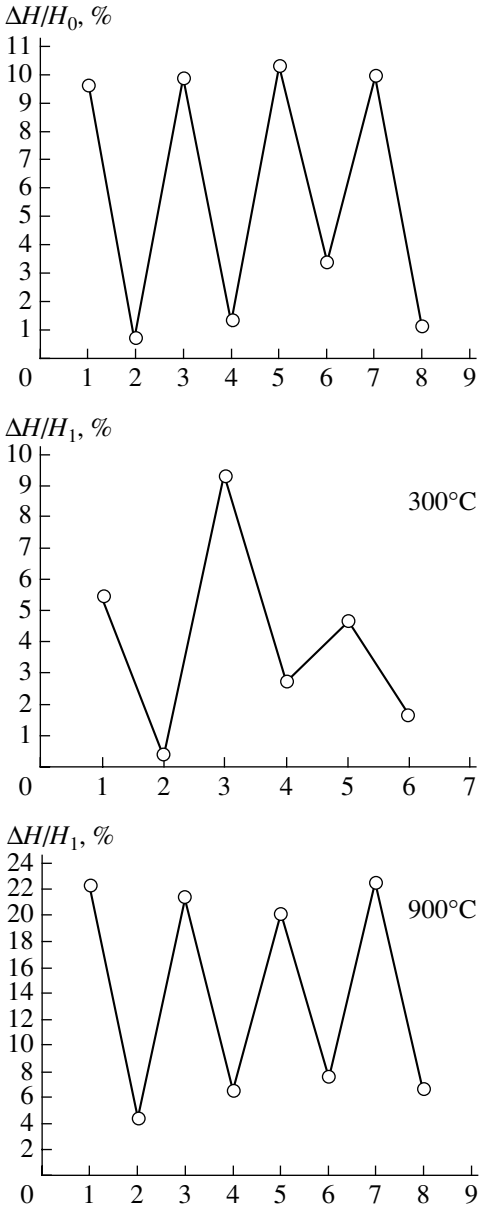

Fig. 3. Changes in the microhardness of the as-prepared samples (upper curve) and the samples annealed at different temperatures during photocycling. Odd and even numbers in the abscissa axis correspond to the postirradiation and postrelaxation states, respectively.

melting point (in K). This correspondence means that the decrease in *H* is related to recrystallization, which occurs just in this temperature range [6]. The behavior of *H* at lower T_{ann} may be associated with processes occurring in the subsystem of point defects (largely in Cottrell atmospheres).

Figure 2 shows the T_{ann} dependence of the relative microhardness variation at a radiation energy density of 3 J/cm^2 (the irradiation time is 100 s). Shown also is the value of $\Delta H/H_0$ in the as-prepared foil. It is seen that the magnitude and even the sign of the change depend on

whether the foil was annealed and, if so, on the annealing temperature. Interestingly, after recrystallization annealing, the effect of illumination on H is twice as large as that for the as-prepared samples. At other values of T_{ann}, the amount of the effect, on the contrary, decreases down to its complete disappearance. After irradiation, the changes relax to zero in approximately a few hours.

The results of repeated irradiations performed after aging (relaxation) also depend on annealing itself and on the annealing temperature. In the as-prepared sample, relaxation returns the microhardness to its initial value and, upon repeated irradiations (photocycling), H each time increases to a value that is close to that achieved upon the first irradiation (Fig. 3). In the samples annealed in the range T_{ann} = 75–800°C, the changes in H upon photocycling turned out to be irregular (poorly reproducible from cycle to cycle). As an example, Fig. 3 shows the results for T_{ann} = 300°C. Such behavior was also observed at other annealing temperatures in this range. At T_{ann} = 900°C, the situation is different: after annealing of the foil at a temperature slightly above the recrystallization temperature, H again starts varying in a regular (sawtooth) manner.

Thus, preannealing has a substantial effect on the photosensitivity of the foils. This finding demonstrates a significant role of the state of defects in the metal and is consistent with the phenomenological model [5], according to which the effect depends on the initial set of "order parameters." On the whole, the results agree with our qualitative model [1–4], where a change in H is related to the modification of the defect system under the action of radiation-induced deformation waves (this relation is rather complicated). However, one cannot rule out the situation where the effect weakens or even disappears at annealing temperatures well above $0.4T_m$ (where the system approaches its equilibrium state), as was observed in the case of Cu–Ni foils [7]. This suggests that the system has to be slightly out of equilibrium in the initial state for the effect to arise. A more detailed explanation of the above dependences calls for a deeper insight into the state of defects before and after annealing.

From the applied standpoint, our results demonstrate that the metal can be returned to the radiation-induced state by repeated irradiations. Another important conclusion is that the amount of the effect can be both high and negligible in the same material, depending on conditions. These facts should be taken into account in both practice and research.

ACKNOWLEDGMENTS

This work was supported by the program "Universities of Russia" (project no. UR.01.01.057) and the Russian Foundation for Basic Research (project no. 02-02-16670).

REFERENCES

1. D. I. Tetelbaum, A. A. Trofimov, A. Yu. Azov, *et al.*, Pis'ma Zh. Tekh. Fiz. **24** (23), 9 (1998) [Tech. Phys. Lett. **24**, 910 (1998)].
2. D. I. Tetelbaum, A. Yu. Azov, and P. I. Golyakov, Pis'ma Zh. Tekh. Fiz. **29** (2), 35 (2003) [Tech. Phys. Lett. **29**, 57 (2003)].
3. D. I. Tetelbaum, Yu. A. Mendeleva, and A. Yu. Azov, Pis'ma Zh. Tekh. Fiz. **30** (11), 65 (2004) [Tech. Phys. Lett. **30**, 471 (2004)].
4. D. I. Tetelbaum, A. Yu. Azov, E. V. Kuril'chik, *et al.*, Vacuum **70**, 169 (2003).
5. S. A. Krivelevich, Vestn. Nizhegorodsk. Univ., Ser. Fiz. Tverd. Tela, No. 2, 71 (1998).
6. S. S. Gorelik and M. Ya. Dashevskiĭ, *Materials Science: Semiconductors and Metals* (Metallurgiya, Moscow, 1973) [in Russian].
7. A. A. Kolotov, F. Z. Gil'mutdinov, and V. Ya. Bayankin, Pis'ma Zh. Tekh. Fiz. **30** (16), 7 (2004) [Tech. Phys. Lett. **30**, 666 (2004)].

Translated by K. Shakhlevich

Technical Physics, Vol. 50, No. 11, 2005, pp. 1528–1530. Translated from Zhurnal Tekhnicheskoĭ Fiziki, Vol. 75, No. 11, 2005, pp. 136–138.

SHORT COMMUNICATIONS

Photoelectron Emission from Granulated Gold Films Activated by Cesium and Oxygen

E. L. Nolle and M. Ya. Schelev

Institute of General Physics, Russian Academy of Sciences, ul. Vavilova 38, Moscow, 119991 Russia

e-mail: nolle@ran.gpi.ru

Received March 14, 2005

Abstract—Granulated gold films activated by cesium and oxygen are found to produce an intense photoelectron emission band about 100 nm wide at a wavelength of 530 nm with a sensitivity of about 4 mA/W in the visible range. This band is likely to be associated with excitation of surface plasmons. The results obtained indicate that, owing to surface photoeffect, gold films activated by Cs and O can be used as fast photocathodes with a time constant of several femtoseconds. © *2005 Pleiades Publishing, Inc.*

It is known that absorption and reflection of light by thin granulated metallic films (unlike by bulk metals) in the visible range are accompanied by the formation of absorption bands due to size effects [1]. As was shown in [2], granulated films of Au nanoparticles exhibit an absorption band near 600 nm and a similar band is observed in films of Ag nanoparticles near 500 nm [3]. According to [2, 3], these bands are due to the excitation of surface plasmons in metallic nanoparticles having the shape of oblate spheroids. The ratio of the substrate area filled by nanoparticles to the total area was equal to $f \approx 10^{-3}$ for Au [2] and $f \approx 0.5$ for Ag [3], which indicated the vertical growth of Au nanoparticles on the substrate surface (their average size was z = 3–4 nm). In [4], we detected intense photoelectron emission (PE) near 500 nm from Ag particles activated by Cs and O, which is likely to be caused by surface plasmons excited in such spheroids. In this case, photoelectron transport to the surface is absent; therefore, one can expect a small time constant (of about several femtoseconds) for photocathodes based on metallic nanoparticles. This time constant is specified by the time it takes for a plasmon to pass through a nanoparticle. The production of such photocathodes is now becoming a topical problem in view of recent advances in femtosecond photoelectronics—a burgeoning area of science and technology [5]. Moreover, metallic photocathodes are the most convenient to produce femtosecond electron pulses by means of powerful pulsed lasers, since they offer a high thermal conductivity, electric conductivity, and specific heat. Such cathodes are exemplified by massive photocathodes with an inactivated surface that operate in the reflection mode at glancing incidence of a light beam on the surface. They exploit the surface photoeffect under one- [6] and multiphoton [7, 8] excitation. However, the sensitivity of these photocathodes is low: for continuous Au films, it is about 3 μA/W at λ = 250 nm [6] and 10^{-2} μA/W at λ = 800 nm [7].

The purpose of this work was to generate surface-plasmon-induced PE from granulated Au films in the visible range and compare this effect with the properties of bulk Au samples and with PE from Ag nanoparticles studied in [4].

The production of granulated Au films, their activation by Cs and O, recording of PE and reflectance spectra, and examination of the film surface compositions by Auger electron spectroscopy (AES) and X-ray photoelectron spectroscopy (XPES) were carried out at a pressure of 10^{-10} Torr using the same technique as that applied for production of Ag films [4]. An Au film of thickness d = 7 nm was evaporated onto a thin ($d \approx$ 3 nm) Al_2O_3 film grown on a thick ($d \approx$ 100 nm) Al film. The Au film was then heated at $T \approx$ 300°C for 20 min. The films thus obtained are usually granulated, as evidenced by XPES spectra, where the Al_{2p} and Al_{2s} peaks from the substrate are approximately equal to the Au_{4f} peak from the Au nanoparticles. Since the elemental sensitivity coefficients of the Al peaks are roughly one order of magnitude lower than those of the corresponding Au peaks, we have $f \approx 0.1$, which indicates vertical growth of the nanoparticles. The Au films were activated by Cs and O without switching off the Cs source. Contrary to the case of Ag films, the O source, which increased the pressure in the chamber by about ten times, was switched on only at the final stage of activation, after sensitivity S had dropped by 30% of a maximum value reached upon activation by Cs alone (Fig. 1, time instant *2*). With the O source switched on, sensitivity S rose by one to two orders of magnitude in both the granulated and continuous Au films. To maximize the sensitivity in the red spectral range, the films were activated first by white light and then by the light passed through a KS-19 red filter ($\lambda \geq$ 700 nm; Fig. 1,

1063-7842/05/5011-1528$26.00

time instant *1*). PE was excited by nonpolarized light incident at an angle of 0°, and the reflected light intensity was measured at an angle of 45° to the normal to the film surface.

Spectral sensitivity $S(\lambda)$ of the continuous films activated by Cs and O in the range under study (λ = 400–800 nm; Fig. 2, curve *2*) is about ten times higher than that of the films activated only by Cs (Fig. 2, curve *1*). Spectrum $S(\lambda)$ for these films consists of one broad band with a maximum (S_m = 1.8 mA/W) at λ_1 = 30 nm. This corresponds to quantum yield Q = 0.52% relative to incident photons. As follows from Fig. 2, the spectral range of this PE band (curve *2*) nearly coincides with spectral range $R(\lambda)$ of the reflection band. The minimum of the latter, R = 40%, lies at $\lambda \le 500$ nm (curve *4*). According to [9], this reflection band is due to interband absorption of light in the volume of Au.

$S(\lambda)$ spectra taken of the granulated films activated by Cs and O contain a new long-wavelength PE band (Fig. 2, curve *3*) about 100 nm wide with a maximum at λ_2 = 530 nm. The sensitivity in this maximum is S_m = 3.9 mA/W, which corresponds to Q = 0.9%. As compared to the continuous films, the PE intensity of the short-wavelength band in the granulated films rises to S_m = 4.3 mA/W (Q = 1.24%), and the reflection band edge shifts toward longer waves (from 570 to 750 nm). The minimum of the reflection band declines to R = 26% at λ = 480 nm (Fig. 2, curve *5*).

The appearance of the new intense PE band with a maximum at λ_2 = 530 nm, whose spectral range (Fig. 2, curve *3*) coincides with that of the reflection band (Fig. 2, curve *5*), in the granulated Au films activated by Cs and O may be explained by the excitation of surface plasmons in Au nanoparticles, just as in similar Ag films [4]. Unlike the Ag films, the Au films do not exhibit a volume plasma resonance at λ = 330 nm because of intense interband absorption, which begins at $\lambda \le 550$ nm [9]. Therefore, unlike in the case of Ag [4], we could not reveal a distinct band due to surface plasmons in the reflection spectra of the granulated Au films because of the shading effect of the band associated with interband absorption. Another dissimilarity from the Ag films is a significant increase in the PE sensitivity in the continuous Au films activated by both Cs and O up to S = 1.8 mA/W in the visible region versus S = 0.19 mA/W for the films activated by Cs alone (Fig. 2; curves *2* and *1*, respectively). Since PE in these films is caused by interband transitions and the work function after activation by Cs and O is lower than that after activation by Cs alone, a larger number of photoelectrons reach the surface and escape into a vacuum before their energy becomes lower than the vacuum level because of scattering. The different results of activation of the Au and Ag films by cesium and oxygen is likely to be related to the difference in their chemical properties: Ag is active with respect to O, forming Ag_2O oxide, and inactive with respect to Cs, whereas

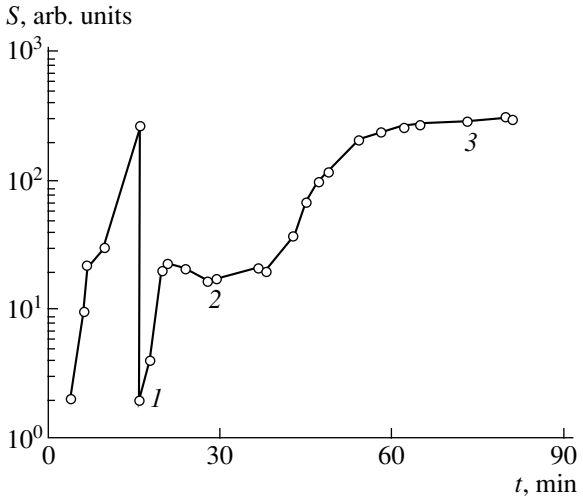

Fig. 1. Variation of the granulated Au film sensitivity with time of activation by Cs and O. The Cs source operates continuously. Indicated are the time instants at which (*1*) KS-19 light filter is introduced, (*2*) oxygen source is switched on, and (*3*) oxygen source is switched off.

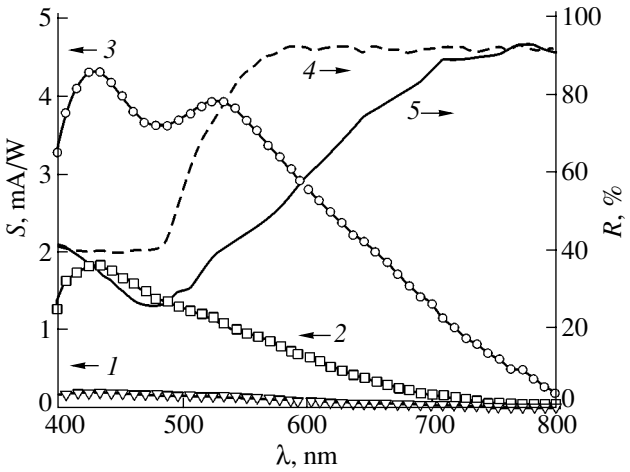

Fig. 2. Sensitivity (S) and reflectance (R) spectra of the Au films: (*1*) continuous film activated by Cs alone, (*2*) continuous film activated by Cs and O, (*3*) granulated film activated by Cs and O, (*4*) continuous film, and (*5*) granulated film.

Au forms a CsAu compound but is inactive with respect to O.

The AES and XPES studies show that the chemical composition of the surface of the Cs- and O-activated Au films is identical to that of the Ag films [4]. Therefore, as in the Ag films, the decrease in the work function of the Au films is caused by a thin (about 1 nm) dipole layer consisting of Cs^+ ion dipoles and Cs–O–Cs dipoles.

Thus, a new intense PE band associated with surface plasmons appears in granulated Au films. At the maximum of this band (λ_2 = 530 nm), we have $S \approx 4$ mA/W,

which is several orders of magnitude higher than the sensitivity of photocathodes made of inactivated continuous metal films [6, 7]. Since photoelectron transport to the surface is absent, both Au and Ag granulated films activated by Cs and O can be used as photocathodes with a resolution of a few femtoseconds for time analysis of fast processes and for generation of pulsed electron beams. Since the granule size is low and vertical growth of Au nanoparticles is slow, semitransparent and low-resistivity Au films evaporated onto a transparent substrate, e.g., onto a SnO_2 film on quartz, may serve as effective metallic photocathodes operating in the transmission mode in the visible spectral range.

ACKNOWLEDGMENTS

This work was supported by the program "Low-Dimensional Quantum Nanostructures" (project no. 4.12) of the Russian Academy of Sciences.

REFERENCES

1. Yu. I. Petrov, *The Physics of Fine Particles* (Nauka, Moscow, 1982) [in Russian].
2. C. G. Granqvist and O. Hunderi, Phys. Rev. B **16**, 3513 (1977).
3. S. W. Kennerly, J. W. Little, R. J. Warmack, *et al.*, Phys. Rev. B **29**, 2926 (1984).
4. E. L. Nolle and M. Ya. Schelev, Pis'ma Zh. Tekh. Fiz. **30** (8), 1 (2004) [Tech. Phys. Lett. **30**, 304 (2004)].
5. M. Ya. Schelev, Usp. Fiz. Nauk **170**, 1002 (2000) [Phys. Usp. **43**, 931 (2000)].
6. S. D. Moustaizis, M. Tatarakis, C. Kalpouros, *et al.*, Appl. Phys. Lett. **60**, 1939 (1992).
7. S. Bastiani-Ceccotti, P. Monchicourt, and T. Lehner, Phys. Rev. B **68**, 245411 (2003).
8. V. M. Shalaev, C. Douketis, T. Haslett, *et al.*, Phys. Rev. B **53**, 11193 (1996).
9. P. B. Johnson and R. W. Christy, Phys. Rev. B **6**, 4370 (1972).

Translated by K. Shakhlevich

Technical Physics, Vol. 50, No. 11, 2005, pp. 1531–1534. Translated from Zhurnal Tekhnicheskoĭ Fiziki, Vol. 75, No. 11, 2005, pp. 139–142.

SHORT COMMUNICATIONS

Calculation of the Properties of a Lens Made of Glass Bricks by the Equivalent-Current Method

D. V. Shannikov, V. V. Surikov, and S. V. Kuz'min

St. Petersburg State Polytechnic University,
Politekhnicheskaya ul. 29, St. Petersburg, 195251 Russia
e-mail: Postbox@stu.neva.ru

Received March 14, 2005

Abstract—The properties of a lens antenna are calculated by the equivalent-current method (second equivalence principle). A Luneberg lens formed by glass bricks is considered. The results of these calculations are compared with experimental data. The possibility is considered of applying the above theoretical method to calculating lens antennas where there is a random deviation of the dielectric constant from a preset distribution. © *2005 Pleiades Publishing, Inc.*

In the present study, we consider antennas of the Luneberg lens type—that is, a spherical lens characterized by central symmetry and a refraction coefficient changing along the radius. It enables one to create a cophased distribution of the field over the antenna aperture, the amplitude distribution of the field at the lens aperture becoming constant for a specific polar diagram of the feeding antenna. The advantages of Luneberg lenses, such as electromechanical scanning over a total sector of angles without rotating the antenna as a discrete unit and the possibility of creating multiray systems by using one lens, are due to central symmetry. However, the technology of manufacturing such lenses is rather complicated. This problem is partly solved by going over from a continuous distribution of the refraction coefficient to a stepwise one—that is, to a spherical lens formed by layers from a homogeneous dielectric material or to a lens from bricks (the latter is considered in [1] and in the present article).

In this study, we determine the diffraction field at a Luneberg lens by using the equivalent-current method (the second equivalence principle proposed by Kontorovich). The method essentially consists in that the dielectric field generating a secondary field is replaced by a system of equivalent currents in a vacuum.

Let us consider one of the Maxwell equations,

$$\mathrm{curl}\mathbf{H} = j\frac{\omega}{c}\varepsilon\mathbf{E} + \frac{4\pi}{c}\mathbf{j}_e,$$

where $\mathbf{j}_e$ is an outside electric current.

This equation can be recast into the form

$$\mathrm{curl}\mathbf{H} = j\frac{\omega}{c}\varepsilon_0\mathbf{E} + \mathbf{j}_e + j\frac{\omega}{c}(\varepsilon - \varepsilon_0)\mathbf{E}$$

$$= j\frac{\omega}{c}\varepsilon_0\mathbf{E} + \frac{4\pi}{c}\mathbf{j}_e + \frac{4\pi}{c}\mathbf{j}_e',$$

where

$$\mathbf{j}_e' = j\frac{\omega}{4\pi}(\varepsilon - \varepsilon_0)\mathbf{E}$$

is an equivalent current.

For a free space, $\varepsilon_0 = 1$; therefore, we have

$$\mathbf{j}_e' = j\frac{\omega}{4\pi}(\varepsilon - 1)\mathbf{E}.$$

For another Maxwell equation, we can perform similar transformations by introducing an equivalent magnetic current.

In accordance with the equivalent-current method, we can represent the polar diagram of the lens being considered in the form

$$F_L(\theta_1) = \int_0^1\int_0^\pi J_0(kr'\sin\theta\sin\theta_1)$$

$$\times\,\Phi(r, \theta, \theta_1)r'^2\sin\theta\frac{E(\theta, r')(\varepsilon(r') - 1)}{\sqrt[4]{\varepsilon(r')}}d\theta dr', \quad (1)$$

$$\Phi(r, \theta, \theta_1) = \exp(jkl_e)\exp(jkr'\cos(\theta)\cos(\theta_1)),$$

where θ_1 is the angle between the direction to the observation point and the axis connecting the center of the lens and the feeding antenna, θ and r' are coordinates of an integration point within the body of the lens (the radius of the lens is taken to be unity), k is the wave vector, $E(\theta, r')$ is the electric-field strength at an integration point, and l_e is the electric length of the ray going from the feeding antenna to the integration point.

The Bessel function in the integrand on the right-hand side of (1) arises upon integration over angle φ. The amplitudes $E(\theta, r')$ and the phases kl_e of the relevant rays were calculated at individual points with a

1063-7842/05/5011-1531$26.00

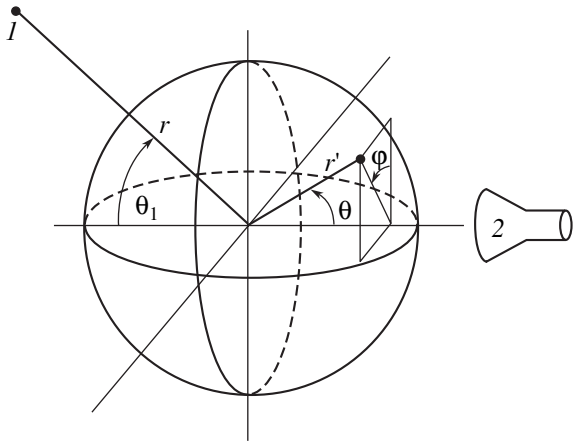

Fig. 1. Geometry of the problem: (*1*) observation point and (*2*) feeding antenna.

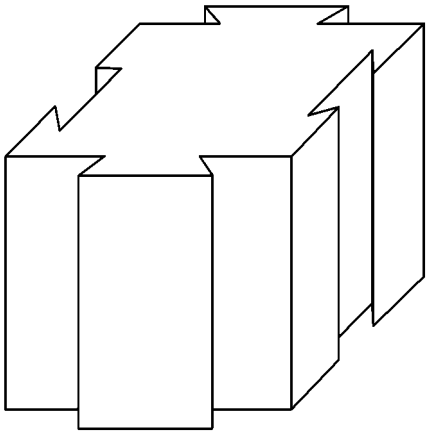

Fig. 2. Shape of a brick.

step of 1° in angle θ and a step of 0.01 in the radius. Also, we employed the principle of geometric optics (in order to determine the trajectories of the rays) and the energy-conservation law. The integral in (1) was evaluated by means of Simpson's rule. In representing the field in form (1), it was assumed that the field within the body of the lens is independent of the angle φ (a corrugated horn was used for a feeding antenna).

Let us consider a lens fabricated by the Konkur enterprise in accordance with [2]. This lens was made from bricks having different dielectric constants. The type of a brick is chosen in such a way as to ensure the closest proximity of its dielectric constant to the dielectric constant of the Luneberg lens at the radius equal to the distance between the lens center and the center of this brick. The shape of a brick is shown in Fig. 2.

The faces of the bricks generate two sets of parallel vertical planes. If we now assume that the coordinates of the brick centers in the horizontal plane are integers, then it turns out that, if their sum is even, the coordinates of the brick centers in the vertical direction are also integers. Otherwise, the bricks are shifted in the vertical direction by half their height.

Figure 3 shows the coordinate dependence of the refraction coefficients in a lens from bricks (solid line) and a Luneberg lens (dotted curve).

A lens from bricks can be considered as a low-turbulent random medium. There exist approximate methods for calculating such media. The Rytov and Born approximations [3] for a spherical wave and a low level of fluctuations of the refraction coefficient (the graph is given in Fig. 4) are the most popular approximations. One can see from Fig. 3 that the deviation of the refraction coefficient from the preset one does not exceed 4%; therefore, it would be legitimate to use the aforementioned approximations.

Since the number of nominal values of the dielectric constant is usually small, the number of regions where the dielectric constant differs from an ideal law is much greater. Moreover, the signs of the deviation of the dielectric constant in neighboring regions are opposite (see Figs. 3, 4). Therefore, one can expect that fields associated with errors in integration will generate a rather small total field, so that the polar diagram of a lens from bricks will not differ substantially from the polar diagram of the respective ideal Luneberg lens (Fig. 5).

The Born approximation, which was used in the present study, can be represented as

$$U(r) = U_0(r) + \int_{V'} k^2 G(r-r')U_0(r')n_1(r')dV', \quad (2)$$

where $U_0(r)$ is the field of the Luneberg lens (undisturbed lens), $U_0(r')$ is the field within the body of the lens, $n_1(r')$ is the deviation of the refraction coefficient from the preset continuous one (see Fig. 4), $G(r-r')$ is the Green's function for a free space, and k is the wave number.

Expression (2) differs from expression (1) in that the unperturbed value of the field is used there for the field itself in the integrand.

In the case being considered, it is not reasonable to use the Rytov approximation because the jumps in $U_0(r)$ may be quite sizable (above 50 dB). The point is that, appearing in the denominator [3, 4], $U_0(r)$ gives rise to large numbers in the integrand. This leads to unreliable results since the number of decimal places admitted by a computer is finite.

The integral in (1) was calculated by the method of rectangles with a step of 1° in angle θ and a step of 0.01 in the radius. The integral in (2) was evaluated by the method of rectangles as well, but, in contrast to the preceding case, use was made of a cubic grid chosen in such a way that there were five grid points over the length of a brick.

One can see from Fig. 4 that the presence of bricks leads to the appearance of an additional background in

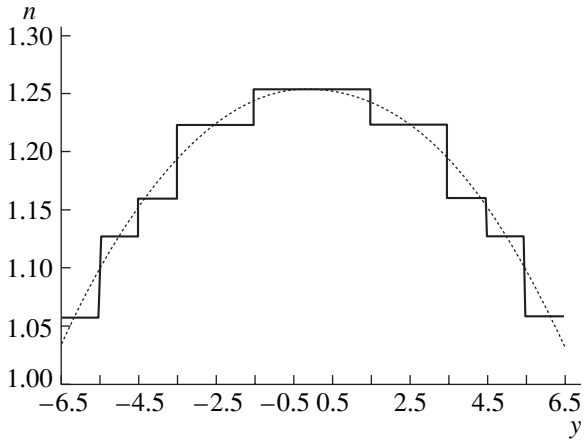

Fig. 3. Refraction coefficient ($x = 0$, $z = 0$).

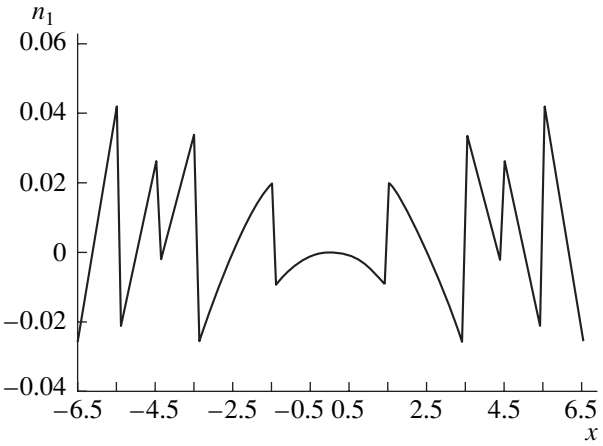

Fig. 4. Deviation of the refraction coefficient ($y = 0$, $z = 0$) within a lens formed by bricks from the value corresponding to the Luneberg lens.

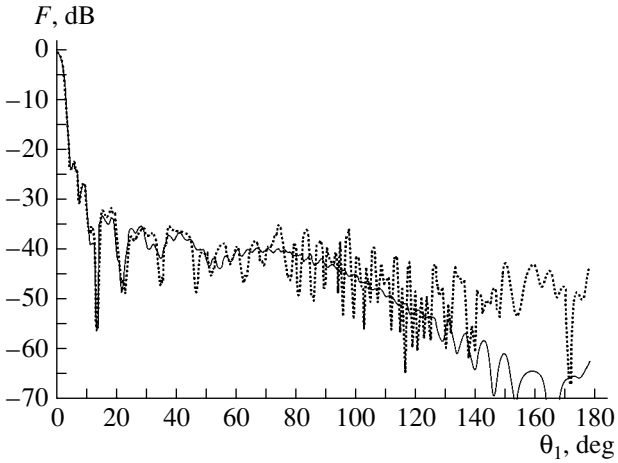

Fig. 5. Polar diagrams of (solid curve) the Luneberg lens and (dotted curve) the lens from bricks at a focal length of $f = 1.4R$, where R is the radius of the length. The remaining parameters are $D/\lambda = 18.3$ and $D = 2R$, λ being the wavelength.

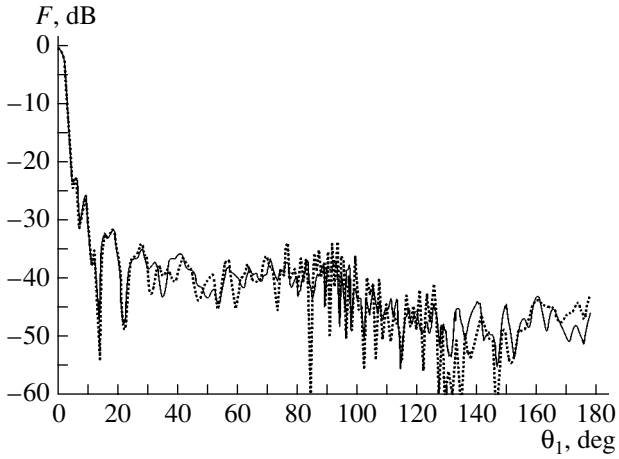

Fig. 6. Averaged theoretical polar diagram (solid curve) and one of the realizations (dotted curve).

the region of far side (E_2) and back radiation at a level of from 40 to 45 dB. The average level of this background can be estimated by calculating the power associated with this background. Indeed, both the linear dimensions and the positions of the regions where there are deviations of the dielectric constant are quasirandom, their linear dimensions being on average equal to half the brick length. It follows that, upon performing summation of the fields from these regions in power [without regard to phases] and normalization to the maximum field, we obtain

$$E_{\text{noise}} = \frac{\sqrt{2\pi\int_0^R\int_0^\pi\left(2\frac{\Delta n}{\sqrt[4]{\varepsilon(r')}}E(\theta, r')r'^2\sin(\theta)\frac{k^2}{4\pi}\right)^2 d\theta dr'}}{E_{\max}},$$

$$E_2 = 20\log(E_{\text{noise}}). \quad (3)$$

This formula is a corollary of formula (1). The factor $k^2/4\pi$ is the coefficient of proportionality between the amplitude of the equivalent current and the amplitude of the field E generated by this current in the far zone.

For the lens being considered, the level of the background in terms of the field was –46 dB.

In order to confirm the possibility of employing the proposed approach, we have measured the polar diagram of a lens built from bricks. In order to increase the dynamical range of these measurements, we used a synchronous detection in processing a relevant signal in a computer. The developed code made it possible to perform an appropriate treatment of resulting data and to construct the polar diagram of the antenna.

It should be noted that the experimental polar diagrams of the antenna were determined for various orientations of the feeding antenna with respect to the

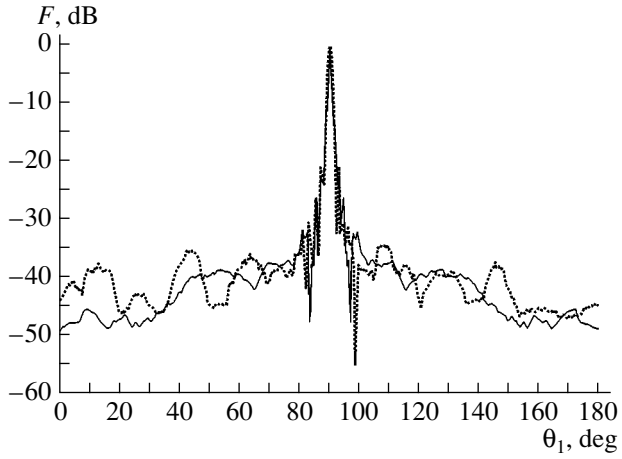

Fig. 7. Experimental (solid curve) and theoretical (dotted curve) polar diagrams of the lens from bricks.

brick planes. We can state that we are dealing with individual realizations of a random process. This process is not steady-state; therefore, it is reasonable to compare averaged theoretical and experimental polar diagrams.

In our experiment, the lens was always arranged in such a way that the brick faces not containing tenons and mortises (see Fig. 2) lay in the plane of angle θ_1. By rotating the lens about the vertical axis, we then obtained a new realization.

Figure 6 shows the calculated polar diagrams (the solid and dotted curves represent, respectively, the polar diagram averaged over four realizations and the polar diagram for one of the realizations). One can see that the distinction between specific realizations is insignificant.

For a lens from bricks, Fig. 7 displays the theoretical (represented by the solid curve in Fig. 6) and the experimental polar diagram averaged over the angle θ_1. The averaging was performed in a window of size 10°, this window being moved over the entire range of the angle θ_1, with the exception of the segment $|\theta_1| < 20°$—that is, over the region of far side lobes.

From this graph, one can see that the approach outlined in the present article yields reliable results over the entire sector of angles. This method may be used to calculate the fields of dielectric antennas belonging to different types and featuring random deviations of the dielectric constant from a preset one.

REFERENCES

1. B. Z. Katsenelenbaum and A. V. Golubyatnikov, Pis'ma Zh. Tekh. Fiz. **24** (15), 69 (1998) [Tech. Phys. Lett. **24**, 611 (1998)].
2. RF Patent No. 2,099,843 (December 20, 1997).
3. A. Ishimaru, *Wave Propagation and Scattering in Random Media* (Academic, New York, 1978; Mir, Moscow, 1981), Vol. 1.
4. E. G. Zelkin and R. A. Petrova, *Lens Antennas* (Sov. Radio, Moscow, 1974) [in Russian].

Translated by A. Isaakyan